Sensitivity optimization for NV-diamond magnetometry

John F. Barry

Lincoln Laboratory, Massachusetts Institute of Technology, Lexington, Massachusetts 02421, USA, Harvard-Smithsonian Center for Astrophysics, Cambridge, Massachusetts 02138, USA, Department of Physics, Harvard University, Cambridge, Massachusetts 02138, USA, and Center for Brain Science, Harvard University, Cambridge, Massachusetts 02138, USA

Jennifer M. Schloss of

Lincoln Laboratory, Massachusetts Institute of Technology, Lexington, Massachusetts 02421, USA, Harvard-Smithsonian Center for Astrophysics, Cambridge, Massachusetts 02138, USA, Center for Brain Science, Harvard University, Cambridge, Massachusetts 02138, USA, and Department of Physics, Massachusetts Institute of Technology, Cambridge, Massachusetts 02139, USA

Erik Bauch

Department of Physics, Harvard University, Cambridge, Massachusetts 02138, USA

Matthew J. Turner

Department of Physics, Harvard University, Cambridge, Massachusetts 02138, USA and Center for Brain Science, Harvard University, Cambridge, Massachusetts 02138, USA

Connor A. Hart

Department of Physics, Harvard University, Cambridge, Massachusetts 02138, USA

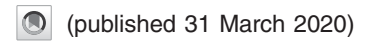
Linh M. Pham

Lincoln Laboratory, Massachusetts Institute of Technology, Lexington, Massachusetts 02421, USA and Harvard-Smithsonian Center for Astrophysics, Cambridge, Massachusetts 02138, USA

Ronald L. Walsworth[‡]

Quantum Technology Center, University of Maryland, College Park, Maryland 20742, USA, Department of Electrical and Computer Engineering, University of Maryland, College Park, Maryland 20742, USA, Department of Physics, University of Maryland, College Park, Maryland 20742, USA, Harvard-Smithsonian Center for Astrophysics, Cambridge, Massachusetts 02138, USA, Department of Physics, Harvard University, Cambridge, Massachusetts 02138, USA,

and Center for Brain Science, Harvard University, Cambridge, Massachusetts 02138, USA



Solid-state spin systems including nitrogen-vacancy (NV) centers in diamond constitute an increasingly favored quantum sensing platform. However, present NV ensemble devices exhibit sensitivities orders of magnitude away from theoretical limits. The sensitivity shortfall both handicaps existing implementations and curtails the envisioned application space. This review analyzes present and proposed approaches to enhance the sensitivity of broadband ensemble-NV-diamond magnetometers. Improvements to the spin dephasing time, the readout fidelity, and the host diamond material properties are identified as the most promising avenues and are investigated extensively. This analysis of sensitivity optimization establishes a foundation to stimulate development of new techniques for enhancing solid-state sensor performance.

DOI: 10.1103/RevModPhys.92.015004

^{*}john.barry@ll.mit.edu †jennifer.schloss@ll.mit.edu ‡walsworth@umd.edu

CONTENTS	
I. Introduction and Background	2
A. NV-diamond magnetometry overview	2
B. Magnetometry introduction	4
C. The NV ⁻ ground-state spin	4
D. Ramsey measurements NV	6
E. Spin dephasing and decoherence	6
F. dc and ac sensing	7
II. Measurement Sensitivity Considerations	7 7
A. Magnetic-field sensitivity B. Alternatives to Ramsey magnetometry	9
Anternatives to Rainsey magnetometry Continuous-wave optically detected magnetic	7
resonance	9
2. Pulsed ODMR	10
C. Parameters limiting sensitivity	13
III. Limits to Relaxation Times T_2^* and T_2	14
A. Motivation to extend T_2^*	14
B. Ensemble and single-spin T_2^*	15
C. Dephasing mechanisms	16
D. Nitrogen limit to T_2^*	17
E. Nitrogen limit to T_2	18
F. 13 C limit to T_2^*	19
G. NV ⁻ limit to T_2^*	20
IV. Methods to Extend T_2^* and T_2	21
A. Dynamical decoupling for ac magnetometry B. Double-quantum (DQ) coherence magnetometry	21 23
C. Spin-bath driving	25
D. Transverse strain and electric-field mitigation	27
V. Methods to Increase Readout Fidelity	28
A. Spin-to-charge conversion (SCC) readout	28
B. Photoelectric (PE) readout	29
C. Ancilla-assisted repetitive readout	30
D. Level-anticrossing-assisted readout	31
E. Improved photon collection methods	32
F. Near-infrared (NIR) absorption readout	33
G. Green absorption readout	35
H. Laser threshold magnetometry	35
VI. Diamond Material Engineering	36
A. Conversion efficiency	36 36
B. NV charge-state efficiency1. Nonoptical effects on NV charge-state efficiency	37
2. Optical effects on NV charge-state efficiency	37
C. Diamond synthesis and high-pressure–high-temperature	
(HPHT) treatment	38
D. Electron irradiation	40
E. Low-pressure-high-temperature (LPHT) annealing	41
F. Other common impurities in synthetic or treated single	
crystal diamond	42
G. Preferential orientation	43
VII. Miscellaneous Sensing Techniques	44
A. Rotary echo magnetometry	44
B. Geometric phase magnetometry	44
C. Ancilla-assisted upconversion magnetometry D. Techniques for the strong NV ⁻ -NV ⁻ interaction	45
regime	45
VIII. Conclusion and Outlook	46
List of Symbols and Abbreviations	48
Acknowledgements	49
Appendix	49
1. Derivations	49
a. Ramsey dc magnetic field measurement	49
b. Spin-projection-noise-limited sensitivity	51

c. Photon-shot-noise-limited sensitivity	51
d. Overhead time	53
2. Optimal precession time	53
3. Considerations for increasing sensor number	54
4. Choosing nitrogen concentration in diamond samples	54
5. Spin resonance linewidth and T_2^*	55
6. Estimating T_2^* from spin resonance linewidths of N_S^0	55
7. Stretched exponential parameter	56
8. Isotopic purity confusion in the literature	57
9. Linear Stark and Zeeman regimes	57
10. Example annealing calculations	60
11. The diamond type classification system	60
References	61

I. INTRODUCTION AND BACKGROUND

A. NV-diamond magnetometry overview

Quantum sensors encompass a diverse class of devices that exploit quantum coherence to detect weak or nanoscale signals. As their behavior is tied to physical constants, quantum devices can achieve accuracy, repeatability, and precision approaching fundamental limits (Budker and Romalis, 2007). As a result, these sensors have shown utility in a wide range of applications spanning both pure and applied science (Degen, Reinhard, and Cappellaro, 2017). A rapidly emerging quantum sensing platform employs atomic-scale defects in crystals. In particular, magnetometry using nitrogen-vacancy (NV) color centers in diamond has garnered increasing interest.

The use of NV centers as magnetic-field sensors was first proposed (Degen, 2008; Taylor *et al.*, 2008) and demonstrated with single NVs (Balasubramanian *et al.*, 2008; Maze *et al.*, 2008) and NV ensembles (Acosta *et al.*, 2009) circa 2008. In the decade following, both single- and ensemble-NV-diamond magnetometers (Doherty *et al.*, 2013; Rondin *et al.*, 2014) found use for applications in condensed matter physics (Casola, van der Sar, and Yacoby, 2018), neuroscience and living systems biology (Schirhagl *et al.*, 2014; Wu *et al.*, 2016), nuclear magnetic resonance (NMR) (Wu *et al.*, 2016), Earth and planetary science (Glenn *et al.*, 2017), and industrial vector magnetometry (Grosz, Haji-Sheikh, and Mukhopadhyay, 2017).

Solid-state defects such as NV centers exhibit quantum properties similar to traditional atomic systems yet confer technical and logistical advantages for sensing applications. NVs are point defects composed of a substitutional nitrogen fixed adjacent to a vacancy within the rigid carbon lattice; see Fig. 1(a). Each NV center's symmetry axis is constrained to lie along one of the four [111] crystallographic directions. While NVs are observed to exist in three charge states (NV-, NV⁰, and NV⁺), the negatively charged NV⁻ center is favored for quantum sensing and quantum information applications (Doherty et al., 2013). The NV- defect exhibits a spin-1 triplet electronic ground state with long spin lifetimes at room temperature; longitudinal relaxation times $T_1 \approx 6$ ms (Jarmola et al., 2012; Rosskopf et al., 2014) are typical, and coherence times T_2 up to a few ms are achievable (Balasubramanian et al., 2009). The defect's spin energy levels are sensitive to magnetic fields, electric fields, strain, and temperature variations (Doherty et al., 2013), allowing NV- to operate as a multimodal sensor. Coherent spin control is achieved by

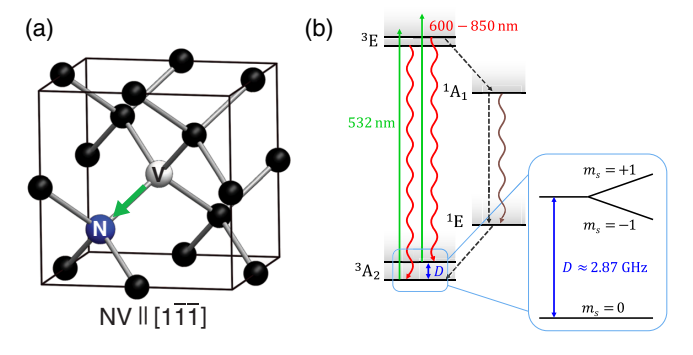


FIG. 1. Overview of the nitrogen-vacancy (NV) center quantum system. (a) Diagram of diamond lattice containing an NV center, which consists of a substitutional nitrogen adjacent to a lattice vacancy. The green arrow marks the NV symmetry axis, oriented along the $\begin{bmatrix} 1\bar{1} \end{bmatrix}$ diamond crystallographic axis for the particular NV center shown here. From Pham, 2013. (b) Energy level diagram for the negatively charged NV⁻ center in diamond, with zero-field splitting D between the ground-state electronic spin levels $m_s = 0$ and $m_s = \pm 1$. The $m_s = \pm 1$ energy levels experience a Zeeman shift in the presence of a magnetic field \vec{B} , which forms the basis for NV⁻ magnetometry. Adapted from Schloss *et al.*, 2018.

application of resonant microwaves (MWs) near 2.87 GHz. Upon optical excitation, nonradiative decay through a spin-state-dependent intersystem crossing (Goldman, Doherty *et al.*, 2015; Goldman, Sipahigil *et al.*, 2015) produces both spin-state-dependent fluorescence contrast and optical spin initialization into the NV⁻ center's $m_s = 0$ ground state; see Fig. 1(b).

Relative to alternative technologies (Grosz, Haji-Sheikh, and Mukhopadhyay, 2017), sensors employing NV⁻ centers excel in technical simplicity and spatial resolution (Grinolds et al., 2014; Arai et al., 2015; Jaskula, Bauch et al., 2017). Such devices may operate as broadband sensors, with bandwidths up to ~100 kHz (Acosta, Jarmola et al., 2010; Barry et al., 2016; Schloss et al., 2018), or as high-frequency detectors for signals up to several GHz (Shin et al., 2012; Cai et al., 2013; Loretz, Rosskopf, and Degen, 2013; Steinert et al., 2013; Tetienne et al., 2013; Pelliccione et al., 2014; Boss et al., 2016, 2017; Hall et al., 2016; Lovchinsky et al., 2016; Pham et al., 2016; Shao et al., 2016; Wood et al., 2016; Aslam et al., 2017; Schmitt et al., 2017; Casola, van der Sar, and Yacoby, 2018; Horsley et al., 2018). Importantly, effective optical initialization and readout of NV- spins does not require narrow-linewidth lasers; rather, a single free-running 532-nm solid-state laser is sufficient. NV-diamond sensors operate at ambient temperatures, pressures, and magnetic fields and thus require no cryogenics, vacuum systems, or tesla-scale applied bias fields. Furthermore, diamond is chemically inert, making NV⁻ devices biocompatible. These properties allow sensors to be placed within ~ 1 nm of field sources (Pham et al., 2016), which enables magnetic-field imaging with nanometer-scale spatial resolution (Grinolds et al., 2014; Arai et al., 2015; Jaskula, Bauch et al., 2017). NV-diamond sensors are also operationally robust and may function at pressures up to 60 GPa (Doherty et al., 2014; Ivády et al., 2014; Hsieh et al., 2019) and temperatures from cryogenic to 600 K (Toyli et al., 2012, 2013; Plakhotnik et al., 2014).

Although single NV⁻ centers find numerous applications in ultra-high-resolution sensing due to their angstrom-scale size (Balasubramanian et al., 2008; Maze et al., 2008; Casola, van der Sar, and Yacoby, 2018), sensors employing ensembles of NV⁻ centers provide improved signal-to-noise ratio (SNR) at the cost of spatial resolution by virtue of statistical averaging over multiple spins (Taylor et al., 2008; Acosta et al., 2009). Diamonds may be engineered to contain concentrations of NV^- centers as high as 10^{19} cm⁻³ (J. Choi et al., 2017), which facilitates high-sensitivity measurements from single-channel bulk detectors as well as wide-field parallel magnetic imaging (Taylor et al., 2008; Steinert et al., 2010, 2013; Pham et al., 2011; Le Sage et al., 2013; Glenn et al., 2015; Davis et al., 2018; Fescenko et al., 2019). These engineered diamonds typically contain NV⁻ centers with symmetry axes distributed along all four crystallographic orientations, each primarily sensitive to the magnetic-field projection along its axis. Thus, ensemble-NV- devices provide full vector magnetic-field sensing without heading errors or dead zones (Maertz et al., 2010; Steinert et al., 2010; Pham et al., 2011; Le Sage et al., 2013; Schloss et al., 2018). NV⁻ centers have also been employed for high-sensitivity imaging of temperature (Kucsko et al., 2013), strain, and electric fields (Dolde et al., 2011; Barson et al., 2017). Recent examples of ensemble-NV⁻ sensing applications include magnetic detection of single-neuron action potentials (Barry et al., 2016); magnetic imaging of living cells (Le Sage et al., 2013; Steinert et al., 2013), malarial hemozoin (Fescenko et al., 2019), and biological tissue with subcellular resolution (Davis et al., 2018); nanoscale thermometry (Kucsko *et al.*, 2013; Neumann et al., 2013); single protein detection (Shi et al., 2015; Lovchinsky et al., 2016); nanoscale and micron-scale NMR (Staudacher et al., 2013; Loretz et al., 2014; Sushkov et al., 2014; DeVience et al., 2015; Rugar et al., 2015; Kehayias et al., 2017; Bucher et al., 2018; Glenn et al., 2018); and studies of meteorite composition (Fu et al., 2014) and paleomagnetism (Farchi et al., 2017; Glenn et al., 2017).

Despite demonstrated utility in a number of applications, the present performance of ensemble-NV⁻ sensors remains far from theoretical limits. Even the most sensitive ensemblebased devices demonstrated to date exhibit readout fidelities $\mathcal{F} \sim 0.01$, limiting sensitivity to at best ~ 100 times worse than the spin-projection limit. Additionally, reported dephasing times T_2^* in NV-rich diamonds remain 100 to 1000 times shorter than the theoretical maximum of $2T_1$ (Jarmola et al., 2012; Bauch et al., 2018, 2019). As a result, whereas present state-of-the-art ensemble-NV⁻ magnetometers exhibit pT/\sqrt{Hz} -level sensitivities, competing technologies such as superconducting quantum interference devices (SQUIDs) and spin-exchange relaxation-free magnetometers exhibit sensitivities at the fT/ $\sqrt{\text{Hz}}$ level and below (Kitching, 2018). This ~1000 times sensitivity discrepancy corresponds to a $\sim 10^6$ times increase in required averaging time, which precludes many envisioned applications. In particular, the sensing times required to detect weak static signals with an NV-diamond sensor may be unacceptably long; for example, biological systems may have only a short period of viability.

In addition, many applications, such as spontaneous event detection and time-resolved sensing of dynamic processes (Marblestone et al., 2013; Shao et al., 2016), are incompatible with signal averaging. Realizing NV-diamond magnetometers with improved sensitivity could enable a new class of scientific and industrial applications poorly matched to bulkier SQUID and vapor-cell technologies. Examples include noninvasive, real-time magnetic imaging of neuronal circuit dynamics (Barry et al., 2016), high throughput nanoscale and micron-scale NMR spectroscopy (Bucher et al., 2018; Glenn et al., 2018; Smits et al., 2019), nuclear quadrupole resonance (NQR) (Lovchinsky et al., 2017), human magnetoencephalography (Hämäläinen et al., 1993), subcellular magnetic resonance imaging (MRI) of dynamic processes (Davis et al., 2018), precision metrology, tests of fundamental physics (Rajendran et al., 2017), and simulation of exotic particles (Kirschner et al., 2018).

This review accordingly focuses on understanding present sensitivity limitations for ensemble-NV⁻ magnetometers to guide future research efforts. We survey and analyze methods for optimizing magnetic-field sensitivity, which we divide into three broad categories: (i) improving spin dephasing and coherence times, (ii) improving readout fidelity, and (iii) improving quality and consistency of host diamond material properties. Given the square-root improvement of sensitivity with the number of interrogated spins, we primarily concentrate on ensemble-based devices with $\gtrsim 10^4$ NV⁻ centers (Acosta et al., 2009; Le Sage et al., 2012; Clevenson et al., 2015; T. Wolf et al., 2015; Barry et al., 2016). However, we also examine single-NV⁻ magnetometry techniques in order to determine their applicability to ensembles. Moreover, while this work primarily treats broadband, time-domain magnetometry from dc up to ~100 kHz, narrowband ac sensing techniques are also analyzed when considered relevant to future dc and broadband magnetometry advances. Alternative phase-insensitive ac magnetometry techniques, such as T_1 relaxometry (Tetienne et al., 2013; Pelliccione et al., 2014; Romach et al., 2015; van der Sar et al., 2015; Hall et al., 2016; Shao et al., 2016; Ariyaratne et al., 2018; Casola, van der Sar, and Yacoby, 2018), are not discussed.

This review is organized as follows: the remainder of Sec. I provides introductory material on NV⁻ magnetometry, with Sec. I.B introducing magnetic-field sensing, Sec. I.C presenting the NV- spin Hamiltonian and its magneticfield-dependent transitions, Sec. I.D describing quantum measurements using the NV- spin, Sec. I.E outlining how spin dephasing and decoherence limit magnetometry, and Sec. I.F summarizing differences between dc and ac sensing approaches while focusing subsequent discussion on dc sensing. Section II concentrates on magnetic-field sensitivity, with Sec. II.A introducing the mathematical formalism governing sensitivity of Ramsey-based ensemble-NV- magnetometers, Sec. II.B reviewing common alternatives to Ramsey protocols for dc magnetometry, and Sec. II.C overviewing key parameters that determine magnetic-field sensitivity. Section III examines the NV⁻ spin ensemble dephasing time T_2^* and coherence time T_2 . In particular, Sec. III.A motivates efforts to extend T_2^* , Sec. III.B highlights relevant definitional differences of T_2^* for ensembles and single spins, Sec. III.C characterizes various mechanisms contributing to NVensemble T_2^* , and Secs. III.D-III.G investigate limits to T_2^* and T_2 from dipolar interactions with specific paramagnetic species within the diamond. Section IV analyzes methods to extend the NV⁻ ensemble dephasing and coherence times using dc and radio-frequency (rf) magnetic fields. Section V analyzes a variety of techniques demonstrated to improve the NV⁻ ensemble readout fidelity. Section VI reviews progress in engineering diamond samples for high-sensitivity magnetometry, primarily focusing on increasing the NV⁻ concentration while maintaining long T_2^* times and good readout fidelity. Section VII analyzes several additional NV-diamond magnetometry techniques not covered in previous sections. Section VIII provides concluding remarks and an outlook on areas where further study is needed. We note that this review aims to comprehensively cover relevant results reported through mid-2017 and provides limited coverage of results published thereafter.

B. Magnetometry introduction

Magnetometry is the measurement of a magnetic field's magnitude, direction, or projection onto a particular axis. A simple magnetically sensitive device is a compass needle, which aligns along the planar projection of the ambient magnetic field. Regardless of sophistication, all magnetometers exhibit one or more parameters dependent upon the external magnetic field. For example, the voltage induced across a pickup coil varies with applied ac magnetic field, as does the resistance of a giant magnetoresistance sensor. In atomic systems such as gaseous alkali atoms, the Zeeman interaction causes the electronic-ground-state energy levels to shift with magnetic field. Certain color centers including NVin diamond also exhibit magnetically sensitive energy levels. For both NV⁻ centers and gaseous alkali atoms, magnetometry reduces to measuring transition frequencies between energy levels that display a difference in response to magnetic fields. Various approaches allow direct determination of a transition frequency; for example, frequency-tunable electromagnetic radiation may be applied to the system, and the transition frequency localized from recorded absorption, dispersion, or fluorescence features. Transition frequencies may also be measured via interferometric techniques, which record a transition-frequency-dependent phase (Rabi, 1937; Ramsey, 1950).

C. The $NV^{\scriptscriptstyle -}$ ground-state spin

The NV⁻ center's electronic-ground-state Hamiltonian can be expressed as

$$\mathcal{H} = \mathcal{H}_0 + \mathcal{H}_{\text{nuclear}} + \mathcal{H}_{\text{elec|str}},\tag{1}$$

where \mathcal{H}_0 encompasses the NV⁻ electron spin interaction with external magnetic field \vec{B} and zero-field-splitting parameter $D \approx 2.87$ GHz, which results from an electronic spin-spin interaction within the NV⁻; $\mathcal{H}_{\text{nuclear}}$ characterizes interactions arising from the nitrogen's nuclear spin; and $\mathcal{H}_{\text{elec}|\text{str}}$ describes the electron spin interaction with electric fields and crystal strain. Defining z to be along the NV⁻ internuclear axis, \mathcal{H}_0 may be expressed as

$$\mathcal{H}_0/h = DS_z^2 + \frac{g_e \mu_B}{h} (\vec{B} \cdot \vec{S}), \tag{2}$$

where $g_e \approx 2.003$ is the NV electronic g factor, μ_B is the Bohr magneton, h is Planck's constant, and $\vec{S} = (S_x, S_y, S_z)$ is the dimensionless electronic spin-1 operator. \mathcal{H}_0 is the simplest Hamiltonian sufficient to model basic NV⁻ spin behavior in the presence of a magnetic field.

The NV⁻ center's nitrogen nuclear spin (I = 1 for ¹⁴N and I = 1/2 for ¹⁵N) creates additional coupling terms characterized by

$$\mathcal{H}_{\text{nuclear}}/h = A_{\parallel} S_z I_z + A_{\perp} (S_x I_x + S_y I_y) + P[I_z^2 - I(I+1)/3] - \frac{g_I \mu_N}{h} (\vec{B} \cdot \vec{I}),$$
 (3)

where A_{\parallel} and A_{\perp} are the axial and transverse magnetic hyperfine coupling coefficients, respectively, P is the nuclear electric quadrupole parameter, g_I is the nuclear g factor for the relevant nitrogen isotope, μ_N is the nuclear magneton, and $\vec{I}=(I_x,I_y,I_z)$ is the dimensionless nuclear spin operator. Experimental values of A_{\parallel} , A_{\perp} , and P are reported in Table XIV. Note that the term proportional to P vanishes for I=1/2 in $^{15}{\rm NV}^-$, as no quadrupolar moment exists for spins I<1.

The NV⁻ electron spin also interacts with electric fields \vec{E} and crystal stress (with associated strain) (Kehayias *et al.*, 2019). In terms of the axial dipole moment d_{\parallel} , transverse dipole moments d_{\perp} and d'_{\perp} , and spin-strain coupling parameters $\{\mathcal{M}_z, \mathcal{M}_x, \mathcal{M}_y, \mathcal{N}_x, \mathcal{N}_y\}$, the interaction is presently best approximated by (van Oort and Glasbeek, 1990; Doherty *et al.*, 2012; Barfuss *et al.*, 2019; Udvarhelyi *et al.*, 2018)

$$\mathcal{H}_{\text{elec|str}}/h = (d_{\parallel}E_z + \mathcal{M}_z)S_z^2 + (d_{\perp}E_x + \mathcal{M}_x)(S_y^2 - S_x^2) + (d_{\perp}E_y + \mathcal{M}_y)(S_xS_y + S_yS_x) + (d'_{\perp}E_x + \mathcal{N}_x)(S_xS_z + S_zS_x) + (d'_{\perp}E_y + \mathcal{N}_y)(S_yS_z + S_zS_y).$$
(4)

Experimental values of d_{\perp} and d_{\parallel} are given in Table XIV. In magnetometry measurements, the terms proportional to $d'_{\perp}E_i + \mathcal{N}_i$ for $i=x,\ y$ are typically ignored, as they are off diagonal in the S_z basis, and the energy level shifts they produce are thus suppressed by D (Kehayias $et\ al.,\ 2019$). Furthermore, many magnetometry implementations operate with an applied bias field \vec{B}_0 satisfying

$$d_{\perp}E_i + \mathcal{M}_i \ll \frac{g_e \mu_B}{h} B_0 \ll D \tag{5}$$

for i=x, y in order to operate in the linear Zeeman regime, where the energy levels are maximally sensitive to magnetic-field changes (see the Appendix, Sec. 9). In the linear Zeeman regime, the terms in $\mathcal{H}_{\text{elec}|\text{str}}$ proportional to $d_{\perp}E_i+\mathcal{M}_i$ can also be ignored. The sole remaining term in $\mathcal{H}_{\text{elec}|\text{str}}$ acts on the

NV⁻ spin in the same way as the temperature-dependent D and is often combined into the parameter D for a given NV⁻ orientation (Glenn *et al.*, 2017). Except for extreme cases such as sensing in highly strained diamonds or in the presence of large electric fields, the values of all the electric field and strain parameters in $\mathcal{H}_{\text{elec}|\text{str}}$ are \sim 1 MHz or lower. Consequently, for most magnetic sensing applications, \mathcal{H}_0 can be taken as the Hamiltonian describing the NV⁻ ground-state spin for each of the hyperfine states.

In the presence of a magnetic field oriented along the NV internuclear axis $\vec{B} = (0, 0, B_z)$, \mathcal{H}_0 is given in matrix form by

$$\mathcal{H}_0^{(z)}/h = \begin{pmatrix} D + \frac{g_e \mu_B}{h} B_z & 0 & 0\\ 0 & 0 & 0\\ 0 & 0 & D - \frac{g_e \mu_B}{h} B_z \end{pmatrix}$$
(6)

with eigenstates $|m_s = 0\rangle$, $|m_s = -1\rangle$, and $|m_s = +1\rangle$ and magnetic-field-dependent transition frequencies

$$\nu_{\pm} = D \pm \frac{g_e \mu_B}{h} B_z,\tag{7}$$

which are depicted in Fig. 2. For the general case of a magnetic field \vec{B} with both axial and transverse components B_z and B_\perp , the transition frequencies are given to third order in $(g_e\mu_B/h)(B/D)$ by

$$\nu_{\pm} = D \left[1 \pm \left(\frac{g_e \mu_B}{h} \frac{B}{D} \right) \cos \theta_B + \frac{3}{2} \left(\frac{g_e \mu_B}{h} \frac{B}{D} \right)^2 \sin^2 \theta_B \right. \\ \left. \pm \left(\frac{g_e \mu_B}{h} \frac{B}{D} \right)^3 \left(\frac{1}{8} \sin^3 \theta_B \tan \theta_B - \frac{1}{2} \sin^2 \theta_B \cos \theta_B \right) \right], (8)$$

where $\tan \theta_B = B_{\perp}/B_z$.

Magnetic sensing experiments utilizing NV⁻ centers often interrogate one of these two transitions, allowing the

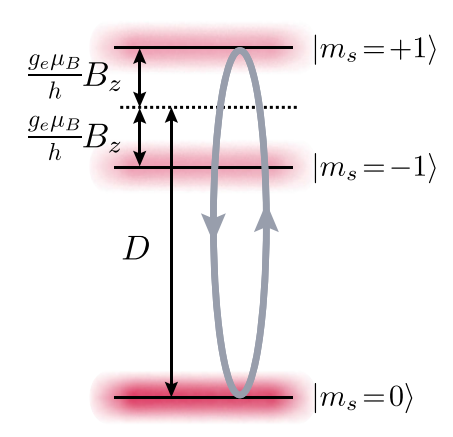


FIG. 2. Energy level diagram for the NV⁻ ground-state spin in the presence of an axial magnetic field B_z and ignoring nuclear spin, as described by Eq. (6). Population in the $|m_s=0\rangle$ state results in higher fluorescence under optical illumination than population in the $|m_s=\pm 1\rangle$ states. In this diagram, resonant MWs (gray oval) address the $|m_s=0\rangle \rightarrow |m_s=+1\rangle$ transition. Equation (9) describes the pseudo-spin-1/2 subspace occupied by these two levels.

unaddressed state to be neglected. For example, choosing the $|0\rangle$ and $|+1\rangle$ states and subtracting a common energy offset allows $\mathcal{H}_0^{(z)}$ from Eq. (6) to be reduced to the spin-1/2 Hamiltonian H given by

$$H/h = \begin{pmatrix} \frac{D}{2} + \frac{1}{2} \frac{g_e \mu_B}{h} B_z & 0\\ 0 & -\frac{D}{2} - \frac{1}{2} \frac{g_e \mu_B}{h} B_z \end{pmatrix}. \tag{9}$$

This simplification is appropriate when off-resonant excitation of the $|m_s = -1\rangle$ state can be ignored and operations on the spin system are short compared to T_1 . From this simple picture, the full machinery typically employed for two-level systems can be leveraged.

D. Ramsey measurements NV-

We now outline Norman Ramsey's Method of separated oscillatory fields when adapted for magnetic-field measurement using one or more NV⁻ centers in a two-level subspace, e.g., $\{|0\rangle, |+1\rangle\}$. After initialization of the spin state to $|0\rangle$, a periodically varying magnetic field $B_1(t)$, with polarization in the x-y plane and frequency ν_+ resonant with the $|0\rangle \leftrightarrow |+1\rangle$ transition, causes spin population to oscillate between the $|0\rangle$ and $|+1\rangle$ states at angular frequency $\Omega_R \propto B_1$, called the Rabi frequency. The resonant field $B_1(t)$ is applied for a particular finite duration $\pi/(2\Omega_R)$ known as a $\pi/2$ pulse, which transforms the initial state $|0\rangle$ into an equal superposition of $|0\rangle$ and $|+1\rangle$. This state is then left to precess unperturbed for duration τ , during which a magnetic-fielddependent phase ϕ accumulates between the two states. Next a second $\pi/2$ pulse is applied, mapping the phase ϕ onto a population difference between $|0\rangle$ and $|+1\rangle$. Figure 3 provides a Bloch sphere depiction of the Ramsey sequence, where the states $|0\rangle$ and $|+1\rangle$ are denoted by $|\uparrow\rangle$ and $|\downarrow\rangle$, respectively. See the Appendix, Sec. 1.a for a full mathematical description of a Ramsey magnetic-field measurement.

The subsequent spin readout process is fundamentally limited by quantum mechanical uncertainty. If a measurement of the final state's spin projection S_z is performed in the $\{|0\rangle, |+1\rangle\}$ basis, only two measurement outcomes are possible: 0 and 1. The loss of information associated with

this projective measurement is commonly referred to as spinprojection noise (Itano *et al.*, 1993). A projection-noiselimited sensor is characterized by a spin readout fidelity $\mathcal{F}=1$. Other considerations, such as photon shot noise, may lead to reductions in the fidelity \mathcal{F} , which degrade magneticfield sensitivity. The sensitivities of S=1/2 magnetometers at the spin-projection and shot-noise limits are discussed in Sec. II.A and treated in detail in the Appendix, Secs. 1.b and 1.c.

E. Spin dephasing and decoherence

Pulsed magnetometry measurements benefit from long sensing intervals τ , as the accumulated magnetic-field-dependent phase ϕ typically increases with τ . For example, in a Ramsey measurement, $\phi = \gamma_e B \tau$ with $\gamma_e = g_e \mu_B / \hbar$; maximal sensitivity of the observable ϕ to changes in B is therefore achieved when $d\phi/dB = \gamma_e \tau$ is maximized. At the same time, contrast degrades with increasing τ due to dephasing, decoherence, and spin-lattice interactions with associated respective relaxation times T_2^* , T_2 , and T_1 . The optimal interrogation time must therefore balance these two competing concerns.

The parameter T_2^* characterizes dephasing associated with static or slowly varying inhomogeneities in a spin system, e.g., dipolar fields from other spin impurities in the diamond, as depicted in Fig. 4. T_2^* is the characteristic 1/e time of a free-induction-decay (FID) measurement, wherein a series of Ramsey sequences are performed with varying free-precession interval τ , and an exponential envelope decay is observed [see Figs. 7(a) and 7(b)]. Inhomogeneous fields limit T_2^* by causing spins within an ensemble to undergo Larmor precession at different rates. As depicted in the second Bloch sphere in Fig. 5, the spins dephase from one another after free-precession intervals $\tau \sim T_2^*$.

Dephasing from fields that are static over the measurement duration can be reversed by application of a π pulse halfway through the free-precession interval. In this protocol (Hahn, 1950), the π pulse alters the direction of spin precession, such that the phase accumulated due to static fields during the second half of the sequence cancels the phase from the first half. Thus, spins in nonuniform fields rephase, producing a recovered signal termed a "spin echo"; see Fig. 5. The decay

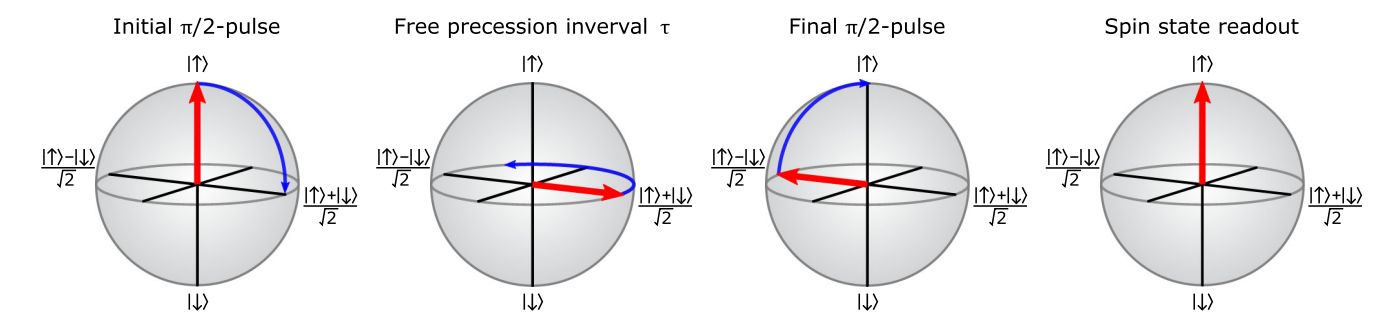


FIG. 3. Bloch sphere depiction of Ramsey sequence. After initialization to the spin state $|\uparrow\rangle$, a sinusoidally varying magnetic field rotates the state vector by $\pi/2$, thus preparing a superposition of $|\uparrow\rangle$ and $|\downarrow\rangle$ spin states. Next the Bloch vector undergoes free precession for duration τ , accumulating a phase ϕ proportional to the static magnetic field being sensed. After time τ , a second $\pi/2$ pulse maps the accumulated phase onto a population difference between the $|\uparrow\rangle$ and $|\downarrow\rangle$ states. Here a $\phi=\pi$ phase accumulation is shown, which maps back to the state $|\uparrow\rangle$. Finally, a projective spin-state measurement detects the population difference, allowing determination of the static magnetic field sensed by the spin.

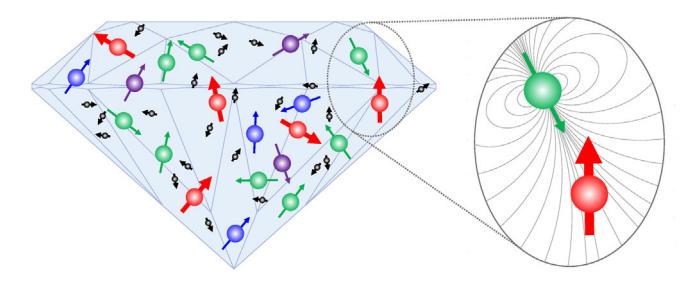


FIG. 4. Diamond containing spin impurities. NV⁻ centers (thick red arrows) experience magnetic fields caused by other spin defects in the diamond, including substitutional nitrogen (thin green arrows), ¹³C nuclei (small black arrows), and other paramagnetic impurities (blue and purple arrows). The inhomogeneous and time-varying dipolar magnetic fields generated by these spins dephase and decohere the NV⁻ spin ensemble.

of this echo signal, due to fields that fluctuate over the course of the measurement sequence, is characterized by the coherence time T_2 , also called the transverse or spin-spin relaxation time. In NV⁻ ensemble systems, T_2 can exceed T_2^* by orders of magnitude (de Lange *et al.*, 2010; Bauch *et al.*, 2018, 2019). As the T_2 -limited spin-echo sequence is intrinsically insensitive to dc magnetic fields, it is frequently employed for detecting ac signals. Meanwhile, the T_2^* -limited Ramsey sequence is commonly employed for dc sensing experiments.

F. dc and ac sensing

Quantum sensing approaches may be divided into two broad categories based on the spectral characteristics of the fields to be detected, summarized in Table I. In particular, do sensing protocols are sensitive to static, slowly varying, or broadband near-dc signals, whereas ac sensing protocols typically detect narrowband, time-varying signals at frequencies up to ~10 MHz (Shin *et al.*, 2012; Cai *et al.*, 2013; Loretz, Rosskopf, and Degen, 2013; Steinert *et al.*, 2013; Boss *et al.*, 2016, 2017; Pham *et al.*, 2016; Shao *et al.*, 2016; Wood *et al.*, 2016; Schmitt *et al.*, 2017), although ac sensing experiments of ~100 MHz signals have also been demonstrated for niche applications (Aslam *et al.*, 2017). Both dc and ac sensors employing NV⁻ ensembles exhibit sensitivities limited, in part, by the relevant NV⁻ spin relaxation times. The dc sensitivity is limited by the ensemble's inhomogeneous

dephasing time T_2^* , which is of the order of 1 μ s in most present implementations. The ac sensitivity is limited by the coherence time T_2 , which, as previously mentioned, is typically 1 to 2 orders of magnitude longer than T_2^* (de Lange et al., 2010; Bauch et al., 2019), and which can be extended through the use of dynamical decoupling protocols to approach the longitudinal spin relaxation time T_1 ; see Sec. IV.A. Additionally, alternative forms of T_1 -limited ac sensing such as T_1 relaxometry allow phase-insensitive detection of signals at frequencies in the ~GHz regime (Tetienne et al., 2013; Pelliccione et al., 2014; Hall et al., 2016; Shao et al., 2016; Casola, van der Sar, and Yacoby, 2018). In general, the enhanced field sensitivities afforded by longer ac sensor coherence times coincide with reduced sensing bandwidth as well as insensitivity to static fields, restricting the application space of sensors employing these techniques; see Table I. This review concentrates primarily on dc sensing protocols with particular focus on sensors designed to detect broadband time-varying magnetic fields from dc to $\sim 100 \text{ kHz}$.

II. MEASUREMENT SENSITIVITY CONSIDERATIONS

A. Magnetic-field sensitivity

The spin-projection-limited sensitivity of an ensemble magnetometer consisting of *N* noninteracting spins is given by (Budker and Romalis, 2007; Taylor *et al.*, 2008)

$$\eta_{\rm sp}^{\rm ensemble} \approx \frac{\hbar}{\Delta m_s g_e \mu_B} \frac{1}{\sqrt{N\tau}},$$
(10)

where $g_e \approx 2.003$ is the NV⁻ center's electronic g factor (Doherty *et al.*, 2013), μ_B is the Bohr magneton, \hbar is the reduced Planck constant, τ is the free-precession (i.e., interrogation) time per measurement, and Δm_s is the difference in spin quantum number between the two interferometry states (e.g., $\Delta m_s = 1$ for a spin S = 1/2 system, and $\Delta m_s = 2$ for a S = 1 system employing $m_s = +1$ and $m_s = -1$ states). Certain pulsed magnetometry schemes such as Ramsey-based protocols can allow sensitivities approaching the spin-projection limit, in part by ensuring that the spin-state readout does not interfere with the magnetic-field interrogation (Ramsey, 1950). However, even when employing Ramsey protocols, NV⁻ ensemble magnetometers suffer from at least three major

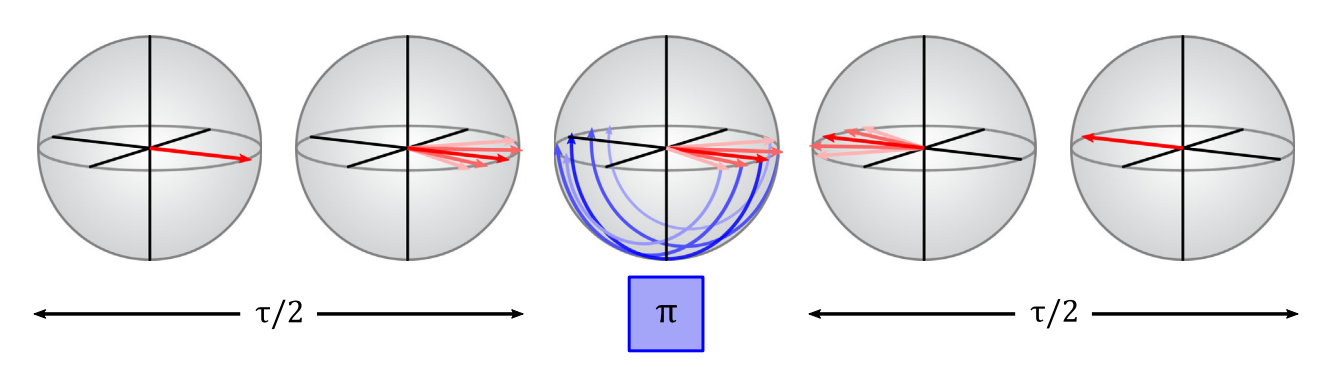


FIG. 5. Recovery of spin phase coherence with central π pulse. Bloch sphere depiction of spin dephasing due to static field inhomogeneities (characterized by T_2^*) followed by application of a π pulse at time $\tau/2$ and then spin rephasing at time τ . The π pulse cancels T_2^* dephasing as well as sensitivity to static signal fields.

TABLE I. Operational regimes and selected applications of broadband dc and ac sensing protocols employing NV^- ensembles in diamond. T_1 relaxometry methods are not considered.

	Broadband dc sensing	ac sensing
Common techniques	Ramsey (Sec. II.A), cw-ODMR (Sec. II.B.1), pulsed ODMR (Sec. II.B.2)	Hahn echo, dynamical decoupling (Sec. IV.A)
Relevant relaxation	Inhomogeneous spin dephasing (T_2^*)	Homogeneous spin decoherence (T_2) and longitudinal relaxation (T_1)
Frequency or bandwidth	0 to \sim 100 kHz (pulsed), 0 to \sim 10 kHz (cw)	Center frequency ~1 kHz to ~10 MHz; bandwidth ≲100 kHz
Example magnetic sensing applications	Biocurrent detection, magnetic particle tracking, magnetic imaging of rocks and meteorites, imaging of magnetic nanoparticles in biological systems, magnetic imaging of electrical current flow in materials, magnetic anomaly detection, navigation	Single biomolecule and protein detection, nanoscale nuclear magnetic resonance, nanoscale electron spin resonance, magnetic resonant phenomena in materials, noise spectroscopy

experimental nonidealities, which deteriorate the achievable magnetic-field sensitivity.

First, for NV⁻ ensemble magnetometers, the spin-state initialization time t_I and readout time t_R may be significant compared to the interrogation time τ . By decreasing the fraction of time devoted to spin precession, the finite values of t_I and t_R deteriorate the sensitivity by the factor

$$\sqrt{\frac{t_I + \tau + t_R}{\tau}}. (11)$$

Second, the conventional NV- optical readout technique (Doherty et al., 2013), which detects the spin-state-dependent fluorescence (also commonly referred to as photoluminescence or PL) in the 600-850 nm band, does not allow singleshot determination of the NV⁻ spin state to the spin-projection limit (i.e., the standard quantum limit) (Itano et al., 1993). An NV⁻ center in the electronically excited spin-triplet state will decay either directly to the spin-triplet ground state or indirectly through a cascade of spin-singlet states (Rogers et al., 2008) via an intersystem crossing (Goldman, Doherty et al., 2015; Goldman, Sipahigil et al., 2015; Thiering and Gali, 2018). Conventional NV- optical readout exploits the $m_s = \pm 1$ states' higher likelihood to enter the singlet-state cascade than the $m_s = 0$ state (see Table XIII). An NV⁻ center that enters the singlet-state cascade does not fluoresce in the 600-850 nm band, whereas an NV⁻ center decaying directly to the spin-triplet ground state can continue cycling between the ground and excited triplet states, producing fluorescence in the 600–850 nm band. The $m_s = \pm 1$ states therefore produce on average less PL in the 600-850 nm band, as shown in Fig. 6. Unfortunately the ~140-200 ns (Acosta, Jarmola et al., 2010; Robledo et al., 2011; Gupta, Hacquebard, and Childress, 2016) spin-singlet cascade lifetime and limited differences in $m_s = \pm 1$ and $m_s = 0$ decay behavior allows for only probabilistic determination of the NV⁻ initial spin state. Following Shields et al. (2015), we quantify the added noise from imperfect readout with the parameter $\sigma_R \ge 1$, such that $\sigma_R = 1$ corresponds to readout at the spin-projection limit. This parameter is the inverse of the measurement fidelity $\mathcal{F} \equiv 1/\sigma_R$. For imperfect readout schemes, the value of σ_R can be calculated as (Taylor et al., 2008; Shields et al., 2015)

$$\sigma_R = \sqrt{1 + \frac{2(a+b)}{(a-b)^2}} \tag{12}$$

$$= \sqrt{1 + \frac{1}{C^2 n_{\text{avg}}}},\tag{13}$$

where a and b, respectively, denote the average numbers of photons detected from the $m_s=0$ and $m_s=\pm 1$ states of a single NV⁻ center during a single readout. In Eq. (13) we identify C=(a-b)/(a+b) as the measurement contrast (i.e., the interference fringe visibility) and $n_{\rm avg}=(a+b)/2$ as the average number of photons collected per NV⁻ center per measurement. Although suboptimal initialization and readout times t_I and t_R can degrade the value of C, it is henceforth assumed that t_I and t_R are chosen optimally.

Third, the sensitivity η is degraded for increased values of τ due to spin dephasing during precession. For Ramsey-type pulsed magnetometry (i.e., with no spin echo), the dephasing

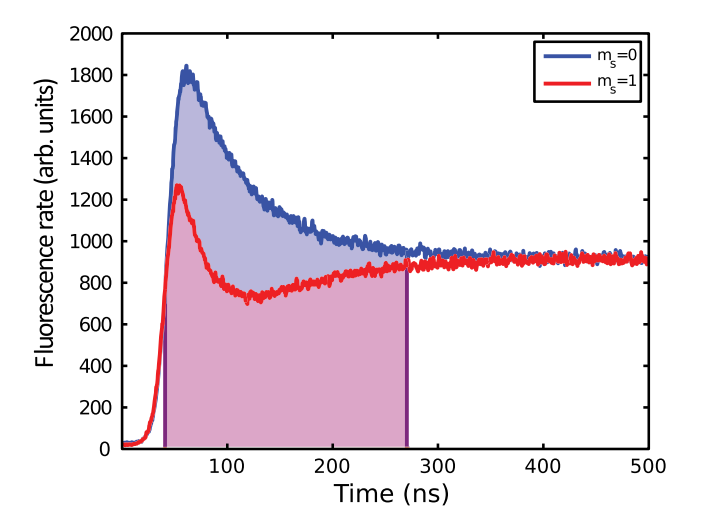


FIG. 6. Fluorescence of the NV⁻ spin states. NV⁻ centers prepared in the $m_s = 0$ state emit photons at a higher rate than centers prepared in the $m_s = \pm 1$ states. This spin-dependent fluorescence forms the basis of conventional NV⁻ readout. Data courtesy of Brendan Shields.

TABLE II. Example literature values for readout schemes employing conventional optical readout or alternative techniques. The parameter σ_R characterizes the factor above the spin-projection limit and \mathcal{N} is the average number of photons collected per measurement. Conventional NV⁻ readout is unable to reach the spin-projection limit ($\sigma_R = 1$), whereas alternative schemes can allow readout to approach this limit. The best demonstrated pulsed readout methods with ensembles are presently $\sim 100 \times$ away from the spin-projection limit.

Reference	Readout method	Single NV ⁻ /ensemble	σ_R	\mathcal{N} (counts/measurement)
Shields et al. (2015)	Conventional	Single	10.6	$9.45 \times 10^5 \text{ cps} \times t_R$
Shields et al. (2015)	Spin-to-charge conversion	Single	2.76	* **
Lovchinsky et al. (2016)	Conventional	Single	35	$\sim 10^5 \text{ cps} \times t_R$
Lovchinsky et al. (2016)	Ancilla-assisted	Single	5	
Fang <i>et al.</i> (2013)	Conventional	Single	80	0.01
Hopper et al. (2016)	Conventional	Single	48	0.04
Hopper et al. (2016)	Spin-to-charge conversion	Single	3	
Jaskula, Shields et al. (2019)	Conventional	Single	54	0.022
Jaskula, Shields et al. (2019)	Spin-to-charge conversion	Single	5	
Neumann, Beck et al. (2010)	Ancilla-assisted	Single	1.1	
Le Sage <i>et al.</i> (2012)	Conventional	Ensemble	67	2×10^{8}
T. Wolf et al. (2015)	Conventional	Ensemble	~1000	10^{12}
Chatzidrosos et al. (2017)	NIR absorption ^a	Ensemble	65	
Barry et al. (2016)	Conventional ^a	Ensemble	~5000	
Schloss et al. (2018)	Conventional ^a	Ensemble	~5000	

^aNonpulsed schemes for comparison.

occurs with characteristic time T_2^* so that η is additionally deteriorated by the factor

$$\frac{1}{e^{-(\tau/T_2^*)^p}},\tag{14}$$

where the value of the stretched exponential parameter p depends on the origin of the dephasing (see the Appendix, Sec. 7). NV⁻ spin resonance line shapes with exactly Lorentzian profiles correspond to dephasing with p = 1, and spin resonance line shapes with Gaussian profiles correspond to p = 2 (see the Appendix, Sec. 5).

Combining Eqs. (10), (11), (12), and (14) gives the sensitivity for a Ramsey-type NV⁻ broadband ensemble magnetometer (Popa *et al.*, 2004) as

$$\eta_{\rm Ramsey}^{\rm ensemble} \approx \underbrace{\frac{\hbar}{\Delta m_s g_e \mu_B} \frac{1}{\sqrt{N\tau}}}_{\rm spin \; projection \; limit} \underbrace{\frac{1}{e^{-(\tau/T_2^*)^p}}}_{\rm spin \; dephasing} \underbrace{\sqrt{1 + \frac{1}{C^2 n_{\rm avg}}}}_{\rm readout} \underbrace{\sqrt{\frac{t_I + \tau + t_R}{\tau}}}_{\rm overhead \; time}, \tag{15}$$

where N is the number of NV⁻ centers in the ensemble and $\Delta m_s = 1$ for the effective S = 1/2 subspace employed for NV⁻ magnetometry using the $m_s = 0$ and $m_s = \pm 1$ basis. However, in the limit of measurement contrast $C \ll 1$ and when the number of photons collected per NV⁻ center per optical readout is much less than 1, the readout fidelity is limited by photon shot noise and can be approximated using $1/\mathcal{F} = \sigma_R \approx 1/(C\sqrt{n_{\rm avg}})$. Defining $\mathcal{N} = Nn_{\rm avg}$ to be the average number of photons detected per measurement from the ensemble of N NV⁻ centers yields the following shotnoise-limited sensitivity equation for a Ramsey scheme (Pham, 2013):

$$\eta_{\text{Ramsey}}^{\text{ensemble,shot}} \approx \frac{\hbar}{\Delta m_s g_e \mu_B} \frac{1}{C e^{-(\tau/T_2^*)^p} \sqrt{\mathcal{N}}} \frac{\sqrt{t_I + \tau + t_R}}{\tau}.$$
(16)

Hereafter, we assume broadening mechanisms produce Lorentzian line shapes, so that p = 1. For negligible t_I and t_R , the optimal measurement time is $\tau = T_2^*/2$, whereas for $t_I + t_R \gg T_2^*$, the optimal τ approaches T_2^* (see the Appendix, Sec. 2). Equation (16) illustrates the benefits attained by increasing the dephasing time T_2^* , the measurement contrast C, the number of NV^- spin sensors N, and the average number of photons detected per NV $^-$ per measurement $n_{\rm avg}$. Table II lists values of σ_R and \mathcal{N} achieved using conventional optical readout in pulsed and cw magnetometry measurements, with both single NV⁻ centers and ensembles. At present, conventional optical readout is insufficient to reach the spinprojection limit for both single- and ensemble-NV⁻ sensors. Section 1 of the Appendix derives the sensitivity for a Ramsey-type magnetometer in both the spin-projection and shot-noise limits.

In addition to Ramsey-type methods, other protocols allow measurement of dc magnetic fields. These alternative methods, including continuous-wave and pulsed optically detected magnetic resonance, offer reduced sensitivity compared to Ramsey-type sequences (for a fixed number of NV⁻ centers addressed), as discussed in the following sections.

B. Alternatives to Ramsey magnetometry

1. Continuous-wave optically detected magnetic resonance

Continuous-wave optically detected magnetic resonance (cw-ODMR) is a simple, widely employed magnetometry method (Fuchs *et al.*, 2008; Acosta *et al.*, 2009; Dréau *et al.*, 2011; Schoenfeld and Harneit, 2011; Tetienne *et al.*, 2012; Barry *et al.*, 2016; Schloss *et al.*, 2018) wherein the MW driving and the optical polarization and readout occur simultaneously; see Fig. 7(c). Laser excitation continuously polarizes NV⁻ centers into the more fluorescent $m_s = 0$ ground

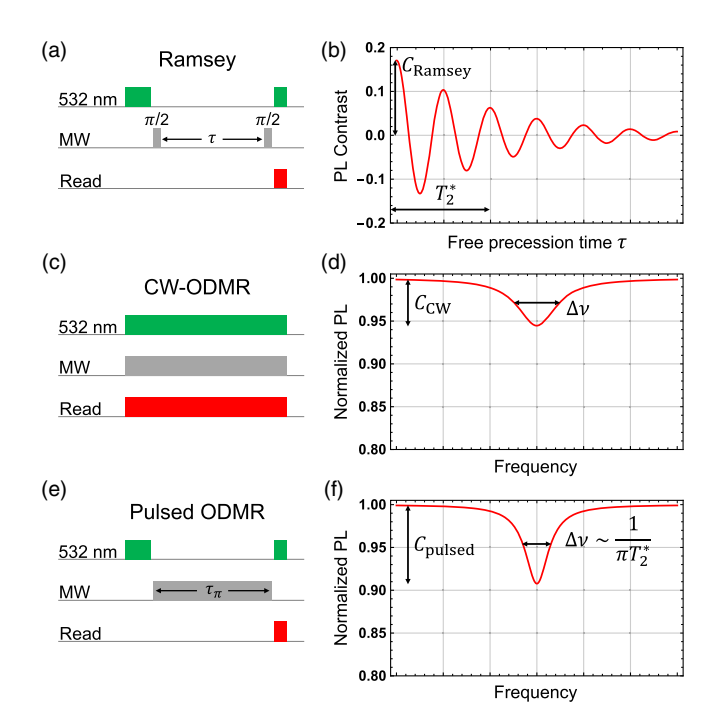


FIG. 7. Overview of Ramsey, cw-ODMR, and pulsed ODMR magnetometry protocols. (a) Schematic of Ramsey magnetometry protocol. (b) Representation of free induction decay associated with a Ramsey protocol vs free-precession time τ . Fringes exhibit contrast C_{Ramsey} and decay exponentially with dephasing time T_2^* . (c) Schematic of cw-ODMR sensing protocol. (d) Representation of cw-ODMR spectrum with contrast C_{cw} and linewidth $\Delta \nu$. (e) Schematic of pulsed ODMR sensing protocol with MW π -pulse time $\tau_{\pi} \sim T_2^*$. (f) Representation of pulsed ODMR spectrum with contrast C_{pulsed} and linewidth $\Delta \nu \sim 1/(\pi T_2^*)$.

state, while MWs tuned near resonance with one of the $m_s = 0 \leftrightarrow m_s = \pm 1$ transitions drive NV⁻ population into the less fluorescent $m_s = \pm 1$ state (reducing the emitted light). A change in the local magnetic field shifts the resonance feature with respect to the MW drive frequency, causing a change in the detected fluorescence, as illustrated in Fig. 7(d).

In the simplest cw-ODMR implementation, the MW frequency is swept across the entire NV⁻ resonance spectrum, allowing all resonance line centers to be determined. Alternatively, the MW frequency may be tuned to a specific resonance feature's maximal slope, so that incremental changes in magnetic field result in maximal changes in PL. The sensitivity of this latter approach can be further improved by modulating the MW frequency to combat noise or by simultaneously exciting multiple hyperfine transitions to improve contrast (Barry *et al.*, 2016; El-Ella *et al.*, 2017; Schloss *et al.*, 2018).

The cw-ODMR implementation does not require pulsed optical excitation, MW phase control, fast photodetectors, multichannel timing generators, or switches; the technique is therefore technically easier to implement than pulsed measurement schemes. Additionally, cw-ODMR is more tolerant of MW inhomogeneities than pulsed schemes and, when properly implemented, may yield similar sensitivities to pulsed magnetometry protocols when a larger number of sensors are interrogated with the same optical excitation power (Barry et al., 2016).

The shot-noise-limited sensitivity of an NV⁻ magnetometer employing cw-ODMR is given by (Dréau *et al.*, 2011; Barry *et al.*, 2016)

$$\eta_{\rm cw} = \frac{4}{3\sqrt{3}} \frac{h}{g_e \mu_B} \frac{\Delta \nu}{C_{\rm cw} \sqrt{R}},\tag{17}$$

with photon-detection rate R, linewidth $\Delta \nu$, and cw-ODMR contrast $C_{\rm cw}$. The prefactor $4/(3\sqrt{3})$ originates from the steepest slope of the resonance line shape when assuming a Lorentzian resonance profile and is achieved for a detuning of $\Delta \nu/(2\sqrt{3})$ from the line center (Vanier and Audoin, 1989). Operation of a cw-ODMR magnetometer can be modeled using the rate equation approach from Dréau *et al.* (2011) and Jensen *et al.* (2013).

However, cw-ODMR is not envisioned for many highsensitivity applications for multiple reasons. First, cw-ODMR precludes use of pulsed methods to improve sensitivity, such as double-quantum (DQ) coherence magnetometry (see Sec. IV.B), and many readout-fidelity enhancement techniques. In particular, the readout fidelity is quite poor compared to conventional pulsed readout schemes, as shown by the last two entries in Table II. Second, cw-ODMR methods suffer from MW and optical power broadening, degrading both $\Delta \nu$ and $C_{\rm cw}$ compared to optimized Ramsey sequences. Optimal cw-ODMR sensitivity is approximately achieved when optical excitation, MW drive, and T_2^* dephasing contribute roughly equally to the resonance linewidth (Dréau et al., 2011). In this low-optical-intensity regime, the detected fluorescence rate per interrogated NVcenter is significantly lower than for an optimized Ramsey scheme, which results in readout fidelities $\sim 10^3$ below the spin-projection limit (Barry et al., 2016). This low optical intensity requirement becomes more stringent as T_2^* increases, meaning that cw-ODMR sensitivity largely does not benefit from techniques to extend T_2^* .

Overall, the combination of poor readout fidelity (and no proposed path toward improvement) combined with an inability to benefit from extended T_2^* suggests that prospects are poor for further sensitivity enhancement over the best existing cw-ODMR devices (Barry *et al.*, 2016; Schloss *et al.*, 2018). Moreover, the poor readout fidelity accompanying the low required initialization intensity is particularly deleterious to applications where volume-normalized sensitivity (i.e., the sensitivity within a unit interrogation volume) is important.

2. Pulsed ODMR

Pulsed ODMR is an alternative magnetometry method first demonstrated for NV $^-$ centers by Dréau *et al.* (2011). Similar to Ramsey and in contrast to cw-ODMR, this technique avoids optical and MW power broadening of the spin resonances, enabling nearly T_2^* -limited measurements. In contrast to Ramsey magnetometry, however, pulsed ODMR is linearly sensitive to spatial and temporal variations in MW Rabi frequency. When such variations are minimal, pulsed ODMR sensitivity may approach that of Ramsey magnetometry without requiring high Rabi frequency (Dréau *et al.*, 2011), making the method attractive when high MW field strengths are not available.

In the pulsed ODMR protocol, depicted schematically in Fig. 7(e), the NV⁻ spin state is first optically initialized to $m_s=0$. Then during the interrogation time τ , a near-resonant MW π pulse is applied with duration equal to the interrogation time $\tau_{\pi}=\tau$, where the Rabi frequency $\Omega_R=\pi/\tau_{\pi}$. Finally, the population is read out optically. A change in the magnetic field detunes the spin resonance with respect to the MW frequency, resulting in an incomplete π pulse and a change in the population transferred to the $m_s=\pm 1$ state prior to optical readout.

For a Lorentzian resonance line shape (see the Appendix, Secs. 5 and 6), the expected shot-noise-limited sensitivity may be calculated starting from the shot-noise-limited cw-ODMR sensitivity given by Eq. (17). For pulsed ODMR, the resonance profile is given by a convolution of the T_2^* -limited line profile and additional broadening from the NV⁻ spin's response to a fixed-duration, detuned MW π pulse, as shown in Fig. 8. When the interrogation time τ_π is set to $\approx T_2^*$, these two broadening mechanisms contribute approximately equally to the resonance linewidth (Dréau *et al.*, 2011). Assuming $\tau_\pi \approx T_2^*$, we write the pulsed ODMR linewidth $\Delta \nu$ as $\Delta \nu \approx \Gamma = 1/(\pi T_2^*)$ [see Fig. 7(f)], while noting that this approximation likely underestimates the linewidth by a factor of 2 or less.

Choosing initialization and readout times t_I and t_R and interrogation time $\tau_{\pi} = T_2^*$ reduces the time-averaged photon collection rate R by the readout duty cycle $t_R/(t_I + T_2^* + t_R)$.

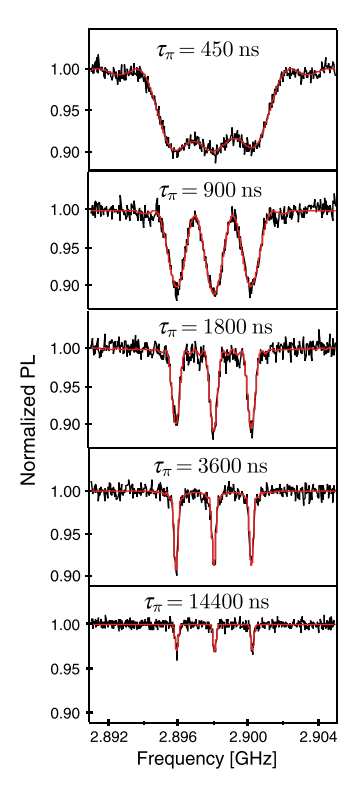


FIG. 8. Pulsed ODMR spectra for various π -pulse durations τ_{π} . When $\tau_{\pi} \ll T_2^*$, the resonance line shape is Fourier broadened beyond the T_2^* -limited linewidth. When $\tau_{\pi} \gg T_2^*$ the photoluminescence (PL) contrast is diminished due to spin dephasing. Choice of $\tau_{\pi} \sim T_2^*$ ($\approx 3~\mu s$ here) allows nearly T_2^* -limited linewidths while preserving PL contrast. From Dréau *et al.*, 2011.

Then defining $\mathcal{N} = Rt_R$ to be the mean number of photons collected per optical readout cycle and replacing $C_{\rm cw}$ with the pulsed ODMR contrast $C_{\rm pulsed}$ yields the pulsed ODMR sensitivity

$$\eta_{\text{pulsed}} \approx \frac{8}{3\sqrt{3}} \frac{\hbar}{g_e \mu_B} \frac{1}{C_{\text{pulsed}} \sqrt{\mathcal{N}}} \frac{\sqrt{t_I + T_2^* + t_R}}{T_2^*}.$$
(18)

The value of $C_{\rm pulsed}$ under optimized conditions is expected to be higher than C_{cw} (for the same number of interrogated NV^- centers and same mean photon collection rate R) because pulsed ODMR enables use of high optical intensities that would degrade C_{cw} (Dréau et al., 2011). Although C_{pulsed} may approach the Ramsey contrast $C_{\rm Ramsey}$ [see Figs. 7(a) and 7(b)], $C_{\text{pulsed}} < C_{\text{Ramsey}}$ is expected in practice for several reasons: first, because the technique requires Rabi frequencies to be of the same order as the NV⁻ linewidth set by T_2^* , the MW drive may be too weak to effectively address the entire inhomogeneously broadened NV⁻ ensemble. Second, while the high Rabi frequencies $\sim 2\pi \times 10 \text{ MHz}$ commonly employed in Ramsey sequences effectively drive all hyperfine-split NV⁻ transitions of ¹⁴NV⁻ or ¹⁵NV⁻ (Acosta et al., 2009), the weaker π pulses required for pulsed ODMR cannot effectively drive all hyperfine transitions with a single tone. Pulsed ODMR operation at the excited-state level anticrossing (Dréau et al., 2011) or utilizing multitone MW pulses (Vandersypen and Chuang, 2005; Barry et al., 2016; El-Ella et al., 2017) could allow more effective driving of the entire NV^- population and higher values of C_{pulsed} . However, when multitone pulses are employed, care should be taken to avoid degradation of C_{pulsed} due to off-resonant MW cross excitation, which may be especially pernicious when the T_2^* -limited linewidth (and thus MW Rabi frequency) is similar to the hyperfine splitting.

Although pulsed ODMR may sometimes be preferable to Ramsey, the former technique ultimately provides inferior sensitivity. Several factors of order $\sqrt{2}$ [which arise from a line-shape-dependent numerical prefactor (Dréau et al., 2011), MW Fourier broadening, nonuniform ensemble driving, and hyperfine driving inefficiencies] combine to degrade the pulsed ODMR sensitivity with respect to that of Ramsey. Furthermore, unlike double-quantum (DQ) Ramsey magnetometry (see Sec. IV.B), pulsed ODMR has not been experimentally demonstrated to mitigate line broadening from temperature fluctuations or other dephasing mechanisms common mode to $|m_s = -1\rangle$ and $|m_s = +1\rangle$. Hypothetical DQ analogs to pulsed ODMR (Taylor et al., 2008; Fang et al., 2013) might likely require, in addition to the sensing π -pulse, high-Rabi-frequency MW pulses to initialize the $|\pm 1\rangle$ superposition states, similar to those employed for DQ Ramsey, which would undermine pulsed ODMR's attractive low MW Rabi frequency requirements.

A generalization of pulsed ODMR is Rabi beat sensing (Rabi, 1937; Fedder *et al.*, 2011), wherein the spins are driven through multiple Rabi oscillations during the interrogation time. Under optimal conditions, Rabi beat magnetometry, like the specific case of pulsed ODMR, may exhibit sensitivity approaching that of Ramsey magnetometry. For the regime

TABLE III. Summary analysis of approaches to optimize ensemble-NV-diamond magnetic sensitivity.

		Sensitivity optimization
Parameter optimized	Method	Method description and evaluation
Dephasing time T_2^*	Double-quantum (DQ) coherence magnetometry (Sec. IV.B)	Doubles effective gyromagnetic ratio. Removes dephasing from mechanisms inducing shifts common to the $ m_s=\pm 1\rangle$ states, such as longitudinal strain and temperature. Minor additional MW hardware usually required. Generally recommended.
	Bias magnetic field (Sec. IV.D)	Suppresses dephasing from transverse electric fields and strain at bias magnetic fields of several gauss or higher. Generally recommended.
	Spin-bath driving (Sec. IV.C)	Mitigates or eliminates dephasing from paramagnetic impurities in diamond. Each impurity's spin resonance must be addressed, often with an individual rf frequency. Additional rf hardware is required. Recommended for many applications.
	Dynamical decoupling (Sec. IV.A)	Refocuses spin dephasing using one or more MW π pulses, extending the relevant relaxation time from T_2^* to T_2 , with fundamental limit set by $2T_1$. Recommended for narrow band ac sensing; generally precludes dc or broadband magnetic sensing.
	Rotary echo magnetometry	Extends measurement time using a MW pulse scheme but offers reduced sensitivity
	(Sec. VII.A)	relative to Ramsey. Not recommended outside niche applications.
	Geometric phase magnetometry (Sec. VII.B)	Offers increased dynamic range, using a MW spin-manipulation method, at the cost of reduced sensitivity relative to Ramsey. Not recommended outside niche applications.
	Ancilla-assisted upconversion	Employs NV ⁻ hyperfine interaction to convert dc magnetic fields to ac fields to be
	magnetometry (Sec. VII.C)	sensed using dynamical decoupling. Operates near ground-state level anticrossing $(10^3~\rm G)$ and offers similar or reduced sensitivity relative to Ramsey. Not generally recommended.
Readout fidelity $\mathcal{F}=1/\sigma_R$	Spin-to-charge conversion readout (Sec. V.A)	Maps spin state to charge state of NV, increasing number of photons collected per measurement. Allows $\sigma_R \approx 3$ for single NV centers, and initial results show improvement over conventional readout for ensembles. Substantially increased readout time likely precludes application when $T_2^* \lesssim 3$ μ s. Requires increased laser complexity. Technique is considered promising; hence, further investigation is warranted.
	Ancilla-assisted repetitive readout (Sec. V.C)	Maps NV ⁻ electronic spin state to nuclear spin state, enabling repetitive readout and increased photon collection. Allows σ_R to approach 1 for single NVs; no fundamental barriers to ensemble application. Substantially increased readout time likely precludes application when $T_2^* \lesssim 3~\mu s$. Requires high magnetic-field strength and homogeneity. Technique is considered promising, although further investigation is warranted.
	Improved photon collection (Sec. V.E)	Improves σ_R by reducing fractional shot noise contribution, subject to unity collection and projection noise limits. Near 100% collection efficiency is possible in principle, making this mainly an engineering endeavor. While many schemes are incompatible with wide-field imaging, the method is generally recommended for optical-based readout of single-channel bulk sensors.
	NIR absorption readout (Sec. V.F)	Probabilistically reads out initial spin populations using optical absorption on the ${}^{1}E \leftrightarrow {}^{1}A_{1}$ singlet transition. Demonstrated σ_{R} values are on par with conventional ensemble readout, and prospects for further improvement are unknown. Technique is best used with dense ensembles and an optical cavity but is hindered by non-NV ⁻
	Photoelectric readout (Sec. V.B)	absorption and nonradiative NV ⁻ singlet decay. Further investigation is warranted. Detects spin-dependent photoionization current. Best for small 2D ensembles; has not yet demonstrated sensitivity improvement with respect to optimized conventional readout.
	Level-anticrossing-assisted readout (Sec. V.D)	Increases the number of spin-dependent photons collected per readout by operation at the excited-state level anticrossing. Universally applicable, but at best offers a $\sqrt{3}$
	Green absorption readout (Sec. V.G)	improvement in σ_R . Not recommended outside niche applications. Probabilistically reads out initial spin populations using optical absorption on the ${}^3A_2 \leftrightarrow {}^3E$ triplet transition. Performs best with order unity optical depth. Demonstrations exhibit contrast below that of conventional readout by a factor of 3
	Laser threshold magnetometry (Sec. V.H)	or more. Prospects are not considered promising. Probes magnetic field by measuring lasing threshold, which depends on NV ⁻ singlet state population. Moderately improved collection efficiency and contrast are predicted compared to conventional readout. Challenges include non-NV ⁻ absorption and system instability near lasing threshold. Prospects are not considered
	Entanglement-assisted magnetometry (Sec. VII.D)	promising. Harnesses strong NV ⁻ dipolar interactions to improve readout fidelity beyond the standard quantum limit. Existing proposals require 2D ensembles, impose long overhead times, and exhibit unfavorable coherence time scaling with number of entangled spins. While existing protocols are not considered promising, further investigation toward developing improved protocols is warranted.

where the Rabi frequency Ω_R is large compared to the resonance linewidth $(\sim 1/T_2^*)$, sensitivity is optimized when the detuning is chosen to be similar to the Rabi frequency $(\Delta \sim \Omega_R)$, when the interrogation time is similar to the dephasing time $(\tau \sim T_2^*)$, see the Appendix, Sec. 2), and when τ is chosen to ensure operation at a point of maximum slope of the Rabi magnetometry curve. However, Rabi beat magnetometry is sensitive to spatial and temporal variations in the MW Rabi frequency Ω_R (Ramsey, 1950). For high values of Ω_R , MW field variations may limit the Rabi measurement's effective T_2^* . Hence, practical implementations of Rabi beat magnetometry on NV⁻ ensembles likely perform best when $\Omega_R \sim 1/T_2^*$, i.e., when the scheme reduces to pulsed ODMR.

C. Parameters limiting sensitivity

Examination of Eq. (15) reveals the relevant parameters limiting magnetic-field sensitivity $\eta_{\text{Ramsey}}^{\text{ensemble}}$: (i) the dephasing time T_2^* ; (ii) the readout fidelity $\mathcal{F}=1/\sigma_R$; (iii) the sensor density [NV⁻] and the interrogated diamond volume V, which together set the total number of sensors $N=[\text{NV}^-]\times V$; (iv) the measurement overhead time $t_O=t_I+t_R$; and (v) the relative precession rates of the two states forming the interferometry measurement. Sensitivity enhancement requires improving one or more of these parameters. As we discuss, parameters (i) and (ii) are particularly far from physical limits and therefore warrant special focus.

- (i) Dephasing time T_2^* : In current realizations, dephasing times in application-focused broadband NV⁻ ensemble magnetometers (Kucsko et al., 2013; Clevenson et al., 2015; Barry et al., 2016; Chatzidrosos et al., 2017) are typically $T_2^* \lesssim 1 \, \mu \text{s}$. Considering the physical limit $T_2^* \le 2T_1$ (Levitt, 2008; Jarmola *et al.*, 2012; Alsid et al., 2019; Bauch et al., 2019), with longitudinal relaxation time $T_1 \approx 6$ ms for NV⁻ ensembles (Jarmola et al., 2012), a maximum $T_2^* \approx 12$ ms is theoretically achievable, corresponding to a sensitivity enhancement of ≈ 100 times. Although the feasibility of realizing T_2^* values approaching $2T_1$ remains unknown, we consider improvement of T_2^* to be an effective approach to enhancing sensitivity; see Sec. III.A. While the stretched exponential parameter p can provide information regarding the dephasing source limiting T_2^* , its value (typically between 1 and 2 for ensembles) does not strongly affect achievable sensitivity (Bauch et al., 2018).
- (ii) Readout fidelity: Increasing readout fidelity $\mathcal{F}=1/\sigma_R$ is another effective method to enhance sensitivity, as fractional fidelity improvements result in equal fractional improvements in sensitivity. With conventional 532 nm fluorescence readout, current NV⁻ ensemble readout fidelities \mathcal{F} are a factor of \gtrsim 67 times removed from the spin-projection limit $\sigma_R=1$ (Le Sage *et al.*, 2012), indicating large improvements might be possible. For comparison, multiple readout methods employing single NV-centers achieve \mathcal{F} within a factor of 5 of the spin-projection limit, i.e., $\sigma_R < 5$ (Shields *et al.*, 2015;

Hopper *et al.*, 2016; Lovchinsky *et al.*, 2016; Ariyaratne *et al.*, 2018; Hopper, Shulevitz, and Bassett, 2018; Jaskula, Shields *et al.*, 2019) with Neumann, Beck *et al.* (2010) achieving $\sigma_R = 1.1$.

In contrast, we believe prospects are modest for improving sensitivity by engineering parameters (iii), (iv), and (v).

- (iii) Sensor number, density, or interrogation volume: In theory, the number of sensors N can be increased without limit. However, practical considerations may prevent this approach. First, a larger value of N (and an associated larger number of photons \mathcal{N}) can increase some types of technical noise that scale as N, e.g., noise from timing jitter in device electronics or from excitation-laser intensity fluctuations. As photon shot noise scales more slowly as \sqrt{N} , achieving a shotnoise-limited sensitivity becomes more difficult with increasing N. Second, large values of N can require impractically high laser powers, since the number of photons needed for NV⁻ spin initialization scales linearly with N. While larger N can be achieved by either increasing the NV- density or increasing the interrogation volume, both approaches result in distinct technical or fundamental difficulties. Increasing N by increasing the interrogation volume with fixed [NV⁻] may increase the diamond cost and creates more stringent uniformity requirements for both the bias magnetic field (to avoid degrading the dephasing time T_2^*) and the MW field (to ensure uniform spin manipulation over the sensing volume). Furthermore, increasing interrogation volume is incompatible with high-spatial-resolution sensing and imaging modalities (Steinert et al., 2010; Pham et al., 2011; Le Sage et al., 2013; Fu et al., 2014; Glenn et al., 2015; Simpson et al., 2016; Glenn et al., 2017; Tetienne et al., 2017). On the other hand, increasing NV⁻ density will increase dephasing from dipolar coupling and decrease T_2^* unless such effects are mitigated; see, e.g., Sec. IV.C. Finally, because sensitivity scales as $1/\sqrt{N}$, we expect increasing N to allow only modest enhancements (e.g., ≤ 5 times) over standard methods. To date no demonstrated high-sensitivity bulk NV-diamond magnetometer (Clevenson et al., 2015; T. Wolf et al., 2015; Barry et al., 2016; Chatzidrosos et al., 2017) has utilized more than a few percent of the available NV⁻ in the diamond, suggesting limited utility for increasing sensor number N in current devices; see the Appendix, Sec. 3 for additional analysis.
- (iv) Overhead time: Although measurement overhead time can likely be decreased to $\sim 1~\mu s$, maximum sensitivity enhancement (in the regime where $T_2^* \sim t_I + t_R$) is expected to be limited to order unity ($\lesssim 3$ times); see Sec. III.A for a more detailed discussion.
- (v) Precession rate: Use of the NV⁻ center's full S=1 spin can allow $\Delta m_s=2$ in Eqs. (15) and (16), i.e., a factor of 2 increase in the relative precession rate of the states employed compared to use of the standard S=1/2 equivalent subspace; see Sec. IV.B

(Fang *et al.*, 2013; Bauch *et al.*, 2018). However, further improvement is unlikely, as the NV⁻ spin dynamics are fixed.

We note that the derivation of Eq. (15) makes certain assumptions (in particular, independence of the N sensors) that do not apply to some exotic approaches, such as exploiting strong NV^--NV^- interactions via Floquet techniques and harnessing entanglement for sensing; see Sec. VII.D (Choi, Yao, and Lukin, 2017b).

Table III summarizes our analysis of present and proposed techniques to optimize ensemble-NV⁻ magnetic-field sensitivity. Table IV summarizes our review of engineering methods for producing optimized diamond samples for high-sensitivity ensemble-NV⁻ magnetometry.

III. LIMITS TO RELAXATION TIMES T_2^* AND T_2

A. Motivation to extend T_2^*

A promising approach to enhance dc sensitivity focuses on extending the dephasing time T_2^* (Bauch *et al.*, 2018). The effectiveness of this approach may be illustrated by close examination of Eqs. (15) and (16). First, optimal sensitivity is obtained when the precession time τ is similar to the dephasing time T_2^* (see the Appendix, Sec. 2), so that the

approximation $\tau \sim T_2^*$ is valid for an optimized system. Therefore, for the simple arguments presented in this section, we assume that T_2^* extensions translate to proportional extensions of the optimal τ . When the dephasing time T_2^* is similar to or shorter than the measurement overhead time $(T_2^* \lesssim t_O \equiv t_I + t_R)$, which may be typical for Ramsey magnetometers employing ensembles of NV⁻ centers in diamonds with total nitrogen concentration $[N^T] = 1$ –20 ppm, the sensitivity enhancement may then be nearly linear in T_2^* , as shown in Fig. 9.

The previously outlined sensitivity scaling can be intuitively understood as follows: when the free-precession time is small relative to the overhead time, i.e., $\tau \sim T_2^* \ll t_O$, doubling T_2^* (thus doubling τ) results in twice the phase accumulation per measurement sequence and only a slight increase in the total sequence duration; in this limit, magnetometer sensitivity is enhanced by nearly a factor of 2. This favorable sensitivity scaling positions T_2^* as an important parameter to optimize when $T_2^* \lesssim t_O$.

Typical NV⁻ ensemble T_2^* values are ~500 ns in $[N^T] \approx 20$ ppm chemical-vapor-deposition-grown diamonds from Element Six, a popular supplier of scientific diamonds. Even when employing extraordinarily optimistic values of $t_I = 1 \ \mu s$ and $t_R = 300$ ns in Ramsey sequences performed

TABLE IV. Summary analysis of diamond engineering parameters and methods for high-sensitivity ensemble-NV⁻ magnetometry. Colored lines indicate methods that may be employed to optimize each parameter.

Diamond material optimization			
Parameter optimized	Method	Method description and evaluation	
N-to-NV conversion efficiency χ (Sec. VI.A)	CVD synthesis (Sec. VI.C)	Common synthesis method that can produce high-quality ensemble-NV diamonds. Relatively easy to control dimensions and concentrations of electronic and nuclear spins. May introduce strain and unwanted impurities, which can limit achievable ζ , χ , and T_2^* . Effective for producing NV ⁻ -rich-layer diamonds.	
NV -to- NV - charge state efficiency ζ (Sec. VI.A)	HPHT synthesis (Sec. VI.C)	Common synthesis method that can produce high-quality ensemble-NV diamonds with lower strain and fewer lattice defects than CVD. Control over doping and impurity concentration may be more difficult than in CVD. Not intrinsically amenable to creating NV ⁻ -rich-layer diamonds. Ferromagnetic metals may incorporate into diamond.	
Paramagnetic impurities (Sec. VI.F)	Irradiation (Sec. VI.D)	Diamond treatment method that, combined with subsequent annealing, converts substitutional nitrogen to NV centers. Electrons are preferred irradiation particle. Dose should be optimized for diamond's nitrogen concentration to create high ζ without degrading χ . Generally recommended with annealing for producing NV ⁻ -rich diamonds.	
Strain (Sec. III.C)	LPHT annealing (Sec. VI.E)	Low-pressure annealing that, combined with prior irradiation, converts substitutional nitrogen to NV centers. Heals some diamond lattice damage. NV centers are created effectively at $\sim 800~^{\circ}\mathrm{C}$; additional treatment at $\sim 1200~^{\circ}\mathrm{C}$ may eliminate some unwanted impurities. Generally recommended with irradiation for producing NV rich diamonds.	
Nuclear spins (Sec. III.F)	HPHT treatment (Sec. VI.C)	High-pressure annealing may reduce strain and eliminate some unwanted impurities. May enable increases in ζ and χ . Recommended for diamonds with balanced aspect ratios.	
	Isotopic enrichment (Sec. III.F)	Diamond synthesis with isotopically enriched source (gas for CVD and typically solid for HPHT) allows reduction of unwanted nuclear spin concentration (e.g., 13 C) and selection of nitrogen isotope (14 N or 15 N) incorporated into NV ⁻ . CVD diamonds with [13 C] ≈ 20 ppm have been synthesized. Recommended for achieving long T_2^* .	
	Surface treatment (Sec. VI.A)	Surface termination with favorable atomic elements can stabilize the desired NV charge state near the surface and extend relaxation times. Generally recommended.	
	Preferential orientation (Sec. VI.G)	CVD synthesis of diamond with NV centers preferentially oriented along a single axis. At present, preferential orientation is only maintained in unirradiated diamonds, largely hindering its capability to produce NV ⁻ -rich diamonds. Not generally recommended.	

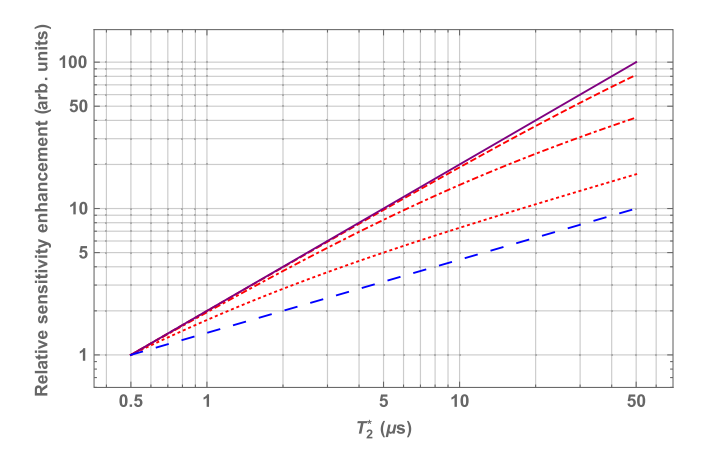


FIG. 9. Sensitivity enhancement scaling with dephasing time T_2^* for a Ramsey-type magnetometer normalized to the same device with $T_2^* = 500$ ns. The different curves assume overhead times $(t_0 = t_I + t_R)$ of 1, 10, and 100 μ s. The sensitivity enhancement is bounded from above by the fractional T_2^* improvement and from below by the square root of the fractional T_2^* improvement. For simplicity the precession time τ is set to T_2^* . See the Appendix, Sec. 2 for details on determining the optimal precession time.

on such ensembles, only roughly one-quarter of the total measurement time is allocated to free precession. In this regime, as discussed, the sensitivity scales as $\sim 1/T_2^*$. Although values of t_I and t_R vary in the literature (see Table V), the use of longer t_I and t_R may be desired to achieve better spin polarization and higher readout fidelity. Notably, initialization times are typically longer for NV-ensembles than for single NV- defects, as higher optical excitation power is required to achieve the NV- saturation intensity over spatially extended ensembles, and, furthermore, nonuniformity in optical intensity (e.g., from a Gaussian illumination profile) can be compensated for by increasing the initialization time (T. Wolf et al., 2015).

Longer dephasing times T_2^* offer additional benefits beyond direct sensitivity improvement. For example, higher T_2^* values may relax certain technical requirements by allowing lower duty cycles for specific experimental protocol steps. In a standard Ramsey-type experiment, the optical initialization and optical readout each occur once per measurement

TABLE V. Initialization and readout times in the literature used for conventional optical readout of NV⁻ defects. In general, NV⁻ ensembles require longer initialization times than single NV⁻ defects, in part due to the often nonuniform optical excitation intensity applied to the ensemble (T. Wolf *et al.*, 2015).

Reference	No. NV ⁻ probed	t_I	t_R
Shields et al. (2015)	Single	150 ns	
de Lange et al. (2012)	Single	600 ns	600 ns
Hopper et al. (2016)	Single	$1 \mu s$	200 ns
Fang et al. (2013)	Single	$2 \mu s$	300 ns
Maze et al. (2008)	Single	$2 \mu s$	324 ns
Neumann et al. (2009)	Single	$3 \mu s$	
Le Sage et al. (2012)	Ensemble	600 ns	300 ns
Bauch et al. (2018)	Ensemble	$20 \mu s$	
T. Wolf et al. (2015)	Ensemble	$100~\mu s$	$10 \mu s$
Mrózek et al. (2015)	Ensemble	1 ms	
Jarmola et al. (2012)	Ensemble	1 ms	

sequence. Assuming a fixed mean number of photons are required for spin polarization and for readout of the NV-ensemble, the time-averaged optical power and resulting heat load are expected to scale as $1/T_2^*$. Reducing heat loads is prudent for minimizing temperature variation of the diamond, which shifts the energy splitting between $|m_s=0\rangle$ and $|m_s=\pm 1\rangle$ and may require correction; see Sec. IV.B. Minimizing heat load is also important for many NV-diamond sensing applications, particularly in the life sciences. Assuming a fixed overhead time t_O , the realization of higher values of T_2^* , and thus τ , necessitates processing fewer photons per unit time, which may relax design requirements for the photodetector front end and associated electronics (Hobbs, 2011).

Extended T_2^* times can provide similar benefits to the MWrelated aspects of the measurement. A standard Ramsey-type measurement protocol employs a MW $\pi/2$ pulse before and after every free-precession interval. If the length of each $\pi/2$ pulse is held fixed, the time-averaged MW power and resulting heat load will scale as $1/T_2^*$. Additionally, higher T_2^* values can allow for more sophisticated, longer-duration MW pulse sequences, in place of simple $\pi/2$ pulses, to mitigate the effects of Rabi frequency inhomogeneities (Vandersypen and Chuang, 2005; Angerer et al., 2015; Nöbauer et al., 2015) or allow for other spin-manipulation protocols. Finally, higher T_2^* values could make exotic readout schemes that tend to have fixed time penalties attractive, such as spin-to-charge conversion readout (Shields et al., 2015) (see Sec. V.A) and ancilla-assisted repetitive readout (Jiang et al., 2009; Lovchinsky et al., 2016); see Sec. V.C.

B. Ensemble and single-spin T_2^*

As discussed, the dephasing time T_2^* is a critical parameter for broadband dc magnetometry. Importantly, T_2^* is defined differently for a single spin than for a spin ensemble. While an ensemble's T_2^* characterizes relative dephasing of the constituent spins, a single spin's T_2^* characterizes dephasing of the spin with itself, i.e., the distribution of phase accumulation from repeated measurements on the spin over time (de Sousa, 2009; Ishikawa *et al.*, 2012). Since this work focuses on ensemble-based sensing, single-spin dephasing times are herein denoted $T_2^{*\rm single}$, while the term T_2^* is reserved for ensemble dephasing times.

Values of $T_2^{* \text{single}}$ are affected by slow magnetic, electric, strain, and temperature fluctuations. Variations in the magnetic environment may arise from dipolar interactions with an electronic or nuclear spin bath. The strength of these fluctuations can vary spatially throughout a sample due to the microscopically nonuniform distribution of bath spins. As a result, different NV⁻ centers in the same sample display different $T_2^{* \text{single}}$ values (Hanson *et al.*, 2006, 2008; Dobrovitski *et al.*, 2008; Ishikawa *et al.*, 2012). For example, an NV⁻ spin in close proximity to several bath spins will experience faster dephasing than an NV⁻ spin many lattice sites away from the nearest bath spin.

Although ensemble T_2^* values are also influenced by spin-bath fluctuations, as discussed in Secs. III.D and III.F, an ensemble T_2^* value is not equal to the most common value of $T_2^{* \text{single}}$ within the ensemble. In particular, the ensemble value is

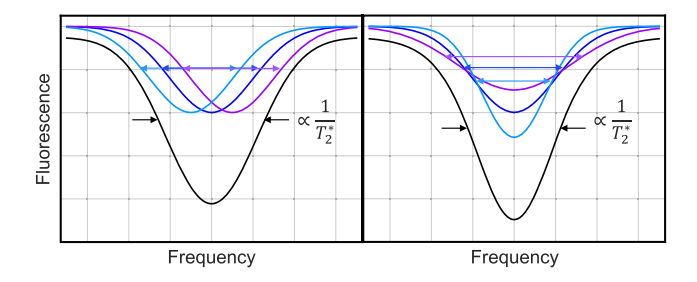


FIG. 10. Contributions of individual spin resonances to the overall spin ensemble line shape. The ensemble resonance line shape is broadened by both the distribution of line centers (left) and the distribution of linewidths (right) of the constituent spins.

limited by sources of zero-frequency noise that do not contribute to $T_2^{*\,\mathrm{single}}$, such as spatially inhomogeneous magnetic fields, electric fields, strain, or g factors (de Sousa, 2009). These inhomogeneities cause a spatially dependent distribution of the single-NV⁻ resonance line centers, which broadens the ensemble resonance line and thus degrades T_2^* . Figure 10 depicts broadening contributions to T_2^* from both varying single-NV⁻ line centers and varying single-NV⁻ linewidths ($\propto 1/T_2^{*\,\mathrm{single}}$). The relative contribution to an ensemble's T_2^* value from these two types of broadening is expected to be sample dependent. Although measurements by Ishikawa $et\ al.\ (2012)$ on a collection of single NV⁻ centers in a sparse sample found the distribution of single-NV⁻ line centers to be narrower than the median single-NV⁻ linewidth, such findings are not expected to hold generally (e.g., due to strain).

Even in the absence of static field inhomogeneities, the spin-bath-noise-limited T_2^* value of an ensemble is expected to be shorter than the most likely $T_2^{*\,\rm single}$ value, as the ensemble value is strongly influenced by the small minority of NV⁻ centers with bath spins on nearby lattice sites (Dobrovitski *et al.*, 2008). In fact, theoretical calculations by Dobrovitski *et al.* (2008) and Hall, Cole, and Hollenberg (2014) reveal that single spins and ensembles interacting with surrounding spin baths each exhibit FID envelopes with different functional forms (see the Appendix, Secs. 5 and 7), a result borne out by NV experiments (Maze *et al.*, 2012; Bauch *et al.*, 2018, 2019). In general, the ensemble T_2^* value cannot be predicted from $T_2^{*\,\rm single}$ of any constituent spin (Dobrovitski *et al.*, 2008), and application of single-spin measurements or theory to ensembles, or vice versa, should be done with great care.

C. Dephasing mechanisms

The various contributions to an NV $^-$ ensemble's spin dephasing time T_2^* can be expressed schematically as

$$\begin{split} &\frac{1}{T_{2}^{*}} \approx \frac{1}{T_{2}^{*}\{\text{electronic spin bath}\}} + \frac{1}{T_{2}^{*}\{\text{nuclear spin bath}\}} \\ &+ \frac{1}{T_{2}^{*}\{\text{strain gradients}\}} + \frac{1}{T_{2}^{*}\{\text{electric field noise}\}} \\ &+ \frac{1}{T_{2}^{*}\{\text{magnetic field gradients}\}} + \frac{1}{T_{2}^{*}\{\text{temperature variation}\}} \\ &+ \frac{1}{T_{2}^{*}\{\text{unknown}\}} + \frac{1}{2T_{1}}, \end{split} \tag{19}$$

where the symbol notation $T_2^*\{X\}$ denotes the hypothetical limit to T_2^* solely due to mechanism X (in the absence of all other interactions or mechanisms). Equation (19) assumes that all mechanisms are independent and that associated dephasing rates add linearly. The second assumption is strictly valid only when all dephasing mechanisms lead to single-exponential free-induction-decay envelopes (i.e., Lorentzian line shapes); see the Appendix, Secs. 5, 6, and 7. Here we briefly discuss each of these contributions to NV^- ensemble dephasing, and in later sections we examine their scalings and how each mechanism may be mitigated.

The electronic spin bath consists of paramagnetic impurity defects in the diamond lattice, which couple to NV⁻ spins via magnetic dipolar interactions. The inhomogeneous spatial distribution and random instantaneous orientation of these bath spins cause dephasing of the NV⁻ spin ensemble (Dobrovitski *et al.*, 2008; Hanson *et al.*, 2008; Bauch *et al.*, 2018, 2019). Electronic spin-bath dephasing can be broken down into contributions from individual constituent defect populations,

$$\begin{split} &\frac{1}{T_{2}^{*}\{\text{electronic spin bath}\}}\\ &=\frac{1}{T_{2}^{*}\{N_{S}^{0}\}}+\frac{1}{T_{2}^{*}\{NV^{-}\}}\\ &+\frac{1}{T_{2}^{*}\{NV^{0}\}}+\frac{1}{T_{2}^{*}\{\text{other electronic spins}\}}. \end{split} \tag{20}$$

Here $T_2^*\{N_S^0\}$ denotes the T_2^* limit from dephasing by paramagnetic substitutional nitrogen defects N_S^0 (S=1/2), also called P1 centers, with concentration $[N_S^0]$ (Smith *et al.*, 1959; Cook and Whiffen, 1966; Loubser and van Wyk, 1978). As substitutional nitrogen is a necessary ingredient for creation of NV^- centers, N_S^0 defects typically persist at concentrations similar to or exceeding NV⁻ (and NV⁰) concentrations and may account for the majority of electronic spin-bath dephasing (Bauch et al., 2018). Section III.D examines $T_2^*\{N_S^0\}$ scaling with $[N_S^0]$. For NV-rich diamonds, dipolar interactions among NV⁻ spins may also cause dephasing of the ensemble, with associated limit $T_2^*\{NV^-\}$. Section III.G examines the $T_2^*\{NV^-\}$ scaling with $[NV^-]$ and other experimental parameters. In NV-rich diamonds, the neutral charge state NV⁰ (S = 1/2) is also present at concentrations similar to [NV⁻] (Hartland, 2014) and may also contribute to dephasing, with limit $T_2^*\{NV^0\}$. The quantity $T_2^*\{\text{other electronic spins}\}$ encompasses dephasing from the remaining defects in the electronic spin bath, such as negatively charged single vacancies (Baranov et al., 2017), vacancy clusters (D. J. Twitchen et al., 1999; Iakoubovskii and Stesmans, 2002), and hydrogen-containing defects (Edmonds et al., 2012).

The quantity T_2^* {nuclear spin bath} in Eq. (19) describes NV⁻ ensemble dephasing from nuclear spins in the diamond lattice. In samples with natural isotopic abundance of carbon, the dominant contributor to nuclear spin-bath dephasing is the ¹³C isotope (I = 1/2), with concentration [13 C] = 10700 ± 800 ppm (Wieser *et al.*, 2013), so that T_2^* {nuclear spin bath} $\approx T_2^*$ { 13 C} (Balasubramanian *et al.*, 2009; Dréau *et al.*, 2012; Zhao, Ho, and Liu, 2012; Hall, Cole, and Hollenberg, 2014).

Other nuclear spin impurities exist at much lower concentrations and thus have a negligible effect on dephasing. The $T_2^*\{^{13}C\}$ scaling with concentration [^{13}C] is discussed in Sec. III.F and can be minimized through isotope engineering (Balasubramanian *et al.*, 2009; Teraji *et al.*, 2013).

Another major source of NV- ensemble dephasing is nonuniform strain across the diamond lattice. Because strain shifts the NV- spin resonances (Dolde et al., 2011; Jamonneau et al., 2016; Trusheim and Englund, 2016), gradients and other inhomogeneities in strain may dephase the ensemble, limiting T_2^* . Strain may vary by more than an order of magnitude within a diamond sample (Bauch et al., 2018) and can depend on myriad diamond synthesis parameters (Gaukroger et al., 2008; Hoa et al., 2014). For a given NV⁻ orientation along any of the [111] diamond crystal axes, strain couples to the NV- Hamiltonian approximately in the same way as an electric field (although with a different coupling strength) (Dolde et al., 2011; Doherty et al., 2012; Barson et al., 2017); see the Appendix, Sec. 9 for further discussion. Thus, the quantity T_2^* {strain gradients} may be separated into terms accounting for strain coupling along (\parallel) and transverse to (\perp) the NV⁻ symmetry axis,

$$\begin{split} \frac{1}{T_2^*\{\text{strain gradients}\}} &= \frac{1}{T_2^*\{\text{strain}_{\parallel}\text{gradients}\}} \\ &+ \frac{1}{T_2^*\{\text{strain}_{\perp}\text{gradients}\}}. \end{split} \tag{21}$$

Application of a sufficiently strong bias magnetic field mitigates the transverse strain contribution to dephasing (Jamonneau *et al.*, 2016) (see Sec. IV.D), while the longitudinal contribution may be mitigated by employing double-quantum coherence magnetometry; see Sec. IV.B.

Inhomogeneous electric fields also cause NV⁻ ensemble dephasing (Jamonneau *et al.*, 2016), with associated limit T_2^* {electric field noise}. This dephasing source may also be broken down into components longitudinal and transverse to the NV⁻ symmetry axis, and the contributions can be suppressed by the same methods as for strain-related dephasing.

In addition, external magnetic field gradients may cause NV^- spin dephasing by introducing spatially varying shifts in the NV^- energy levels across an ensemble volume, with associated limit T_2^* {magnetic field gradients}. Design of uniform bias magnetic fields minimizes this contribution to NV^- ensemble dephasing and is largely an engineering challenge given that modern NMR magnets can exhibit sub-ppb uniformities over their cm-scale sample volumes (Vandersypen and Chuang, 2005).

Even though T_2^* is considered the inhomogeneous dephasing time, homogeneous time-varying electric and magnetic fields may appear as dephasing mechanisms if these fields fluctuate over the course of multiple interrogation and readout sequences. Such a scenario could result in the unfortunate situation where the measured value of T_2^* depends on the total measurement duration; see Sec. A.2. By the same argument, temperature fluctuations and spatial gradients can also appear as dephasing mechanisms and can limit the measured T_2^* . Temperature variations cause expansion and contraction of the diamond crystal lattice, altering the NV⁻ center's zero-field

splitting parameter D (dD/dT = -74 kHz/K) (Acosta, Bauch, Ledbetter *et al.*, 2010) and, depending on experimental design, may also shift the bias magnetic field. Finally, we include a term in Eq. (19) for as-of-yet unknown mechanisms limiting T_2^* , and we note that T_2^* is limited to a theoretical maximum value of $2T_1$ (Levitt, 2008; Myers, Ariyaratne, and Jayich, 2017).

Importantly, Eq. (19) shows that the value of T_2^* is primarily set by the dominant dephasing mechanism. Therefore, when seeking to extend T_2^* , one should focus on reducing whichever mechanism is dominant until another mechanism becomes limiting. O'Keeffe *et al.* (2019) aptly expressed the proper strategy as a "shoot the alligator closest to the boat" approach. For example, even if the dephasing due to substitutional nitrogen is substantially decreased in a particular experiment, the improvement in T_2^* may be much smaller if, say, strain inhomogeneity then becomes a limiting factor; at that point it becomes more fruitful to shift focus toward reducing strain-induced dephasing.

D. Nitrogen limit to T_2^*

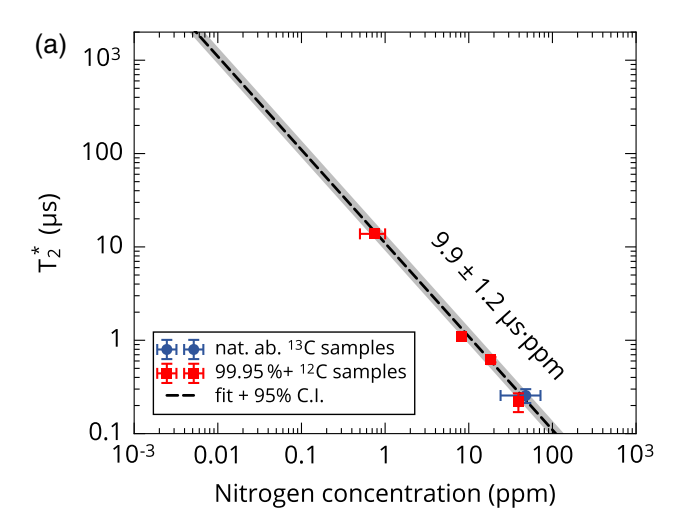
In nitrogen-rich diamonds, the majority of electronic spins contributing to the spin bath originates from substitutional nitrogen defects, since N_S^0 may donate its unpaired electron to another defect X and become spinless N_S^+ , via the process (Khan *et al.*, 2009)

$$N_S^0 + X^0 \leftrightarrow N_S^+ + X^-.$$
 (22)

In these samples, the electronic spin concentration is closely tied to the total concentration of substitutional nitrogen donors $[N_S^T]$, and thus T_2^* {electronic spin bath} is primarily set by $[N_S^T]$. In unirradiated nitrogen-rich diamonds, however, N_S^0 serves as the primary contributor to the electronic spin bath (Bauch *et al.*, 2018). The N_S^0 contribution to dephasing obeys

$$\frac{1}{T_2^*\{N_S^0\}} = A_{N_S^0}[N_S^0],\tag{23}$$

where $[N_S^0]$ is the concentration of neutral substitutional nitrogen, and $A_{\rm N_c^0}$ characterizes the magnetic dipole interaction strength between NV⁻ spins and N_S⁰ spins. The inverse linear scaling of $T_2^*\{N_S^0\}$ is supported by both theory (Abragam, 1983a; Taylor et al., 2008; Zhao, Ho, and Liu, 2012; Wang and Takahashi, 2013; Bauch et al., 2019) and experiment (van Wyk et al., 1997; Bauch et al., 2018, 2019). However, reported values of the scaling factor $A_{N_0^0}$ from theoretical spin-bath simulations vary widely; for example, Zhao, Ho, and Liu (2012) predicted $A_{\text{N}_c^0} = 56 \text{ ms}^{-1} \text{ ppm}^{-1}$, whereas Wang and Takahashi (2013) predicted $A_{N_0^0}$ = 560 ms⁻¹ ppm⁻¹, a 10 times discrepancy. Bauch et al. (2018, 2019) measured $T_2^*\{N_S^0\}$ on five samples in the range $[N_S^0] = 0.75-60$ ppm (see Fig. 11) and determined $A_{N_S^0} =$ $101 \pm 12 \text{ ms}^{-1} \text{ ppm}^{-1}$, such that for a sample with $[N_s^0] =$ 1 ppm, $T_2^*\{N_S^0\} = 9.9 \pm 1.2 \ \mu s$. The experimental value of $A_{N_0^0}$ is consistent with numerical simulations in the same work



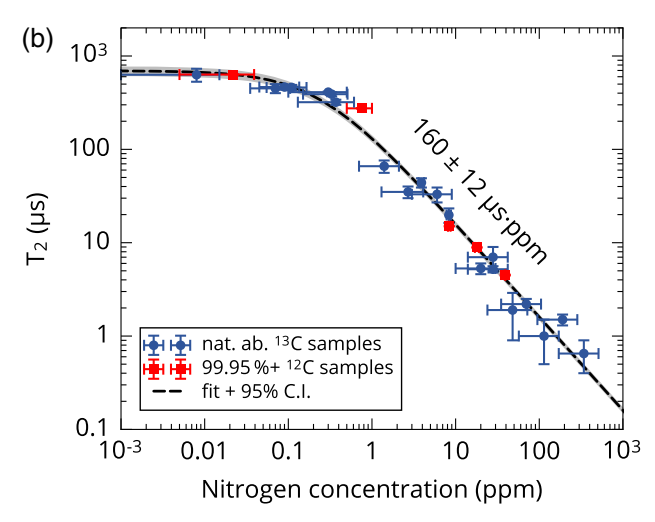


FIG. 11. Substitutional nitrogen spin-bath contribution to ensemble-NV⁻ dephasing time T_2^* and coherence time T_2 . (a) Measured spin-bath contribution to T_2^* vs nitrogen concentration measured by secondary ion mass spectrometry (SIMS) for five diamond samples. Fit yields $1/T_2^*\{N_S^0\} = A_{N_S^0}[N_S^0]$ with $A_{N_S^0} = 101 \pm 12 \text{ ms}^{-1} \text{ ppm}^{-1}$. (b) Measured Hahn echo T_2 vs nitrogen concentration for 25 diamond samples. The linear contribution to the fit is attributed to substitutional nitrogen and yields $1/T_2\{N_S^0\} = B_{N_S^0}[N_S^0]$ with $B_{N_S^0}[N_S^0] = 6.25 \pm 0.47 \, \text{ms}^{-1} \, \text{ppm}^{-1}$. The nitrogen-independent contribution to the fit is given by $T_2\{\text{other}\} = 694 \pm 82 \, \mu \text{s}$. Adapted from Bauch *et al.*, 2019.

(Bauch *et al.*, 2019). They calculated the second moment of the dipolar-broadened single NV⁻ ODMR linewidth (Abragam, 1983a, 1983b) for 10^4 random spin-bath configurations and, by computing the ensemble average over the distribution of single-NV⁻ linewidths (Dobrovitski *et al.*, 2008), found good agreement with the experimental value $A_{\text{N}_8^0} = 101 \text{ ms}^{-1} \text{ ppm}^{-1}$.

Electron paramagnetic resonance (EPR) measurements of nitrogen N_S^0 defects in diamond (van Wyk *et al.*, 1997) from 63 samples also confirm the scaling $1/T_2^* \propto [N_S^0]$ (see the Appendix, Sec. 6 and Fig. 35) and the approximate scaling constant $A_{N_S^0}$. With the likely assumption that the dephasing time for ensembles of substitutional nitrogen spins in a nitrogen

spin bath can approximate $T_2^*\{N_S^0\}$ for NV⁻ ensembles (Dale, 2015) (see the Appendix, Sec. 6), the measurements by van Wyk *et al.* (1997) suggest $A_{N_S^0} \approx 130 \text{ ms}^{-1} \text{ ppm}^{-1}$, which is in good agreement with the measured $A_{N_S^0} = 101 \pm 12 \text{ ms}^{-1} \text{ ppm}^{-1}$ from Bauch *et al.* (2019); see the Appendix, Secs. 5 and 6.

In addition, the data in van Wyk *et al.* (1997) suggest that dipolar dephasing contributions from 13 C at natural isotopic abundance (10 700 ppm) (Wieser *et al.*, 2013) and from substitutional nitrogen are equal for $[N_S^0] = 10.8$ ppm. The measured values of $A_{N_S^0}$ (Bauch *et al.*, 2018) and $A_{^{13}\text{C}}$ (see Sec. III.F) for NV⁻ ensembles predict the two contributions to be equal at $N_S^0 = 10.6$ ppm, which is consistent to within experimental uncertainty.

In the Appendix, Sec. 4, we present a simple toy model (Kleinsasser *et al.*, 2016) for the case when nitrogen-related defects dominate T_2^* . In this regime, under the assumption that the conversion efficiency of total nitrogen to NV⁻, NV⁰, and N_S⁺ is independent of the total nitrogen concentration [N^T], the dephasing time T_2^* scales inverse linearly with [N^T], while the number of collected photons $\mathcal N$ scales linearly with [N^T]. These scalings result in a shot-noise-limited sensitivity $\eta \propto 1/\sqrt{\mathcal N T_2^*}$, which is independent of [N^T]. However, as discussed in Sec. II.C and the Appendix, Sec. 3, technical considerations favor lower nitrogen concentrations [N^T], which result in lower photon numbers $\mathcal N$ and longer dephasing times T_2^* (Kleinsasser *et al.*, 2016).

E. Nitrogen limit to T_2

Contributions to the NV⁻ spin dephasing time T_2^* from static and slowly varying inhomogeneities are largely mitigated by employing a $\pi/2 - \pi - \pi/2$ Hahn echo pulse sequence; see Sec. IV.A. In contrast to a $\pi/2 - \pi/2$ Ramsey sequence (see the Appendix, Sec. 1.a), the added π pulse reverses the precession direction of the sensor spins halfway through the free-precession interval. As a result, any net phase accumulated by the NV⁻ spin state due to a static magnetic field vanishes, as the accumulated phase during the first interval (before the π pulse) cancels the accumulated phase during the second interval (after the π pulse). Consequently, the characteristic decay time of the NV⁻ spin state measured through the Hahn echo, denoted by T_2 (the coherence time), is substantially longer than the inhomogeneous dephasing time T_2^* , typically exceeding the latter by 1 to 2 orders of magnitude (de Lange *et al.*, 2010; Bauch *et al.*, 2019). By design the Hahn echo sequence and its numerous extensions (Meiboom and Gill, 1958; Gullion, Baker, and Conradi, 1990; Wang et al., 2012) restrict sensing to ac signals, typically within a narrow bandwidth, preventing their application in dc sensing experiments. Nonetheless, the Hahn echo T_2 plays a crucial role in diamond sample characterization and for ac sensing protocols (Sec. IV.A) and merits brief discussion here.

Like T_2^* , T_2 depends on the nitrogen concentration $[N_S^0]$, which sets both the average dipolar-coupling strength between NV⁻ and nitrogen bath spins, i.e., $A_{N_s^0}[N_s^0]$ from Eq. (23), as well as the average coupling strength between nitrogen bath spins (de Sousa, 2009; Bar-Gill *et al.*, 2012). Furthermore, it

can be shown that when nitrogen is the dominant decoherence mechanism, $T_2\{N_S^0\}$ depends inverse linearly on the nitrogen concentration $[N_S^0]$ (Bauch *et al.*, 2019), revealing a close relationship to $T_2^*\{N_S^0\}$. The dependence of $T_2\{N_S^0\}$ on $[N_S^0]$ was recently determined experimentally through NV⁻ ensemble measurements on 25 diamond samples [see Fig. 11(b)], yielding (Bauch *et al.*, 2019)

$$\frac{1}{T_2\{N_S^0\}} = B_{N_S^0}[N_S^0]. \tag{24}$$

Here $B_{\rm N_S^0}=6.25\pm0.47~{\rm ms^{-1}\,ppm^{-1}}$, such that an NV-ensemble in a 1-ppm-nitrogen sample is expected to exhibit $T_2\simeq 160\pm 12~\mu {\rm s}$. The scaling in Eq. (24) should also be compared to that of $T_2^*\{{\rm N_S^0}\}$ [Eq. (23)], with $T_2\{{\rm N_S^0}\}/T_2^*\{{\rm N_S^0}\}=B_{{\rm N_S^0}}/A_{{\rm N_S^0}}\approx 16$. A straightforward application of these results is the calibration of the total nitrogen spin concentration in diamond samples through T_2^* measurements, T_2 measurements, or both, provided that nitrogen remains the primary source of dephasing and decoherence in such samples. Here T_2 measurements are advantageous over T_2^* (or linewidth) measurement schemes, as the latter are more likely to be limited by non-nitrogen dephasing mechanisms (Bauch *et al.*, 2018).

Lastly, we note that the inverse linear scaling of $T_2^*\{N_S^0\}$ and $T_2\{N_S^0\}$ with $[N_S^0]$, as well as the hierarchy $T_2\gg T_2^*$, is consistent with earlier EPR studies of N_S^0 nitrogen defects in nitrogen-rich diamonds (van Wyk *et al.*, 1997; Stepanov and Takahashi, 2016) and other comparable spin systems in silicon (Abe *et al.*, 2010; Witzel *et al.*, 2010). Predicting the values of $B_{N_S^0}$ and $A_{N_S^0}$ for NV⁻ based on equivalent EPR scaling parameters measured with P1 centers in diamond (van Wyk *et al.*, 1997) is expected to be crudely effective. However, accuracy at the 10% level or better likely requires accounting for various experimental specifics (e.g., the magnetic field value) (Hall, Cole, and Hollenberg, 2014).

F. ¹³C limit to T_2^*

Dipolar coupling between NV⁻ electronic and ¹³C nuclear spins can also limit T_2^* (Dobrovitski *et al.*, 2008; Balasubramanian *et al.*, 2009; Zhao, Ho, and Liu, 2012; Hall, Cole, and Hollenberg, 2014). Reducing the ¹³C content below the natural abundance concentration [13 C] = 10700 ± 800 ppm $\approx 1.1\%$ (Wieser *et al.*, 2013) through isotope engineering is the most direct way to mitigate this effect (Balasubramanian *et al.*, 2009; Itoh and Watanabe, 2014; Bauch *et al.*, 2018). In the "dilute" spin limit where [13 C]/[12 C] $\ll 0.01$ (Kittel and Abrahams, 1953), the 13 C dephasing contribution is well approximated by

$$\frac{1}{T_2^*\{^{13}C\}} = A_{^{13}C}[^{13}C], \tag{25}$$

where $A_{^{13}\text{C}}$ is a constant characterizing the magnetic dipole interaction strength between NV⁻ spins and ^{13}C nuclear spins, in accordance with theoretical predictions (Kittel and Abrahams, 1953; Abragam, 1983c; Dobrovitski *et al.*,

2008; Hall, Cole, and Hollenberg, 2014); see the Appendix, Sec. 8. Although experimental measurements relating T_2^* to [13 C] are available only for single NV $^-$ centers (Balasubramanian *et al.*, 2009; Mizuochi *et al.*, 2009) and not to date for NV $^-$ ensembles, the scaling in Eq. (25) is consistent with experimental findings in a similar ensemble spin system: EPR linewidth measurements on substitutional phosphorus spin ensembles in a 28 Si crystal exhibit the same scaling for various dilute concentrations of 29 Si (Abe *et al.*, 2010; Morishita *et al.*, 2011). Figure 4(b) depicted in Abe *et al.* (2010) suggests that Eq. (25) is approximately valid for [29 Si]/[18 Si] $\lesssim 0.05$, so it is plausible that $A_{^{13}$ C can be inferred from measurements on diamonds with natural 13 C isotopic abundance where [13 C]/[12 C] ≈ 0.0107 . We make this assumption henceforth.

While the value of $A_{^{13}\text{C}}$ is not known precisely for NV-ensembles, T_2^* measurements in diamond with natural ^{13}C abundance set an approximate upper bound on $A_{^{13}\text{C}}$, since necessarily $1/T_2^* > 1/T_2^*\{^{13}\text{C}\}$. Figure 12 shows a double-quantum Ramsey FID for a diamond with natural ^{13}C abundance and low nitrogen concentration; these data suggest $A_{^{13}\text{C}} \approx 0.100 \text{ ms}^{-1} \text{ ppm}^{-1}$. With this value for $A_{^{13}\text{C}}$, the expected limit for a 99.999% ^{12}C isotopically enriched diamond is $T_2^*\{^{13}\text{C}\} \approx 1 \text{ ms}$, at which point dipolar interaction with ^{13}C nuclear spins is unlikely to be the leading-order dephasing mechanism [see Eq. (19)]. Comparing $A_{^{13}\text{C}}$ with the measured $A_{N^0} = 101 \text{ ms}^{-1} \text{ ppm}^{-1}$ for dephasing of NV- ensembles by

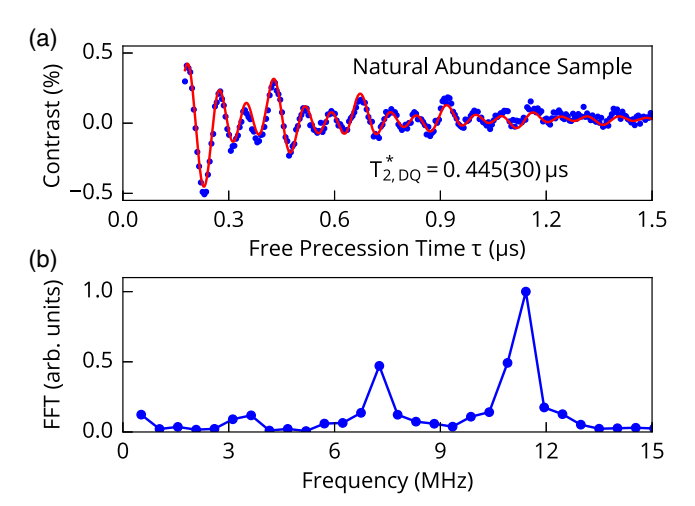


FIG. 12. T_2^* measurement of a low-nitrogen-content diamond with natural abundance $[^{13}\mathrm{C}] = 10\,700$ ppm to assess the $^{13}\mathrm{C}$ contribution to dephasing. (a) Double-quantum (DQ) Ramsey free induction decay (FID) and associated fit suggest T_2^* is 445 ns in the DQ basis. These data set a bound $A_{^{13}\mathrm{C}} < 0.105~\mathrm{ms}^{-1}~\mathrm{ppm}^{-1}$. Correcting for the test diamond's approximately known $[\mathrm{N}_\mathrm{S}^0] \approx 0.5~\mathrm{ppm}$ content allows further refinement to $A_{^{13}\mathrm{C}} \approx 0.100~\mathrm{ms}^{-1}~\mathrm{ppm}^{-1}$. (b) Fourier transform of the FID shown in the top panel. The three peaks arise from hyperfine interactions associated with the NV⁻ center's $^{14}\mathrm{N}$ nuclear spin I=1 and exhibit intrapeak spacing double that of an equivalent single-quantum Ramsey measurement. The unbalanced peak heights are attributed to nuclear spin polarization induced by the 150 G bias magnetic field.

substitutional nitrogen (see Sec. III.D), dephasing from natural abundance $[^{13}C] = 10\,700$ ppm and substitutional nitrogen with concentration $[N_S^0] = 10.6$ ppm should be equivalent, which is in good agreement with van Wyk *et al.* (1997), who observed equivalence for $[N_S^0] \approx 10.8$ ppm. Conveniently, it is easy to remember that $T_2^*\{^{13}C\}$ is 1 μ s for natural abundance ^{13}C diamond to better than 10%.

The bound on $A_{^{13}\text{C}}$ previously derived can be crudely confirmed using a mix of theoretical predictions from Hall, Cole, and Hollenberg (2014) and data from Maze *et al.* (2012). Maze *et al.* (2012) found the most probable T_2^* for a single NV⁻ center in natural isotopic diamond to be $T_2^{*\{\text{single},\text{mp}\}} = 1.8 \pm 0.6 \,\mu\text{s}$ [measured in a 20 G bias field, Fig. 4(a) in Maze *et al.* (2012)]. From relations in Hall, Cole, and Hollenberg (2014) we estimate $A_{^{13}\text{C}}$ in terms of the coupling constant $A_{^{13}\text{C}}^{\text{single}}$ for a single NV⁻, $A_{^{13}\text{C}} \approx 2.2 A_{^{13}\text{C}}^{\text{single},\text{mp}}$, which yields $A_{^{13}\text{C}} = 0.11 \pm 0.04 \,\text{ms}^{-1} \,\text{ppm}^{-1}$.

The measured value $A_{^{13}\text{C}} \approx 0.100~\text{ms}^{-1}~\text{ppm}^{-1}$ is also in reasonable agreement with first-principles theoretical calculations by Hall, Cole, and Hollenberg (2014), suggesting $A_{^{13}\text{C}} \approx 0.057~\text{ms}^{-1}~\text{ppm}^{-1}$ for NV⁻ ensembles in natural isotopic diamond in tens-of-gauss bias fields. Note that the experimental determination of $A_{^{13}\text{C}}$ outlined in this section represents an upper bound on the true value of $A_{^{13}\text{C}}$ in the dilute (dipolar-broadened) limit; if substantial broadening arises from Fermi-contact contributions in addition to dipolar interactions in natural abundance ^{13}C samples, or if $[^{13}\text{C}] = 10\,700~\text{ppm}$ does not qualify as the dilute limit (Kittel and Abrahams, 1953; Abragam, 1983c), the value of $A_{^{13}\text{C}}$ given here will be overestimated.

Engineering diamonds for low ¹³C content may be challenging (Markham et al., 2011; Dwyer, Pomeroy, and Simons, 2013; Teraji et al., 2013). The isotopic purity of a diamond grown by plasma-enhanced chemical vapor deposition (PE-CVD) is expected to be limited by the purity of the carbon source gas, which is most commonly methane (CH₄). However, diamonds grown with isotopically enriched methane may exhibit higher fractional ¹³C content than the source gas due to extraneous carbon sources in the CVD chamber (Dwyer, Pomeroy, and Simons, 2013). Nonetheless, Teraji et al. achieved $[^{12}C] = 99.998\%$ as measured by secondary ion mass spectrometry (SIMS) when using isotopically enriched methane with 99.999% 12 C (i.e., ${}^{[13}$ C) ≤ 10 ppm) (Teraji et al., 2013, 2015). Although such isotopically enriched methane is currently 10³-10⁴ times more expensive than natural abundance CH₄, order unity conversion of the methane's carbon content into diamond is attainable (Teraji et al., 2013).

G. NV⁻ limit to T_2^*

Dipolar interactions among negatively charged NV⁻ centers may also limit the dephasing time T_2^* . Dephasing from NV⁻-NV⁻ interactions arises from NV⁻ spins in both the same and different groups as the NV⁻ centers used for sensing, where groups are defined as follows: NV⁻ centers with approximately the same spin resonance frequency are

considered to be in the same group, whereas spins with different resonance frequencies are in different groups (Kucsko *et al.*, 2018). Depending on the strength and angle of the applied bias field, the spin resonances of the four NV⁻ orientations may be spectrally separated, or two or more may be overlapped, changing the fraction of NV⁻ spins in the same group; see Fig. 13. The NV⁻-NV⁻ dipolar contribution to T_2^* is then given by

$$\frac{1}{T_{2}^{*}\{NV^{-}\}} = \frac{1}{T_{2}^{*}\{NV^{-}\}_{\parallel}} + \frac{1}{T_{2}^{*}\{NV^{-}\}_{\parallel}}$$

$$= \varsigma_{\parallel}A_{NV_{\parallel}^{-}}[NV_{\parallel}^{-}] + \varsigma_{\parallel}A_{NV_{\parallel}^{-}}[NV_{\parallel}^{-}]. \quad (26)$$

Here $[NV_{\parallel}^{-}]$ is the concentration of NV⁻ spins in the group being used for sensing and $[NV_{\parallel}^{-}]$ is the concentration of NV⁻ spins in other groups, with $[NV_{\parallel}^{-}] + [NV_{\parallel}^{-}] = [NV_{\text{total}}^{-}]$; the constants $A_{NV_{\parallel}^{-}}$ and $A_{NV_{\parallel}^{-}}$ characterize the dipolar interaction strength for pairs of NV⁻ spins in the same group and different groups, respectively; and ς_{\parallel} and ς_{\parallel} are dimensionless factors of order unity accounting for (imperfect) initialization of NV⁻ centers (Doherty *et al.*, 2013). For example, off-resonant NV⁻ populations polarized into the spinless $m_s = 0$ state during initialization should not contribute to dephasing of the NV⁻ centers used for sensing, giving $\varsigma_{\parallel} \simeq 0$.

Flip-flop interactions between NV⁻ spins in different groups are off resonant and are thus suppressed, whereas flip-flop interactions can occur resonantly between spins in the same group. The extra resonant interaction terms in the dipole-dipole Hamiltonian for spins in the same group result in a slightly increased dephasing rate (Abragam, 1983a; Kucsko *et al.*, 2018). Following Abragam (1983a), it is expected that $A_{\rm NV_{\parallel}}=(3/2)A_{\rm NV_{\parallel}}$.

The lack of published data at present for $T_2^*\{NV^-\}$ in samples with varying NV^- concentration prevents definitive determination of A_{NV_\parallel} and $A_{NV_\#}$. However, both terms can be estimated from the experimentally determined value of

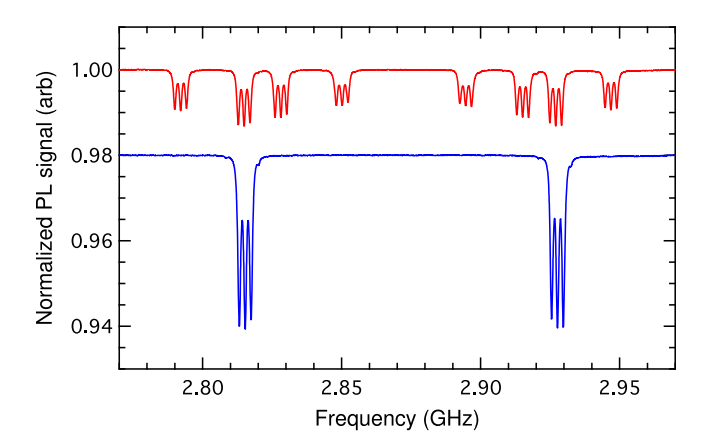


FIG. 13. Example ODMR spectra from the same NV⁻ ensemble in different applied bias magnetic fields. A bias field with a different projection on each of the four NV⁻ crystallographic orientations separates the $m_s = 0 \leftrightarrow m_s = \pm 1$ spin resonances into distinct groups (red). A bias field that projects equally onto all four orientations overlaps the spin resonances (blue, offset for clarity).

 $A_{\rm N_S^0}=101\pm12~{\rm ms^{-1}\,ppm^{-1}}$ (Bauch *et al.*, 2019), which describes the scaling of NV⁻ ensemble T_2^* with substitutional nitrogen concentration; see Sec. III.D. Assuming an NV⁻ electronic spin bath couples to NV⁻ sensor spins with approximately the same strength as a substitutional nitrogen spin bath (Hanson *et al.*, 2008), and accounting for the higher spin multiplicity of NV⁻ centers ($S_{\rm NV^-}=1$) compared to substitutional nitrogen spins ($S_{\rm N_S^0}=1/2$), we calculate (Abragam, 1983a)

$$\begin{split} A_{\text{NV}_{\#}} &\simeq \sqrt{\frac{S_{\text{NV}^{-}}(S_{\text{NV}^{-}}+1)}{S_{\text{N}_{\text{S}}^{0}}(S_{\text{N}_{\text{S}}^{0}}+1)}} A_{\text{N}_{\text{S}}^{0}} \\ &\simeq \sqrt{8/3} A_{\text{N}_{\text{S}}^{0}} \\ &\simeq 165 \text{ ms}^{-1} \text{ ppm}^{-1} \end{split} \tag{27}$$

and find $A_{\mathrm{NV}_{\parallel}^-} = (3/2)A_{\mathrm{NV}_{\parallel}^-} \simeq 247~\mathrm{ms}^{-1}~\mathrm{ppm}^{-1}$. From this argument, although the precise value of $T_2^*\{\mathrm{NV}^-\}$ depends on experimental conditions including optical initialization fraction (determining ς_{\parallel} and ς_{\dag}) and bias magnetic field orientation (setting the ratio $[\mathrm{NV}_{\parallel}^-]/[\mathrm{NV}_{\dag}^-]$), the value of $T_2^*\{\mathrm{NV}^-\}$ for a given NV^- concentration is well approximated (up to a factor of order unity) by the dephasing time $T_2^*\{\mathrm{N}_S^0\}$ for an identical concentration of N_S^0 spins.

Magnetometer operation in the NV--NV- interaction limit may occur as the N-to-NV⁻ conversion efficiency E_{conv} approaches its theoretical limit of 50% (Felton et al., 2009; Pham et al., 2011); see Sec. VI.A. Under these circumstances, and when other sources of dephasing can be neglected [e.g., magnetic, electric, and strain gradients as well as ¹³C nuclear spins (see Sec. III.F) and other paramagnetic defects (see Sec. VI.F)], the interaction among NV⁻ spins becomes the dominant source of dephasing. However, maximal N-to-NVconversion efficiency is not necessarily required to operate in the NV⁻-NV⁻ interaction limit. When $E_{\rm conv}$ < 50%, dephasing due to other paramagnetic impurities may be reduced through spin-bath driving techniques described in Sec. IV.C. Spin-bath driving can also decouple the NV⁻ centers in different groups from the NV⁻ centers in the group used for sensing (Bauch et al., 2018), suppressing the second term in Eq. (26) $(1/T_2^*\{NV^-\}_{\sharp})$ and leaving only the first term $(1/T_2^*\{NV^-\}_{\parallel})$ as a fundamental limit to NV⁻ ensemble T_2^* .

While this section has focused on the negatively charged NV⁻ center, NV centers are also present in the neutral charge state NV⁰ (S=1/2); see Sec. VI.A. NV⁰ has not been observed in its ground state in EPR, a phenomenon tentatively attributed to resonance line broadening from dynamic Jahn-Teller distortion (Felton *et al.*, 2008). Similarly, magnetic noise created by NV⁰ may be reduced by this motional-narrowing-type effect to less than otherwise expected for an S=1/2 defect; see Sec. IV.C. Consequently, the contribution of NV⁰ spins to dephasing of NV⁻ spins may be smaller than expected. More recent work, however, suggests an alternative hypothesis: the NV⁰ ground state is not visible in EPR due to large strain effects (Barson *et al.*, 2019). What little, if any, NV⁺ is present in the sample is expected to be spinless (see Table IX) and should not contribute substantially to dephasing.

Recently, several protocols have been proposed to mitigate strong NV⁻-NV⁻ dipolar interactions and extend T_2^* (O'Keeffe et al., 2019) or T_2 (Choi, Yao, and Lukin, 2017a) while retaining magnetic field sensitivity. In addition, it was proposed that under certain circumstances the NV⁻-NV⁻ dipolar interaction could enhance magnetometry sensitivity through enabling entanglement of multiple NV- centers (Choi, Yao, and Lukin, 2017b); see Sec. VII.D. Harnessing entanglement could enable superior scaling of measurement SNR with the number of spins addressed N, exceeding the standard quantum limit SNR $\propto \sqrt{N}$ and approaching the Heisenberg limit, SNR $\propto N$. Controlled coupling of NV⁻ spin pairs (Neumann et al., 2010; Bernien et al., 2013; Dolde et al., 2013; Yamamoto, Müller et al., 2013; Hensen et al., 2015; Jakobi et al., 2016) has been demonstrated; however, applying entanglement-enhanced techniques to larger ensembles is expected to be challenging.

IV. METHODS TO EXTEND T_2^* AND T_2

A. Dynamical decoupling for ac magnetometry

While this review primarily addresses the broadband dc sensing modality of ensemble-NV⁻ magnetometers, many of the sensitivity-improvement techniques described herein can also be applied to detecting narrow-band ac magnetic fields. Here we provide a brief overview of standard ac sensing schemes, we discuss several approaches to improving ac magnetic field sensitivity, and we highlight challenges unique to the ac sensing modality.

The Hahn echo (alternatively referred to as the spin echo) protocol, shown in Fig. 14, builds upon the Ramsey protocol with an additional central MW π pulse, which refocuses dephasing of the NV⁻ spin ensemble (Hahn, 1950). The decay of spin coherence measured with this pulse sequence is characterized by T_2 , which is typically 1 to 2 orders of magnitude longer than T_2^* in NV⁻ ensemble measurements; see Secs. III.C, III.D, and III.E. Furthermore, while the refocusing pulse decouples the NV- spin from dc magnetic fields, its presence makes Hahn echo measurements particularly sensitive to oscillating magnetic fields with period T_B matching the spin interrogation time τ of the pulse sequence. In the ideal case where the 3 MW pulses are commensurate with consecutive nodes of the ac magnetic field, the sensitivity of a Hahn-echo-based measurement limited by shot noise and spin-projection noise is given by

 $\eta_{\rm echo}^{\rm ensemble}$

$$\approx \underbrace{\frac{\pi}{2} \frac{\hbar}{\Delta m_s g_e \mu_B} \frac{1}{\sqrt{N\tau}}}_{\text{spin projection limit}} \underbrace{\frac{1}{e^{-(\tau/T_2)^p}}}_{\text{spin decoherence}} \underbrace{\sqrt{1 + \frac{1}{C^2 n_{\text{avg}}}}}_{\text{readout}} \underbrace{\sqrt{\frac{t_I + \tau + t_R}{\tau}}}_{\text{overhead time}},$$
(28)

where Δm_s is the spin-projection quantum number difference between the two states in the interferometry measurement, N is the number of interrogated spins, τ is the full field interrogation time, p is a stretched exponential parameter set by ensemble averaging of the local NV⁻ spin environments (see the Appendix, Sec. 7), C is the measurement contrast prior to precession (see Sec. II.A), $n_{\rm avg}$ is the average number of

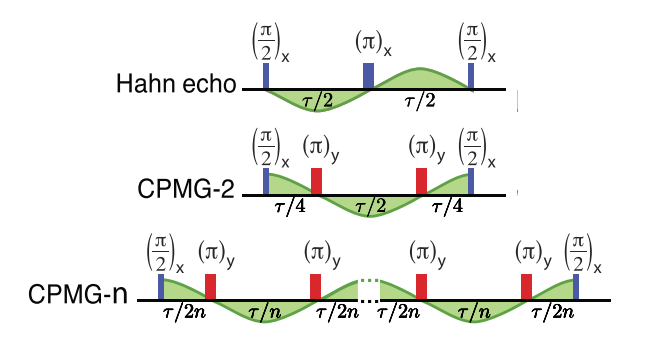


FIG. 14. Select pulse sequences for ac magnetometry. The Hahn echo sequence includes a refocusing π pulse midway through the interrogation time, allowing phase-sensitive lock-in-type measurements of ac magnetic fields (top). Hahn echo is maximally sensitive to ac fields with nodes coincident with the 3 MW pulses. Detection of ac fields with the quadrature phase can be achieved using the Carr-Purcell-Meiboom-Gill-2 (CPMG-2) sequence (middle). Employing additional π pulses (CPMG-n) achieves more efficient decoupling of the NV $^-$ from substitutional nitrogen and other paramagnetic defects in the diamond and provides sensitivity to higher-frequency ac magnetic fields (bottom). From Pham, Bar-Gill, Belthangady *et al.*, 2012.

photons detected per NV⁻ center per readout, and t_I and t_R are the optical initialization and readout times, respectively. For more realistic measurements in which the pulse sequence cannot be phase locked to the ac magnetic field, the magnetic sensitivity is degraded by $\sqrt{2}$. Equation (28) describes the amplitude of the sinusoid yielding an SNR of 1 following historical convention Taylor *et al.*, 2008. Since the root-mean-square (rms) value of this sinusoid is smaller by $\sqrt{2}$, the sensitivity referenced to rms amplitude is also smaller by $\sqrt{2}$.

The shot-noise-limited sensitivity given by Eq. (28) has several key differences to that of a Ramsey-based dc sensing protocol [Eq. (16)]. First, since typically $T_2 \gg T_2^*$, ac sensing schemes can achieve better sensitivity than dc sensing schemes. Second, choice of spin interrogation time τ is more straightforward for Ramsey schemes than for echo-based schemes. For Ramsey-based sensing of dc or quasistatic fields, $\tau \sim T_2^*$ is optimal; see the Appendix, Sec. 2. In contrast, while $\tau \sim T_2$ is optimal for Hahn echo-based protocols, τ should also be matched to the period T_B of the ac magnetic field to be measured. As a result the scheme is maximally sensitive to fields of period $T_B \sim T_2$, with a detection bandwidth set by the relevant filter function (Cywiński et al., 2008). Finally, coherent interactions between the NV⁻ spin and other spin impurities in the diamond can modulate the Hahn echo coherence envelope. At best, these effects introduce collapses and revivals that do not affect T_2 and merely complicate the NV⁻ magnetometer's ability to measure ac magnetic fields of arbitrary frequency. When the bias magnetic field is aligned to the NV⁻ internuclear axis in diamond samples containing a natural abundance of ¹³C, collapse-and-revival oscillations occur with frequency set by the ¹³C Larmor precession. At worst, misalignment between the bias magnetic field and the NV⁻ internuclear axis results in anisotropic hyperfine interactions, which enhance the nuclear spin Larmor precession rate for ¹³C (and ¹⁵N in ¹⁵NV diamonds) as a function of separation between the nuclear spins and NV⁻ centers (Childress et al., 2006; Maurer *et al.*, 2010). These effects ensemble average to an effectively shorter coherence time T_2 (Stanwix *et al.*, 2010), which degrades ac sensitivity.

Despite these differences, the Ramsey and spin-echo measurement schemes share many of the same components; consequently, many techniques for improving spin readout fidelity (analyzed in Sec. V) apply to both dc and ac sensing modalities. For example, ancilla-assisted repetitive readout (Sec. V.C), level-anticrossing-assisted readout (Sec. V.D), and improved fluorescence collection methods (Sec. V.E) increase the number of detected photons per measurement \mathcal{N} ; preferential NV⁻ orientation (Sec. VI.G) enhances the measurement contrast C; and spin-to-charge-conversion (SCC) readout (Sec. V.A) and NV⁻ charge-state optimization (Sec. VI.B) increase both C and \mathcal{N} . We note that, because typically $T_2 \gg T_2^*$, advanced readout techniques such as repetitive readout and SCC readout presently offer greater sensitivity improvement for ac schemes than for dc schemes, as their long-readout-time requirements introduce smaller fractional overhead in ac measurements with longer interrogation times.

Additionally, techniques to extend T_2^* for dc and broadband magnetometry may also improve ac magnetic field sensitivity. For example, DQ coherence magnetometry (Sec. IV.B) is expected to improve ac sensitivity both by introducing a factor of 2 increase in the NV⁻ spin precession rate (Fang *et al.*, 2013; Mamin *et al.*, 2014) and, in certain cases, by extending the NV⁻ coherence time T_2 (Angerer *et al.*, 2015). Similarly, spin-bath driving (Sec. IV.C) which suppresses magnetic noise, or operation at a sufficiently strong bias magnetic field (Sec. IV.D) which suppresses electric and strain noise, may extend T_2 .

Another technique for enhancing NV⁻ magnetic sensitivity, unique to the ac sensing modality, is the application of multipulse sequences, whose timing is based on the Carr-Purcell-Meiboom-Gill (CPMG) family of pulse sequences well known in NMR (Cywiński et al., 2008; Pham, 2013); see Fig. 14. By applying additional MW π pulses at a rate of $1/(2T_B)$, these multipulse sequences (i) extend the NV⁻ coherence time T₂ by more effectively decoupling the NV⁻ spins from magnetic noise and (ii) increase the time during which the NV⁻ spins interrogate the ac magnetic field. The coherence time has been found to scale with a power law s $(T_2 \to T_2^{(k)} = T_2 k^s)$ as a function of the number of pulses k(Pham, Bar-Gill, Belthangady et al., 2012), where s is set by the noise spectrum of the decohering spin bath and is typically sublinear. For example, a bath of electronic spins, such as N_s^0 defects in diamond, exhibits a Lorentzian noise spectrum and results in a power-law scaling of the coherence time with s = 2/3, assuming the electronic spin bath is the dominant decoherence source (de Sousa, 2009). The multipulse ac magnetic field sensitivity limited by shot noise and spinprojection noise is given by

$$\approx \underbrace{\frac{\pi}{2} \frac{\hbar}{\Delta m_s g_e \mu_B} \frac{1}{\sqrt{N\tau}}}_{\text{spin projection limit}} \underbrace{\frac{1}{e^{-[\tau/(k^* T_2)]^p}}}_{\text{spin decoherence}} \underbrace{\sqrt{1 + \frac{1}{C^2 n_{\text{avg}}}}}_{\text{readout}} \underbrace{\sqrt{\frac{t_I + \tau + t_R}{\tau}}}_{\text{overhead time}} \tag{29}$$

with an optimal number of pulses

$$k_{\text{opt}} = \left[\frac{1}{2p(1-s)} \left(\frac{2T_2}{T_B}\right)^p\right]^{1/[p(1-s)]},$$
 (30)

for an ac magnetic field with period T_B , assuming full interrogation time $\tau = (k/2)T_B$ and π pulses commensurate with the nodes of the oscillating magnetic field. As before, the sensitivity is degraded by $\sqrt{2}$ when measuring ac magnetic fields with unknown phase. Like Eq. (28), Eq. (29) describes the amplitude of the sinusoid yielding an SNR of 1 following historical convention (Taylor *et al.*, 2008). Since the rms value of this sinusoid is smaller by $\sqrt{2}$, the sensitivity referenced to rms amplitude is also smaller by $\sqrt{2}$.

Equations (29) and (30) illustrate that multipulse measurement schemes improve sensitivity to magnetic fields with periods $T_R < T_2$ and enable sensing of higher frequencies than can be accessed with Hahn echo-based measurements. For example, Pham, Bar-Gill, Belthangady et al. (2012) demonstrated a 10 times improvement (compared to the Hahn echo) in ensemble ac sensitivity at 220 kHz by using a multipulse sequence. However, the increased number of control pulses, which are typically imperfect due to NV⁻ hyperfine structure and inhomogeneities in the system, can result in cumulative pulse error and thus degraded ac sensitivity (Wang et al., 2012). Compensating pulse sequences, including schemes in the XY, concatenated, and BB-n families, may be employed to restore ac field sensitivity in the presence of pulse errors (Gullion, Baker, and Conradi, 1990; Wang et al., 2012; Low, Yoder, and Chuang, 2014; Farfurnik et al., 2015; Rong et al., 2015).

The ac sensing techniques are also pertinent to noise spectroscopy. By mapping out a diamond's spin-bath spectral noise profile, tailored sensing protocols can be designed to more efficiently extract target signals. To this end, dynamical decoupling sequences, such as those in the CPMG and XY families, are employed for noise mapping (Bar-Gill et al., 2012, 2013; Romach et al., 2015; Chrostoski, Sadeghpour, and Santamore, 2018; Bauch et al., 2019). By varying both the total precession time and the number of refocusing pulses, noise at a variable target frequency can be isolated, ultimately allowing measurement of the entire spin-bath spectral noise profile. However, such measurements are often complicated by nonidealities in certain sequences' filter functions, such as sensitivity to harmonics or the presence of side lobes (Cywiński et al., 2008). Recently, ac magnetometry protocols with enhanced spectral resolution have been demonstrated, such as the dynamic sensitivity control (known as DYSCO) sequence and its variants (Lazariev et al., 2017; Romach et al., 2019), which provide simpler, single-peaked filter functions at the cost of reduced sensitivity. Additional dynamical decoupling sequences with increased spectral resolution or other advantages have been employed (Boss et al., 2017; Schmitt et al., 2017; Glenn et al., 2018; Hernández-Gómez et al., 2018) or proposed (Cywiński et al., 2008; Zhao, Wrachtrup, and Liu, 2014; Poggiali, Cappellaro, and Fabbri, 2018).

A final consideration in the application of multipulse sequences for enhancing ac magnetometry with NV $^-$ centers is that extension of the T_2 coherence time (and thus enhancement of ac magnetic field sensitivity) is eventually limited by

the T_1 spin-lattice relaxation time, beyond which increasing the number of π pulses is ineffective. This limitation can be overcome by reducing the magnetometer operating temperature, thereby suppressing the two-phonon Raman process that dominates NV⁻ spin-lattice relaxation near room temperature and extending T_1 (Jarmola *et al.*, 2012). Multipulse sequences performed at 77 K have demonstrated > 100 times extensions in T_2 compared to room temperature measurements (Bar-Gill *et al.*, 2013), and corresponding improvements to ac magnetic field sensitivity are expected.

Although the limit $\{T_2, T_2^*\} \le 2T_1$ is well established theoretically (Yafet, 1963; Slichter, 1990) and observed in other spin systems (Bylander et al., 2011), the maximum T_2 values achieved in NV-diamond through dynamical decoupling protocols have historically never exceeded measured values of T_1 , with Bar-Gill et al. (2013) achieving $T_2 = 0.53(2)T_1$ for NVs in bulk diamond and Myers et al. (2014) and Romach et al. (2015) observing $T_2 \lesssim 0.1T_1$ for shallow NVs. While this discrepancy is not fully resolved, it is partially accounted for by the observation that the typical measurement protocol for T_1 [e.g., that described by Pham (2013)] yields a T_1 value that does not encompass all possible decays of the full spin-1 system but rather only the decay $T_1^{(0)}$ in the pseudo-spin-1/2 subspace of $|0\rangle$ and either $|+1\rangle$ or $|-1\rangle$ (Myers, Ariyaratne, and Jayich, 2017). The value of T_1 for the full S=1 system is typically shorter than $T_1^{(0)}$ thanks to non-negligible decay from $|+1\rangle$ to $|-1\rangle$ and vice versa. This spin-1 T_1 , which can be measured using methods described by Myers, Ariyaratne, and Jayich (2017), is the relevant relaxation time limiting T_2 and T_2^* .

B. Double-quantum (DQ) coherence magnetometry

Standard NV⁻ magnetometry techniques, such as cw-ODMR (Sec. II.B.1), pulsed ODMR (Sec. II.B.2), and pulsed Ramsey or echo-type schemes (Sec. IV.A), are typically performed in the pseudo-spin-1/2 single-quantum (SQ) subspace of the NV⁻ ground state, with the $|m_s=0\rangle$ and either the $|m_s=+1\rangle$ or the $|m_s=-1\rangle$ spin state ($\Delta m_s=1$) employed for sensing. In contrast, double-quantum (DQ) coherence magnetometry ($\Delta m_s=2$) works as follows for a Ramsey-type implementation; see Fig. 15. First an equal superposition of the $|+1\rangle$ and $|-1\rangle$ states is prepared [e.g., $|+_{DQ}\rangle=(1/\sqrt{2})(|+1\rangle+|-1\rangle)$]. Then, after a free-precession interval, the final population in $|+_{DQ}\rangle$ is mapped back to $|0\rangle$, allowing for a magnetic-field-dependent population difference between $|0\rangle$ and $|-_{DQ}\rangle$ to be read out optically.

Use of the full spin-1 nature of the NV⁻ center and the double-quantum basis $\{|-1\rangle, |+1\rangle\}$ allows for several sensing advantages. First, at fixed magnetic field, an NV⁻ spin prepared in a superposition of the $|+1\rangle$ and $|-1\rangle$ states precesses at twice the rate as in the standard SQ subspace of $\{|0\rangle, |-1\rangle\}$ or $\{|0\rangle, |+1\rangle\}$, enabling enhanced magnetometer sensitivity. Moreover, measurements in the DQ basis are differential in that noise sources perturbing the $|0\rangle \leftrightarrow |+1\rangle$ and $|0\rangle \leftrightarrow |-1\rangle$ transitions in the common mode are effectively rejected. Sources of common-mode noise may include temperature fluctuations, which enter the NV⁻ Hamiltonian via the zero-field splitting parameter D ($\partial D/\partial T \approx -74$ kHz/K) (Acosta, Bauch, Ledbetter *et al.*, 2010; Kucsko

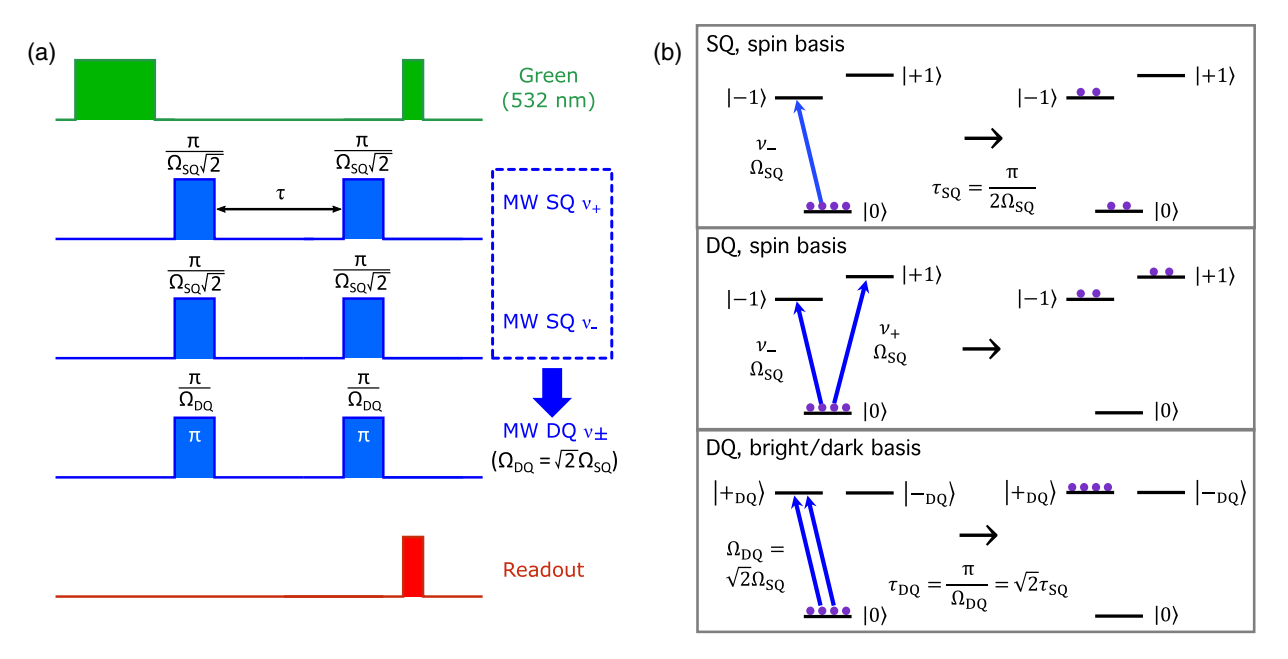


FIG. 15. (a) Pulse sequence for Ramsey-type double-quantum (DQ) coherence magnetometry, as implemented by Bauch *et al.* (2018). The single-quantum (SQ) $|0\rangle \leftrightarrow |+1\rangle$ and $|0\rangle \leftrightarrow |-1\rangle$ transitions are driven by MWs at or near respective resonance frequencies ν_+ and ν_- . For simultaneously applied resonant MWs with Rabi frequencies $\Omega_+ = \Omega_- = \Omega_{SQ}$, double-quantum (DQ) transitions occur between $|0\rangle$ and an equal superposition of $|+1\rangle$ and $|-1\rangle$ with corresponding DQ Rabi frequency $\Omega_{DQ} = \sqrt{2}\Omega_{SQ}$. A DQ Ramsey sequence requires MW pulses of duration $\tau_{DQ} = \pi/\Omega_{DQ} = \pi/(\Omega_{SQ}\sqrt{2})$ to prepare the state used for sensing. (b) Comparison between a conventional SQ $\pi/2$ pulse on a single transition (top panel) and a DQ π pulse used to prepare the superposition state $|+_{DQ}\rangle = (1/\sqrt{2})(|+1\rangle + |-1\rangle)$ for the sequence in (a) (lower two panels). The middle panel shows the DQ state preparation pulse in the bare spin basis, while the bottom panel shows the same pulse in the basis of $|0\rangle$ and the bright and dark states $|+_{DQ}\rangle$ and $|-_{DQ}\rangle$, i.e., the orthogonal superposition states, respectively, coupled to and blind to the MW drive. During a DQ Ramsey free-precession interval, spin population oscillates between $|+_{DQ}\rangle$ and $|-_{DQ}\rangle$ (as these states are not energy eigenstates), at a rate proportional to the magnetic field. For additional details see Sec. 5.2 in Schloss (2019). Adapted from Schloss, 2019.

et al., 2013; Toyli et al., 2013); axial strain gradients; axial electric fields; and transverse magnetic fields. For a detailed discussion, see Bauch et al. (2018).

If the spin-bath environment is dominated by magnetic noise, as is common for high-nitrogen and natural 13 C abundance diamond samples, measurements in the DQ basis exhibit an increased linewidth and shortened associated dephasing time, as the 2 times enhanced sensitivity to magnetic fields causes the spin ensemble to dephase twice as quickly as in the SQ basis, i.e., $T_{2,\text{DQ}}^* \approx T_{2,\text{SQ}}^* / 2$. The increased dephasing and decoherence is confirmed experimentally for single NV $^-$ centers by Fang *et al.* (2013), who observed a 2 times decrease in T_2^* , and Mamin *et al.* (2014), who observed an ≈ 2 times decrease in the Hahn echo coherence time T_2 . Similar results are reported for NV $^-$ ensembles (Bauch *et al.*, 2018; Kucsko *et al.*, 2018).

In the SQ basis, nonmagnetic noise sources such as temperature fluctuations, electric-field noise, and inhomogeneous strain may also contribute to spin dephasing; see Sec. III.C. However, values of T_2^* in the DQ basis are insensitive to these commonmode noise sources. When such noise dominates dephasing in the SQ basis, the DQ dephasing time $T_{2,\mathrm{DQ}}$ may exceed $T_{2,\mathrm{SQ}}$, allowing for additional sensitivity improvement. For example, DQ measurements reported by Bauch *et al.* (2018) on NV⁻ ensembles demonstrate a ~6 times increase in T_2^* (narrowing of linewidth) in an isotopically purified, low-nitrogen diamond,

leading to an effective 13 times enhancement in phase accumulation per measurement when considering the twice faster precession rate in the DQ basis. For the specific samples investigated, Bauch *et al.* (2018) found the standard SQ basis T_2^* to be limited by strain inhomogeneities, whereas the T_2^* value measured in the DQ basis was likely primarily limited by interactions with residual ¹³C nuclear spins (~100 ppm). This T_2^* limitation emphasizes the importance of isotopic purification when low-nitrogen samples are employed; see Sec. III.F.

For ac magnetometry, dephasing due to strain inhomogeneities and temperature fluctuations can be largely alleviated by using Hahn echo or similar dynamical decoupling sequences (see Sec. IV.A) (Pham, 2013). Nevertheless, double-quantum coherence magnetometry should still yield benefits. First, ensemble ac magnetometry benefits from the expected $\sqrt{2}$ times sensitivity gain due to twice faster precession (Fang *et al.*, 2013). Second, sensitivity may be further enhanced if $T_{2,\mathrm{DQ}}$ exceeds $T_{2,\mathrm{SQ}}/2$. For example, Angerer *et al.* (2015) observed $T_{2,\mathrm{SQ}}=1.66\pm0.16$ ms and $T_{2,\mathrm{DQ}}=2.36\pm0.09$ ms for a single near-surface NV⁻ center with $T_{2,\mathrm{SQ}}$ likely limited by electric-field noise. In addition to magnetic sensing, measurements employing the full spin-1 basis can enhance sensitivity for temperature sensing (Toyli *et al.*, 2013) and noise spectroscopy applications (Kim *et al.*, 2015; Myers, Ariyaratne, and Jayich, 2017).

As shown schematically in Fig. 15, implementation of double-quantum coherence magnetometry is a straightforward

extension of standard pulsed magnetometry. The DQ technique requires applying MW pulses to drive both the $|0\rangle \leftrightarrow$ $|-1\rangle$ and $|0\rangle \leftrightarrow |+1\rangle$ transitions. For sufficiently large magnetic fields, these two transitions must be addressed with separate and phase-locked MW frequencies (Mamin et al., 2014; Angerer et al., 2015). While equal Rabi frequencies on the two transitions are desirable, the MW pulse durations may be adjusted to compensate for unequal Rabi frequencies. MW pulses for each spin transition may be applied simultaneously (Fang et al., 2013; Mamin et al., 2014; Bauch et al., 2018), as depicted in Fig. 15(a), or sequentially (Toyli et al., 2013). At low magnetic field, electric field, and strain, a single MW frequency is adequate (Fang et al., 2013). In either case, care must be taken to ensure that both the upper and lower spin transitions are addressed with adequate MW pulses to achieve an equal superposition of $|+1\rangle$ and $|-1\rangle$ (Mamin *et al.*, 2014; Bauch et al., 2018). Because of the minimal increase in experimental complexity, the ability to suppress commonmode noise sources, and the increased spin precession rate, we expect DQ coherence magnetometry to become standard for high-performance pulsed measurement dc magnetometers employing NV⁻ ensembles.

C. Spin-bath driving

Residual paramagnetic impurity spins in diamond contribute to NV⁻ dephasing, thereby reducing T_2^* . This effect can be mitigated by directly driving the impurity spins, which is particularly useful when dynamical decoupling (see Sec. IV.A) of the NV⁻ sensor spins is not applicable, such as in dc sensing protocols. This technique, termed spin-bath driving, has been successfully demonstrated with substitutional nitrogen spins N_S^0 (S=1/2) (de Lange *et al.*, 2012; Knowles, Kara, and Atatüre, 2014; Bauch *et al.*, 2018). Because of the high typical concentrations of N_S^0 spins in NV-rich diamonds, we focus our discussion on this implementation.

In pulsed spin-bath driving [see Fig. 16(a)], a resonant π pulse is applied to the N_S^0 spins halfway through the NV⁻ Ramsey sequence, decoupling the N_S^0 spins from the NV⁻ spins in analogy with a refocusing π pulse in a Hahn echo sequence (see Fig. 14) (de Lange *et al.*, 2012; Bauch *et al.*, 2018). Alternatively, the spin bath can be driven continuously [see Fig. 16(b)] (de Lange *et al.*, 2012; Knowles, Kara, and

Atatüre, 2014; Bauch *et al.*, 2018). In the latter case, the driving Rabi frequency $\Omega_{\rm N}$ must significantly exceed the NV⁻-N_S⁰ coupling rate $\gamma_{\rm N}$ (i.e., satisfy $\Omega_{\rm N}/\gamma_{\rm N}\gg 1$) to achieve effective decoupling. [Note that $\gamma_{\rm N}\sim 2\pi\times (0.01$ –10) MHz for nitrogen concentrations in the 1–1000 ppm range (see Sec. III.D).] Under this condition, the nitrogen spins undergo many Rabi oscillations during the characteristic dipolar interaction time $1/\gamma_{\rm N}$. As a result, the NV⁻ ensemble is decoupled from the nitrogen spin bath and the NV⁻ dephasing time is enhanced. This phenomenon is similar to motional narrowing observed in many NMR and electron spin resonance (ESR) systems, such as rotation- and diffusion-induced time averaging of magnetic field imhomogeneities (Abragam, 1983c; Slichter, 1990).

de Lange et al. (2012) performed pulsed spin-bath driving in a diamond with $[N^T] \lesssim 200$ ppm and increased T_2^* for a single NV⁻ 1.6 times, from 278 to 450 ns. Similarly, Knowles, Kara, and Atatüre (2014), extended T_2^* for an individual NV⁻ from 0.44 to 1.27 μ s, a 2.9 times improvement, using continuous spin-bath driving in nanodiamonds with $[N] \lesssim 36$ ppm. An NV⁻ ensemble study by Bauch *et al.* (2018) found that if another mechanism, such as lattice strain or magnetic field gradients, is the dominant source of dephasing, spin-bath driving becomes less effective, as shown in Fig. 17; see also Sec. III.C. Nonetheless, at high nitrogen concentrations ($[N_S^T] \gtrsim 1$ ppm), NV⁻ ensemble dephasing due to dipolar interaction with nitrogen spins can be greatly reduced by spin-bath driving (Bauch et al., 2018), as shown in Fig. 18 and also demonstrated in single-NV⁻ experiments (de Lange et al., 2012; Knowles, Kara, and Atatüre, 2014).

To effectively suppress NV⁻ dephasing, typically all nitrogen spin transitions must be driven. Elemental nitrogen occurs in two stable isotopes, ¹⁴N with 99.6% natural isotopic abundance and ¹⁵N with 0.4% natural isotopic abundance. Diamonds may contain predominantly ¹⁴N, where the 99.6% natural abundance purity is typically deemed sufficient, or ¹⁵N, which requires isotopic purification. ¹⁴N exhibits nuclear spin I = 1 while ¹⁵N exhibits nuclear spin I = 1/2, resulting in three and two magnetic-dipole-allowed transitions for each isotope, respectively (Smith *et al.*, 1959; Cook and Whiffen, 1966; Loubser and van Wyk, 1978). As with NV⁻ centers, substitutional nitrogen defects possess a trigonal symmetry as a result of a Jahn-Teller distortion (Davies, 1979, 1981; Ammerlaan and Burgemeister, 1981). The Jahn-Teller

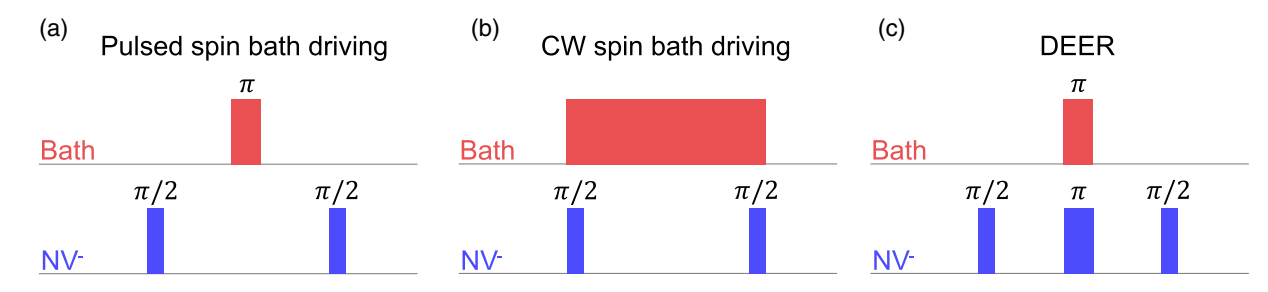


FIG. 16. Selected pulse sequences for concurrent manipulation of NV⁻ spins and the surrounding paramagnetic spin bath. (a) Pulsed spin-bath driving protocol combining a Ramsey sequence on the NV⁻ center(s) with a central rf π pulse on the spin bath. (b) Continuous spin-bath driving protocol combining a Ramsey sequence with continuous resonant rf spin-bath drive. (c) Hahn echo-based double electron-electron resonance (DEER) protocol consisting of a Hahn echo sequence performed on the NV⁻ center(s) combined with a resonant rf π pulse performed on the spin bath. Adapted from Bauch *et al.*, 2018.

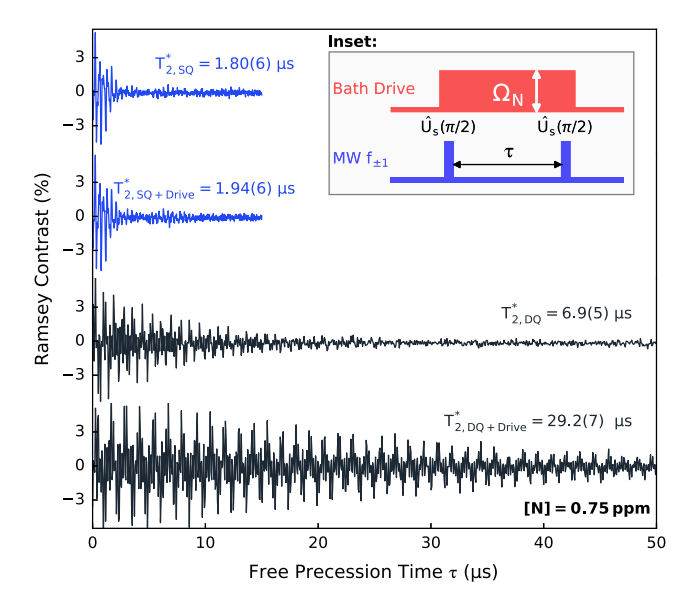


FIG. 17. Ensemble free-induction-decay envelopes as measured using SQ and DQ Ramsey magnetometry, with and without continuous spin-bath driving. Measurements are shown for the following: in the SO basis without spin-bath driving (first from top), in the SQ basis with spin-bath driving (second from top), in the DQ basis without spin-bath driving (third from top), and in the DQ basis with spin-bath driving (fourth from top). Measurements in the DQ basis mitigate strain-induced dephasing, while spinbath driving mitigates dipolar dephasing from the paramagnetic substitutional nitrogen in the diamond. The data illustrate the synergistic effect of combining DQ coherence magnetometry and spin-bath driving; the aggregate approach vastly outperforms either technique employed independently. Even with twice faster precession, T_2^* is extended from 1.8 to 29 μ s. The DQ protocol with spin-bath driving is depicted in the inset. From Bauch et al., 2018.

distortion defines a symmetry axis along any of the four crystallographic [111] axes, leading to four groups of N_0^S spins. For an axial bias magnetic field B_0 satisfying $(g_e\mu_B/\hbar)B_0\gg A_{\rm HF}$, where $A_{\rm HF}\sim 100$ MHz is the substitutional nitrogen hyperfine interaction, m_s and m_I are good quantum numbers, and the ¹⁴N spectrum consequently exhibits up to 12 distinct resonances, each of which needs to be driven (de Lange *et al.*, 2012; Belthangady *et al.*, 2013). If B_0 is aligned with any of the diamond [111] axes, the 12 resonances reduce to six partially degenerate groups with multiplicity 1:3:1:3:3:1; see Fig. 19(a). Similarly, the ¹⁵N spectrum shows up to eight distinct resonances, which reduce to four partially degenerate groups with multiplicity 1:3:3:1 for B_0 aligned to an NV internuclear axis; see Fig. 19(b).

Spin-bath driving is expected to be easiest to execute when the bias magnetic field B_0 and hyperfine coupling $A_{\rm HF}$ are not of the same order. When $(g\mu_B/h)B_0 \sim A_{\rm HF}$, additional nuclear-spin-non-conserving transitions arise, resulting in reduced oscillator strength for the nuclear-spin-conserving transitions. Thus, given fixed rf power, the drive efficiency for each addressed transition decreases. Although spin-bath driving has to date been demonstrated only in the regime $(g\mu_B/h)B_0 \gtrsim A_{\rm HF}$ (de Lange *et al.*, 2012; Knowles, Kara, and

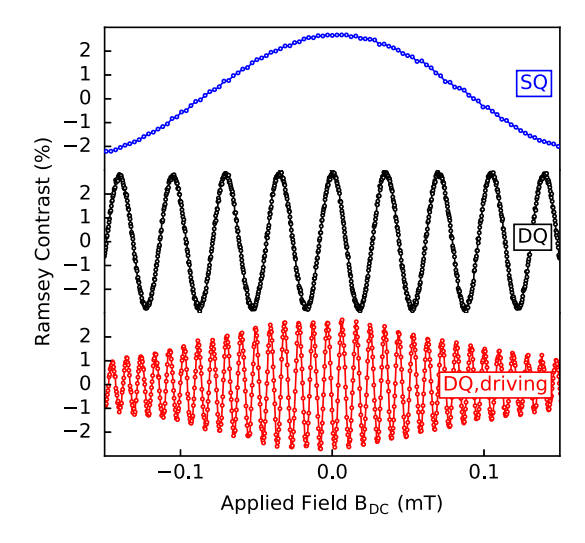


FIG. 18. Ramsey interference fringes vs an applied test magnetic field, measured in the (top) SQ basis, (middle) DQ basis, and (bottom) DQ basis with $N_{\rm S}^0$ spin-bath driving. The longer dephasing times achieved when combining DQ coherence magnetometry and spin-bath driving allow for denser Ramsey fringes and enhanced sensitivity. The decreased contrast for magnetic fields > 0.05 mT in the bottom plot results from magnetic-field-induced detuning of the nitrogen spin resonances with respect to the rf drive frequencies. From Bauch *et al.*, 2018.

Atatüre, 2014; Bauch *et al.*, 2018), we expect driving in the $(g\mu_B/h)B_0 \ll A_{\rm HF}$ regime to also be effective.

The N_S^0 electron spin resonance spectra for ^{14}N and ^{15}N are readily observed in EPR experiments; see, for example, Smith et al. (1959) and Drake, Scott, and Reimer (2016). Alternatively, the nitrogen resonance spectra in a diamond can be characterized with NV- centers using a Hahn echobased double electron electron resonance (DEER) technique (de Lange et al., 2012; Bauch et al., 2018). In this case, the NV^- electronic spin is made sensitive to decoherence from N_s^0 target impurity spins via application of frequency-selective π pulses at the targeted spins' resonance frequency. A schematic of the DEER pulse sequence is shown in Fig. 16(c), and the resulting DEER spectra for both nitrogen isotopes are compared in Fig. 19. Extra resonance features associated with substitutional-nitrogen-related dipole-forbidden transitions and additional paramagnetic spins are also commonly observed and may reveal additional sources of dephasing.

The experimental requirements for effective spin-bath driving depend on the substitutional nitrogen concentration. At lower impurity concentrations, reduced spin-bath drive strength (i.e., rf power) is needed to mitigate nitrogen-induced dephasing. However, dephasing mechanisms unrelated to nitrogen may exhibit larger relative contributions to T_2^* in this regime, limiting the achievable T_2^* increase from nitrogen spin-bath driving. In particular, in samples with nitrogen content $[N_S^0] \lesssim 1$ ppm, lattice-strain gradients may dominate the ensemble dephasing time, as found by Bauch *et al.* (2018). In this instance, strain-insensitive measurement techniques, such as double-quantum coherence magnetometry (see Sec. IV.B), must be employed for spin-bath driving to extend T_2^* . In the intermediate regime ($[N_S^0] \sim 1$ ppm), where strain gradients and NV⁻ dipolar interactions with the nitrogen spin

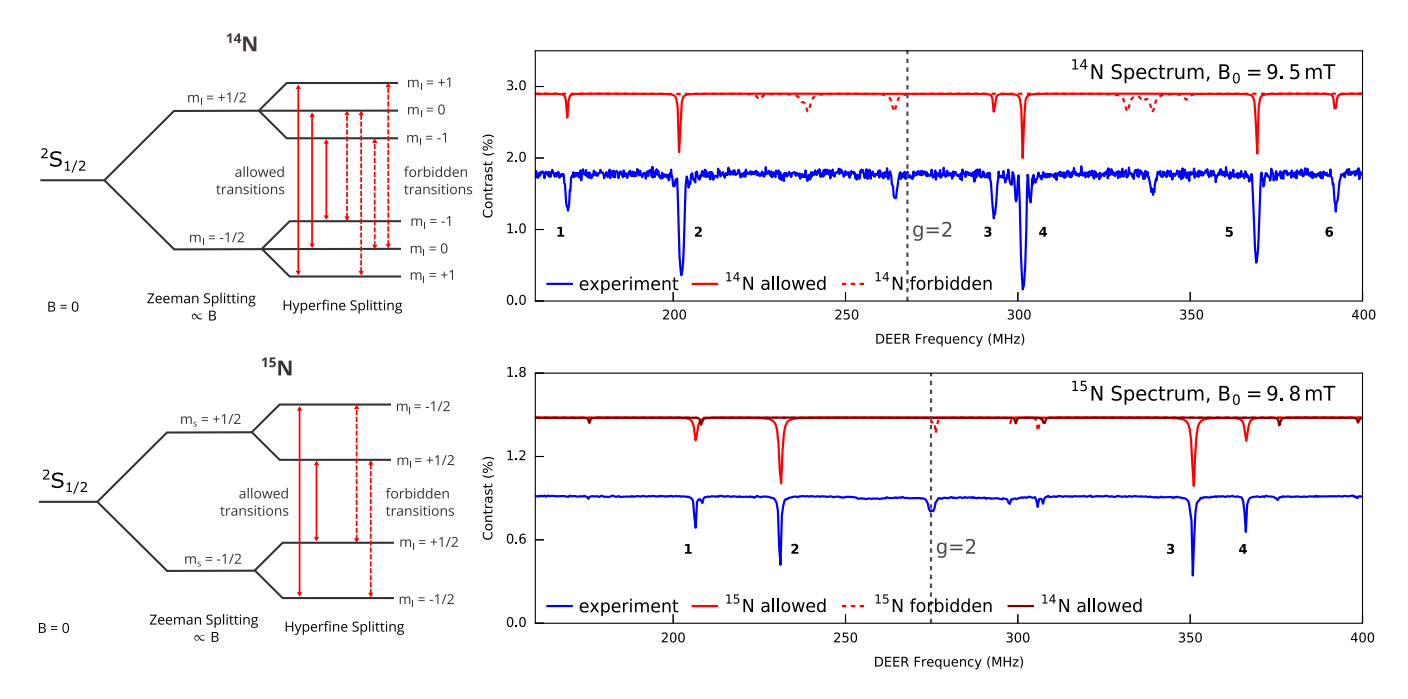


FIG. 19. (Left panels) Substitutional nitrogen N_S^0 spin energy levels and (right panels) associated double electron-electron resonance (DEER) spectra, for (top) ¹⁴N and (bottom) ¹⁵N. Simulated spectra depict allowed-transition resonances ($\Delta m_I = 0$) of the primary nitrogen isotope, forbidden-transition resonances ($\Delta m_I \neq 0$) of the primary nitrogen isotope, and spurious features associated with allowed transitions of impurity isotopes. The simulated data resonance linewidths and amplitudes are chosen to approximately match the experimental data. Spectra are simulated for and experimentally measured in an external magnetic field aligned along the diamond crystallographic [111] axis. Adapted from Bauch *et al.*, 2018.

bath are of similar magnitude, neither spin-bath driving nor DQ coherence magnetometry alone can achieve significant enhancement of the dephasing time. However, Bauch *et al.* (2018) demonstrated a \sim 16 times improvement in T_2^* (effectively a \sim 32 times improvement when considering the twice faster precession rate in the DQ basis) for a $[N_S^0] \simeq 0.75$ ppm diamond when both techniques were combined, as shown in Fig. 18. In contrast, employing spin-bath driving alone improved the dephasing time only by \sim 1.1 times (see Fig. 17), as strain-induced dephasing was left unmitigated.

In nitrogen-rich diamonds ($[N_S^0] \gtrsim 1$ ppm), achieving the motional narrowing condition $\Omega_N/\gamma_N\gg 1$ may be technically difficult; increases in $[N_S^0]$ necessitate linear proportional increases in Ω_N , which correspond to quadratic increases in the rf power required (Bauch *et al.*, 2018). We expect both pulsed and continuous spin-bath driving in nitrogen-rich samples to be ultimately limited by parasitic effects. These effects include induced ac Zeeman shifts, strain gradients, and sample heating due to the strong applied rf fields (Knowles, Kara, and Atatüre, 2014).

We note that spin-bath driving should be applicable to any paramagnetic spin species in diamond, such as dark electron spins (i.e., optically inactive paramagnetic defects), NV⁻ centers, or even nuclear spins. The effectiveness of the driving for dilute bath spins (fractional concentration $\ll 0.01$) is expected to depend on the target spin's concentration but not its gyromagnetic ratio, as both Ω_N and γ_N vary linearly with the target spin's gyromagnetic ratio. In other words, species with small gyromagnetic ratios are difficult to drive but also do not contribute much to dephasing for a given concentration (Bauch *et al.*, 2018). Given its relatively high

concentration, spin-bath driving of the 13 C in a natural abundance diamond ([13 C] = 10 700 ppm) is expected to be quite challenging (Bauch *et al.*, 2019). Lastly, as the nitrogen spin bath contributes to T_2 decoherence (Bar-Gill *et al.*, 2012; Pham, Bar-Gill, Belthangady *et al.*, 2012), nitrogen spin-bath driving would be expected to extend the Hahn echo T_2 and, to a lesser extent, coherence times achieved with dynamical decoupling sequences (Bauch *et al.*, 2018).

D. Transverse strain and electric-field mitigation

Spatial and temporal variations in electric fields or in diamond crystal strain can degrade T_2^* , as described in Secs. III.C and IV.B. Measurements performed in the NV⁻ spin's double-quantum basis are insensitive to variations in the axial components of the electric field E_z and spin-strain coupling \mathcal{M}_{7} , as these terms cause common-mode shifts in the energies of the $|+1\rangle$ and $|-1\rangle$ states (Barson *et al.*, 2017; Glenn et al., 2017). In contrast, broadening due to transverse electric fields E_x , E_y and transverse spin-strain couplings \mathcal{M}_x and \mathcal{M}_{v} may remain in DQ measurements (Barson et al., 2017; Udvarhelyi et al., 2018). However, by operating at a sufficiently strong axial bias magnetic field $B_{0.7}$, the resonance line broadening from inhomogeneities in E_x , E_y , \mathcal{M}_x , and \mathcal{M}_y can be mitigated (Jamonneau et al., 2016; Schloss et al., 2018), as illustrated in Fig. 20 and discussed further in the Appendix, Sec. 9.

The frequency shifts of the NV⁻ ground-state spin resonances due to transverse strain and electric fields at zero magnetic field are given by

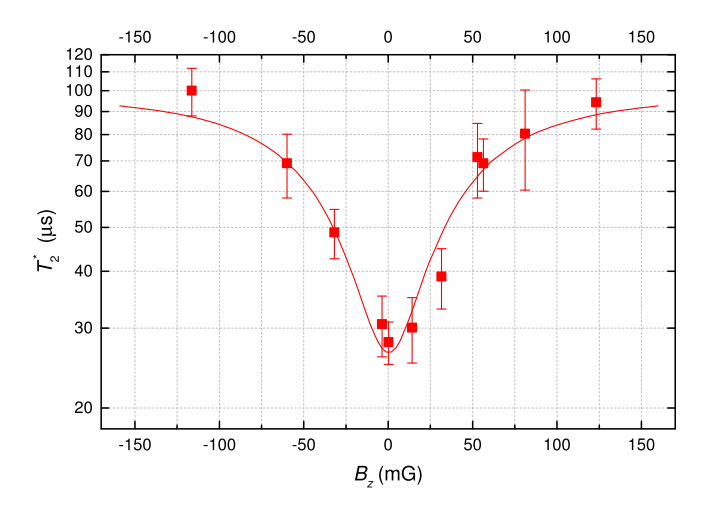


FIG. 20. Suppression of dephasing from transverse electric fields and strain. For the single NV⁻ center measured by Jamonneau *et al.* (2016), the dephasing time $T_2^{*\rm single}$ at zero magnetic field is limited by electric-field fluctuations transverse to the NV⁻ symmetry axis, E_x and E_y . An applied axial magnetic field suppresses this source of dephasing by decoupling the NV⁻ center from transverse electric fields and strain. For magnetic fields larger than ~100 mG, the value of $T_2^{*\rm single}$ is limited by magnetic noise, reaching ~100 μ s in this isotopically enriched, $[^{13}{\rm C}] = 20$ ppm sample. For NV⁻ ensembles at zero magnetic field, in addition to temporal fluctuations in E_x and E_y that limit $T_2^{*\rm single}$, spatial variations in E_x and E_y and in the transverse spinstrain coupling terms \mathcal{M}_x and \mathcal{M}_y may also limit T_2^* for ensembles. Adapted from Jamonneau *et al.*, 2016.

$$\pm \xi_{\perp} = \pm \sqrt{(d_{\perp}E_x + \mathcal{M}_x)^2 + (d_{\perp}E_y + \mathcal{M}_y)^2},$$
 (31)

where $d_{\perp}=0.17~{\rm Hz/(V/m)}$ (van Oort and Glasbeek, 1990; Dolde et~al., 2011; Michl et~al., 2019) is the transverse electric dipole moment of the NV⁻ ground-state spin. Application of an external axial magnetic field $B_{0,z}$ introduces additional magnetic-field-dependent shifts and suppresses the effect of $\pm \xi_{\perp}$ on the spin resonances. When $\beta_z \equiv (g_e \mu_B/h) B_{0,z} \gg \xi_{\perp}$, contributions to T_2^* from temporal fluctuations or spatial variations in ξ_{\perp} (Fang et~al., 2013; Jamonneau et~al., 2016) are diminished; see the Appendix, Sec. 9. For the nanodiamonds characterized by Jamonneau et~al. (2016), with $\xi_{\perp}=7~{\rm MHz},~B_{0,z}\sim30~{\rm G}$ is required to suppress the contribution to T_2^* from transverse electric fields and strain. For the lower-strain bulk diamonds used by Fang et~al. (2013) and Jamonneau et~al. (2016), with $\xi_{\perp}\sim10~{\rm kHz},~B_{0,z}\lesssim100~{\rm mG}$ is sufficient.

V. METHODS TO INCREASE READOUT FIDELITY

A. Spin-to-charge conversion (SCC) readout

Spin-to-charge conversion (SCC) readout is an alternative to conventional fluorescence-based readout of the NV⁻ spin state. The technique was demonstrated for single NVs (Shields *et al.*, 2015; Hopper *et al.*, 2016; Jaskula, Shields *et al.*, 2019; Ariyaratne *et al.*, 2018) and for small ensembles in nanodiamonds (Hopper *et al.*, 2018) and bulk diamond (Jayakumar

et al., 2018). In SCC readout, the NV⁻ center's spin state is mapped optically onto the NV's neutral and negative charge states (NV⁰ and NV⁻). The charge state, and thus the original NV- spin information, can then be accurately read out by exploiting differences in the NV⁰ and NV⁻ wavelengthdependent excitation and associated fluorescence (Waldherr et al., 2011; Aslam et al., 2013). Key advantages of SCC readout over conventional spin-state-dependent fluorescence readout are (i) a slightly increased spin contrast (Jaskula, Shields et al., 2019), and (ii) the ability to read out the charge state for extended durations and thus collect more photons per readout, leading to high-fidelity charge-state determination. Larger photon numbers per readout reduce the relative contribution of shot noise to the measurement, allowing for readout fidelities within order unity of the spin-projection limit $\sigma_R = 1$; see definition in Sec. II.A.

Successful spin-to-charge conversion requires control of the NV charge state. Characterization of charge dynamics under optical excitation (Beha et al., 2012; Aslam et al., 2013; Hacquebard and Childress, 2018; Manson et al., 2018) indicate power- and wavelength-selective photoionization processes, which allow for controlled switching between NV[−] and NV⁰. For example, green ~532 nm light transfers single NV centers preferentially to NV- with 70%-75% probability (Waldherr et al., 2011; Beha et al., 2012; Aslam et al., 2013); strong yellow ~589 nm (Hopper et al., 2018) or red ~637 nm (Shields et al., 2015; Jaskula, Shields et al., 2019) light can selectively ionize NV⁻ to NV⁰ via absorption of two photons by an electron in the triplet ground state; and near-infrared ~900–1000 nm (Hopper et al., 2016) can similarly ionize NV⁻ via absorption of two photons by an electron in the singlet metastable state. Readout of the NV⁻ charge state is commonly performed by applying weak yellow laser light at ~594 nm. At intensities well below the NV⁻ saturation intensity $I_{\rm sat} \sim 1-3 \text{ mW}/\mu\text{m}^2$ (Wee *et al.*, 2007), yellow light efficiently excites the NV⁻ electronic spin transition with zero phonon line (ZPL) at 637 nm without inducing ionization, while hardly exciting the NV⁰ transition (with ZPL at 575 nm) (Waldherr et al., 2011; Beha et al., 2012; Aslam et al., 2013). Through introduction of a photondetection threshold combined with appropriate spectral filtering, NV- (which fluoresces under the yellow excitation) may thus be distinguished from NV⁰ (which produces little if any fluorescence). Figure 21(a) displays a photon-count histogram characteristic of single-NV charge readout reproduced from Bluvstein, Zhang, and Jayich (2019). The clear separation of photon distributions from NV⁰ and NV⁻ at low excitation powers allows charge-state determination with fidelity > 99% (Hopper, Shulevitz, and Bassett, 2018).

The seminal work by Shields *et al.* (2015) demonstrated SCC readout on a single-NV center in type IIa diamond nanobeams; see the Appendix, Sec. 11 for an overview of diamond types. First, utilizing green laser light [see Fig. 21(b)] and appropriate MWs, the NV center is prepared in the $m_s = 0$ or one of the $m_s = \pm 1$ spin states of the NV⁻ triplet electronic ground state. A moderate power, 594 nm yellow "shelving" pulse (145 μ W, ~0.9 mW/ μ m²) then excites the spin population to the triplet excited state. Because of the spin-dependent intersystem crossing from the triplet excited state,

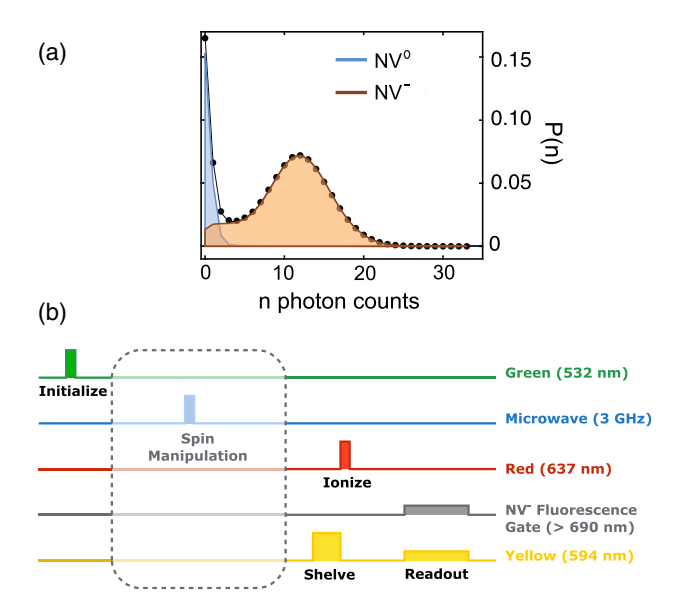


FIG. 21. (a) Probability histogram depicting photon emission from NV^0 and NV^- under weak yellow excitation. The striking difference in the photon emission rate between NV^0 and NV^- allows the NV charge state to be determined with fidelity $\gtrsim 99\%$. Adapted from Bluvstein, Zhang, and Jayich, 2019. (b) Schematic of the SCC readout protocol used by Shields *et al.* (2015). Adapted from Jaskula, Shields *et al.*, 2019.

the $m_s=0$ population is more likely to decay back to the ground state, whereas the $m_s=\pm 1$ population is more likely to be shelved into the metastable singlet states. The spin-to-charge conversion is then realized with a ~10 ns high intensity resonant 637-nm pulse (22.5 mW, ~140 mW/ μ m²), which ionizes (i.e., converts NV⁻ to NV⁰) the triplet ground-state population, corresponding to $m_s=0$, but leaves the shelved population corresponding to $m_s=\pm 1$ unaffected. Last, the NV charge state is read out by applying weak ~594 nm light. The ~594 nm light with lower energy than the NV⁰ ZPL at 575 nm ensures that only NV⁻ is excited while the weak intensity [~1–10 μ W, ~6–60 μ W/ μ m², Fig. 21(a)] ensures that NV⁻ is not ionized during readout.

The single-NV SCC result by Shields et al. (2015) achieves a factor over spin-projection noise $\sigma_R = 2.76$ ($\mathcal{F} = 1/\sigma_R =$ 0.36, see comparison in Table II). As the fidelity of the charge readout process itself approaches unity ($\mathcal{F}^{CR} = 0.975$), the dominant inefficiency is attributed to the imperfect spin-tocharge conversion step ($\mathcal{F}^{SCC} = 0.37$). Several alternative SCC readout variants have been demonstrated, providing similar sensitivity gains while offering reduced experimental complexity (Hopper et al., 2018), or utilizing the singlet state for ionization (Hopper et al., 2016). For all SCC readout implementations, however, the improved values of σ_R come at the cost of substantially prolonged spin readout times t_R , which increase the sequence's overhead time and diminish the overall sensitivity improvement; see Sec. II.A. For example, the best reported readout fidelity ($\mathcal{F} = 0.36$) (Shields et al., 2015) is achieved for readout times $t_R = 700 \,\mu\text{s}$, which exceed conventional fluorescence-based readout times $(t_R \sim 300 \text{ ns})$ by $\sim 1000 \text{ times}$. SCC readout is therefore most advantageous for measurement modalities with long sensing intervals (e.g., T_1 relaxometry and ac field sensing), where the penalty due to additional readout overhead is less severe. To date, the best SCC readout demonstrations improve field sensitivity only when interrogation times exceed ~10 μ s (Shields *et al.*, 2015; Hopper *et al.*, 2018), which further motivates improvement of spin ensemble properties to achieve sufficiently long dephasing times; see Sec. III.A.

Given the clear success of SCC readout with single NVs, application to NV⁻-rich ensembles is a logical progression, especially given the low conventional readout fidelities achieved for NV⁻-rich ensembles ($\mathcal{F} \lesssim 0.015$, Table II). However, the prospect for SCC readout to substantially improve \mathcal{F} in NV⁻ ensembles likely hinges on whether the additional complex charge dynamics present in NV-rich diamonds can be mitigated (Hopper et al., 2018). Promising SCC readout results on small NV ensembles in type Ib nanodiamonds by Hopper et al., (2018) demonstrated $\sigma_R = 20$, compared to $\sigma_R = 70$ with conventional readout in the same setup, which resulted in improved sensing performance for interrogations times $> 6 \mu s$ (Hopper et al., 2018). However, this and other studies (J. Choi et al., 2017; Manson et al., 2018) reported intricate NV⁻ and NV⁰ charge dynamics absent in single-NV experiments. The effectiveness of SCC readout in the complex charge environment inherent to NV-rich ensembles (e.g., due to ionization and charge dynamics of substitutional nitrogen and other impurity defects) warrants further investigation; see Sec. VI.B. Nevertheless, SCC readout overcomes one sensing disadvantage specific to ensembles, namely, that NV- orientations not being used for sensing can be preferentially transferred to NV⁰ during the ionization step. This results in reduced background fluorescence and potentially allows for an additional ~2 times sensitivity improvement relative to conventional NV⁻ readout. Overall, beyond the long overhead times already discussed, SCC readout's demanding power requirements are expected to further hamper ensemble-based implementation. In particular, high required optical intensities ($\geq 150 \text{ mW/}\mu\text{m}^2$) (Shields et al., 2015; Hopper et al., 2016, 2018) suggest scaling of SCC readout to larger bulk sample sizes ($\gtrsim 100 \times 100 \ \mu m^2$) will be challenging.

B. Photoelectric (PE) readout

Another method to interrogate the NV⁻ spin state is photoelectric (PE) readout, which relies on measuring a current of charge carriers resulting from NV⁻ photoionization (Bourgeois et al., 2015, 2017; Gulka et al., 2017; Hrubesch et al., 2017; Siyushev et al., 2019). Since NV⁻ photoionization is spin-state dependent (see Secs. V.A and VI.B) (Shields et al., 2015), the spin state can be inferred from the photocurrent signal in analogy to fluorescence-based readout. Figure 22 shows a photoelectrically detected magnetic resonance (PDMR) spectrum measured simultaneously with an ODMR spectrum. One claimed benefit of PE readout is that the photoelectron collection efficiency can approach unity (Bourgeois et al., 2015).

In PE readout, a bias voltage is applied across electrodes fabricated on the diamond surface. An excitation laser induces NV⁻ photoionization, and the ejected electrons generate a current, which is collected at the electrodes. NV⁻

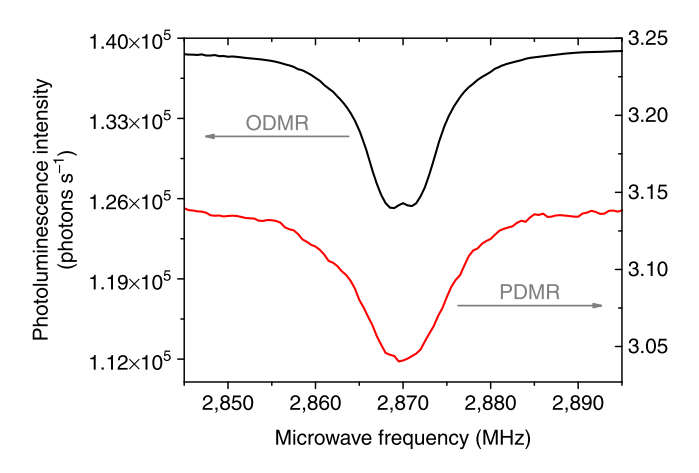


FIG. 22. Photoelectrically detected magnetic resonance (PDMR) of NV⁻ centers. Spectra are simultaneously measured by ODMR (black line, top) and PDMR (red line, bottom) in the absence of an external magnetic field. From Bourgeois *et al.*, 2015.

photoionization may occur via single- or two-photon excitation. Single-photon ionization of the NV⁻ 3A_2 electronic ground state requires photon energies of 2.7 ± 0.1 eV or higher (wavelength \lesssim 460 nm) (Aslam *et al.*, 2013; Deák *et al.*, 2014; Bourgeois *et al.*, 2017; Londero *et al.*, 2018). PE readout implementations employing lower photon energies, such as from 532 nm (2.33 eV) light common for spin-state initialization, ionize the NV⁻ centers via a two-photon process, namely, $^3A_2 \rightarrow ^3E \rightarrow$ conduction band (see Fig. 30) (Heremans *et al.*, 2009; Bourgeois *et al.*, 2015, 2017; Gulka *et al.*, 2017). Whereas the rate of single-photon ionization scales linearly with optical intensity (Hacquebard and Childress, 2018), two-photon ionization depends quadratically on intensity (Aslam *et al.*, 2013).

Optically illuminating the diamond for PE readout may also induce background photocurrent from ionization of other defects present in the sample. Most unfortunately, 532 nm green light ionizes substitutional nitrogen N_S^0 defects in a single-photon process (Heremans *et al.*, 2009). The background N_S^0 photocurrent may exceed the signal NV⁻ photocurrent, resulting in poor NV⁻ measurement contrast. This problem is exacerbated for excitation intensities well below the NV⁻ saturation intensity, where two-photon NV⁻ ionization may be weak compared to single-photon ionization of N_S^0 , and at elevated nitrogen concentrations $[N_S^0] \gg [NV^-]$ (Bourgeois *et al.*, 2017; Londero *et al.*, 2018).

Multiple approaches can partially mitigate the unwanted photocurrent associated with $N_{\rm S}^0$ ionization. For example, lock-in techniques can remove the dc background from the nitrogen photocurrent (Gulka *et al.*, 2017). Additionally, a shorter-wavelength laser can be employed to induce single-photon ionization from the $NV^{-3}A_2$ state, thereby improving the NV^{-1} ionization rate relative to that of $N_{\rm S}^0$. However, Bourgeois *et al.* (2017) observed that, under optimized experimental conditions, single-photon ionization using 450 nm light provides no contrast improvement compared to two-photon ionization with 532 nm light.

A variety of challenges accompanies implementation of PE readout, not only for single NV⁻ centers and small NV⁻

ensembles (Bourgeois *et al.*, 2015, 2017; Gulka *et al.*, 2017; Hrubesch *et al.*, 2017; Siyushev *et al.*, 2019), but also for envisioned extensions to larger detection volumes $\gtrsim (100 \ \mu\text{m})^3$ using NV-rich diamonds. In addition to background photocurrent from ionization of nitrogen and other defects, another expected obstacle to PE readout is electrical cross talk between MW-delivery electrodes (used to manipulate the NV⁻ spin states) and photocurrent-detection electrodes (Gulka *et al.*, 2017; Siyushev *et al.*, 2019). Fluctuations in the applied electric field could also add additional measurement noise by coupling to fluctuations in photoelectric collection efficiency.

Scaling PE readout implementations to larger NV⁻ ensembles may introduce additional challenges. Because the electrodes reside on the diamond surface, collecting photocurrent from NV⁻ centers located $\gtrsim 100~\mu m$ deep may prove difficult (Bourgeois *et al.*, 2015). Achieving the necessary bias electric-field strength and uniformity over $\gtrsim (100~\mu m)^3$ volumes may also be challenging; bias electric-field gradients across large detection volumes could reduce NV⁻ ensemble T_2^* values. Moreover, the presence of charge traps in NV-rich diamonds might hinder photoelectric collection efficiency (see Sec. VI.F), especially from deeper NV⁻ centers. In addition, Johnson noise in the readout electrodes may induce magnetic field fluctuations that could limit the achievable sensitivity (Kolkowitz *et al.*, 2015).

In certain PE readout implementations, the detected signal amplitude may be increased by photoelectric gain, an intrinsic charge-carrier amplification arising from the diamond's charge dynamics and the electrode boundary conditions (Rose, 1963; Bourgeois et al., 2015; Hrubesch et al., 2017). However, photoelectric gain is expected to be diminished in NV-rich diamonds due to charge traps, nonuniform electric fields, and space-charge limitations (Bube, 1960; Rose, 1963; Bourgeois et al., 2015). The applicability of photoelectric gain to improving PE readout fidelity in ensemble-based extensions remains to be shown. Although PE readout shows promise for nanoscale sensing and integrated quantum devices (Morishita et al., 2020) and may prove beneficial when combined with p-i-n structures (Kato et al., 2013), this technique's utility for ensemble magnetometry in NV-rich diamonds remains unknown.

C. Ancilla-assisted repetitive readout

In conventional readout, the fast ~500 ns repolarization of the NV⁻ electronic spin limits the number of photons an NV⁻ emits before all initial spin-state information is lost; see Fig. 6. Even when implementing conventional readout with the best present collection efficiencies, the average number of collected photons per NV⁻ center $n_{\rm avg}$ is less than 1, and for many implementations $n_{\rm avg} \ll 1$, making photon shot noise the dominant contributor to the parameter σ_R [see Eq. (13), Table II, Sec. V.E]. An alternative method to increase the readout fidelity $\mathcal{F} = 1/\sigma_R$ circumvents this problem by instead first mapping the initial NV⁻ electronic spin-state information onto an ancilla nuclear spin. In the second step, the ancilla nuclear spin state is mapped back onto the electron spin, which is then detected using conventional

fluorescence-based readout. This second step may be repeated many times with each marginal readout improving the aggregate readout fidelity, as shown in Figs. 23(a) and 23(b). While first demonstrated with a nearby ¹³C nuclear spin as the ancilla (Jiang *et al.*, 2009), the technique was later realized using the NV⁻ center's ¹⁴N (Neumann, Beck *et al.*, 2010) and ¹⁵N nuclear spin (Lovchinsky *et al.*, 2016). In the ¹³C realization (Jiang *et al.*, 2009; Maurer *et al.*, 2012), the coupling to the ancilla spin depends on the distance between the NV⁻ defect and the nearby ¹³C atom, making the technique difficult to implement for NV⁻ ensembles where this distance varies. This discussion instead focuses on the more scalable realization using the NV⁻ nitrogen nuclear spin as the ancilla, which ensures the electron spin to ancilla spin coupling remains fixed over the NV⁻ ensemble.

Figure 23(c) shows a quantum circuit diagram from Lovchinsky *et al.* (2016) depicting the repetitive readout scheme. After the final MW pulse in an NV⁻-sensing protocol, the NV⁻ electronic spin state (denoted by subscript *e*) is mapped onto the nitrogen nuclear spin state (subscript *n*).

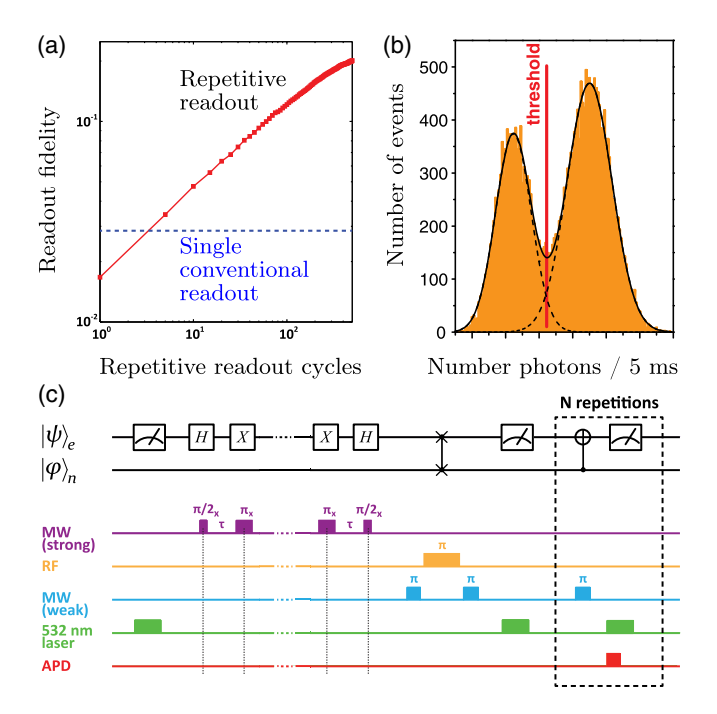


FIG. 23. Overview of ancilla-assisted repetitive readout. (a) Readout fidelity \mathcal{F} is improved with the number of repetitive readout cycles. Fidelity for repetitive readout (red) is plotted relative to a single conventional readout (dashed blue). From Lovchinsky et al., 2016. (b) The clear difference in total number of collected photons associated with the initial m_s states allows determination of m_s with fidelity approaching 1 in some implementations. Here $\mathcal{F} \approx 0.92$. From Neumann, Beck et al., 2010. (c) Quantum circuit diagram and magnetometry pulse sequence with detection via ancilla-assisted repetitive readout. Application of an rf π pulse between two weak MW π pulses maps the NV- electronic spin superposition onto the ancilla nuclear spin. Subsequently, the superposition state may be repeatedly mapped back onto the electronic spin via a weak MW π pulse and optically read out without destroying the ancilla spin's quantum state. Adapted from Lovchinsky et al., 2016.

Lovchinsky et al. (2016) achieved this mapping using a SWAP gate $(CNOT_{e|n} - CNOT_{n|e} - CNOT_{e|n})$, where CNOT denotes a controlled NOT gate. The SWAP gate consists of a MW π pulse, then an rf π pulse, then another MW π pulse, where the MW pulses flip the electronic spin and the rf pulse flips the nuclear spin. This procedure swaps the electronic and nuclear spin states, importantly, storing the electronic spin-state information in the ancilla nuclear spin. Then an optical pulse repolarizes the electronic spin to $m_s = 0$. Next a set of repetitive readouts is performed. In each readout, the nuclear spin state is copied back onto the electronic spin with a MW pulse (a $CNOT_{e|n}$ gate), and then the electronic spin is optically read out without affecting the nuclear spin state. This process can be repeated many times ($\gtrsim 10^2$) and is limited, in principle, by the nuclear spin lifetime $T_{1,n}$. In Lovchinsky *et al.* (2016), while the initial rf pulse used in the SWAP gate requires \sim 50–60 μ s, each readout cycle requires only \sim 1 μ s. The large number of readouts allows the aggregate readout fidelity $\mathcal{F}=$ $1/\sigma_R$ to approach 1; notably, Neumann, Beck et al. (2010) achieved $\mathcal{F} = 0.92$ ($\sigma_R = 1.1$), as depicted in Fig. 23(b).

Extending ancilla-assisted repetitive readout to ensembles is expected to be fruitful but necessitates overcoming further challenges. The scheme requires a large magnetic field to minimize coupling between the NV⁻ nuclear and electronic spins, with Neumann, Beck et al. (2010) and Lovchinsky et al. (2016) employing fields of 6500 and 2500 G, respectively. Further, the bias magnetic field must be precisely aligned along a single NV⁻ symmetry axis, presently precluding its use for sensing from more than one NV⁻ orientation (Schloss et al., 2018). Even slight angular misalignments introduce measurement backaction on the nuclear spin I_z , which spoils $T_{1,n}$ (Neumann, Beck et al., 2010). The reduction in $T_{1,n}$ limits the available readout duration. Ensemble implementations would therefore require highly uniform bias magnetic fields over ensemble sensing volumes, conceivably on the $\sim (100 \ \mu \text{m})^3$ scale. Engineering such fields is within current technical capability but difficult nevertheless; see Sec. III.C and Vandersypen and Chuang (2005). Additionally, the MW and rf control pulses would ideally manipulate the entire ensemble uniformly; spatial inhomogeneities of the control pulses are likely to result in reduced readout fidelity unless mitigated (Vandersypen and Chuang, 2005). Assuming that sufficiently strong and homogeneous Bo fields and MW driving can be realized, and that the additional overhead time is acceptable, repetitive readout appears to be a promising but technically demanding method to improve $\mathcal F$ for ensembles.

D. Level-anticrossing-assisted readout

In conventional readout (Doherty *et al.*, 2013), the readout fidelity $\mathcal{F}=1/\sigma_R$ depends on the number of photons $n_{\rm avg}$ collected per measurement sequence [see Eq. (13)]. The value of $n_{\rm avg}$ is limited by the time the spin population originally in the $m_s=\pm 1$ states spends shelved in the singlet state before decaying to the triplet $m_s=0$ state. Steiner *et al.* (2010) engineered the NV⁻ spin to pass through the singlet state multiple times before repolarization, extending the readout duration per sequence to increase $n_{\rm avg}$, as depicted in Fig. 24. Using NV⁻ centers with ¹⁴N, which has nuclear spin I=1,

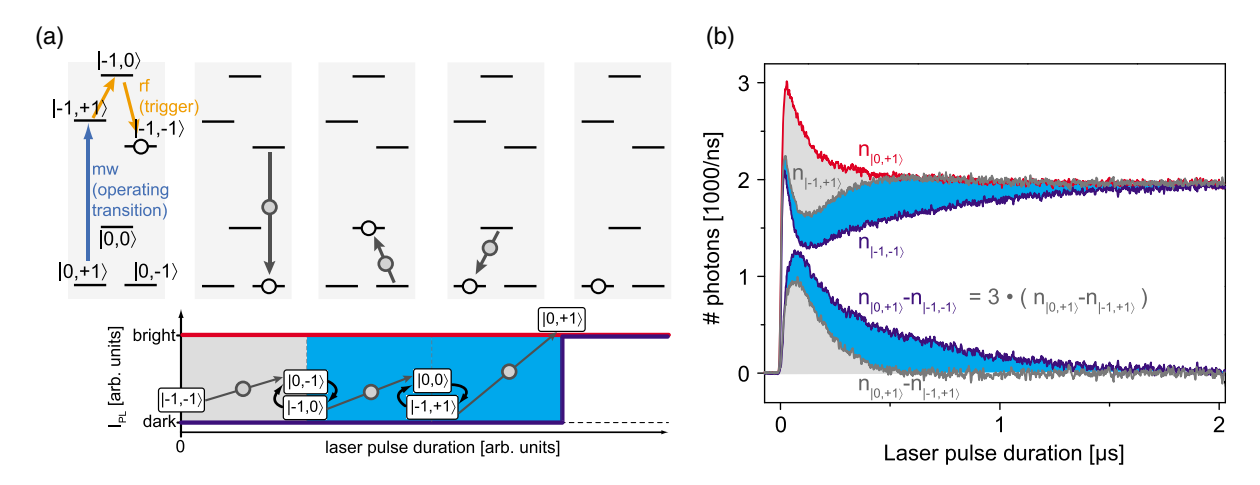


FIG. 24. Level-anticrossing-assisted readout. At the excited-state level anticrossing near B=500 G, green optical excitation polarizes NV⁻ into the spin state $|m_s=0,m_I=+1\rangle$. (a) Upon completion of a sensing sequence, two rf pulses transfer population in the electronic spin state $|m_s=0\rangle$ from the nuclear spin state $|m_I=+1\rangle$ to $|m_I=-1\rangle$ without affecting the $|m_s=0\rangle$ state. During optical readout, this population passes three times through the singlet states before being repolarized to $|m_s=0,m_I=+1\rangle$, increasing the time over which the state-dependent fluorescence contrast persists. (b) Time-resolved photon detection comparing conventional readout (gray) and LAC-assisted readout (blue). The optimal readout duration is extended by 3 times, and the difference in detected photon number between the two spin states is increased by 3 times. From Steiner *et al.*, 2010.

three cycles through the singlet state occur during readout, yielding a ~ 3 times increase in $n_{\rm avg}$ and thus a $\sim \sqrt{3}$ times improvement in the fidelity \mathcal{F} . For NV⁻ centers with ¹⁵N with I=1/2, the spin passes only twice through the singlet state before repolarization, yielding only a $\sim \sqrt{2}$ times improvement in \mathcal{F} .

The technique is implemented as follows: the bias field B_0 is tuned to the excited-state level anticrossing at $B_{\rm LAC} \approx$ 500 G (Fuchs et al., 2008; Neumann, Beck et al., 2010) to allow resonant flip-flops between the NV⁻ center's electronic spin and its ¹⁴N nuclear spin (I = 1). Operation at the level anticrossing polarizes the nuclear spin into the state $|m_I|$ +1 (Jacques et al., 2009). Upon completion of a sensing sequence, immediately prior to readout, the NV- electronic spin occupies a superposition of the states $|m_s = 0, m_I = +1\rangle$ and $|m_s = -1, m_I = +1\rangle$. Before the NV⁻ electronic spin state is read out using a conventional green laser pulse, two sequential rf π pulses flip the nuclear spin into the $m_I = -1$ state, conditional on the electronic spin occupying the $m_s =$ −1 state. This CNOT gate relies on the rf drive's being resonant with the nuclear transitions between the m_I states for the population in the $m_s = -1$ state and off resonant for the population in the $m_s = 0$ state. During readout, the population in $|m_s = -1, m_I = -1\rangle$ cycles through the long-lived singlet state three times before the information stored in the NVelectronic spin is lost, allowing more signal photons to be collected. After the first and second passes through the singlet to the $m_s = 0$ state, an electron-nuclear spin flip-flop returns the electronic spin state to $m_s = -1$, as shown in Fig. 3(a) of Steiner et al. (2010), enabling another cycle through the singlet state. The third pass repolarizes the NV⁻ spin into the stable $|m_s = 0, m_I = +1\rangle$ state.

This technique's utility for magnetic sensing depends on whether the $\leq \sqrt{3}$ times increase in fidelity \mathcal{F} outweighs the cost of additional overhead time [see Eq. (11)] introduced by the rf pulses. Although Steiner *et al.* (2010) assert that

microsecond-scale rf nuclear spin π pulses are attainable, achieving such nuclear Rabi frequencies over large ensemble volumes $\sim (100 \ \mu \text{m})^3$ may prove very difficult, making this method impractical for NV⁻ ensembles with $T_2^* \lesssim 1 \ \mu \text{s}$. Additional challenges for implementation with NV⁻ ensembles include realizing the requisite uniformity in the MW and rf fields and in the 500 G bias magnetic field over ensemble volumes. Finally, the scheme presently precludes sensing from more than one NV⁻ orientation (Schloss *et al.*, 2018).

E. Improved photon collection methods

In the limit of low contrast, the readout fidelity \mathcal{F} is proportional to the square root of the average number of photons collected per NV⁻ per measurement, i.e., $\mathcal{F} \propto \sqrt{\mathcal{N}/N} = \sqrt{n_{\rm avg}}$ [see Eq. (13)]. Under these conditions, sensitivity can be enhanced by increasing the geometric collection efficiency $\eta_{\rm geo}$, defined as $\mathcal{N}/\mathcal{N}_{\rm max}$, where \mathcal{N} and $\mathcal{N}_{\rm max}$ are, respectively, the numbers of photons collected from and emitted by the NV⁻ ensemble per measurement.

Efficient photon collection in diamond is hindered by totalinternal-reflection confinement resulting from diamond's high refractive index of approximately 2.41. For example, air and oil-immersion objectives, with numerical apertures of 0.95 and 1.49, respectively, provide calculated collection efficiencies of only 3.7% and 10.4%, respectively, for photons emitted directly through the {100} diamond surface (Le Sage et al., 2012), as depicted in Fig. 25. Although antireflection coatings can allow for higher collection efficiencies, present implementations demonstrate only modest improvement (Yeung et al., 2012). While great effort has resulted in high values of $\eta_{\rm geo}$ for single-NV⁻ centers through the use of various nanofabrication approaches (Babinec et al., 2010; Hadden et al., 2010; Choy et al., 2011, 2013; Marseglia et al., 2011; Schröder et al., 2011; Yeung et al., 2012; Neu et al., 2014; Riedel et al., 2014; Li et al., 2015; Momenzadeh et al., 2015;

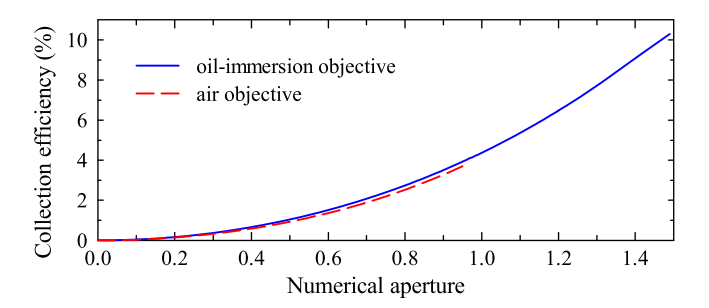


FIG. 25. Calculated collection efficiencies of NV $^-$ fluorescence by oil-immersion or air microscope objectives through the $\{100\}$ surface of a diamond chip, as a function of numerical aperture. From Le Sage *et al.*, 2012.

Shields *et al.*, 2015; Häberle *et al.*, 2017), such methods do not easily translate to large ensembles.

Successful approaches for bulk ensemble magnetometers have thus far focused on collecting NV⁻ fluorescence that has undergone total internal reflection in the diamond (Le Sage et al., 2012; T. Wolf et al., 2015). While absorption of NVfluorescence by various defects may limit $\eta_{\rm geo}$ (Khan et al., 2009, 2013) for some diamonds, nitrogen (Weerdt and Collins, 2008) and NV⁻ centers (Fraczek et al., 2017) are expected to hardly absorb in the NV⁻ PL band ~600–850 nm. Le Sage et al. (2012) demonstrated a collection efficiency of 39% by detecting fluorescence from the four sides of a rectangular diamond chip surrounded by four photodiodes; see Fig. 26. However, the increased experimental complexity associated with employing four detectors in contact with the diamond may be problematic for certain applications. In another approach, T. Wolf et al. (2015) employed a trapezoidally cut diamond chip and a parabolic concentrator to improve collection efficiency. Although T. Wolf et al. calculated η_{geo} to be between 60% and 65%, this result is not confirmed experimentally. Ma et al. (2018) demonstrated a collection efficiency of 40% by eliminating all air interfaces between the diamond and detector, in conjunction with coupling prisms which direct light exiting the diamond's four side faces to the detector.

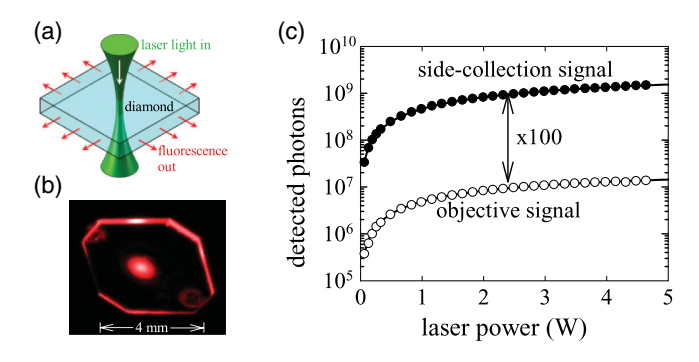


FIG. 26. Fluorescence side-collection method. (a) Green optical excitation is applied normal to the large face of the diamond chip, and red fluorescence is collected from the sides. (b) Red fluorescence from actual diamond chip. (c) The depicted implementation results in a 100 times increase in detected photons relative to a 0.4 numerical aperture air objective. From Le Sage *et al.*, 2012.

In the future, collection efficiency in bulk NV-diamond magnetometers is expected to improve to near 100%, limited only by losses due to absorption. For example, light lost from the top and sides of the diamond in the work of T. Wolf et al. (2015) could be redirected to the detector by coating the sides of the diamond with a metallic (Choy et al., 2011) or dielectric reflector (Boesch et al., 2016). T. Wolf et al. (2015) might have also seen an improvement in collection efficiency by designing an optimized parabolic concentrator rather than using a commercially available part. Hypothetical geometries for light collection using parabolic or ellipsoidal reflectors have been discussed by Boesch et al. (2016). Whereas multiple-reflection methods are suitable for bulk magnetometers, increasing $\eta_{\rm geo}$ by collecting light undergoing multiple reflections in the diamond may substantially complicate the accurate image reconstruction for NV- magnetic imaging microscopes (Steiner et al., 2010; Pham et al., 2011; Le Sage et al., 2013).

It is also natural to consider exploiting the Purcell effect to improve readout fidelity. By engineering physical structures around a chosen NV- center or ensemble, several works have increased the triplet excited state's radiative decay rate (Choy et al., 2011; Kaupp et al., 2016; Riedel et al., 2017). The increased radiative decay allows for more PL photons to be collected from the population originally in $|m_s = 0\rangle$, while the population originally in $|m_s = \pm 1\rangle$ is shelved in the singlet states. Although theoretical investigations suggest that Purcell enhancement might improve readout fidelity (S. A. Wolf et al., 2015) or leave fidelity unchanged (Babinec et al., 2012), the only reported experimental demonstration of Purcellenhanced NV⁻ spin readout to date finds reduced fidelity (Bogdanov et al., 2017). Bogdanov et al. surmise that charge effects related to dense NV- ensembles may contribute to the observed fidelity decrease. Achieving high Purcell factors for NV⁻-ensemble applications may also impose undesirable geometric constraints. For a clear and detailed discussion of radiative lifetime engineering for NV⁻ spin readout, see the work of Hopper, Shulevitz, and Bassett (2018). Along similar lines, a recent proposal suggested that near-infrared (NIR) fluorescence-based readout could exhibit improved fidelity over conventional readout when combined with Purcell enhancement (Meirzada et al., 2019). While this scheme requires high IR excitation intensities likely incompatible with large NV⁻ ensembles, it may show utility for small ensembles within a confocal volume.

F. Near-infrared (NIR) absorption readout

The sensitivity of conventional fluorescence-based readout is limited by shot noise on the collected photons due to low fluorescence contrast C [see Eq. (12)]. As an alternative to fluorescence-based readout, population in one or both NV-singlet states may be directly probed via absorption, giving a probabilistic measure of the initial m_s spin state prior to readout. While the upper singlet state 1A_1 lifetime $\lesssim 1$ ns at room temperature (Acosta, Jarmola *et al.*, 2010; Ulbricht and Loh, 2018) is likely too short for such an approach to be effective, the lower singlet state 1E lifetime $\sim 140-220$ ns at room temperature (Acosta, Jarmola *et al.*, 2010; Robledo *et al.*, 2011; Gupta, Hacquebard, and Childress, 2016) makes

measuring the ^{1}E population via absorption on the $^{1}E \leftrightarrow ^{1}A_{1}$ transition at 1042 nm viable.

Near-infrared (NIR) absorption has attractive benefits for certain applications. (a) Contrast (and therefore sensitivity) is not reduced by background fluorescence from non-NVdefects (such as NV⁰). (b) The directional nature of the 1042 nm probe light allows maximal collection efficiency (ignoring absorptive losses) to be obtained more easily than in a fluorescence-based measurement; for example, this benefit was exploited in the first demonstration of microwave-free magnetometry with NV⁻ centers (Wickenbrock et al., 2016). (c) Owing to the upper singlet ${}^{1}A_{1}$ lifetime of $\lesssim 1$ ns (Acosta, Jarmola et al., 2010; Ulbricht and Loh, 2018), the saturation intensity of the ${}^{1}E \leftrightarrow {}^{1}A_{1}$ transition is unusually large $(I_{1042}^{\text{sat}} \sim 50 \text{ MW/cm}^2)$ (Dumeige et al., 2013), allowing high intensity 1042 nm probe radiation to be used, so that fractional shot noise is reduced to well below that of an equivalent fluorescence-based measurement (Acosta, 2011). (d) NIR absorption readout is nondestructive, allowing for a single NV⁻ center in the ¹E singlet state to absorb multiple 1042 nm photons before eventual decay to the ${}^{3}A_{2}$ triplet. In principle, such absorption by a single NV- center can allow readout fidelity near the spin-projection limit, even in the presence of non-negligible optical losses.

NIR absorption readout has been successfully implemented in several proof-of-principle magnetometers. In the first demonstration (Acosta, Bauch, Jarmola *et al.*, 2010), a diamond containing [NV⁻] \sim 16 ppm was continuously illuminated with 532 nm radiation (driving the $^3A_2 \leftrightarrow ^3E$ transition to optically polarize the NV⁻ spin state) and 1042 nm NIR radiation (resonantly addressing the $^1E \leftrightarrow ^1A_1$ transition), as shown in Fig. 27(a). MW radiation transfers population between the ground-state Zeeman sublevels. In this first demonstration (Acosta, Bauch, Jarmola *et al.*, 2010), a single pass of the 1042 nm radiation through the diamond sample resulted in a peak-to-peak contrast of \sim 0.003 at room temperature.

The contrast can be enhanced by increasing the number of NV⁻ defects interacting with each 1042 nm photon, such as by employing a higher NV- density or a larger diamond. Alternatively, for a fixed number of NV⁻ centers, the 1042 nm radiation can be recirculated through the diamond. An NIR absorption magnetometer employing an optical cavity to increase the 1042 nm interaction length was analyzed by Dumeige et al. (2013), and Jensen et al. (2014) experimentally realized a peak-to-peak contrast of 7.1% when the bias magnetic field was directed along the [100] crystallographic direction (making the magnetic resonances of all four NVorientations degenerate). For this demonstration, the diamond is antireflection coated (Yeung et al., 2012) and placed in the center of a dual-wavelength optical cavity, which allows for recirculation of both 1042 and 532 nm radiation. The more efficient use of the 532 nm light enabled by the cavity allows for both a larger NV⁻ ensemble to be addressed and a higher degree of spin initialization into the $m_s = 0$ state. Ultimately, the device of Jensen et al. (2014) achieves a sensitivity of 2.5 nT/ $\sqrt{\text{Hz}}$, well above the shot-noise limit of 70 pT/ $\sqrt{\text{Hz}}$.

A notable recent implementation of NIR absorption (Chatzidrosos et al., 2017) is depicted in Fig. 27(b). One

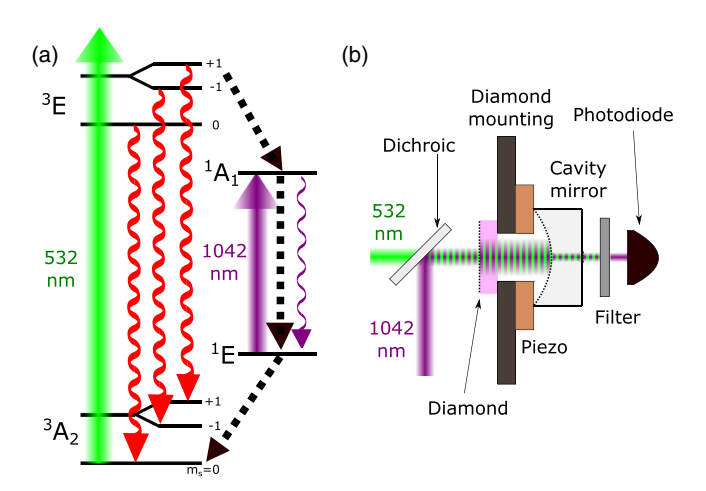


FIG. 27. NIR absorption readout. (a) Level diagram for the NV-center. Population accumulating in the 1E singlet state is probed via absorption of 1042 nm radiation resonantly addressing the $^1E \leftrightarrow ^1A_1$ transition. (b) Miniature NIR cavity-enhanced diamond magnetometer as described by Chatzidrosos *et al.* (2017). Dashed black lines depict surfaces forming the dual-wavelength optical cavity. Components pertaining to MW delivery are omitted for clarity.

diamond face forms a reflector, while the addition of a dual-wavelength concave mirror results in an optical cavity with a finesse of 160 and a cylindrical sensing volume of ~76 μ m diameter and ~390 μ m length (Chatzidrosos *et al.*, 2017). With 500 mW of 532 nm radiation and 80 mW of 1042 nm radiation, a dc magnetic field sensitivity of 28 pT/ $\sqrt{\rm Hz}$ is achieved with this compact setup, with a bandwidth of about 530 Hz. The shot-noise-limited sensitivity is 22 pT/ $\sqrt{\rm Hz}$, and the spin-projection-noise-limited sensitivity is 0.43 pT/ $\sqrt{\rm Hz}$.

The NIR absorption approach is hindered, however, by several nonidealities, which thus far have limited readout fidelity to values far from the spin-projection-noise limit, similar to conventional optical readout [i.e., $\sigma_R = 65$ for the NIR absorption approach of Chatzidrosos et al. (2017) versus $\sigma_R \approx 67$ for the conventional readout of Le Sage *et al.* (2012)]. First, the predominantly nonradiative decay of the ${}^{1}A_{1}$ singlet greatly reduces the absorption cross section σ_{1042} of the ${}^{1}E \leftrightarrow$ ${}^{1}A_{1}$ transition compared to a radiative-decay-only transition (Rogers et al., 2008; Acosta, Jarmola et al., 2010). Estimates suggest $\sigma_{1042} = 3^{+3}_{-1} \times 10^{-18} \text{ cm}^2$ (Dumeige *et al.*, 2013; Kehayias *et al.*, 2013; Jensen *et al.*, 2014), whereas the purely radiative ${}^{3}A_{2} \leftrightarrow {}^{3}E$ transition is measured to have a much larger absorption cross section $\sigma_{532} \approx 3 \times 10^{-17} \text{ cm}^2$ for 532 nm excitation, as shown in Table XV. Realizing the full potential of this method requires 1042 nm laser intensities of order $I_{1042}^{\text{sat}} \sim 50 \text{ MW/cm}^2$ (Jensen *et al.*, 2014). This saturation intensity appears to limit interrogation cross sections to $\leq 100 \ \mu \text{m}^2$ for $\sim 100 \ \text{mW}$ scale 1042 nm radiation powers, assuming a cavity finesse of ~160. Laser intensities of this magnitude may lead to undesirable ionization dynamics (see Sec. VI.B). We note that many absorption cross section measurements neglect ionization-recombination dynamics, which may skew reported values (Meirzada et al., 2018, 2019). Second, as described by Dumeige et al. (2013),

nonresonant losses for 1042 nm radiation compromise sensitivity by reducing the effective achievable collection efficiency. For example, Chatzidrosos *et al.* (2017) found that 80 mW of 1042 nm radiation input to the dual-wavelength cavity resulted in 4.2 mW transmitted to the detector. Third, the NIR absorption has been demonstrated only for dense ensembles with $[NV^T] \sim 10$ ppm to ensure appreciable 1042 nm absorption; the performance of this method for diamonds with more dilute NV^- concentrations and longer T_2^* values remains unknown and will likely depend on the scaling of cavity finesse with $[N^T]$ or $[NV^T]$ density.

While NIR absorption readout is effective and may find preference for certain applications (Wickenbrock *et al.*, 2016; Chatzidrosos *et al.*, 2017), without further advances enabling readout fidelity enhancement (e.g., reduced 1042 nm non-resonant absorption or reduced nonradiative 1A_1 singlet decay rate), this method will remain approximately on par with conventional fluorescence readout while requiring the non-trivial overhead of an NIR single frequency laser and an optical cavity.

G. Green absorption readout

Alternatively, NV⁻ readout may be achieved by monitoring absorption of green probe laser radiation, which off-resonantly drives the triplet ${}^3A_2 \leftrightarrow {}^3E$ transition (Bauch, 2010; Walsworth, 2017). When resonant MWs drive the $m_s=0 \leftrightarrow m_s=-1$ or $m_s=0 \leftrightarrow m_s=+1$ ground-state spin transitions and facilitate population transfer to the NV⁻ singlet states, it is expected that the 3A_2 state will be depleted, resulting in *increased* green probe transmission and *decreased* red fluorescence. For absorption measurements (both NIR and green), the change in transmitted light upon resonant MW drive is expected to mirror the change in fluorescence light up to a scaling constant since transmission is minimal when fluorescence is maximal, and vice versa (Bauch, 2010). Data consistent with this understanding are shown in Fig. 28 for NV⁻ centers illuminated with 514 nm light.

The absorption contrast $C_{\rm absorb}$ may differ substantially in magnitude from the fluorescence contrast $C_{\rm fluor}$ (see Fig. 28). Because absorption measurements monitor transmitted light, the detected signal (and thus $C_{\rm absorb}$) depends on the optical depth of the absorbing material. For example, even for the idealized case where $C_{\rm fluor}=1$, if only a small fraction of the incident light is absorbed in the absence of MWs, the change in transmission upon application of resonant MWs will necessarily also be small, yielding a low absorption contrast $C_{\rm absorb}$. Additionally, the absorption contrast may be further decreased due to the presence of nonradiative decay pathways.

Observed magnitudes of $C_{\rm absorb}$ in the literature are lower than $C_{\rm fluor}$ by ~ 3 times (Bauch, 2010; Le Sage and Arai, 2011) or more. For example, (Ahmadi *et al.* (2017, 2018a, 2018b) used a cw-ODMR-based magnetometer employing a resonant optical cavity to recycle the green excitation light through the diamond multiple times, and observed $C_{\rm fluor} \sim 0.01$ (which is typical) while measuring $C_{\rm absorb} \sim 10^{-6}$. Ahmadi *et al.* (2018a) performed magnetometry with the same experimental setup simultaneously using both green absorption and red fluorescence, as shown in

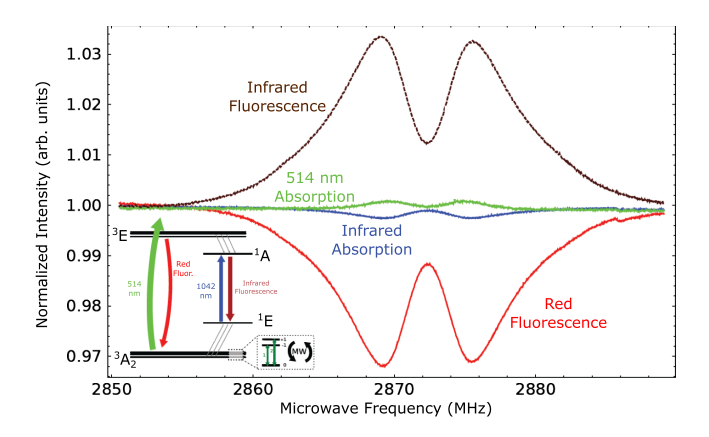


FIG. 28. Simultaneous measurement of absorption and fluorescence on both the triplet and singlet NV⁻ electronic transitions (see inset). For both transitions, the absorption and fluorescence features have opposite signs and mirror one another up to a scaling factor. Adapted from Bauch, 2010.

Fig. 29. The green absorption yields $\sim 100 \text{ nT}/\sqrt{\text{Hz}}$ sensitivity, while the conventional readout based on red fluorescence reaches $\sim 400 \text{ pT}/\sqrt{\text{Hz}}$, about 250 times better. As with NIR absorption readout (see Sec. V.F), recycling the green excitation light via a resonant optical cavity can increase the absorption signal by (i) addressing a larger NV⁻ population, (ii) improving initialization into the $m_s = 0$ state, or (iii) enhancing C_{absorb} . Although effectively implemented absorption readout may achieve higher optical collection efficiency than fluorescence detection, the low realized absorption contrasts are a current major drawback.

Furthermore, absorption behavior for 532 nm probe radiation can result in increased probe laser transmission under resonant MW application (Bauch, 2010; Le Sage and Arai, 2011), leading to an anomalous inversion of the green absorption signal. This deviation from the expected behavior was independently observed in multiple research groups (Bauch, 2010; Le Sage and Arai, 2011). The anomalous $C_{\rm absorb}$ reveals a strong wavelength and power dependence (Bauch, 2010), which suggests that green absorption readout is hindered by an unknown effect competing with and sometimes dominating the otherwise expected behavior. The wavelength and power dependence of this effect suggests that NV⁰/NV⁻ charge dynamics could play a role. Further investigation of this behavior might reveal presently unknown NV dynamics. Overall, given the low absorption contrast C_{absorb} , and the as-yet unknown mechanism of anomalous absorption behavior, the utility of green absorption readout remains questionable.

H. Laser threshold magnetometry

Another approach for bulk NV⁻ magnetometry is the creation of a NV-diamond-based laser threshold magnetometer, as suggested by Jeske, Cole, and Greentree (2016). Lasing is induced on the NV⁻ $^3E(v=0) \leftrightarrow ^3A_2(v' \ge 1)$ transition; then, when a magnetic-field-dependent population accumulates in the singlet state, the lasing threshold increases, and the laser's output power is reduced. As theoretically

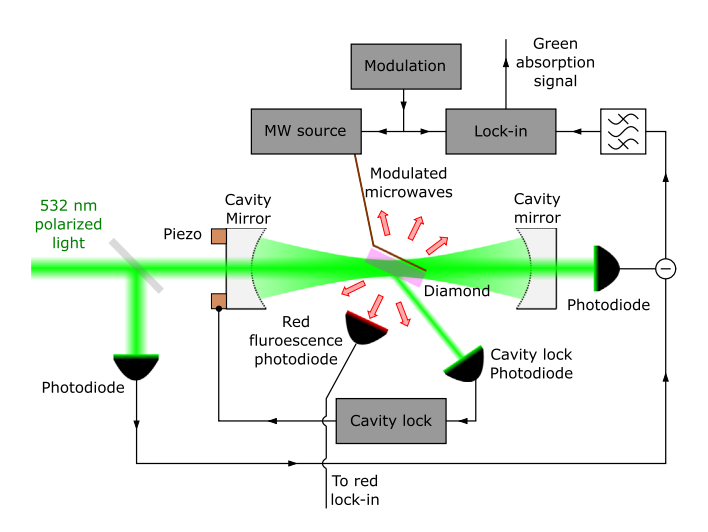


FIG. 29. Cavity-enhanced magnetometry based on green absorption as demonstrated by Ahmadi *et al.* (2018a, 2018b). A power buildup cavity allows green excitation light to pass through the diamond sample multiple times, increasing the effective path length. The red fluorescence is measured simultaneously along with the green absorption. Adapted from Ahmadi *et al.*, 2018b.

outlined by Jeske et al. (2017) and Savitski (2017), the laser threshold approach has a number of benefits relative to generic cw-ODMR methods (Sec. II.B.1): (i) effective contrast is enhanced near the lasing threshold due to competition between stimulated and spontaneous emission, and (ii) collection efficiency is substantially improved by virtue of the lasing process. Although the emission cross sections for NV⁻ and NV⁰ have been measured (Fraczek et al., 2017), and stimulated emission from NV- was recently demonstrated (Jeske et al., 2017), substantial work remains to address potential problems. For example, absorption by substitutional nitrogen or other defects may obstruct the lasing process (Dodson et al., 2011), and it will need to be shown that other sources of noise affecting the lasing threshold or output power can be either controlled or normalized out (Jeske, Cole, and Greentree, 2016). More concerning, however, is that both theory (DeGiorgio and Scully, 1970) and experiment (Lim, Chern, and Otsuka, 2002) find large laser field fluctuations in the vicinity of the lasing threshold.

VI. DIAMOND MATERIAL ENGINEERING

A. Conversion efficiency

In an idealized case in which all other parameters are held constant, increasing the NV⁻ density in a fixed detection volume will result in enhanced sensitivity. Since the NV⁻ density is limited by the density of nitrogen introduced into the diamond, the N-to-NV⁻ conversion efficiency

$$E_{\rm conv} \equiv \frac{[\rm NV^-]}{[\rm N^T]} \tag{32}$$

must be increased in order to achieve a high density of NV⁻ spins while minimizing the concentration of residual paramagnetic substitutional nitrogen. Converting a substitutional

nitrogen N_S into a NV⁻ defect requires both introducing a vacancy to a lattice site adjacent to a substitutional nitrogen (to create the NV) and capturing an electron (to change the NV center's charge state to NV⁻). We denote the efficiency with which nitrogen atoms in the diamond are converted to NVs as

$$\chi = \frac{[NV^{\mathrm{T}}]}{[N^{\mathrm{T}}]},\tag{33}$$

where $[N^T] = [N_S^0] + [N_S^+] + [NV^-] + [NV^0] + [NV^+] + [N^{other}]$ accounts for the concentration of substitutional nitrogen N_S in the neutral and ionized charge states, NV centers in all three charge states, and other nitrogen-containing defects in the diamond, such as NVH (see Sec. VI.F). We define the fraction of NV centers residing in the negative charge state as the charge-state efficiency ζ ,

$$\zeta = \frac{[NV^{-}]}{[NV^{T}]} = \frac{[NV^{-}]}{[NV^{-}] + [NV^{0}] + [NV^{+}]},$$
 (34)

so that $E_{\rm conv} = \chi \zeta$. Although Hauf *et al.* (2014) and Pfender *et al.* (2017) showed evidence for NV⁺, this state has thus far required application of external voltages for observation. The rest of this section therefore assumes that [NV⁺] is negligible and can be ignored.

As the N-to-NV^T conversion efficiency χ is determined by the physical location of nitrogen and vacancies in the diamond lattice, the value of χ is expected to be invariant under ambient conditions. Modification of χ requires a condition severe enough to rearrange atoms within the diamond lattice, such as irradiation, implantation, high temperature, or high pressure. With suitable electron irradiation and subsequent annealing, N-to-NV^T conversion efficiencies approaching 1 can be achieved, although such high values are not necessarily desirable (see Secs. VI.D and VI.E).

In contrast, the charge-state efficiency ζ depends on local conditions in the diamond and can be affected by external fields and optical illumination. Increasing ζ benefits sensitivity in two ways: first, by increasing the NV⁻ concentration and thus the number of collected photons \mathcal{N} from the NV⁻ ensemble, and second, by decreasing the concentration of NV⁰ and the associated background fluorescence, which improves measurement contrast. In the following section, we discuss factors contributing to the charge-state efficiency and methods to optimize it for sensing.

B. NV charge-state efficiency

The charge-state efficiency ζ from Eq. (34) depends on many factors both internal and external to the diamond. For both native NVs (Iakoubovskii, Adriaenssens, and Nesladek, 2000) and NVs created by irradiation and annealing of nitrogen-rich diamonds (Mita, 1996), the NV⁻ and NV⁰ charge states can coexist in a single sample. In general, for a given sample and experimental procedure, the steady-state charge-state efficiency is difficult to predict. Contributing factors include the concentration of substitutional nitrogen and other defects serving as charge donors or acceptors (Groot-Berning *et al.*, 2014) and their microscopic distributions (Collins, 2002;

Doi et al., 2016); the wavelength, intensity, and duty cycle of optical illumination (Manson and Harrison, 2005; Aslam et al., 2013; Doi *et al.*, 2016; Ji and Dutt, 2016); the application of a bias voltage (Grotz et al., 2012; Kato et al., 2013; Doi et al., 2014; Schreyvogel et al., 2014); and, for near-surface NVs, the diamond surface termination (Santori et al., 2009; Fu et al., 2010; Rondin et al., 2010; Hauf et al., 2011; Cui and Hu, 2013; Chu et al., 2014; Groot-Berning et al., 2014; Osterkamp et al., 2015; Newell, Dowdell, and Santamore, 2016; Kageura et al., 2017; Yamano et al., 2017). The charge-state efficiency is likely affected by the conditions of diamond growth, as well as the irradiation dose (Mita, 1996) (see Sec. VI.D), the annealing duration and temperature, and possibly the operation temperature (Manson and Harrison, 2005). Moreover, the value of the charge-state efficiency ζ during an NV⁻ sensing procedure can be difficult to measure. NVs may be reversibly converted between NV- and NV0 by various optical and nonoptical processes (Khan et al., 2009; Aslam et al., 2013; Bourgeois et al., 2017). Because ζ is strongly affected by the illumination laser intensity and wavelength (Aslam et al., 2013; Bourgeois et al., 2017), characterization of ζ by methods such as Fouriertransform infrared spectroscopy (FTIR), ultraviolet-visible spectroscopy (known as UV-Vis), and EPR may be misrepresentative of NV charge-state behavior under the optical illumination employed in most NV-diamond-sensing devices.

1. Nonoptical effects on NV charge-state efficiency

Here we discuss the charge-state efficiency ζ in nitrogenrich diamond in the absence of optical illumination. For shallow NVs, the charge state is strongly affected by the surface chemical termination (Fu et al., 2010; Rondin et al., 2010; Hauf et al., 2011; Cui and Hu, 2013; Groot-Berning et al., 2014). Based on the work of Groot-Berning et al. (2014), surface termination should provide enhanced charge-state stability to a depth of at least 60 nm, and possibly farther (Malinauskas et al., 2008; Santori et al., 2009). The chargestate efficiency ζ can also be controlled electrically (Grotz et al., 2012; Kato et al., 2013; Doi et al., 2014; Hauf et al., 2014; Schreyvogel et al., 2014, 2015; Karaveli et al., 2016; Forneris et al., 2017; Murai et al., 2018). Because diamond is an approximately 5.47 eV wide band gap insulator (Wort and Balmer, 2008), Collins (2002) contends that an NV center's charge-state depends less on the position of the Fermi level and more on the distance to the nearest charge donor. In nitrogen-rich diamonds, these donors are mainly substitutional nitrogen defects N_S , and the charge-state efficiency ζ is seen to increase with the concentration [N_S] (Collins, 2002; Manson and Harrison, 2005). Other defects in the diamond lattice can alter ζ as well; for example, Groot-Berning et al. 2014 found that the NVs in separate implanted regions containing phosphorus (an electron donor) and boron (an electron acceptor) increased and decreased, respectively, the NV charge-state efficiencies.

Introduction of electron donors other than nitrogen into diamond might appear to be a promising avenue for increasing the NV charge-state efficiency. For example, phosphorus (Groot-Berning *et al.*, 2014; Doi *et al.*, 2016; Murai *et al.*, 2018), with a donor level 0.6 eV below the conduction band (Katagiri *et al.*, 2004), is a shallower donor than nitrogen,

which lies 1.7 eV below the conduction band (Farrer, 1969; Wort and Balmer, 2008). However, creating *n*-doped diamond through the introduction of phosphorus has proven difficult (Kalish, 1999), as phosphorus doping is correlated with the introduction of a deep acceptor tentatively identified as the phosphorus vacancy (PV) (Jones, Lowther, and Goss, 1996). Moreover, irradiation and annealing to create NV centers may further convert desirable substitutional phosphorus into PVs (Jones, Lowther, and Goss, 1996). PVs in diamond will compete with NVs for electrons, undermining the benefit of phosphorus doping to the charge-state efficiency. Additionally, PL emission at wavelengths overlapping the NV⁻ PL spectrum was observed in phosphorus-doped diamond (Cao *et al.*, 1995), further complicating the use of phosphorus in NV-diamond sensing. For additional discussion, see Doherty *et al.* (2016).

The irradiation and annealing procedures applied to increase the N-to-NV^T conversion efficiency χ can also affect the charge-state efficiency ζ . In type Ib diamonds grown by high-pressure-high-temperature (HPHT) synthesis (see Sec. VI.C), with $[N_S] \gtrsim 50$ ppm, ζ approaching 1 is seen after low- and moderate-dose irradiation and annealing (Mita, 1996; Manson and Harrison, 2005). As discussed in Sec. VI.D, at higher irradiation doses, the NV⁰ concentration is seen to abruptly increase (Mita, 1996), which can be attributed to the combination of an insufficient concentration of nitrogen defects N_S available to donate electrons to the increasing overall NV population, and an increase in deep acceptor states such as multivacancy defects (D. J. Twitchen *et al.*, 1999; Pu, Avalos, and Dannefaer, 2001).

2. Optical effects on NV charge-state efficiency

Optical illumination of diamond may also change the NV charge-state efficiency ζ through ionization of NV⁻ to NV⁰ and also the recombination of NV⁰ back to NV⁻ (Manson and Harrison, 2005; Waldherr et al., 2011; Aslam et al., 2013; Hopper et al., 2016, 2018). The steady-state value of ζ is seen to depend on the illumination intensity and wavelength, although most of the reported measurements have been taken on single-NV centers (Waldherr et al., 2011; Aslam et al., 2013; Hopper et al., 2016). For example, an excitation wavelength band from 510 to 540 nm was found to produce the most favorable single-NV charge-state efficiency in steady state compared to longer and shorter wavelengths (Aslam et al., 2013). In particular, when single NVs were illuminated by 532 nm light at intensities typical for pulsed sensing protocols (Waldherr et al., 2011; Hopper et al., 2016) or similar wavelength light at lower intensities (Aslam et al., 2013), a charge-state efficiency $\zeta \sim 70\%$ –75% was observed. However, the value of ζ under these conditions is likely to differ for dense NV ensembles (Manson and Harrison, 2005; Meirzada et al., 2018). For example, measurements by Manson and Harrison (2005) on an NV ensemble in a diamond with $[N_s^T] \sim 70$ ppm and $[NV^T] \sim 1$ ppm show the chargestate efficiency dropping to ~50% as the 532 nm power approaches the saturation power of the NV⁻ optical transition. More study is required to determine the relative contributions to the NV ensemble ζ of optical charge-state switching, the presence of nearby charge donors or acceptors, and other effects.

Recently, several studies on single-NV centers have shown improved optical initialization to NV- by applying NIR in combination with the 532 nm green excitation light (Hopper et al., 2016; Ji and Dutt, 2016; Chen et al., 2017). This enhanced charge-state initialization has been demonstrated with 780 nm cw radiation (Chen et al., 2017), 1064 nm cw radiation (Ji and Dutt, 2016), and 900-1000 nm pulsed radiation, achieving in the third case $\zeta > 90\%$ (Hopper et al., 2016). The effect is theoretically explained as follows: After absorption of a green photon to enter the electronically excited state, an NV⁰ absorbs an NIR photon, which promotes a hole to the valence band and forms NV- (Hopper et al., 2016; Ji and Dutt, 2016). The mechanism, visualized schematically in Fig. 30, is the same as the two-photon ionization and recombination of NV⁻ and NV⁰ by 532 nm radiation, but with the second absorbed photon being an NIR photon. Hopper et al. (2016) found the NV⁰-to-NV⁻ recombination process to occur with up to a ~7 times higher likelihood than the analogous ionization process converting NV⁻ to NV⁰, wherein the excited-state NV- absorbs an NIR photon, promoting an electron to the conduction band.

NIR enhancement of the charge-state efficiency is expected to be compatible with pulsed initialization and readout. However, when employing 532 nm intensities $I \approx I_{\rm sat} \approx 2.7~{\rm mW/\mu m^2}$ (Wee *et al.*, 2007) typical for pulsed experiments, Hopper *et al.* (2016) found enhancements in ζ to be lessened compared to operation at lower green intensity. Furthermore, if the charge switching rate under green-plus-NIR illumination approaches or exceeds the optical spin polarization rate, spin readout-fidelity can be degraded by the increased photoionization during the readout pulse. Ji and Dutt (2016) and Chen *et al.* (2017) reported charge switching rates near $\sim 1~\mu s^{-1}$, approaching the lower singlet-state decay rate of $4~\mu s^{-1}$ (Acosta, Jarmola *et al.*, 2010). Nonetheless, Hopper *et al.* achieved enhanced charge-state initialization with much lower charge switching rates of $\sim 10~{\rm ms}^{-1}$.

Further work is required to determine if the NIR-plus-green illumination technique can be extended to increase the charge-state efficiency ζ in NV ensembles. While the technique has

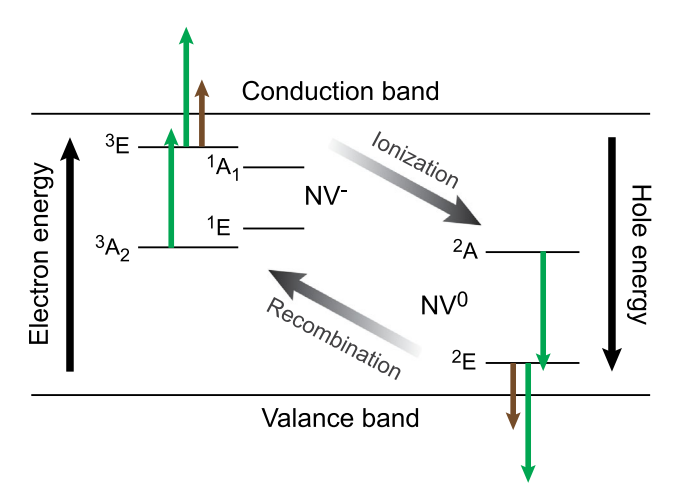


FIG. 30. Energy level diagrams for NV^- and NV^0 , representing optical ionization and recombination processes through absorption of either two 532 nm photons (green arrows) or a 532 nm photon and an NIR photon (brown arrows).

shown success for near-surface NV centers, Meirzada et al. (2018) observed no enhancement in the NV- PL from NIRplus-green illumination compared to green-only excitation for NV centers in bulk diamond. Moreover, even if NIR-plusgreen illumination can enhance the ensemble value of ζ , the power requirements may limit the technique's application to large ensembles. Although the required NIR power for confocal setups addressing single NV- centers or small ensembles is modest (\sim milliwatt), the NIR intensity is $\gtrsim 10$ times higher than the typical 532 nm intensities used for NV spin initialization ($I_{\text{NIR}} \approx 23I_{\text{sat}}^{532 \text{ nm}}$) by Hopper *et al.* (2016). Thus, when applying the technique to macroscopic ensemble volumes, the maximum addressable ensemble size will quickly be limited by the available laser power. For example, a $(50 \ \mu\text{m})^2$ spot would require $\gtrsim 100 \ \text{W}$ of NIR (Wee et al., 2007). At present, NIR enhancement of charge-state efficiency appears to be unlikely to yield substantial improvements to ensemble-NV⁻ magnetometer sensitivities.

C. Diamond synthesis and high-pressure-high-temperature (HPHT) treatment

Fabricated bulk diamonds are commonly synthesized using one of two methods. In high-pressure-high-temperature (HPHT) synthesis, a process mimicking natural diamond formation, a carbon source material is mechanically compressed (pressure > 5 GPa) and heated (temperatures ≥1250 °C) to create conditions where diamond is the thermodynamically favored carbon allotrope. Dissolving the carbon source (typically graphite) in a metal "solvent catalyst" can increase the growth rate, decrease the required temperature and pressure, and allow for better composition control. Consequently, solvent catalysts are nearly always employed. A small seed diamond facilitates the growth; the dissolved carbon precipitates out of the metal catalyst solution and crystallizes onto the seed diamond, growing the size. Nitrogen easily incorporates into the diamond lattice, and is historically the primary impurity element in HPHT diamonds. However, nitrogen content in HPHT-synthesized diamonds can be reduced by varying the atomic composition of the metal solvent catalyst to "getter" the nitrogen, and recent advances in getter technology have allowed for direct creation of electronic grade HPHT diamond with $[N_S^0] \lesssim 5$ ppb (D'Haenens-Johansson et al., 2015; Tallaire, Mille et al., 2017). Kanda (2000), Dobrinets, Vins, and Zaitsev (2013), and Palyanov et al. (2015) discuss HPHT synthesis in detail.

Plasma-enhanced chemical vapor deposition (PE-CVD) diamond synthesis (Angus, Will, and Stanko, 1968) is a popular alternative to HPHT synthesis, which can leverage established semiconductor fabrication techniques. In the most widespread variant of this method, employing homoepitaxial growth, a diamond seed is exposed to a hydrocarbon plasma consisting of approximately 95%–99% hydrogen, with the balance composed of carbon and possibly other species such as oxygen or argon. Methane is the most popular carbon source. Radicalized carbon atoms bond with the growth surface, forming a mixture of sp^2 and sp^3 bonded orbitals. Although hydrogen etches both sp^2 and sp^3 bonded carbon, the etch rate for sp^2 bonded carbon is much greater

(Schwander and Partes, 2011) and if the hydrogen etching and carbon deposition rates are carefully tuned, diamond synthesis can be achieved (Angus, Will, and Stanko, 1968). Unlike HPHT synthesis, PE-CVD (alternatively simply called CVD) synthesis can easily allow the production of thin or deltadoped layers from nanometer to micron scale (Ohno *et al.*, 2012; McLellan *et al.*, 2016), masked synthesis of diamond structures (Zhang and Hu, 2016), or layered epitaxial growth required for *p-i-n* (Kato *et al.*, 2013) or *n-i-n* structures, the latter of which consists of an intrinsic region sandwiched between two *n*-doped regions (Murai *et al.*, 2018).

For the past 15 years, the majority of NV-diamond literature has employed diamonds grown by PE-CVD. First, much early work focused on single NV⁻ centers, and most HPHT-synthesized diamonds were not available at that time with the requisite low-nitrogen concentration (≲100 ppb), as HPHT impurity control can be challenging (Gaukroger et al., 2008; Martineau et al., 2009). Second, the layered deposition inherent to CVD allows for straightforward growth of epitaxial layers (as would be required for magnetic imaging devices) and the application of semiconductor techniques to control diamond composition. Third, the PE-CVD method was historically more popular with commercial collaborators (such as Element Six and Apollo Diamond) responsible for producing the majority of scientific diamonds containing NV⁻ centers.

In addition, several challenges accompany direct HPHT synthesis of high-quality NV diamonds. For one, solventcatalyst incorporation into the diamond lattice may result in metal inclusions with size visible to the naked eye. Such inclusions could be particularly problematic for magnetic sensing applications, since the common materials employed in solvent-catalyst alloys are the ferromagnetic elements Fe, Co, and Ni (Palyanov et al., 2015). The purity of HPHTsynthesized diamonds may be limited by the solid precursor materials, which may not be available with as high chemical or isotopic purity as the gas-phase precursor elements employed for CVD synthesis. Finally, the HPHT process is not intrinsically amenable to fabrication of NV--rich layers, as are needed for imaging applications. In spite of these challenges, HPHT-fabricated diamonds with good characteristics for ensemble-NV⁻ dc magnetometry—including long T_2^* ($\gtrsim 2~\mu s$), high E_{conv} ($\sim 30\%$), and $[N^T] \sim 1-4$ ppm—have recently been reported in the literature (Grezes et al., 2015; T. Wolf et al., 2015; Stürner et al., 2019); see Table VI.

While the exact motivation for HPHT diamond synthesis is not always explicitly stated (Teraji et al., 2013), HPHT

synthesis may circumvent undesired characteristics inherent to CVD-synthesized diamonds (Charles et al., 2004; Hartland, 2014). A serious disadvantage of CVD synthesis is the incorporation of unwanted impurities and charge traps into the lattice (see Sec. VI.F). In addition, CVD-grown diamonds may display undesirable strain nonuniformities or contain a high dislocation density. For example, CVD-grown diamonds sometimes exhibit a brown coloration, which is attributed to vacancy cluster incorporation during synthesis (Hounsome et al., 2006; Khan et al., 2013). As vacancy clusters, chains, and rings are typically paramagnetic (Lomer and Wild, 1973; Iakoubovskii and Stesmans, 2002; Baker, 2007; Yamamoto et al., 2013), these clusters can increase NV- ensemble dephasing, reducing T_2^* . Additionally, since such vacancy chains and clusters are deeper electron acceptors than NV-(Khan et al., 2009; Edmonds et al., 2012), their presence may decrease measurement contrast (Tallaire, Mayer et al., 2017). Naturally occurring diamond that has not undergone irradiation rarely contains vacancies (Mainwood, 1999), suggesting that vacancies and vacancy clusters should be uncommon in well-synthesized HPHT diamond. As point defects, dislocations, and other extended defects are believed to be the dominant sources of strain in type IIa diamonds (Fisher et al., 2006), HPHT-synthesized diamonds may also exhibit lower strain than their CVD-grown counterparts. While dislocation densities of $\approx 10^4 - 10^6$ cm⁻² are typical in CVD-grown diamonds (Achard et al., 2014), certain HPHT-synthesized diamonds can demonstrate dislocation densities of $\approx 100-1000 \text{ cm}^{-2}$ (Martineau et al., 2009; Tallaire, Mille et al., 2017) and substantially lower strain (D'Haenens-Johansson et al., 2014, 2015).

Although more research is needed, it has been observed that the high quantity of hydrogen present during CVD growth can result in hydrogen incorporation into the diamond lattice (Charles *et al.*, 2004; Goss *et al.*, 2014); see Sec. VI.F. In contrast, diamonds synthesized directly by HPHT are unlikely to have hydrogen defects, as only one hydrogen-related defect has been found to incorporate into HPHT-synthesized diamond (Hartland, 2014).

Alternatively, mixed-synthesis approaches can combine the strengths of CVD and HPHT. One popular method is HPHT treatment, where an existing CVD diamond is heated and subjected to high pressure, resulting in atomic-scale reconfigurations of atoms in the lattice while leaving the macroscale diamond largely unchanged (Dobrinets, Vins, and Zaitsev, 2013). HPHT treatment effectively removes single vacancies (Collins, Kanda, and Kitawaki, 2000; Dobrinets, Vins, and

TABLE VI. Partial literature survey of diamonds with properties well suited to ensemble-NV⁻ magnetometry. Diamonds with long T_2^* , high N-to-NV⁻ conversion efficiency E_{conv} , and $[\text{NV}^-] \gtrsim 1$ ppm are expected to be particularly favorable for high-sensitivity magnetometry applications. Ellipses indicate values not reported or unknown.

Reference	T_2^*	T_2	$E_{ m conv}$	[NV ⁻]	$[NV^0]$	$[N^T]$	[¹³ C]	Synthesis
Grezes et al. (2015)	~2.6 µs	84 μs	29%	0.4 ppm	0.4 ppm	1.4 ppm	300 ppm	HPHT
T. Wolf et al. (2015)		~50 µs	30%	0.9 ppm		3 ppm		HPHT
Zheng et al. (2019)	$\geq 1.4 \ \mu s$			~0.9 ppm		> 2.9 ppm	300 ppm	HPHT
Hartland (2014)			28%	1.2 ppm	0.7 ppm	4.1 ppm	10 700 ppm	CVD + HPHT
Schloss (2019)	1.55 μ s	15.7 μ s	~30%	~3 ppm	· · · ·	~10 ppm	100 ppm	CVD
Barry et al. (2016)	580 ns	$5.1~\mu s$	6.3%	~1.7 ppm		27 ppm	10 ppm	CVD
Schloss et al. (2018)	450 ns	7 μs	~14%	3.8 ppm	2.0 ppm	~28 ppm	10 700 ppm	CVD

Zaitsey, 2013) and causes vacancy clusters to dissociate (Collins, Kanda, and Kitawaki, 2000; Dobrinets, Vins, and Zaitsey, 2013) or aggregate (Bangert et al., 2009). Thus, this method is effective to treat CVD-grown diamonds, which can exhibit vacancies and vacancy clusters (Charles et al., 2004; Khan et al., 2013; Hartland, 2014). The approach of applying HPHT treatment to CVD diamonds was proposed by Twitchen, Geoghegan, and Perkins, (2010) and realized by Hartland (2014), wherein a CVD-grown diamond was HPHT treated after synthesis but prior to irradiation and subsequent annealing (see Secs. VI.D and VI.E). The diamond referenced by Hartland (2014) exhibits a notably high 30% conversion efficiency $E_{\text{conv}} = [\text{NV}^-]/[\text{N}^{\text{T}}]$ as shown in Table X. A similar process pioneered by Lucent Diamonds employs HPHT treatment of diamonds prior to irradiation and annealing (Vins, 2007). This process results in a final material with an intense red hue and photoluminescence dominated by NVemission (Wang et al., 2005; Dobrinets, Vins, and Zaitsev, 2013), suggesting that HPHT treatment can be effective to increase the charge-state efficiency ζ , likely by eliminating charge traps.

However, HPHT treatment cannot address all diamond deficiencies, CVD related or otherwise. For example, should a CVD-synthesized diamond incorporate high concentrations of hydrogen or other elemental impurities into the diamond lattice during growth, HPHT treatment is ineffective to remove these impurities (Charles *et al.*, 2004). Such treatment is also limited to diamonds with balanced aspect ratios, as thin plates or rods will likely crack under the high applied pressure.

In addition to HPHT treatment of existing diamonds, other mixed-synthesis approaches have also been pursued. For example, utilizing type IIa HPHT seeds for CVD growth rather than CVD-grown seeds can yield material with lower strain and reduced densities of dislocations and other unwanted defects (Gaukroger *et al.*, 2008; Martineau *et al.*, 2009; Hoa *et al.*, 2014; Tallaire, Mille *et al.*, 2017). Another mixed-synthesis method exploits the fine composition control and high chemical purities available with CVD synthesis to create the carbon precursor for HPHT synthesis (Teraji *et al.*, 2013). The diamond composition can thus be carefully controlled, and HPHT synthesis can take advantage of high-purity or isotopically enriched gaseous sources (e.g., methane or $^{15}N_2$).

Given the prominent role lattice defects and elemental impurities play in determining the charge-state efficiency and coherence times for NV⁻, additional research focused on synthesizing sensing-optimized diamonds is warranted.

D. Electron irradiation

For unmodified as-grown CVD diamond, realized conversion efficiency values $E_{\rm conv}$ can be far less than unity, as

shown in Table VII, where the majority of substitutional nitrogen is not converted to NV⁻ (Edmonds et al., 2012; Hartland, 2014). In fact, for some CVD diamonds (see Table VIII), the concentration of grown-in monovacancies is insufficient to achieve good $E_{\rm conv}$ for total nitrogen concentration $[N^T] \gtrsim 1$ ppm regardless of location; even if every monovacancy were adjacent to a substitutional nitrogen, the conversion efficiency E_{conv} would still be low (Mainwood, 1999; Deák et al., 2014). However, the monovacancy concentration can be augmented after growth by irradiating the diamond with energetic particles. The high-energy irradiating particles knock carbon atoms out of the diamond lattice, creating both interstitial carbon atoms and monovacancies (D. Twitchen et al., 1999; Newton et al., 2002). Although theoretical calculations have not yet completely converged with experimental observations (Deák et al., 2014; Zaitsev, Moe, and Wang, 2017), the widely accepted model posits that, upon subsequent annealing (discussed in Sec. VI.E), diffusing vacancies are captured by substitutional nitrogen atoms, forming NV centers (Acosta et al., 2009). Primary considerations in the irradiation process are the particle type, energy, and dose.

The irradiation of diamond has been performed using a variety of particles: protons, ionized deuterium atoms, neutrons, and electrons (Ashbaugh, 1988). Gamma ray irradiation from ⁶⁰Co has also been used (Ashbaugh, 1988; Campbell and Mainwood, 2000). Many of these particles are suboptimal for NV creation, however, where only single monovacancies V⁰ are desired, and other created defects are likely deleterious. A particular problem for certain irradiation methods is the production of "knock-on atoms" (Campbell and Mainwood, 2000; Davies et al., 2001), where the irradiating particle has sufficient energy not only to displace an initial carbon atom from the lattice but also to impart enough kinetic energy to that carbon that it displaces additional carbon atoms, resulting in localized lattice damage (Buchan et al., 2015). Although annealing (see Sec. VI.E) can partially alleviate such damage, the lattice damage can never be completely repaired (Balmer et al., 2009; Twitchen, Geoghegan, and Perkins, 2010; Fávaro de Oliveira et al., 2016, 2017; Lobaev et al., 2017) and may result in unwanted paramagnetic defects or charge traps. For irradiation with protons, neutrons, or ionized deuterium atoms, damage from such knock-on atoms can be severe. Similar lattice damage occurs from ion implantation of various species such as nitrogen (Naydenov et al., 2010; Yamamoto et al., 2013; Fávaro de Oliveira et al., 2017), carbon (Naydenov et al., 2010; Schwartz et al., 2011), and helium nuclei (Waldermann et al., 2007; Schwartz et al., 2011; Himics et al., 2014; McCloskey et al., 2014; Kleinsasser et al., 2016). Electrons, with their lower mass, transfer less kinetic energy to the carbon atoms and are therefore better

TABLE VII. Native N-to-NV⁻ conversion efficiencies E_{conv} and total nitrogen concentrations [N^T] in unmodified bulk CVD diamond.

$E_{ m conv}$	$[N^T]$	Growth location	Reference
0.0007-0.005	0.3–30 ppm	Element Six	Edmonds <i>et al.</i> (2012)
0.0006-0.03	0.35–2.4 ppm	Apollo Diamond Inc.	Edmonds <i>et al.</i> (2012)
0.02-0.03	4 ppm	Warwick University	Hartland (2014)

TABLE VIII. Native monovacancy concentrations in unmodified bulk CVD diamond.

$V^{0} = V^{-1}$	Reference
60 ppb	Rutledge and Gleason, (1998)
$\lesssim 20 \text{ ppb}$	Twitchen, Geoghegan,
	and Perkins (2010)
≲0.03 ppb	Mainwood (1999)

suited to creating isolated monovacancies. Electron irradiation is favored over gamma ray irradiation because the former can be accomplished in hours, whereas the latter, when implemented using ⁶⁰Co, can take weeks (Collins, 2007). In summary, electron irradiation is preferred to create NV⁻ ensembles optimized for sensing applications (Uedono *et al.*, 1999; Campbell *et al.*, 2002; Twitchen, Geoghegan, and Perkins, 2010), as this method allows for evenly distributed monovacancies to be created throughout the diamond in a timely manner, with less lattice damage than alternative methods.

Theoretical calculations predict that monovacancy creation requires electron energies $\gtrsim 165 \text{ keV}$ (Campbell et al., 2002), roughly consistent with experiments observing vacancy creation down to 145 keV (McLellan et al., 2016; Eichhorn, McLellan, and Jayich, 2019). Older, less reliable experiments find vacancy creation for electron irradiation along the [100] direction at 180 keV but not 170 keV (Koike, Parkin, and Mitchell, 1992). Crude estimates suggest electron irradiation energies lower than ~0.8 MeV will create mainly single vacancies (Mitchell, 1965; Loubser and van Wyk, 1978) and avoid producing multivacancy complexes. While this estimate is consistent with that of Dannefaer, Mascher, and Kerr (1992), where divacancies are detected after irradiation with 3.5 MeV electrons, Twitchen, Geoghegan, and Perkins (2010), however, found no evidence of vacancy pairs after irradiation with 4.6 MeV electrons, suggesting that several-MeV irradiation energies may be safe. The optimal irradiation energy may also depend on sample geometries; thicker diamonds should require higher energies to ensure that vacancies are created uniformly through the entire thickness (Campbell and Mainwood, 2000; Twitchen, Geoghegan, and Perkins, 2010). For small ensembles close to the diamond surface, an electron microscope can provide the needed irradiation (Kim et al., 2012; Schwartz et al., 2012; McLellan et al., 2016; Farfurnik et al., 2017). More study is required to resolve remaining discrepancies between experimental data and detailed simulations of the electron irradiation process (Campbell and Mainwood, 2000; Campbell et al., 2002). For example, recent measurements of monovacancy density profiles versus depth, as judged by GR1 intensities in 1 MeV electron irradiated diamonds (Zaitsev, Moe, and Wang, 2017), are inconsistent with Monte Carlo simulations of Campbell and Mainwood (2000) and Campbell et al. (2002).

The irradiation dose should also be approximately matched to the diamond's total nitrogen concentration [N T], as suggested in Sec. VI.A; if too many vacancies are created, then > 50% of N $_{S}$ will be converted to NV 0 , and the number of electrons donated by the remaining N $_{S}$ will be insufficient to

convert every NV⁰ to NV⁻. Figure 2 of Mita (1996) illustrates the importance of matching the irradiation dose to $[N^T]$ to achieve maximal E_{conv} . When determining the irradiation dose, in situ recombination between a vacancy and an interstitial carbon should be accounted for (Campbell and Mainwood, 2000; Davies et al., 2001). Current estimates suggest approximately 30% (Campbell and Mainwood, 2000) to 50% (Davies et al., 2001) of initially created vacancies are immediately lost to spontaneous recombination. For example, using 1 MeV electrons [generating $\sim 2 \times 10^{-4}$ vacancies/(electron μ m) according to Campbell and Mainwood (2000)] and assuming that 40% of vacancies recombine immediately and that two nitrogens are required to make a single NV- center, we expect a sample with $[N^T] \sim 1$ ppm to require a dose of 7.3×10^{16} cm⁻². However, fine-tuning of the irradiation dose is often done empirically, suggesting either the presence of dynamics more complicated than those included in the simple model presented here (i.e., the presence of other vacancy traps, the formulation of divacancies, loss at surfaces, etc.) or errors in the measured electron flux or substrate temperature (Campbell and Mainwood, 2000). For example, while the production rate of neutral monovacancies from irradiation with 2 MeV electrons is found to be temperature independent from room temperature to ~300 °C, the rate decreases notably at higher temperatures (Newton et al., 2002).

E. Low-pressure-high-temperature (LPHT) annealing

For the successful creation of NV⁻ centers, substitutional nitrogen and monovacancies must be relocated to occupy adjacent sites in the diamond lattice. This process can be accomplished via diffusion at elevated temperature, i.e., annealing. Since monovacancies migrate in the neutral charge state V⁰ (Breuer and Briddon, 1995) with an activation energy of $E_a = 2.3 \pm 0.3$ eV (Davies *et al.*, 1992; Mainwood, 1999), compared to measured values of $E_a = 4.8-6.2$ eV for substitutional nitrogen (Dobrinets, Vins, and Zaitsev, 2013; Deák et al., 2014; Jones et al., 2015), neutral monovacancies diffuse throughout the lattice during annealing until they reach the more immobile nitrogens. The negatively charged monovacancy's higher activation energy (Breuer and Briddon, 1995) ensures that monovacancy diffusion occurs predominantly in the neutral charge state (Breuer and Briddon, 1995), although a negative monovacancy can convert to a neutral monovacancy in a reversible charge transfer process (Davies *et al.*, 1992). The diffusion constant D of the neutral monovacancy is (Hu et al., 2002; Orwa et al., 2012)

$$D = D_0 e^{-E_a/k_B T}, (35)$$

where k_B is the Boltzmann constant, T is the temperature, and D_0 is a diffusion prefactor; see the Appendix, Sec. 10. Measurements of the diffusion constant D have yielded $\sim 1.1 \text{ nm}^2/\text{s}$ at 750 °C (Martin *et al.*, 1999) and 1.8 nm²/s at 850 °C (Alsid *et al.*, 2019), suggesting values for D_0 in agreement with an independently measured upper bound (Acosta *et al.*, 2009), and in moderate agreement with first-principles theoretical calculations (Fletcher and Brown, 1953); see the Appendix, Sec. 10. Other sources, however, find or employ different values for D_0 or E_a (Hu *et al.*, 2002;

Orwa *et al.*, 2012; Onoda *et al.*, 2017), suggesting that further measurements are warranted. Once an NV center is formed, the deeper binding energy of the nitrogen-vacancy bond relative to the neutral vacancy ensures that the bound vacancy does not diffuse away (Goss *et al.*, 2005; Hartland, 2014).

The procedure described here is commonly termed lowpressure-high-temperature (LPHT) annealing to distinguish it from HPHT annealing (discussed in Sec. VI.C). Given the role of diffusion in LPHT treatment, the annealing temperature and annealing duration are important control parameters. A temperature of ~800 °C is usually employed (Botsoa et al., 2011), given that monovacancies become mobile around 600°C (Davies and Hamer, 1976; Davies et al., 1992; Uedono et al., 1999; Kiflawi et al., 2007), and annealing times of several hours are typical; e.g., Acosta et al. (2009) used 2 h, Lawson et al. (1998) used 4 h, Twitchen, Geoghegan, and Perkins (2010) used 8 h, Barry et al. (2016) used 12 h, and Fraczek et al. (2017) used 16 h. Diamonds with lower values of [N^T] are expected to require longer annealing times due to the greater initial distances between vacancies and substitutional nitrogens. A study by Element Six found no observable deleterious changes in diamond properties between samples that were annealed at \sim 800 °C for \sim 8 h and samples that were annealed at the same temperature for longer periods (Twitchen, Geoghegan, and Perkins, 2010). This ~800 °C annealing step is typically performed under vacuum or in a nonoxidizing, inert gaseous environment to avoid graphitization (Dobrinets, Vins, and Zaitsev, 2013). Under vacuum, the present understanding is that diamond graphitization begins roughly around 1500 °C (Davies and Evans, 1972).

Although the 800 °C LPHT treatment is effective to create NVs, unwanted defects may form as well. For example, diffusing monovacancies can combine to form divacancies (D. J. Twitchen et al., 1999), which are immobile at 800 °C. As divancies are deeper electron acceptors than NVs (Deák et al., 2014; Miyazaki et al., 2014), their presence reduces $E_{\rm conv}$. To mitigate divacancy formation, electron irradiation with in situ (i.e., simultaneous) annealing has been proposed (Nöbauer et al., 2013). Under such conditions, single vacancies are continuously created in an environment consisting primarily of substitutional nitrogen (and, as the process progresses, NVs), thereby reducing divacancy formation. Although the preliminary work of Nöbauer et al. (2013) found that electron irradiation with in situ annealing increased T_2^* , no increase in E_{conv} was observed, and further investigation is warranted.

Following NV formation, further LPHT annealing above 800 °C may reduce strain or paramagnetic impurities resulting from lattice damage. For example, divacancies can combine into other defects at ~900 °C (D. J. Twitchen *et al.*, 1999). Reduction of a given defect species may be effected by consolidation into other larger defect species, which may be paramagnetic (Lomer and Wild, 1973; Baker, 2007; Yamamoto *et al.*, 2013; Hartland, 2014). Annealing to temperatures of 1000 to 1200 °C was shown to extend the T_2 of both single NV centers (Naydenov *et al.*, 2010; Yamamoto *et al.*, 2013) and ensembles (Tetienne *et al.*, 2018) created by ion implantation. As this increase was attributed to a reduction in paramagnetic

multivacancy defects (Yamamoto *et al.*, 2013; Tetienne *et al.*, 2018), improvement in T_2^* is expected as well, although this expectation has not been systematically confirmed in experiment. Practically, this additional LPHT treatment is limited by the temperature at which NVs anneal out, which is typically around $1400-1500\,^{\circ}\mathrm{C}$ (Zaitsev, 2001; Pinto *et al.*, 2012; Hartland, 2014) and can vary depending on the presence of other defect species within the diamond (Zaitsev, 2001). While a systematic study of annealing temperatures and durations is warranted for engineering optimal samples for ensemble-NV-sensing, a standard recipe for samples is at least several hours at $\sim 800\,^{\circ}\mathrm{C}$, followed by several more hours at $\sim 1200\,^{\circ}\mathrm{C}$ (Chu *et al.*, 2014; Fraczek *et al.*, 2017; Breeze *et al.*, 2018). Some sample calculations for annealing are detailed in the Appendix, Sec. 10.

F. Other common impurities in synthetic or treated single crystal diamond

Unwanted species in the diamond lattice can degrade magnetometer performance by decreasing the NV charge-state efficiency $\zeta = [\text{NV}^-]/[\text{NV}^\text{T}]$, creating local magnetic noise, or reducing the fraction of substitutional nitrogen N_S converted to NV⁻. This section restricts detailed discussion to multivacancy clusters and NVH (Khan *et al.*, 2013), species present in diamond at sufficient concentrations to likely affect NV spin and charge dynamics. Newton (2007) and Deák *et al.* (2014) include extended discussions of other defects; see also Table IX for relevant defects commonly found in diamond.

Multivacancy clusters are common in some diamonds grown by CVD (Pu et al., 2000; Hounsome et al., 2006) and are believed to cause the brown coloration in CVD-grown diamond (Hounsome et al., 2006; Fujita et al., 2009). During CVD synthesis, the diamond surface can become rough and stepped. When these steps are rapidly covered with additional deposited material, small voids—i.e., clusters of

TABLE IX. Common defects in diamond and their ground-state electronic spin.

Diamond defect	Ground-state spin
N_c^0	S = 1/2
$egin{array}{c} N_{ m S}^0 \ N_{ m S}^+ \end{array}$	S = 0
NV^-	S = 1
NV^0	S = 1/2
NV^+	S = 0
NVH-	S = 1/2
NVH^0	S = 0
$egin{array}{l} N_2^0 \ N_2^+ \ N_2 V^- \end{array}$	S = 0 (Tucker, Newton, and Baker, 1994)
N_2^{\mp}	S = 1/2
$N_2^2V^-$	S = 1/2
N_2V^0	S = 0
N_3V^0	S = 1/2
N_2VH^0	S = 1/2
VH-	S = 1
VH^0	S = 1/2
V_nH^-	S=1
V-	S = 3/2 (Baranov <i>et al.</i> , 2017)
V^0	S = 0 (Baranov et al., 2017)
V^+	S = 1/2 (Baranov <i>et al.</i> , 2017)
VV^-	S = 3/2 (Kirui, van Wyk, and Hoch, 2013)
VV^0	S = 1 (D. J. Twitchen <i>et al.</i> , 1999)

vacancies—can be left in the diamond (Hounsome et al., 2006; Khan et al., 2013). Multivacancy cluster incorporation has been observed to increase at high growth rates (Hounsome et al., 2006) and may be correlated with nitrogen content (Pu et al., 2000). Using positron annihilation, Dannefaer, Bretagnon, and Kerr (1993) found that the density of multivacancy clusters was roughly 10^{17} – 10^{18} cm⁻³ for their growth conditions. Such vacancy clusters can trap electrons (Campbell et al., 2002; Jones et al., 2007; Edmonds et al., 2012; Deák et al., 2014), reducing the ratio of NV⁻ to NV⁰ and also generating magnetic noise resulting from their trapped unpolarized electron spins. The neutral divacancy V_2^0 (Lea-wilsonf, Lomer, and Wyk, 1995; D. J. Twitchen *et al.*, 1999; Deák et al., 2014; Slepetz and Kertesz, 2014) and neutral multivacancy chains $(V_n^0, n \ge 3)$ are paramagnetic (Lomer and Wild, 1973; Iakoubovskii and Stesmans, 2002; Baker, 2007) and increase environmental magnetic noise. Irradiation or implantation followed by annealing can also produce such defects (Naydenov et al., 2010; Yamamoto et al., 2013). Low-pressure-high-temperature annealing is effective to remove certain multivacancy clusters. However, as the removal of multivacancy clusters is effected by aggregating these species together or combining them with other defects, the reduction of smaller multivacancy defects may be accompanied by an increase in larger multivacancy clusters or other defects. HPHT treatment effectively removes single vacancies (Dobrinets, Vins, and Zaitsev, 2013) and causes some vacancy clusters to dissociate (Dobrinets, Vins, and Zaitsey, 2013), which may aggregate to form different multivacancy clusters (Bangert et al., 2009); see Sec. VI.C.

Another common impurity in diamond is hydrogen, which gives rise to many defects (Zaitsev, 2001; Dobrinets, Vins, and Zaitsev, 2013; Goss et al., 2014). For typical CVD diamond growth, the plasma is composed predominantly of hydrogen (≥95%) (Tokuda, 2015), which can incorporate into single crystal diamond at concentrations as high as 1000 ppm (Sakaguchi et al., 1999). The hydrogen incorporation rate into the lattice is partially dependent upon the diamond growth recipe (Tang, Neves, and Fernandes, 2004), and further investigation into the hydrogen quantity incorporated and methods to mitigate hydrogen incorporation is warranted. Hydrogen-related defects may influence the NV charge state (Hauf et al., 2011; Lyons and de Walle, 2016). Additionally, at high enough concentrations, the nuclear spin of hydrogen may result in non-negligible dephasing or decoherence. At present we are unaware of any published method to effectively remove hydrogen from the bulk diamond lattice (Charles et al., 2004; Hartland, 2014).

The presence of hydrogen in the diamond lattice can enable formation of the NVH defect (Glover *et al.*, 2003), wherein the hydrogen occupies the vacancy of an NV. In as-grown nitrogenenriched CVD diamond, the ratio of $([N_S^+]+[N_S^0])\!:\![NVH^-]\!:\![NV^-]$ was found to be approximately 300:30:1 by Edmonds *et al.* (2012), and 52:7:1 by Hartland (2014). The NVH species is undesirable because (i) it lowers the conversion efficiency of incorporated nitrogen to NV centers; (ii) it reduces the concentration of substitutional nitrogen N_S available to donate electrons to turn NV^0 defects into NV^- ; (iii) NVH competes with NV as an electron acceptor; (iv) NVH $^-$ is paramagnetic,

causing magnetic noise; and (v) the hydrogen in NVH may rapidly tunnel among the three adjacent carbon atoms at gigahertz frequencies, resulting in high-frequency magnetic or electric noise (Edmonds, 2008).

No known treatment can transform existing NVH defects into NV defects. The NVH complex is stable against annealing up to approximately 1600 °C but anneals out completely by 1800 °C (Khan *et al.*, 2013; Hartland, 2014). However, removal of NVH via annealing is not associated with increased NV concentration; rather, further isochronal annealing to 2000 and 2200 °C is accompanied by increases in N_2VH^0 and N_3VH^0 species (Hartland, 2014), suggesting that the NVH concentration is reduced via aggregation of NVH with one or more nitrogen atoms. NVH 0 exhibits absorption at 3123 cm $^{-1}$ (Cann, 2009) but is otherwise not known to be optically active.

Diamonds subject to temperatures at which substitutional nitrogen or interstitial nitrogen become mobile may exhibit defects consisting of aggregated nitrogen, such as N₂ (Davies, 1976; Boyd, Kiflawi, and Woods, 1994; Tucker, Newton, and Baker, 1994), N₂V (Green et al., 2015), N₂VH (Hartland, 2014), N₃V (Green, Breeze, and Newton, 2017), N₃VH (Liggins, 2010; Hartland, 2014), N₄V (Bursill and Glaisher, 1985), or other aggregated nitrogen defects (Goss et al., 2004). The presence of aggregated nitrogen defects reduces the quantity of nitrogen available to form NV centers or donate electrons to NV⁰ to form NV⁻. Nitrogen aggregates can also cause additional paramagnetic noise. Other defects such as VH (Glover, 2003; Glover et al., 2004), V₂H (Shaw et al., 2005; Cruddace, 2007), and OV (Cann, 2009; Hartland, 2014) have been identified in synthetic diamond and may act as charge acceptors or create additional paramagnetic noise. However, most defects discussed in this section are observed at concentrations low enough to be neglected for diamonds fabricated for NV⁻ magnetometry, as shown in Table X, reproduced from Hartland (2014). Additional defect species are inferred to exist from charge conservation arguments but have not been directly observed (Khan et al., 2009). More research is needed to better understand defects in synthetic diamond grown for magnetometry applications.

G. Preferential orientation

In naturally occurring and many fabricated diamonds, NV-centers are distributed evenly among all four crystallographic orientations. However, under certain circumstances, CVD-grown diamond can exhibit preferential orientation of NV-centers along certain crystallographic axes (Edmonds *et al.*, 2012; Pham, Bar-Gill, Le Sage *et al.*, 2012). Several research groups have achieved almost perfect alignment of all NV-centers along a single [111] axis. Michl *et al.* (2014) demonstrated 94% alignment, Lesik *et al.* (2014) demonstrated 97% alignment, and Fukui *et al.* (2014) demonstrated 99% alignment. The mechanism for preferential orientation was explained by Miyazaki *et al.* (2014).

An ensemble-NV⁻ magnetometer utilizing a single NV⁻ orientation in a diamond with no preferential orientation suffers from reduced measurement contrast due to unwanted PL from NV⁻ centers of other orientations. A diamond with 100% preferential orientation may allow a 4 times increase in

TABLE X. Concentrations of quantifiable defects in sample GG1 in the as-grown state and after each treatment stage. From Hartland, 2014.

Defect	As grown	1500 °C anneal	Irradiation	800 °C anneal
$[N_S^0]$ (ppb)	1620 (160)	1100 (100)	200 (20)	120 (15)
$[N_S^+]$ (ppb)	1500 (150)	2200 (250)	3000 (300)	1000 (100)
$[NV^0]$ (ppb)	≤ 10	≤ 10	≤ 10	695 (70)
$[NV^-]$ (ppb)	60 (5)	40 (5)	35 (5)	1160 (120)
[NVH ⁰] (ppb)	500 (50)	310 (30)	380 (40)	290 (30)
[NVH ⁻] (ppb)	405 (40)	200 (20)	Obscured	20 (5)
$[N_2VH^0]$ (ppb)	< 0.1	22 (3)	Obscured	24 (5)
$[V_nH^-]$ (ppb)	3.1 (1)	≤ 0.1	25 (3)	41 (4)

contrast. In practice, though, the enhancement is typically somewhat less than 4 times, since polarized excitation light can already be used to selectively address particular NV⁻ orientations (Lesik *et al.*, 2014), and high bias fields can suppress fluorescence from off-axis NV⁻ centers (Epstein *et al.*, 2005; Tetienne *et al.*, 2012).

Diamonds grown with preferential orientation have at least two main drawbacks. First, NV- concentrations for preferentially grown diamonds in the literature are currently relatively low (Fukui et al., 2014; Lesik et al., 2014; Michl *et al.*, 2014), typically around 10^{12} cm⁻³ although concentrations up to 10¹⁵ cm⁻³ have been achieved (Tahara et al., 2015). Second, it appears that the N-to-NV⁻ conversion efficiency cannot be increased through irradiation and subsequent annealing without destroying the preferential alignment, although conflicting evidence on this topic has been reported (Fukui et al., 2014). Since electron irradiation followed by annealing can increase the N-to-NV conversion efficiency by ~10 to 100 times, preferential orientation is not currently believed to be a viable method to achieve better ensemble magnetometry sensitivity. However, it is possible that future technical advances or treatment could alter this understanding. Additionally, preferential orientation precludes the implementation of vector magnetometry (Schloss et al., 2018).

VII. MISCELLANEOUS SENSING TECHNIQUES

A. Rotary echo magnetometry

Broadband magnetometry can also be performed using a MW pulse scheme called a rotary echo (Aiello, Hirose, and Cappellaro, 2013; Mkhitaryan and Dobrovitski, 2014; Mkhitaryan, Jelezko, and Dobrovitski, 2015). In this technique pioneered by Aiello, Hirose, and Cappellaro (2013), rotary echoes are produced by periodic reversals of the driving field. The simplest protocol inverts the phase of the driving field to reverse the sign of the Rabi oscillations. The rotary echo technique may have utility for certain niche applications such as event detection (Aiello, Hirose, and Cappellaro, 2013), but the method so far yields worse sensitivity than a Ramsey protocol. Like other dynamicaldecoupling-type methods, rotary echo can be tailored to reject noise at certain frequencies and also has applications for certain narrow-band ac sensing, such as detection of individual nuclear spins (Mkhitaryan, Jelezko, and Dobrovitski, 2015).

B. Geometric phase magnetometry

In the presence of particular dc and rf magnetic fields, an NV⁻ spin may accumulate a measurable geometric phase (Berry, 1984) in addition to a dynamical phase. Following demonstrations of control and readout of an NV⁻ center's geometric phase (Maclaurin *et al.*, 2012; Arroyo-Camejo *et al.*, 2014; Zu *et al.*, 2014; Yale *et al.*, 2016; Zhou *et al.*, 2017), Arai *et al.* (2018) implemented geometric phase measurements for dc magnetometry. In their protocol, depicted in Fig. 31, the phase of a MW Rabi drive is swept adiabatically around a closed phase-space loop during two intervals separated by a central π pulse. Whereas the π pulse cancels the dynamic phase accumulated during the sequences, the acquired geometric phase depends on the strength of the dc

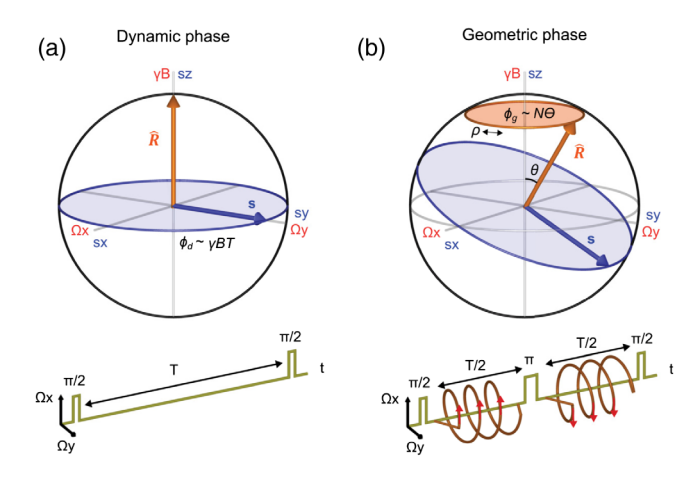


FIG. 31. Comparison of dynamic and geometric phase magnetometry. For dynamic phase magnetometry (i.e., Ramsey), the Bloch vector (blue arrow) is optically prepared and then rotated by a $\pi/2$ pulse to the equator. The Bloch vector then precesses about the fixed Larmor vector (orange arrow) before being mapped into a population difference by a second $\pi/2$ pulse and read out optically. (b) For geometric phase magnetometry, the Bloch vector is optically prepared and then rotated to the equator. Additional off-resonant driving then rotates the Larmor vector about the z axis. As the spins precess, a geometric phase proportional to the product of the solid angle (orange disk) and the number of Larmor vector rotations is acquired in addition to the dynamic phase. To cancel the dynamic phase while continuing geometric phase accrual, a π pulse and a reversal of the off-resonant drive are inserted at the sequence midpoint. Last, the Bloch vector is mapped onto a population difference by a second $\pi/2$ pulse and read out optically. From Arai et al., 2018.

magnetic field. While this technique enables wide-dynamic-range field sensing by avoiding a 2π phase ambiguity inherent to Ramsey magnetometry, it is unlikely to enhance sensitivity with respect to optimized Ramsey.

C. Ancilla-assisted upconversion magnetometry

A magnetometry scheme pioneered by Liu, Ajoy, and Cappellaro (2019) utilizes frequency upconversion via an ancilla nuclear spin to make broadband measurements of an external magnetic field. The method works as follows: A large magnetic field is aligned along the NV⁻ internuclear axis and tuned to near the ground-state level anticrossing (GSLAC) at \approx 1024 G, allowing the relative strengths of the Zeeman term and the hyperfine coupling of the NV⁻ electronic spin to the ancilla nuclear spin to be precisely tuned. In this regime, the NV⁻ electronic spin is first-order insensitive to magnetic fields perpendicular to the NV- symmetry axis. However, an applied transverse magnetic field B_{\perp} modulates the strength of the hyperfine interaction, resulting in amplitude modulation of the electronic spin energy level at the nuclear spin precession frequency. The modulation deviation is proportional to B_{\perp} . Thus, by performing standard ac magnetometry at the nuclear spin precession frequency, the magnitude of the perpendicular magnetic field B_{\perp} can be detected.

The technique is intriguing because (i) it allows the effective gyromagnetic ratio of the sensor to be tuned, and (ii) it enables the use of ac magnetometry techniques including dynamical-decoupling protocols to sense dc fields for durations on the order of T_2 or longer; see Sec. IV.A. However, the method is expected (and observed) to upmodulate both magnetic signals and magnetic noise, including spin-bath noise, to the ac measurement band. Further, the improved dephasing times are achieved primarily by decreasing the effective gyromagnetic ratio (i.e., the ratio relating \boldsymbol{B}_{\perp} to an energy level shift) relative to the native NV- electronic gyromagnetic ratio. Although the scheme enables vector sensing from a single NV- center and may be compatible with NV⁻ spin ensembles, the method presently precludes sensing from multiple NV⁻ orientations. So far there has been no experimental demonstration of improved sensitivity using this method relative to that of an optimized Ramsey-type equivalent. The requirement for ≈ 1000 G axial fields is also disadvantageous and likely prevents utilization of off-axis NV⁻ centers for sensing.

D. Techniques for the strong NV⁻-NV⁻ interaction regime

Dipolar interactions among NV⁻ spins contribute to ensemble-NV⁻ dephasing, as described in Sec. III.G. When NV⁻ centers compose the majority of spin defects in diamond, or when a different majority spin species is decoupled from the NV⁻ centers via spin-bath driving, NV⁻-NV⁻ interactions may degrade relaxation times T_2^* , T_2 , and T_1 (J. Choi *et al.*, 2017), limiting the sensitivity of both dc and ac magnetometers. Measurement protocols that decouple or leverage these like-spin interactions while retaining sensitivity to magnetic signals offer an avenue to surpass this sensitivity limit.

Proposed techniques to improve sensitivity in the limit of strong NV--NV- interactions may be separated into two

categories. Protocols in the first category mitigate dipolar interactions between like spins to extend either the dephasing time T_2^* (O'Keeffe *et al.*, 2019) for dc sensing or the coherence time T_2 (Choi, Yao, and Lukin, 2017a) for ac sensing. However, these techniques partially decouple the spins from the fields to be sensed, which may counteract the sensitivity enhancement from T_2^* or T_2 extension. Protocols in the second category harness like-spin interactions (Raghunandan, Wrachtrup, and Weimer, 2018) and may generate entangled many-body states (Choi, Yao, and Lukin, 2017b). Measurements of an entangled spin state comprising N spins can beat the standard quantum limit for spin-projection noise $[\eta \propto 1/\sqrt{N}]$, see Eq. (10)], and may approach the Heisenberg limit $(\eta \propto 1/N)$ (Gammelmark and Mølmer, 2011; Choi, Yao, and Lukin, 2017b).

To illuminate the promise and challenges associated with entanglement-enhanced techniques, we focus on the specific protocol proposed by Choi, Yao, and Lukin (2017b). The technique, which is expected to be applicable to NV⁻ centers, utilizes strong like-spin interactions to create quantum correlated states sensitive to ac magnetic fields. The proposed scheme, outlined schematically in Fig. 32, generates entanglement within a 2D array of spins by first polarizing the individual spins along a transverse magnetic field (which for NV- centers may be a MW-frequency field) and then adiabatically decreasing the field toward a quantum critical point. For the measurement to be compatible with global NVensemble readout, the system approaches the quantum critical point, generating entanglement, without crossing over the quantum phase transition to a Greenberger-Horne-Zeilinger (GHZ) state. In the measurement step, periodic transverse magnetic field π pulses are applied to the ensemble, allowing axial ac magnetic fields to excite the many-body system. The number of excitations detected after the transverse field returns to its original value provides a measure of the strength of the ac magnetic field.

Importantly, the entangled state's coherence time, denoted as \bar{T}_2 , is no longer limited by like-spin interactions, but by

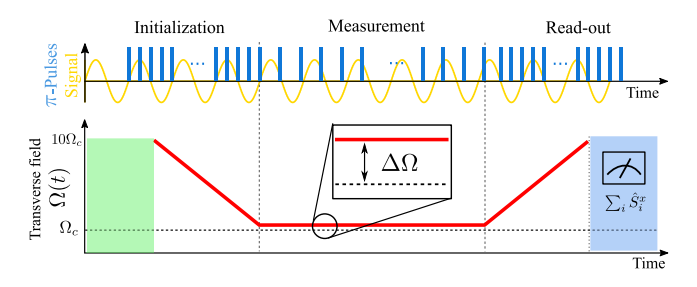


FIG. 32. Schematic diagram of entanglement-enhanced sensing protocol. During the initialization, measurement, and readout steps, the amplitude of a transverse magnetic field Ω and the repetition frequency of additional transverse magnetic field π pulses are tuned. In the initialization stage, a correlated many-body spin state is generated as Ω is decreased toward a quantum critical point at $\Omega_{\rm C}$. At the end of the measurement period, an axial ac magnetic field signal is mapped onto the total magnetization of the ensemble, which for NV⁻ centers can be detected using conventional readout. From Choi, Yao, and Lukin, 2017b.

external noise. That is, if the coherence time T_2 is separated into contributions from NV⁻-NV⁻ dipolar interactions and from other noise (including spin-lattice relaxation) as

$$\frac{1}{T_2} = \frac{1}{T_2 \{\text{NV}^--\text{NV}^-\}} + \frac{1}{T_2 \{\text{other}\}},$$
 (36)

then the entangled state's coherence time \bar{T}_2 is only a function of $T_2\{\text{other}\}$. Therefore, when NV⁻-NV⁻ interactions dominate, \bar{T}_2 may be comparable to or exceed T_2 , yielding improved ac magnetic field sensitivity via both the increased coherence time and reduced readout noise.

However, when the noise on each spin in the entangled ensemble is independent, \bar{T}_2 is expected to diminish linearly with the number of entangled spins N (i.e., $\bar{T}_2 \propto 1/N$), which at best cancels the sensitivity enhancement obtained from the $1/\sqrt{N}$ reduction in spin-projection noise compared to the standard quantum limit. Even without improved ac magnetic sensitivity, the scheme is expected to provide an increased measurement bandwidth by enabling faster field sampling than conventional sensing. When the dominant noise limiting the NV⁻ ensemble's spin coherence time is instead set by spatially correlated noise, such as dipolar interactions with nearby magnetic dipoles of a different species (Choi, Yao, and Lukin, 2017b), enhanced ac magnetic field sensitivity from reduced spin-projection noise may again be possible. Although the protocol may also be compatible with broadband dc magnetometry, the scaling of the correlated ensemble's effective T_2^* with entangled number of spins N remains unclear. Further investigation is required to determine if this protocol could yield a sensitivity improvement over conventional dc magnetometry.

While the approach proposed by Choi, Yao, and Lukin (2017b) represents an important milestone toward magnetometry enhanced by NV--NV- dipolar interactions, the protocol is expected to be challenging to execute. First, the mean NV⁻-NV⁻ separation distance $\langle r_{NV^-,NV^-} \rangle$ must be small compared to the average distance to the nearest paramagnetic defect $\langle r_{\text{NV-other}} \rangle$, but large compared to the thickness L of any (quasi-)two-dimensional NV⁻ layer, i.e., $\langle r_{\rm NV^-,other} \rangle >$ $\langle r_{\rm NV^-,NV^-} \rangle > L$. This hierarchy indicates that for a typical NV⁻-rich diamond with $\langle r_{\rm NV^- \, NV^-} \rangle \sim 10$ nm, the NV⁻ layer thickness L should be less than a few nanometers. Shallow nitrogen implantation into diamond (Pham et al., 2011; Glenn et al., 2017) or nitrogen delta-doping during CVD growth (Ohno et al., 2012; Osterkamp et al., 2015) can yield layers that approach the appropriate thickness. Crucially, this 2D requirement restricts the practical NV⁻ ensemble size, which may limit achievable sensitivity (see Sec. II.C and the Appendix, Sec. 3) when considering wide-field imaging and bulk magnetometry applications. Second, since the preparation and readout steps require a slow adiabatic field ramp, the practical requirement that these steps occur within time \bar{T}_2 limits the degree of achievable entanglement. Consequently, the protocol will most likely entangle subensembles much smaller than the total ensemble size. Disorder (i.e., static field inhomogeneity) in the ensemble, e.g., from the random positioning of NV⁻ centers, also restricts the maximum entangled subensemble size. Both of these mechanisms are expected to increase the measurement's spin-projection noise above the Heisenberg limit, further restricting the parameter regime where sensitivity enhancements are possible. In spite of the serious challenges and limitations, the proposed technique remains a promising first step toward practical schemes harnessing the full quantum nature of NV⁻ ensembles for sensitivity enhancement.

Additionally, with entangled and individually addressable spins, a wealth of proposed quantum error correction (QEC) sensing schemes may become more experimentally feasible (Kessler et al., 2014; Waldherr et al., 2014; Bonato et al., 2016; Cramer et al., 2016; Unden et al., 2016; Layden and Cappellaro, 2018; Layden et al., 2019). QEC protocols mitigate certain relaxation mechanisms by encoding quantum information into redundant degrees of freedom (Degen, Reinhard, and Cappellaro, 2017). Certain OEC implementations have already shown extension of NV- spin coherence (Unden et al., 2016), although all demonstrations so far have employed at most a handful of spins. To date, most QEC studies concentrate on methods to correct noise along a different axis from the signal (e.g., errors that cause spin flips rather than dephasing), limiting their use for extending T_2^* or T_2 . Recently, however, QEC schemes to correct dephasing-type errors have been proposed (Layden and Cappellaro, 2018; Layden et al., 2019).

In the near future, ensemble-NV⁻ sensing at the standard quantum limit is likely to outperform entanglement-enhanced schemes, as argued by Braun *et al.* (2018). Nonetheless, further development of these techniques remains an important endeavor toward enabling long-term sensitivity improvements approaching fundamental limits.

VIII. CONCLUSION AND OUTLOOK

The recent excitement accompanying quantum sensing with nitrogen-vacancy centers in diamond is well motivated, as NV-diamond sensors promise many advantages over alternative sensing technologies. NV⁻ centers provide precision and repeatability similar to atomic systems in a robust solid-state package with less experimental complexity. Furthermore, NV⁻-based devices can operate under ambient conditions and record spatial variations at length scales inaccessible to most other quantum sensors.

Efforts to optimize performance of ensemble-NV⁻ sensors are particularly warranted, as these devices at present have greater potential for improvement than other NV⁻ sensing platforms. Historically, the NV-diamond community has focused on optimizing few- or single-NV⁻ sensors, while the best demonstrated ensemble-NV⁻ devices exhibit sensitivities orders of magnitude away from theoretical limits (Taylor *et al.*, 2008).

Consequently, this work provides a comprehensive survey of methods for optimizing broadband magnetometry from dc to $\sim 100~\rm kHz$ using ensembles of NV⁻ centers. We explore strategies to enhance sensitivity toward physical limits, both through highlighting key parameters (Sec. II.C) and through evaluating proposed methods to improve those parameters. After identifying Ramsey magnetometry as the most promising sensing protocol (Secs. II.A and II.B), we focus on understanding and improving the spin dephasing time T_2^* (Secs. III

and IV), the spin readout fidelity $\mathcal{F} \equiv 1/\sigma_R$ (Sec. V), and the host diamond material properties (Sec. VI). Next we summarize our analyses within these broad categories, and we recommend areas where future study could lead to improvements in magnetometer sensitivity and performance.

Measurements employing Ramsey-type protocols with NV^- ensembles are limited by T_2^* , which presently remains orders of magnitude shorter than the physical limit of $2T_1$. The magnetic field sensitivity improves nearly linearly with T_2^* extension when the measurement overhead time is significant $(t_0 \gtrsim T_2^*)$, as is common for present-day ensemble-NV⁻ magnetometers. Therefore, this work focuses on understanding limitations to T_2^* and methods to extend T_2^* in NV-rich diamonds. Among the factors limiting T_2^* are magnetic-field, electric-field, and strain gradients. External bias-magneticfield gradients may be mitigated through experimental design. Whereas internal strain and electric-field gradients can be more difficult to eliminate outright, the NV⁻ ensemble can be made insensitive to such gradients through operation at sufficiently strong bias magnetic fields (Sec. IV.D) and employment of double-quantum coherence magnetometry (Sec. IV.B). Ensemble-NV⁻ T_2^* values may also be limited by dipolar interactions with the diamond's inhomogeneous paramagnetic spin bath. We determine the individual contributions to T_2^* from substitutional nitrogen N_S^0 electronic spins (Sec. III.D), ¹³C nuclear spins (Sec. III.F), and NV⁻ spins (Sec. III.G). Recent experiments determine T_2 and T_2^* dependencies on nitrogen concentration to better than 10% (Bauch et al., 2018, 2019). We suggest reducing the unwanted bath-spin concentrations through (i) diamond growth using isotopically purified ¹²C (Sec. III.F), and (ii) diamond treatment via optimized electron irradiation and annealing procedures (Sec. VI). We also identify spin-bath driving using strong, resonant rf fields as an effective measure to decouple N_s⁰ and other impurity spins from the NV⁻ ensemble (Sec. IV.C). Recent work implementing spin-bath driving combined with double-quantum coherence magnetometry in NV^- ensembles demonstrates T_2^* extension by more than 16 times (Bauch et al., 2018). We expect continued progress on this front; one avenue opened up when T_2^* is increased to the NV--NV- dipolar interaction limit is the exploration of enhanced sensing techniques harnessing quantum entanglement (Choi, Yao, and Lukin, 2017b); see Sec. VII.D.

In Sec. V we survey existing techniques to improve ensemble-NV⁻ readout fidelity $\mathcal{F} = 1/\sigma_R$, which, for conventional fluorescence-based readout, is currently limited to ~0.015; see Table II. We analyze methods that allow readout fidelities for single NV- centers and small ensembles in nanodiamonds to approach the spin-projection limit, including spin-to-charge conversion readout (Sec. V.A) and ancillaassisted repetitive readout (Sec. V.C). However, no demonstrated method has substantially outperformed conventional fluorescence-based readout for large NV- ensembles; see Table II. Nonetheless, we anticipate that with careful experimental design and advances in diamond-sample engineering, fidelity-enhancement methods so far limited to single spins or small ensembles may be extended to large NV- ensembles. Additionally, given that any method employing optical readout benefits from increased collection efficiency, such optimizations (Sec. V.E) remain worthwhile for improving magnetometer sensitivity.

As optimal sensing techniques require codevelopment with diamond samples tailored to these techniques, this work reviews diamond fabrication and relevant material properties in Sec. VI. In particular, we focus on methods to engineer lab-grown diamond samples optimized for ensemble-NV magnetometry. We analyze growth via chemical vapor deposition, high-pressure-high-temperature synthesis, and mixedsynthesis methods (Sec. VI.C). We examine how diamond synthesis and treatment can be used to engineer high N-to-NV conversion efficiencies $E_{\rm conv}$, and we investigate methods to improve and stabilize the charge-state efficiency $\zeta = [NV^-]/$ [NV^T] (Sec. VI.B). We also investigate undesired defects commonly found in NV-rich diamond samples (Sec. VI.F). These defects, including multivacancy clusters and hydrogenrelated impurities, may both trap charges in the diamond and contribute to the dipolar spin bath, reducing both E_{conv} and T_2^* .

Although present understanding of diamond synthesis, treatment, and characterization is extensive and spans multiple decades, further work is needed to reproducibly create NV-rich diamond samples with low strain, low concentrations of unwanted impurities, and high NV- concentrations. In particular, advancing diamond materials science to enable longer native T_2^* values is a worthwhile pursuit; e.g., although the NV⁻ center's sensitivity to strain can be reduced (Secs. IV.B and IV.D), employing low-strain host diamonds is preferable regardless. Importantly, a robust and optimized protocol for diamond irradiation and annealing that takes nitrogen concentration into account should be established (Secs. VI.D and VI.E). Furthermore, widespread access to high-quality scientific diamonds is imperative and would greatly accelerate advances in NV-diamond-related research. Presently, diamonds with natural carbon isotopic abundance, suboptimal nitrogen concentrations, and undesired strain and surface characteristics are widely employed by the community solely because most research groups lack access to optimized diamond samples.

In addition, many aspects of NV physics, and charge dynamics for ensembles, in particular, remain poorly understood and warrant further investigation. We anticipate that additional knowledge could be harnessed to improve sensor performance, similar to how the study of NV⁻ and NV⁰ ionization characteristics under low optical intensity by Aslam et al. (2013) prompted the development of spin-to-charge conversion readout. Further examination of charge dynamics under magnetometer operating conditions (e.g., high optical intensity) is expected to yield fruitful insight. For NV-rich diamonds, systematic studies of (i) NV⁻ ionization (from both the singlet and triplet excited states), and (ii) recombination from the NV⁰ excited state versus optical wavelength and intensity would be particularly useful. Such studies would address present knowledge gaps and could inform diamondengineering protocols to better stabilize the NV⁻ charge state in ensemble-based devices. These investigations could also lay the groundwork for new sensitivity-enhancement techniques tailored to ensembles. In addition, continued basic research into the NV⁻ center is warranted. For example, while four electronic states of NV- have been observed, two additional predicted states have not yet been experimentally confirmed (Jensen, Kehayias, and Budker, 2017).

We also expect unanticipated creative ideas to emerge that further enhance readout fidelity, dephasing time T_2^* , and overall magnetic field sensitivity. Ensemble-NV⁻ magnetometers are already relevant in wide-varying sensing applications, thanks to key advances made over the past decade, which we have summarized here. Moreover, NV-diamond quantum sensing is a quickly developing platform, well positioned to continue improving, with significant advancements possible before fundamental limits are reached. By combining the knowledge collected here with likely future advances, we expect further expansion of applications of quantum sensors based on NV⁻ ensembles in diamond.

LIST OF SYMBOLS AND ABBREVIATIONS

CPMG	Carr-Purcell-Meiboom-Gill		
	(pulse sequences)		
cw	continuous wave		
CVD	chemical vapor deposition		
DEER	double electron-electron reso-		
	nance		
DQ	double quantum		
EPR	electron paramagnetic resonance		
ESR	electron spin resonance		
FID	free induction decay		
GSLAC	ground-state level anticrossing		
HPHT	high-pressure-high-temperature		
LAC	level anticrossing		
LPHT	low-pressure-high-temperature		
MW	microwave		
NIR	near infrared		
NMR	nuclear magnetic resonance		
NQR	nuclear quadrupole resonance		
ODMR	optically detected magnetic		
	resonance		
PDMR	photoelectrically detected mag-		
	netic resonance		
PE	photoelectric (readout)		
PL	photoluminescence		
rf	radio frequency		
SCC	spin-to-charge conversion		
SQ	single quantum (standard basis)		
T_1	longitudinal (spin-lattice) relax-		
	ation time, s		
T_2	coherence time (transverse re-		
	laxation time), s		
T_2^*	dephasing time (free-induction-		
	decay time), s		
$T_2^{* \text{single}}$	single-NV ⁻ dephasing time, s		
η	magnetic field sensitivity, T/\sqrt{Hz}		
τ	interrogation time (free-		
	precession time for Ramsey), s		
t_I, t_R, t_O	initialization, readout, and over-		
	head time, s; $t_O \equiv t_I + t_R$		

	structured armomential more mater
p D D	stretched exponential parameter static (bias) and microwave
B_0, B_1	magnetic field, T
v	electronic spin gyromagnetic ra-
γ_e	tio, s ⁻¹ /T; $\equiv g_e \mu_B / \hbar$
$\mathcal F$	readout fidelity; $\equiv 1/\sigma_R$
σ_R	factor above spin-projection
O K	noise; $\equiv 1/\mathcal{F}$
Ω_R	Rabi frequency, s ⁻¹
$\nu, \Delta \nu$	ODMR center frequency and
-,	linewidth, Hz
Γ	dephasing or decay rate, s ⁻¹
C	measurement contrast (fringe
	visibility)
$C_{\rm cw}, C_{\rm pulsed}$	cw-ODMR contrast, pulsed
·	ODMR contrast
N	number of sensors (NV ⁻ centers
	in ensemble)
n_{avg}	average collected photons per
	readout per NV ⁻
\mathcal{N}	average collected photons per
	readout from an NV ⁻ ensemble
[X]	concentration of species X ,
	cm ⁻³ or ppm
$[NV^{-}], [NV^{0}],$	negative, neutral, and total NV
and [NV ^T]	concentration, cm ⁻³ or ppm
$[N^T]$	total nitrogen concentration in
D.10.1 D.1.	the lattice, cm ⁻³ or ppm
$[N_S^0], [N_S^+],$	neutral, positive, and total sub-
and $[N_S^T]$	stitutional nitrogen concentra-
T*(V)	tions, cm ⁻³ or ppm
$T_2^*\{X\}$	contribution to T_2^* from mechanism Y_1 s
A .	nism X , s dipolar interaction strength be-
$A_{ m N_S^0}$	-
A	tween N _S ⁰ and NV ⁻ , s ⁻¹ /ppm
$A_{^{13}\mathrm{C}}$	dipolar interaction strength be-
$A_{ ext{NV}_{\parallel}^-}$	tween ¹³ C and NV ⁻ , s ⁻¹ /ppm
$\Delta_{NV_{-}}$	dipolar interaction strength be- tween NV ⁻ spins in the same
	group (same resonance fre-
A	quency), s ⁻¹ /ppm
$A_{ ext{NV}_{rac{1}{2}}}$	dipolar interaction strength be-
	tween NV ⁻ spins in different
	groups (different resonance
D .	frequencies), s ⁻¹ /ppm
$B_{ m N_S^0}$	proportionality factor for N_S^0
11	contribution to T_2 , s ⁻¹ /ppm
H S m	Hamiltonian, J
S, m_s	electronic spin, electronic spin
I, m_I	projection nuclear spin, nuclear spin
1, 1111	projection spin, nuclear spin
	projection

$\{ 0\rangle, -1\rangle, +1\rangle\}$	NV ⁻ ground-state spin eigen- states
D	zero field splitting parameter,
	Hz; ≈2.87 GHz
\mathcal{M}_z , \mathcal{M}_x , \mathcal{M}_y , \mathcal{N}_x ,	spin-strain coupling parameters,
and \mathcal{N}_{y}	Hz
E_x , E_y , and E_z	electric-field components, V/m
d_{\perp},d_{\parallel}	NV- transverse, axial (longi-
— II	tudinal) electric dipole moment,
	Hz/(V/m)
ξ_{\perp}	transverse strain and electric-
•=	field coupling parameter, Hz
β_z	axial magnetic-field coupling
7.4	parameter, Hz; $\equiv (g\mu_B/h)B_z$
$E_{\rm conv}$	total N-to-NV ⁻ conversion effi-
Conv	ciency; $\equiv [NV^-]/[N^T]$
	2 3, 2 3
χ	N-to-NV conversion efficiency;
	$\equiv [NV^T]/[N^T]$
ζ	NV-to-NV ⁻ charge-state effi-
	ciency; $\equiv [NV^-]/[NV^T]$

ACKNOWLEDGMENTS

J. F. B., J. M. S., and E. B. contributed equally to this work. The authors thank Eisuke Abe, Victor Acosta, Ashok Ajoy, Scott Alsid, Keigo Arai, Nithya Arunkumar, Ania Bleszynski-Jayich, Dolev Bluvstein, Danielle Braje, Dominik Bucher, Alexei Bylinskii, Paola Cappellaro, Soonwon Choi, Colin Connolly, Alexandre Cooper, Andrew Edmonds, Michael Geis, David Glenn, Ben Green, Kohei Itoh, Jean-Christophe Jaskula, Pauli Kehayias, Mark Ku, Junghyun Lee, David Le Sage, Igor Lovchinsky, Matthew Markham, Claire McLellan, Idan Meirzada, Gavin Morley, Mark Newton, Michael O'Keeffe, David Phillips, Emma Rosenfeld, Brendan Shields, Swati Singh, Matthew Steinecker, and Daniel Twitchen for helpful comments and discussions. This material is based upon work supported by, or in part by, the U.S. Army Research Laboratory and the U.S. Army Research Office under Grant No. W911NF-15-1-0548; the National Science Foundation (NSF) Electronics, Photonics and Magnetic Devices (EPMD) program under Grant No. ECCS-140875; the NSF Physics of Living Systems (PoLS) program under Grant No. PHY-1504610; the NSF Integrated Support Promoting Interdisciplinary Research and Education (INSPIRE) programs under Grant No. EAR-1647504; the Air Force Office of Scientific Research Award No. FA9550-17-1-0371; the Defense Advanced Research Projects Agency Quantum Assisted Sensing and Readout (DARPA QuASAR) program under Contract No. HR0011-11-C-0073; and Lockheed Martin under Contract No. A32198. J. M. S. was partially supported by a Fannie and John Hertz Foundation Graduate Fellowship and a NSF Graduate Research Fellowship under Grant No. 1122374.

APPENDIX

1. Derivations

a. Ramsey dc magnetic field measurement

The following is a derivation of a Ramsey-type pulsed magnetometry sequence (see Fig. 7) using a magnetic dipole moment. Here the magnetic moment is taken to be an NVcenter's ground-state electronic spin, although this discussion applies to any two-level system sensitive to magnetic fields, including atomic vapors and other solid-state defects. Although the NV- ground-state spin is a triplet with S=1, a bias magnetic field B_0 can be applied along the NV⁻ symmetry axis to split the $m_s = +1$ and $m_s = -1$ energy levels so that resonant MWs may selectively drive the $m_s = 0$ to $m_s = +1$ (or $m_s = 0$ to $m_s = -1$) transition. Any off-axis magnetic-field component B_{\perp} can be ignored so long as $(\gamma_e B_\perp)^2 / [(2\pi D)^2 \pm (\gamma_e B_0)^2] \ll 1$, where D = 2.87 GHz is the zero-field splitting and $\gamma_e = g_e \mu_B / \hbar$ is the gyromagnetic ratio of the NV- electronic spin. Here the NV- center's nuclear spin is also ignored, as well as static electric fields or strain. We describe this two-level subspace as a pseudo-spin-1/2 system with $|m_s = +1\rangle = |\downarrow\rangle$, $|m_s = 0\rangle = |\uparrow\rangle$, and the Hamiltonian

$$\begin{split} H &= (2\pi D + \gamma_e B) S_z \\ &= \frac{\hbar}{2} \binom{2\pi D + \gamma_e B}{0} \frac{0}{-2\pi D - \gamma_e B}, \end{split} \tag{A1}$$

expressed in the $\{|\downarrow\rangle, |\uparrow\rangle\}$ basis, where we take S_z to be the spin-1/2 z-projection operator with units of $\hbar/2$; and $B=B_0+B_{\rm sense}$ is the total magnetic field projection along the NV⁻ symmetry axis (the z axis), which is the sum of the applied bias field and an unknown dc field to be sensed. Here terms in the Hamiltonian proportional to the identity matrix have been dropped, as they introduce only a global phase to the states' time evolution. In the bias field B_0 the spin resonance frequency is $\omega_0=2\pi D+\gamma_e B_0$. Spin operators are expressed in the S_z basis in terms of the Pauli matrices $\vec{S}=(\hbar/2)\vec{\sigma}$, yielding

$$H = \frac{\hbar\omega_0}{2}\sigma_z + \frac{\hbar}{2}\gamma_e B_{\text{sense}}\sigma_z. \tag{A2}$$

As described herein, a Ramsey sequence consists of two $\pi/2$ pulses of an oscillating magnetic field resonant with the transition between $|\uparrow\rangle$ and $|\downarrow\rangle$, which are separated by a free-precession time τ . The sequence begins at time t=0, with the spin polarized to $|\psi(0)\rangle = |\uparrow\rangle$. An oscillating magnetic field oriented perpendicular to the NV⁻ symmetry axis $\vec{B}_1(t) = B_1\cos(\omega t)\hat{y}$ with angular frequency $\omega\approx\omega_0$ is turned on abruptly. Without loss of generality \vec{B}_1 is assumed to be polarized along the y axis. For $B_1\gg B_{\rm sense}$, the second term in H can be dropped, thereby ignoring effects of the unknown dc sensing field while the oscillating field is on. The Hamiltonian for the system driven by this oscillating field, denoted $H_{\rm driv}$, becomes

$$H_{\rm driv} = \frac{\hbar\omega_0}{2}\sigma_z + \frac{\hbar}{2}\gamma_e B_1 \cos(\omega t)\sigma_y. \tag{A3}$$

We proceed in the interaction picture, with

$$H_0 = \frac{\hbar \omega_0}{2} \sigma_z \tag{A4}$$

and

$$H_1 = \frac{\hbar}{2} \gamma_e B_1 \cos(\omega t) \sigma_y. \tag{A5}$$

This step is equivalent to transforming into a rotating frame with angular frequency ω_0 . The interaction-picture state vector $|\tilde{\psi}(t)\rangle$ is defined in terms of the Schrödinger-picture state vector $|\psi(t)\rangle$ as $|\tilde{\psi}(t)\rangle = U_0^\dagger(t)|\psi(t)\rangle$ with $U_0(t) = e^{-iH_0t/\hbar}$. This state evolves according to $|\tilde{\psi}(t)\rangle = \tilde{U}_1(t)|\tilde{\psi}(0)\rangle$ where $\tilde{U}_1(t) = e^{-i\tilde{H}_1t/\hbar}$, with

$$\begin{split} \tilde{H_1} &= U_0^\dagger(t) H_1 U_0(t) \\ &= \frac{\hbar}{4} \gamma_e B_1 \\ &\times \begin{pmatrix} 0 & -i (e^{i(\omega_0 + \omega)t} + e^{i(\omega_0 - \omega)t}) \\ i (e^{-i(\omega_0 - \omega)t} + e^{-i(\omega_0 + \omega)t}) & 0 \end{pmatrix}. \end{split} \tag{A6}$$

The transformed interaction Hamiltonian \tilde{H}_1 is simplified by assuming resonant driving of the spin with $\omega = \omega_0$ and by making the rotating wave approximation, dropping off-resonant terms rotating at $2\omega_0$, to yield

$$\tilde{H}_{1} \approx \frac{\hbar}{4} \gamma_{e} B_{1} \sigma_{y}. \tag{A7}$$

This Hamiltonian causes the spin system to undergo Rabi oscillations at angular frequency $\Omega = \gamma_e B_1/2$. The oscillating field $\vec{B}_1(t)$ is turned off abruptly after a duration

$$\tau_{\pi/2} = \frac{\pi}{2\Omega} = \frac{\pi}{\gamma_e B_1},\tag{A8}$$

so that

$$\begin{split} |\tilde{\psi}(\tau_{\pi/2})\rangle &= \exp\left(-i\frac{\gamma_e B_1 \sigma_y \tau_{\pi/2}}{4}\right) |\tilde{\psi}(0)\rangle \\ &= \exp\left(-i\frac{\pi}{4}\sigma_y\right) |\uparrow\rangle \\ &= \frac{1}{\sqrt{2}} \begin{pmatrix} 1 & -1 \\ 1 & 1 \end{pmatrix} \begin{pmatrix} 0 \\ 1 \end{pmatrix} \\ &= \frac{1}{\sqrt{2}} (-|\downarrow\rangle + |\uparrow\rangle), \end{split} \tag{A9}$$

which uses the identity $e^{-i\theta\hat{n}\cdot\vec{\sigma}} = \cos(\theta)I - i\sin(\theta)(\hat{n}\cdot\vec{\sigma})$, where \hat{n} is a unit vector on the Bloch sphere. This constitutes a $\pi/2$ pulse on the spin.

Next the magnetic moment undergoes free precession in the absence of $\vec{B}_1(t)$ for a sensing time τ . During this time the system Hamiltonian returns to H from Eq. (A1). We continue to use the interaction picture with

$$H_0 = \frac{\hbar \omega_0}{2} \sigma_z, \tag{A10}$$

and with new interaction Hamiltonian H_1' determined by $\vec{B}_{\rm sense} = B_{\rm sense} \hat{z}$ as

$$H_1' = \frac{\hbar}{2} \gamma_e B_{\text{sense}} \sigma_z. \tag{A11}$$

Recognizing that H_1' commutes with H_0 , the transformed interaction Hamiltonian $\tilde{H}_1' \equiv U_0^{\dagger}(t)H_1'U_0(t) = H_1'$, and thus the interaction-picture state vector $|\tilde{\psi}(t)\rangle$ evolves under H_1' into

$$\begin{split} |\tilde{\psi}(\tau_{\pi/2} + \tau)\rangle &= e^{-iH'_1\tau/\hbar} |\tilde{\psi}(\tau_{\pi/2})\rangle \\ &= \frac{1}{\sqrt{2}} (-e^{-i\phi/2} |\downarrow\rangle + e^{i\phi/2} |\uparrow\rangle), \end{split} \tag{A12}$$

where

$$\phi = \gamma_e B_{\text{sense}} \tau \tag{A13}$$

is the phase accumulated due to $B_{\rm sense}$ in the interaction picture. (If $B_{\rm sense}=0$, the state vector $|\tilde{\psi}(t)\rangle$ accumulates no phase, as H_1' vanishes and the entire Hamiltonian $H=H_0$.)

To complete the sequence, a second oscillating field $\vec{B}_2(t) = \vec{B}_2 \cos(\omega t)$, again with $\omega = \omega_0$, is applied for a $\pi/2$ pulse. As with the first $\pi/2$ pulse, $B_{\rm sense} \ll B_2$ is assumed so that additional spin state evolution due to $B_{\rm sense}$ can be ignored. The polarization of $\vec{B}_2(t)$ is chosen to be along \hat{n} in the x-y plane at an angle θ with respect to \hat{y} , the polarization direction of the first $\pi/2$ pulse $\vec{B}_1(t)$. After again making the rotating wave approximation, the transformed interaction Hamiltonian, \tilde{H}_1'' is given by

$$\tilde{H}_{1}^{"} \approx \frac{\hbar}{4} \gamma_{e} B_{2} [\cos(\vartheta) \sigma_{y} - \sin(\vartheta) \sigma_{x}]$$
 (A14)

and

$$\begin{split} |\tilde{\psi}(\tau_{\pi/2} + \tau + \tau_{\pi/2})\rangle \\ &= e^{-i\tilde{H}_1''\tau_{\pi/2}/\hbar} |\tilde{\psi}(\tau_{\pi/2} + \tau)\rangle \\ &= \frac{1}{\sqrt{2}} \begin{pmatrix} 1 & -e^{-i\vartheta} \\ e^{i\vartheta} & 1 \end{pmatrix} \frac{1}{\sqrt{2}} \begin{pmatrix} -e^{-i\phi/2} \\ e^{i\phi/2} \end{pmatrix}, \quad (A15) \end{split}$$

which, up to a global phase, is equal to

$$|\tilde{\psi}\rangle = \cos\left(\frac{\phi - \theta}{2}\right)|\downarrow\rangle + ie^{i\theta}\sin\left(\frac{\phi - \theta}{2}\right)|\uparrow\rangle.$$
 (A16)

The phase accumulated during τ is thus mapped on to a population difference between the $|\downarrow\rangle$ and $|\uparrow\rangle$ states. The population difference is detected by measuring the rotating-frame observable \tilde{S}_z , which is equal to the fixed-frame spin-projection operator S_z , as S_z commutes with H_0 . The value of B_{sense} is determined by relating this measured observable to ϕ :

$$\begin{split} \langle S_z \rangle &= \frac{\hbar}{2} \langle \tilde{\psi} | \sigma_z | \tilde{\psi} \rangle \\ &= \frac{\hbar}{2} \left[\cos^2 \left(\frac{\phi - \vartheta}{2} \right) - \sin^2 \left(\frac{\phi - \vartheta}{2} \right) \right] \\ &= \frac{\hbar}{2} \cos(\phi - \vartheta) \\ &= \frac{\hbar}{2} \cos(\gamma_e B_{\text{sense}} \tau - \vartheta). \end{split} \tag{A17}$$

The cosinusoidal fluctuations in $\langle S_z \rangle$ are termed Ramsey fringes. Common choices of ϑ are 0 and $\pi/2$. The case where $\vartheta=0$ (respectively, $\vartheta=\pi/2$) is commonly called cosine (sine) magnetometry, as the observable $\langle S_z \rangle$ varies as the cosine (sine) of $B_{\rm sense}$ for fixed τ . For ensembles of NV⁻ centers, $\langle S_z \rangle$ is measured by reading out the spin-state-dependent fluorescence over a predetermined readout window of several hundred nanoseconds (see Fig. 6), as discussed in Sec. II.A and later in the Appendix, Sec. 1.c.

For small $B_{\rm sense}$ such that $\phi \ll 2\pi$, Eq. (A17) can be linearized about $\phi = 0$ for any value of ϑ except $\vartheta = 0$. The values of $B_{\rm sense}$ and ϕ can then be related to a small change in the observable $\delta \langle S_z \rangle = \langle S_z \rangle|_{\phi} - \langle S_z \rangle|_{0}$ as follows:

$$\begin{split} B_{\text{sense}} &= \frac{\phi}{\gamma_e \tau} \approx \frac{1}{\gamma_e \tau} \frac{\delta \langle S_z \rangle}{[d \langle S_z \rangle / d\phi]|_0} \\ &\approx \frac{1}{\gamma_e \tau} \frac{(2/\hbar) \langle S_z \rangle|_{\phi} - \cos(\vartheta)}{\sin(\vartheta)}. \end{split} \tag{A18}$$

For $\theta = \pi/2$, the slope of the Ramsey fringe is maximized, and Eq. (A18) reduces to

$$B_{\rm sense} \approx \frac{2}{\hbar \gamma_e \tau} \langle S_z \rangle.$$
 (A19)

For $\theta=0$, where the linearization method fails, the linear term $\delta\langle S_z\rangle$ vanishes, as the slope of the Ramsey fringe goes to zero; a small $B_{\rm sense}$ produces to lowest order a quadratic change in $\langle \tilde{S}_z \rangle$.

b. Spin-projection-noise-limited sensitivity

The spin-projection-noise-limited magnetic field sensitivity is defined as the field δB at which the size of the signal $\delta \langle S_z \rangle$ due to δB is equal to the uncertainty in the signal, i.e., when $\delta \langle S_z \rangle = \Delta S_z$, where $\Delta S_z = \sqrt{\langle S_z^2 \rangle - \langle S_z \rangle^2}$ is the standard deviation of a series of identical measurements of δB . From Eq. (A18) assuming precession time τ , this minimum field is

$$\delta B_{\rm sp} = \frac{1}{\gamma_e \tau} \frac{\Delta S_z}{|d\langle S_z \rangle / d\phi|}.$$
 (A20)

When M uncorrelated consecutive measurements are taken, each with precession time τ over a total measurement time $t_{\rm meas}$, the minimum field is modified by the factor $\sqrt{1/M} = \sqrt{\tau/t_{\rm meas}}$, yielding

$$\delta B_{\rm sp} = \frac{1}{\gamma_e} \frac{1}{\sqrt{\tau t_{\rm meas}}} \frac{\Delta S_z}{|d\langle S_z\rangle/d\phi|}.$$
 (A21)

The spin-projection-noise-limited sensitivity of a Ramsey magnetometry measurement is then

$$\eta_{\rm sp} = \delta B_{\rm sp} \sqrt{t_{\rm meas}} = \frac{1}{\gamma_e \sqrt{\tau}} \frac{\Delta S_z}{|d\langle S_z \rangle/d\phi|}.$$
(A22)

The quotient $\Delta S_z/|d\langle S_z\rangle/d\phi|$ is calculated as follows:

$$\langle S_z \rangle = \frac{\hbar}{2} \cos(\phi - \vartheta),$$
 (A23)

$$\frac{d\langle S_z \rangle}{d\phi} = -\frac{\hbar}{2}\sin(\phi - \theta),\tag{A24}$$

$$\langle S_z^2 \rangle = \frac{\hbar^2}{4} \langle \tilde{\psi} | \sigma_z^2 | \tilde{\psi} \rangle$$

$$= \frac{\hbar^2}{4} \left[\cos^2 \left(\frac{\phi - \vartheta}{2} \right) + \sin^2 \left(\frac{\phi - \vartheta}{2} \right) \right]$$

$$= \frac{\hbar^2}{4}, \qquad (A25)$$

$$\Delta S_z = \sqrt{\langle S_z^2 \rangle - \langle S_z \rangle^2}$$

$$= \sqrt{\frac{\hbar^2}{4} \left[1 - \cos^2 (\phi - \vartheta) \right]}$$

$$= \frac{\hbar}{2} |\sin(\phi - \vartheta)|, \qquad (A26)$$

$$\frac{\Delta S_z}{|d\langle S_z \rangle / d\phi|} = 1. \qquad (A27)$$

Equation (A27) illustrates that the signal-to-noise ratio of a spin-projection-noise-limited measurement is independent of the value of ϕ or ϑ . The projection noise ΔS_z is exactly equal to the slope of the Ramsey fringe $|d\langle S_z\rangle/d\phi|$. As a result, a magnetometer limited by spin-projection noise has the same sensitivity regardless of where on the Ramsey fringe the measurement is taken, which is given by

$$\eta_{\rm sp} = \delta B_{\rm sp} \sqrt{t_{\rm meas}} = \frac{1}{\gamma_{\rm e} \sqrt{\tau}}.$$
(A28)

For sensing with an ensemble of N independent spins, the sensitivity $\eta_{\rm sp}^{\rm ensemble}=\eta_{\rm sp}/\sqrt{N}$ such that

$$\eta_{\rm sp}^{\rm ensemble} = \frac{1}{\gamma_e \sqrt{N\tau}}.$$
(A29)

c. Photon-shot-noise-limited sensitivity

The previous discussion considered a direct measurement of S_z . The measurement technique for NV⁻ spins, optical readout, instead indirectly probes the spin through measuring the spin-state-dependent fluorescence. Shot noise in the collected fluorescence must be incorporated into the measurement uncertainty and sensitivity.

To phenomenologically introduce Poisson fluctuations from the fluorescence photons into the sensitivity, the optical readout procedure is treated as a mapping of the spin eigenstates onto two light field modes: $|m_s=+1\rangle=|\downarrow\rangle\rightarrow|\beta\rangle$ and $|m_s=0\rangle=|\uparrow\rangle\rightarrow|\alpha\rangle$, where $|\alpha\rangle$ and $|\beta\rangle$ are coherent

states defined by $\hat{a}|\alpha\rangle = \alpha|\alpha\rangle$ and $\hat{b}|\beta\rangle = \beta|\beta\rangle$. We define $a = |\alpha|^2$ as the mean number of photons in $|\alpha\rangle$ and $b = |\beta|^2$ as the mean number of photons in $|\beta\rangle$. Since the $|m_s = 0\rangle$ state produces more fluorescent photons during readout than the $|m_s = +1\rangle$ state, a > b. The final spin state $|\tilde{\psi}\rangle$ from Eq. (A16) is mapped onto the photon field state

$$|\psi_{\rm ph}\rangle = \cos\left(\frac{\phi - \theta}{2}\right)|\beta\rangle + ie^{i\theta}\sin\left(\frac{\phi - \theta}{2}\right)|\alpha\rangle.$$
 (A30)

A measurement of the spin state has become a measurement of the number of photons collected from the two light fields $\hat{N} = \hat{a}^{\dagger} \hat{a} + \hat{b}^{\dagger} \hat{b}$. Defining $\varphi = \phi - \vartheta$,

$$\begin{split} \langle \hat{N} \rangle &= \langle \psi_{\text{ph}} | (\hat{a}^{\dagger} \hat{a} + \hat{b}^{\dagger} \hat{b}) | \psi_{\text{ph}} \rangle \\ &= b \cos^{2} \left(\frac{\varphi}{2} \right) + a \sin^{2} \left(\frac{\varphi}{2} \right) \\ &= b \left(\frac{1 + \cos(\varphi)}{2} \right) + a \left(\frac{1 - \cos(\varphi)}{2} \right), \end{split} \tag{A31}$$

where the two light fields are assumed to be noninterfering so that $\hat{a}|\beta\rangle = \hat{b}|\alpha\rangle = 0$ and $\langle \alpha|\beta\rangle = \langle \beta|\alpha\rangle = 0$.

The sensitivity of a magnetometer employing optical readout is written in the same way as the spin-projection-noiselimited sensitivity given in Eq. (A22), but with the observable S_z replaced by \hat{N} :

$$\eta_{\text{opt}} = \delta B_{\text{opt}} \sqrt{t_{\text{meas}}} = \frac{1}{\gamma_e \sqrt{\tau}} \frac{\Delta \hat{N}}{|d\langle \hat{N} \rangle / d\phi|},$$
(A32)

where $\Delta \hat{N} = \sqrt{\langle \hat{N}^2 \rangle - \langle \hat{N} \rangle^2}$. The derivative of $\langle \hat{N} \rangle$ with respect to ϕ is

$$\frac{d\langle \hat{N} \rangle}{d\phi} = \frac{d\langle \hat{N} \rangle}{d\varphi} = \frac{a-b}{2} \sin(\varphi). \tag{A33}$$

Recalling the operator commutation relation $[\hat{a}, \hat{a}^{\dagger}] = 1$, $\Delta \hat{N}$ is calculated as

$$\begin{split} \langle \hat{N}^{2} \rangle &= \langle (\hat{a}^{\dagger} \hat{a} + \hat{b}^{\dagger} \hat{b}) (\hat{a}^{\dagger} \hat{a} + \hat{b}^{\dagger} \hat{b}) \rangle \\ &= \langle \psi_{\mathrm{ph}} | (\hat{a}^{\dagger} \hat{a} \hat{a}^{\dagger} \hat{a} + \hat{b}^{\dagger} \hat{b} \hat{b}^{\dagger} \hat{b}) | \psi_{\mathrm{ph}} \rangle \\ &= \langle \psi_{\mathrm{ph}} | [\hat{a}^{\dagger} (\hat{a}^{\dagger} \hat{a} + 1) \hat{a} + \hat{b}^{\dagger} (\hat{b}^{\dagger} \hat{b} + 1) \hat{b}] | \psi_{\mathrm{ph}} \rangle \\ &= b(b+1) \left(\frac{1 + \cos(\varphi)}{2} \right) + a(a+1) \left(\frac{1 - \cos(\varphi)}{2} \right), \end{split} \tag{A34}$$

$$\langle \hat{N} \rangle^2 = b^2 \left(\frac{1/2 + \cos(\varphi)}{2} \right) + a^2 \left(\frac{1/2 - \cos(\varphi)}{2} \right) + \left(\frac{b^2}{4} + \frac{a^2}{4} \right) \cos^2(\varphi) + \frac{ba}{2} \sin^2(\varphi), \tag{A35}$$

$$\Delta \hat{N} = \sqrt{\langle \hat{N}^2 \rangle - \langle \hat{N} \rangle^2}
= \sqrt{\left(\frac{b^2}{4} - \frac{ba}{2} + \frac{a^2}{4}\right) \sin^2(\varphi) + b\left(\frac{1 + \cos(\varphi)}{2}\right) + a\left(\frac{1 - \cos(\varphi)}{2}\right)}
= \sqrt{\frac{(a - b)^2}{4} \sin^2(\varphi) + b\cos^2\left(\frac{\varphi}{2}\right) + a\sin^2\left(\frac{\varphi}{2}\right)}.$$
(A36)

Using Eqs. (A33) and (A36), the sensitivity reduces to

$$\frac{\Delta \hat{N}}{|d\langle N \rangle / d\phi|} = \sqrt{\frac{[(a-b)^2/4]\sin^2(\varphi) + b\cos^2(\varphi/2) + a\sin^2(\varphi/2)}{[(a-b)^2/4]\sin^2(\varphi)}}.$$
(A37)

For the case $\varphi = \pi/2$, the sensitivity is optimized, yielding

$$\frac{\Delta \hat{N}}{|d\langle \hat{N} \rangle / d\phi|} = \sqrt{\frac{(a-b)^2/4 + (a+b)/2}{(a-b)^2/4}}$$

$$= \sqrt{1 + 2(a+b)/(a-b)^2}.$$
(A38)

We identify C = (a-b)/(a+b) as the measurement contrast (i.e., the fringe visibility), and $n_{\rm avg} = (a+b)/2$ as the average number of photons collected per measurement (per spin, if the measurement is on an ensemble). The contrast C depends on the degree of initial polarization of the spin state and the readout duration. Measurement contrast also diminishes with increased free-precession time due to spin dephasing and docoherence, parametrized by T_2^* , as shown in

Eq. (14). However, since this degradation affects both the shot-noise and spin-projection-noise terms in the measurement sensitivity $\eta_{\rm opt}$, it is included explicitly rather than incorporated into C. Thus, the sensitivity (neglecting overhead time) for a Ramsey measurement on a single spin with both photon shot noise and spin-projection noise is given by

$$\eta_{\text{opt}} = \delta B_{\text{opt}} \sqrt{t_{\text{meas}}} = \frac{1}{\gamma_e e^{-(\tau/T_2^*)^p} \sqrt{\tau}} \sqrt{1 + \frac{1}{C^2 n_{\text{avg}}}}.$$
(A39)

(See the Appendix, Sec. 7 for discussion of the stretched exponential parameter p.) When sensing with an ensemble of N independent spins, the sensitivity is given by

$$\eta_{\text{opt}}^{\text{ensemble}} = \frac{\eta_{\text{opt}}}{\sqrt{N}}.$$
(A40)

In conventional NV⁻ optical readout, measurement contrast is low (\lesssim 15%), and the number of photons $n_{\rm avg}$ collected per spin is at most the order of unity (see Table II) and is often much less due to imperfect collection efficiency. Thus, $C^2n_{\rm avg}\ll 1$, and shot noise becomes the dominant contribution to the magnetic field sensitivity, which in the absence of overhead time is given by

$$\eta_{\text{shot}} \approx \frac{1}{\gamma_e} \frac{1}{Ce^{-(\tau/T_2^*)^p} \sqrt{n_{\text{avg}}\tau}}$$
(A41)

and

$$\eta_{\rm shot}^{\rm ensemble} \approx \frac{1}{\gamma_e} \frac{1}{C e^{-(\tau/T_2^*)^p} \sqrt{N n_{\rm avg} \tau}}. \tag{A42}$$

d. Overhead time

The previous sensitivity equations have neglected any optical initialization or readout time, as well as the finite duration of the two $\pi/2$ pulses of the Ramsey sequence. Grouping all of these factors into an experimental overhead time t_O , we find the sensitivity factor for M measurements each with sensing time τ over a total time $t_{\rm meas}$ is $\sqrt{1/M} = \sqrt{(\tau + t_O)/t_{\rm meas}}$, yielding a sensitivity limited by shot noise and spin-projection noise of

$$\eta_{\text{opt}} = \delta B_{\text{opt}} \sqrt{t_{\text{meas}}} = \frac{1}{\gamma_e e^{-(\tau/T_2^*)^p}} \frac{\sqrt{\tau + t_O}}{\tau} \sqrt{1 + \frac{1}{C^2 n_{\text{avg}}}}.$$
(A43)

2. Optimal precession time

The optimal precession time τ to achieve the best Ramsey magnetometry sensitivity [Eq. (16)] depends on the value of the stretched exponential parameter p, the initialization time

 t_I , and the readout time t_R . By defining the overhead time per measurement as $t_O = t_I + t_R$, Eq. (16) reduces to

$$\eta \propto \frac{1}{e^{-(\tau/T_2^*)^p}} \frac{\sqrt{\tau + t_O}}{\tau}.$$
 (A44)

For $t_O \ll T_2^*$, sensitivity is optimized when $\tau \approx T_2^*/2$ for $1 \le p \le 2$. Particularly, for $t_O = 0$ and p = 1 or p = 2 (see the Appendix, Sec. 7), sensitivity is exactly optimized for $\tau = T_2^*/2$. As t_O increases from zero, the optimal precession time increases as well, asymptotically approaching $\tau = T_2^*$ when $t_O \gg T_2^*$ for p = 1. Figure 33 shows the optimal precession time τ for various combinations of p and t_O . For clarity the optimal precession time is normalized to the dephasing time in the employed measurement basis (DQ or SQ). Equation (A44) and thus Fig. 33 also apply for Hahn echo [Eq. (28)] with T_2^* replaced by T_2 ; see Sec. IV.A.

In practice, additional experimental factors warrant consideration when choosing the Ramsey free-precession time τ . For example, because time-varying electric and magnetic fields and temperature may mask as dephasing mechanisms, the measured value of T_2^* depends on the measurement duration. Thus, if the time required to measure the value of T_2^* is significantly longer than the duration of a magnetic field measurement, field fluctuations may artificially reduce the measured value of T_2^* measurement could lead to a suboptimal choice of τ (Bauch et al., 2018). Therefore, care should be taken when choosing the appropriate free-precession time τ for a magnetometry experiment.

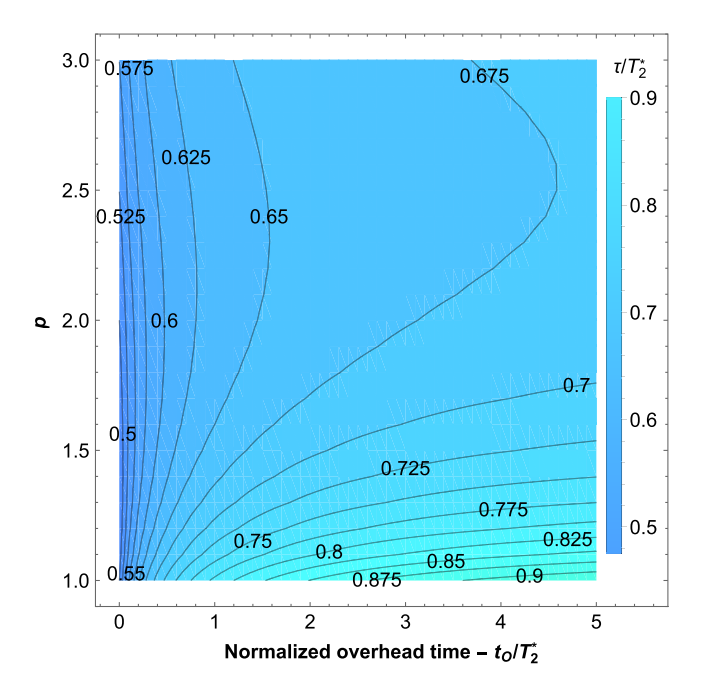


FIG. 33. Optimal precession time τ for pulsed magnetometry protocols. The contour plot shows precession time τ to achieved optimal sensitivity, in units of T_2^* , for different stretched exponential parameters p and different overhead times t_Q .

3. Considerations for increasing sensor number

Increasing the number N of interrogated NV⁻ centers by increasing either the interrogation volume or the NV⁻ density may be partially effective to improve magnetic field sensitivity. In this instance, the number of photons detected per measurement $\mathcal N$ increases with the number of sensors N. However, a series of practical factors may hinder this strategy. First, sensitivity enhancement exhibits sublinear scaling with N and the associated number of photons detected per measurement $\mathcal N$, i.e., $\eta \propto 1/\sqrt{\mathcal N}$, making significant sensitivity improvements from increasing N difficult.

Additional technical difficulties may arise when increasing N, such as the photon number requirement for optical initialization. Assuming that each interrogated NV^- center requires m photons for optical initialization, each measurement is expected to require an energy of

$$E_{\rm init} = Nm \frac{hc}{\lambda},\tag{A45}$$

where h is Planck's constant, c is the speed of light, and λ is the excitation wavelength. If measurements are performed every T_2^* , the required mean power is

$$P_{\text{init}} = \frac{Nm}{T_2^*} \frac{hc}{\lambda}.$$
 (A46)

For example, initialization of all 1.76×10^{14} NV⁻ centers in a 1 mm³ diamond with 1 ppm [NV⁻] would require $E_{\rm init} = 200~\mu\rm J$, using a crude guess of m=3 (see Table XIII). Assuming $T_2^*=1~\mu\rm s$, the required power is $P_{\rm init}=200~\rm W$. Equation (A46) illustrates the fact that achieving a sensitivity improvement by increasing the NV⁻ ensemble size will increase $P_{\rm init}$ unless T_2^* is increased as well. For experimental approaches employing an acousto-optic modulator to gate a cw laser, the required cw laser power will be higher as many photons are wasted.

Another difficulty encountered when increasing the number of interrogated NV⁻ centers N (and thus detected photon number \mathcal{N}) is that reaching the shot noise limit can become challenging for large values of \mathcal{N} . For example, the absolute noise contributed by some systematic (not stochastic) noise sources scales linearly with the number of photons detected, i.e., $\propto k_1 \mathcal{N}$, where $k_1 \ll 1$. In comparably proportional units, shot noise scales as $\propto \sqrt{\mathcal{N}}$. For $\mathcal{N} > 1/k_1^2$, the systematic noise will be larger than shot noise. Primary examples of such noise sources include laser intensity noise in all implementations, timing jitter in the readout pulse length for Ramsey and pulsed ODMR, and MW amplitude noise in cw-ODMR.

Last, increases in interrogation volume or NV⁻ density are both accompanied by unique challenges independent of those associated with increases in sensor number N. For example, larger sensing volumes require better engineering to ensure the bias magnetic field and the MW field are uniform over the sensing volume (Abe and Sasaki, 2018; Eisenach *et al.*, 2018). Alternatively, increasing NV⁻ density necessarily positions NV⁻ spins (and all other nitrogen-related paramagnetic spins) closer together, which results in increased dipolar dephasing

and shorter associated T_2^* values, canceling the sensitivity improvement from addressing more NV⁻ spins.

4. Choosing nitrogen concentration in diamond samples

The following discussion parallels the clear analysis presented by Kleinsasser *et al.* (2016), which the reader is encouraged to review. Equation (19) can be simplified by grouping all non-nitrogen-related broadening mechanisms together, yielding

$$\frac{1}{T_2^*} = \frac{1}{T_2^* \{N_S^0\}} + \frac{1}{T_2^* \{NV^-\}} + \frac{1}{T_2^* \{NV^0\}} + \frac{1}{T_2^* \{\text{other}\}}, \quad (A47)$$

where we ignored typically less common defects in fully treated diamond (i.e., irradiated, annealed, etc.) such as NVH⁻, N₂V⁻, etc. (Hartland, 2014); and T_2^* {other} denotes the T_2^* limit from all non-nitrogen-related dephasing mechanisms. Equation (A47) can be rewritten as

$$\begin{split} \frac{1}{T_2^*} &= A_{\text{N}_{\text{S}}^0}[\text{N}^{\text{T}}][1 - E_{\text{conv}} - E_{\text{conv}}^0 - E_{\text{conv}}^{\text{N}_{\text{S}}^+}] + A_{\text{NV}^-}[\text{N}^{\text{T}}][E_{\text{conv}}] \\ &+ A_{\text{NV}^0}[\text{N}^{\text{T}}][E_{\text{conv}}^0] + \frac{1}{T_2^*\{\text{other}\}}, \end{split} \tag{A48}$$

where $E_{\rm conv} \equiv [{\rm NV^-}]/[{\rm N^T}]$, $E_{\rm conv}^0 \equiv [{\rm NV^0}]/[{\rm N^T}]$, and $E_{\rm conv}^{{\rm N}_S^+} \equiv [{\rm N}_S^+]/[{\rm N^T}]$ are the conversion efficiencies from the total nitrogen concentration $[{\rm N^T}]$ to $[{\rm NV^-}]$, $[{\rm NV^0}]$, and $[{\rm N}_S^+]$, respectively. The A_X coefficients characterize the magnetic dipole interaction strength between NV^- spins and spin species X. The value of $A_{{\rm N}_S^0}$ is defined in Eq. (23), the value of $A_{{\rm NV^-}}$ is defined in Sec. III.G, and in this section for reasons of compactness we do not differentiate between $A_{{\rm NV}_\parallel}$ and $A_{{\rm NV^-}_{\parallel}}$. The value of $A_{{\rm NV^0}}$ is defined so that the NV^- dephasing from NV⁰ satisfies

$$\frac{1}{T_2^*\{NV^0\}} = A_{NV^0}[NV^0]. \tag{A49}$$

Under the assumption that E_{conv} , E_{conv}^0 , $E_{\text{conv}}^{N_5^+}$ are independent of $[N^T]$, consolidation yields

$$\frac{1}{T_2^*} = \kappa[N^T] + \frac{1}{T_2^*\{\text{other}\}},\tag{A50}$$

where

$$\kappa = A_{\text{N}_{\text{S}}^{0}} [1 - E_{\text{conv}} - E_{\text{conv}}^{0} - E_{\text{conv}}^{\text{N}_{\text{S}}^{+}}] + A_{\text{NV}^{-}} [E_{\text{conv}}]$$

$$+ A_{\text{NV}^{0}} [E_{\text{conv}}^{0}]. \tag{A51}$$

The detected number of PL photons per measurement is $\mathcal{N} \propto [\mathrm{N^T}] E_{\mathrm{conv}} V n_{\mathrm{avg}}$, where V is the interrogation volume. For simplicity we consider the limit where initialization and readout times t_I and t_R are negligible, so that sensitivity is

$$\eta \propto \sqrt{\frac{1}{\mathcal{N}T_2^*}} = \sqrt{\frac{1}{E_{\text{conv}}Vn_{\text{avg}}}} \sqrt{\kappa + \frac{1}{[\mathbf{N}^{\text{T}}]T_2^*\{\text{other}\}}}, \quad (A52)$$

which suggests that for

$$[N^{T}] \gg \frac{1}{\kappa T_{2}^{*}\{\text{other}\}}$$
 (A53)

sensitivity is independent of [N^T]. Qualitatively, this can be interpreted as follows: when T_2^* is limited by nitrogen-related dephasing mechanisms (i.e., NV-, NV0, NS0), and again assuming $E_{\text{conv}}, E_{\text{conv}}^0$, and $E_{\text{conv}}^{N_S^+}$ are independent of $[N^T]$, decreasing $[N^T]$ increases T_2^* by the same fractional quantity that the NV⁻ ensemble photoluminescence \mathcal{N} is decreased. However, when T_2^* is limited by other broadening mechanisms unrelated to nitrogen, decreasing [N^T] decreases the collected fluorescence \mathcal{N} without any corresponding T_2^* increase. The implications here are significant: this analysis suggests that while there is not a unique value of [N^T] for maximal sensitivity, there is a minimum value. In other words, if nitrogen-related broadening is a small contributor to T_2^* , the nitrogen content should be increased; the increased resulting PL will favorably offset the decrease in T_2^* , resulting in overall enhanced sensitivity.

A few points are in order regarding this analysis. Experimental considerations can also set an upper bound on the most desirable total nitrogen concentration [N^T]. For example, the larger detected photon number $\mathcal N$ associated with higher values of [N^T] can present technical challenges (see the Appendix, Sec. 3). Moreover, this analysis considers the simple limit where the initialization and readout times are negligible; accounting for this fixed overhead time [see Eqs. (11), (15), and (16)] favors trading off nitrogen concentration density for longer values of T_2^* in order to reduce the fractional overhead time devoted to initialization and readout. Overall, combined experimental and theoretical considerations suggest that for best sensitivity nitrogen content should be decreased until nitrogenrelated broadening is similar to broadening unrelated to nitrogen, i.e.,

$$\kappa[{\rm N^T}] \approx \frac{1}{T_2^* \{ {\rm other} \}}. \tag{A54} \label{eq:assumption}$$

5. Spin resonance linewidth and T_2^*

The quantity T_2^* , which characterizes the time scale of the FID, is inversely proportional to the natural spin resonance linewidth in the absence of power broadening. Exact conversion between T_2^* and linewidth requires knowledge of the functional form of the FID or the resonance line shape (Kwan and Yen, 1979; Abragam, 1983c). Ramsey fringes decaying with an FID envelope $\propto e^{-t/T_2^*}$ indicate a Lorentzian spin resonance profile with full width at half maximum (FWHM) $\Gamma = 1/(\pi T_2^*)$, as shown by the Fourier transform pair:

$$\mathcal{F}_{t}[e^{2\pi i f_{0} t} e^{-t/T_{2}^{*}}](f) = \frac{1}{\pi} \frac{1/(2\pi T_{2}^{*})}{[1/(2\pi T_{2}^{*})]^{2} + (f - f_{0})^{2}}$$

$$= \frac{1}{\pi} \frac{\Gamma/2}{(\Gamma/2)^{2} + (f - f_{0})^{2}},$$
(A55)

valid for $t \ge 0$, where f_0 is the Ramsey fringe frequency. A Gaussian decay envelope $\propto e^{-(t/T_2^*)^2}$ corresponds to a resonance with a Gaussian profile, with standard deviation $\sigma = 1/(\sqrt{2\pi}T_2^*)$ as shown by the Fourier transform pair

$$\mathcal{F}_{t}[e^{2\pi i f_{0} t} e^{-(t/T_{2}^{*})^{2}}](f) = \sqrt{\pi} T_{2}^{*} e^{-[\pi T_{2}^{*} (f - f_{0})]^{2}}$$

$$= \frac{1}{\sigma \sqrt{2\pi}} e^{-(f - f_{0})^{2} / (2\sigma^{2})}.$$
(A56)

6. Estimating T_2^* from spin resonance linewidths of N_S^0

Although sensor performance is dictated by T_2^* of the NV-ensemble, T_2^* values of other paramagnetic defects within the diamond, such as substitutional nitrogen defects, can provide useful information on sources of NV- spin dephasing. Such T_2^* values can be extracted from linewidth measurements, for example, from EPR. Accurate conversion from the EPR linewidth to paramagnetic-defect T_2^* enables leveraging of existing diamond EPR data (van Wyk *et al.*, 1997) to better understand the contributions of different noise sources to NV-ensemble T_2^* values.

EPR linewidths are commonly tabulated by their peak-to-peak widths ΔB , where ΔB denotes the magnetic field spacing between extrema of the resonance line first derivative (Poole, 1996). In linear frequency units, this peak-to-peak width is $\delta = (g\mu_B/h)\Delta B$. Accurately relating δ and T_2^* requires the resonance line shape to be known (Kwan and Yen, 1979). For example, a Lorentzian profile with FWHM Γ , expressed in frequency units, has $\delta = \Gamma/\sqrt{3}$ and $\Gamma = 1/(\pi T_2^*)$ (see the Appendix, Sec. 5). Combining these relations yields $T_{2\text{Lor}}^* = 1/(\sqrt{3}\pi\delta)$. A Gaussian line shape with the same measured peak-to-peak linewidth δ has standard deviations of $\sigma = \delta/2$ and $\sigma = 1/(\sqrt{2}\pi T_2^*)$ (see the Appendix, Sec. 5). Thus, $T_{2\text{Gau}}^* = \sqrt{2}/(\pi\delta)$, which is $\sqrt{6}$ times longer than $T_{2\text{Lor}}^*$. A visual comparison of these relationships is displayed in Fig. 34.

Diamond EPR literature results may report values of δ without giving the associated resonance line shape, preventing accurate determination of T_2^* from δ . For example, linewidth measurements by van Wyk *et al.* (1997) on substitutional nitrogen defects N_S^0 in diamond indicate a scaling $1/T_2^*\{N_S^0\} = A_{N_S^0}[N_S^0]$ with varying nitrogen concentration $[N_S^0]$, but the scaling factor $A_{N_S^0}$ cannot be accurately determined without knowledge of the line shape.

Theoretical and experimental results on dipolar-coupled spin systems suggest a Lorentzian resonance line shape when spin-bath interactions are the dominant source of line broadening (Kittel and Abrahams, 1953; Abragam, 1983c; Dobrovitski *et al.*, 2008; Hall, Cole, and Hollenberg, 2014). Furthermore, Ramsey measurements with NV⁻ spin ensembles show FID envelopes well fit by $e^{-(t/T_2^*)^p}$ with

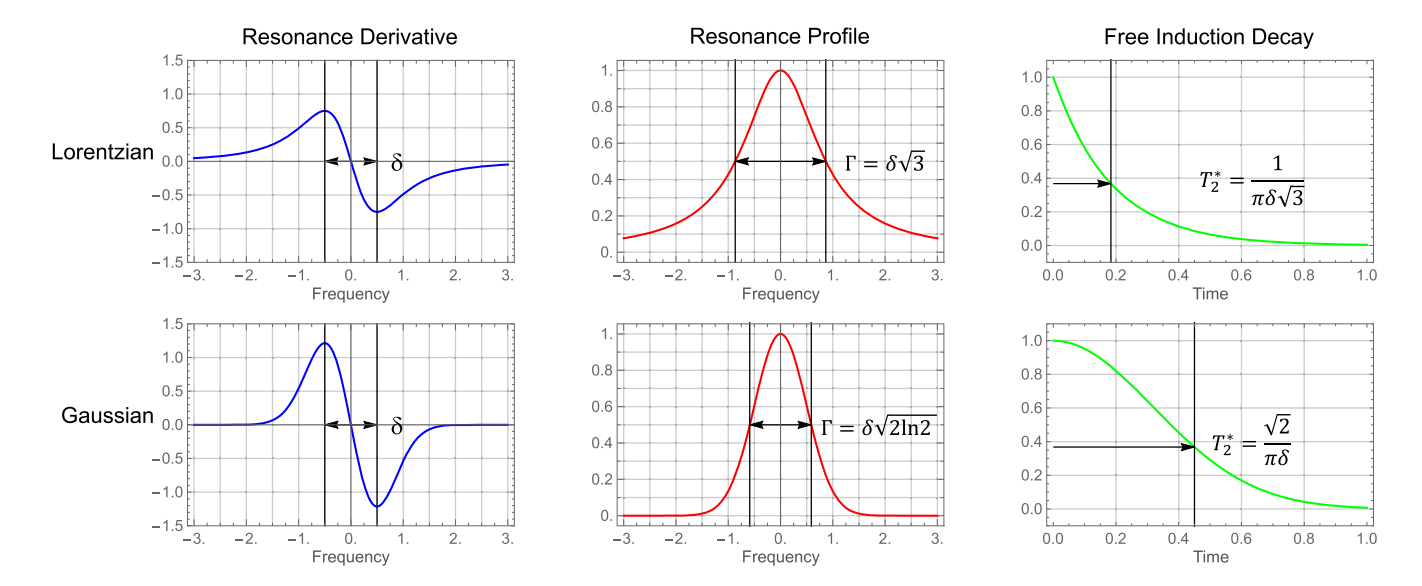


FIG. 34. Resonance derivatives, resonance profiles, and FID envelopes for Lorentzian and Gaussian line-shape profiles with the same peak-to-peak widths δ . Full width at half maximum linewidths Γ and FID decay envelope times T_2^* are indicated and expressed in terms of the peak-to-peak width δ , a commonly reported parameter characterizing linewidth in EPR data.

 $p \sim 1$, corresponding to a Lorentzian line shape [see the Appendix, Sec. 7, Fig. 34 and Bauch *et al.* (2018)] when T_2^* is expected to be spin-bath limited.

Assuming a Lorentzian profile when converting δ values from van Wyk et al. (1997) to T_2^* values yields $A_{N_0^0} \approx$ 130 ms⁻¹ ppm⁻¹ for nitrogen spins in a nitrogen spin bath; see Fig. 35. This calculated scaling factor is considered to be an upper bound because (i) a Gaussian or Voigt profile would result in a smaller value of $A_{\rm N_c^0}$ than that calculated by assuming a Lorentzian profile, as $1/T_{2\text{Gau}}^* = 1/(\sqrt{6}T_{2\text{Lor}}^*)$; and (ii) other sources of broadening may contribute to the EPR linewidths observed by van Wyk et al. (1997). In the latter case the true contribution to dephasing from dipolar interactions between N_S^0 spins would be smaller than that estimated from the measured δ . Nitrogen-spin-bath induced dephasing of N_S⁰ and NV⁻ is expected to be similar, as the dipolar coupling between two N_S⁰ spins is similar to the dipolar coupling between an N_S and an NV⁻ for equivalent separation (Hanson et al., 2008). Thus, the spin-bath-limited linewidth of nitrogen defects in diamond measured via EPR can serve as a proxy for the spin-bath limited linewidth of NV⁻ centers. The value of $A_{\rm N_c^0} \approx 130~{\rm ms^{-1}\,ppm^{-1}}$ for $\rm N_S^0$ from the data in van Wyk et al. (1997) serves as an independent estimate of $A_{N_s^0}$ for NV^- centers in a nitrogen spin bath. This value is in reasonable agreement with the measured $A_{\text{N}_{\text{c}}^0} \approx 101 \text{ ms}^{-1} \text{ ppm}^{-1} \text{ for NV}^$ ensembles from Bauch et al. (2018).

7. Stretched exponential parameter

Equations (A55) and (A56) show that the spin resonance line shape can be parametrized by the stretched exponential parameter p of the FID envelope $e^{-(t/T_2^*)^p}$. We note that for the idealized case of a purely Lorentzian line shape p = 1 and for a purely Gaussian line shape p = 2. The exact ODMR line shape and value of p are well characterized for single spins under a variety of environmental conditions (Dobrovitski et al., 2008; Hanson et al., 2008; de Sousa, 2009; Maze et al., 2012; Hall, Cole, and Hollenberg, 2014). For example, a single spin experiencing dipolar coupling to a surrounding bath of spins displays an FID envelope with stretched exponential parameter p = 2 (Dobrovitski et al., 2008; de Sousa, 2009; Maze et al., 2012; Hall, Cole, and Hollenberg, 2014); for a Gaussian ODMR line shape, see Table XI and Fig. 34. Meanwhile, NV⁻ ensembles with linewidths limited by dipolar coupling to a spin bath are predicted (Dobrovitski et al., 2008; Hall, Cole, and Hollenberg, 2014) and measured (MacQuarrie et al., 2015; Bauch et al., 2018) to exhibit FID envelopes with p = 1 (for a Lorentzian ODMR line shape, see Table XI and Fig. 34). However, experimental Ramsey measurements on NV- ensembles may sometimes exhibit decay envelopes with $p \neq 1$, suggesting the presence of other broadening mechanisms such as strain gradients, magnetic field gradients, or temperature fluctuations (Bauch et al., 2018). A noninteger p for an ensemble may also indicate the presence of more complex dephasing and decoherence

TABLE XI. Stretched exponential parameters p associated with free induction decay envelopes for single NV⁻ centers and NV⁻ ensembles in dipolar-coupled spin baths.

Ramsey T_2^* decay	p	Reference (experiment)	Reference (theory)
Single NV ⁻	2	Maze et al. (2012)	Dobrovitski <i>et al.</i> (2008), de Sousa (2009), and Hall, Cole, and Hollenberg (2014)
NV ⁻ ensemble	1	MacQuarrie et al. (2015) and Bauch et al. (2018)	Dobrovitski <i>et al.</i> (2008) and Hall, Cole, and Hollenberg (2014)

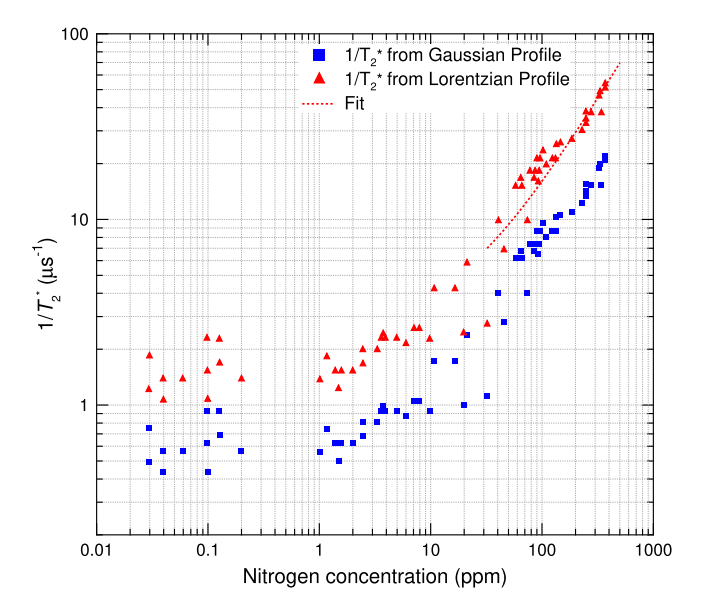


FIG. 35. Bounds on $1/T_2^*$ of N_S^0 defects (P1 centers) as determined from P1 EPR linewidth measurements in diamonds with a range of nitrogen impurity concentrations, calculated assuming Gaussian (blue squares) and Lorentzian (red triangles) EPR line shapes. A fit to the function $1/T_2^* = A_{N_S^0}[N_S^0] + b$ assuming a Lorentzian line shape (red dotted line) yields $A_{N_S^0} \approx 130 \text{ ms}^{-1} \text{ ppm}^{-1}$ for nitrogen spins in a nitrogen spin bath (see the main text). Adapted from van Wyk *et al.*, 1997.

dynamics, including spatial inhomogeneity, than can be encompassed by a single decay time constant. In some cases the decay may be better described by a sum (Cao, 1994) or a product of multiple decay curves with different values of T_2^* and p. For example, a product of two FID decays, one with p=1 and one with p=2, corresponds to a Voigt profile line shape. Allowing p to vary when fitting FID envelopes crudely accounts for these sorts of line-shape variations while requiring only a single additional fit parameter. Therefore, Ramsey FID measurements exhibiting $1 \le p \le 2$ for some NV⁻ ensembles may suggest contributions to the ODMR lines from both Lorentzian and Gaussian broadening mechanisms (Bauch $et\ al.$, 2018).

Hahn echo T_2 decays of single NV⁻ spins have been predicted (de Sousa, 2009) and measured (de Lange *et al.*, 2010) to exhibit a stretched exponential parameter p=3 when T_2 is limited by spin-bath noise. In contrast, Hahn echo decay envelopes for ensembles of NV⁻ spins have been seen to exhibit p varying from \sim 0.5 to 3, depending on the dominant contributors to the spin bath and the bias magnetic field angle (Stanwix *et al.*, 2010; Bauch *et al.*, 2019).

8. Isotopic purity confusion in the literature

In Sec. III.F, we discussed the T_2^* limit imposed by [13 C], which is described by an inverse linear scaling in Eq. (25), reproduced as

$$\frac{1}{T_2^*\{^{13}C\}} = A_{^{13}C}[^{13}C], \tag{A57}$$

where $A_{\rm ^{13}C} \approx 0.100~{\rm ms^{-1}\,ppm^{-1}}$. Although such inverse linear scaling with [13 C] is predicted by several theoretical calculations (Kittel and Abrahams, 1953; Abragam, 1983c; Dobrovitski *et al.*, 2008; Hall, Cole, and Hollenberg, 2014), some experiments based on single NV⁻ centers (incorrectly we believe) suggest an inverse square root scaling (Balasubramanian *et al.*, 2009; Mizuochi *et al.*, 2009), i.e.,

$$\frac{1}{T_2^{*\{\text{single}\}} \{^{13}\text{C}\}} = A_{^{13}\text{C}}^{\{\text{single}\}} \sqrt{[^{13}\text{C}]}$$
 (A58)

for single NV⁻ centers in the dilute limit ($[^{13}C]/[^{12}C] \ll 0.01$). Mizuochi *et al.* (2009) derived the data from mean T_2^* values taken from many single NV⁻ defects in the diamond. However, Eq. (A58) conflicts with theoretical calculations by both Dobrovitski *et al.* (2008) and Hall, Cole, and Hollenberg (2014) explicitly for single NV⁻ centers. Both sources instead suggest that for the mean single NV⁻ center,

$$\frac{1}{T_2^{*\{\text{single}\}}\{^{13}\text{C}\}} = A_{^{13}\text{C}}^{\{\text{single}\}}[^{13}\text{C}], \tag{A59}$$

similar to Eq. (25).

We hypothesize that the origin of this discrepancy is omission of nitrogen broadening in the study by Mizuochi et al. (2009), as summarized in Table XII. Using $1/T_2^{*\{\text{single}\}}\{N_S^0\} = A_{N_S^0}^{\text{single}}[N_S^0]$ (see Sec. III.D), we roughly estimate $A_{N_S^0}^{\text{single}} = 56 \text{ ms}^{-1} \text{ ppm}^{-1}$ from Zhao, Ho, and Liu (2012). For the lowest ^{13}C sample in the data from Mizuochi et al. (2009), which has $[N_S^0] \sim 1$ ppm, this estimate predicts a nitrogen-limited $T_2^{*\{\text{single}\}}\{N_S^0\}$ of $\sim 18~\mu\text{s}$, close to the actual reported T_2^* measurement. Neglecting the additional nitrogen contribution to $T_2^{*\{\text{single}\}}$ for the lowest ^{13}C sample likely caused Mizuochi et al. to overestimate the contribution of ^{13}C to T_2^* and draw incorrect conclusions on the scaling of T_2^* with $[^{13}\text{C}]$.

Balasubramanian *et al.* (2009) reported linewidths of 210 and 55 kHz for diamonds with 1.1% and 0.3% 13 C, respectively, data which are clearly consistent with Eq. (25). However, Balasubramanian *et al.* (2009) interpreted their data using formalism appropriate for 13 C $\gtrsim 10\%$ (Abragam, 1983c), which results in them employing Eq. (A58).

As discussed in Sec. III.F, Eq. (25) has been experimentally verified in the dilute limit in a similar system (Abe *et al.*, 2010). Given that the mean single-NV⁻ FID time is longer than the ensemble FID time by roughly a factor of 2 in diamond with natural abundance ¹³C [see Sec. III.F and Maze *et al.* (2012)], if Eq. (A58) were also correct, then at sufficiently low ¹³C concentration, an NV⁻ ensemble would dephase more slowly than its constituent spins. This prediction conflicts with the present understanding that $T_2^{*\{\text{single}\}}\{^{13}\text{C}\} > T_2^*\{^{13}\text{C}\}$ regardless of concentration; see Sec. III.B

9. Linear Stark and Zeeman regimes

Here we describe the coupling of electric fields, strain, and magnetic fields to the NV⁻ spin resonances in the regimes of

TABLE XII. The three diamonds used in Mizuochi *et al.* (2009). The calculated value of $T_2^{*\{\text{single}\}}\{^{13}\text{C}\}$ is derived using the mean value of $T_2^{*}=2.3~\mu\text{s}$ for single NV⁻ centers in a natural abundance ^{13}C sample measured with a bias field of 20 G (Maze *et al.*, 2012), so that $T_2^{*\{\text{single}\}}\{^{13}\text{C}\}=2.3~\mu\text{s}\times0.0107/[^{13}\text{C}]$. The calculated value of $T_2^{*\{\text{single}\}}\{N_S^0\}$ is estimated using the simulation in Fig. 1 of Zhao, Ho, and Liu (2012) which predicts $T_2^{*\{\text{single}\}}\{N_S^0\}=18\pm1~\text{ps}/[N_S^0]$.

[¹³ C] (ppm)	Measured $T_2^{*\{\text{single}\}}$ (μ s) (Mizuochi <i>et al.</i> , 2009)	Synthesis	[N _S] (ppm)	Calculated $T_2^{*\{\text{single}\}}\{^{13}\text{C}\}$ (μ s) (This work)	Calculated $T_2^{*\{\text{single}\}}\{N_S^0\}$ (μ s) (This work)
10 700	3.3	CVD	< 0.001	2.3	≳18 000
3 500	6.2	CVD	< 0.001	7	≥18 000
300	18	HPHT	~1	82	~18

both low and high axial bias magnetic field $B_{0,z}$. This treatment draws heavily on the equations and analysis in Jamonneau *et al.* (2016). While understanding of strain's effect on the NV⁻ spin continues to evolve (Doherty *et al.*, 2013; Barson *et al.*, 2017; Barfuss *et al.*, 2019; Udvarhelyi *et al.*, 2018), we take the NV⁻ ground-state spin Hamiltonian in the presence of a bias magnetic field \vec{B}_0 , an electric field \vec{E} , and intrinsic crystal strain to be (Doherty *et al.*, 2013; Udvarhelyi *et al.*, 2018)

$$\begin{split} H/h &= (D + \mathcal{M}_z + d_{\parallel}E_z)S_z^2 \\ &+ \frac{g_e\mu_B}{h}(B_{0,z}S_z + B_{0,x}S_x + B_{0,y}S_y) \\ &+ (d_{\perp}E_x + \mathcal{M}_x)(S_y^2 - S_x^2) \\ &+ (d_{\perp}E_y + \mathcal{M}_y)(S_xS_y + S_yS_x) \\ &+ \mathcal{N}_x(S_xS_z + S_zS_x) + \mathcal{N}_y(S_yS_z + S_zS_y). \end{split} \tag{A60}$$

Here S_i with i=x, y, and z are the dimensionless spin-1 projection operators; D is the NV⁻ zero field splitting (≈ 2.87 GHz at room temperature); $d_{\parallel}=3.5\times 10^{-3}$ Hz/(V/m) and $d_{\perp}=0.17$ Hz/(V/m) are the axial and transverse electric dipole moments (van Oort and Glasbeek, 1990; Dolde *et al.*, 2011; Michl *et al.*, 2019), see Table XIV; and \mathcal{M}_z , \mathcal{M}_x , \mathcal{M}_y , \mathcal{N}_x , and \mathcal{N}_y are spin-strain coupling parameters.

The Hamiltonian can be simplified when D is large compared to all other coupling terms, i.e., in the regime of low magnetic field, electric field, and strain. In particular, energy level shifts associated with transverse magnetic field components $B_{0,x}$ and $B_{0,y}$ (Jamonneau *et al.*, 2016), and with

spin-strain coupling parameters \mathcal{N}_x and \mathcal{N}_y , are suppressed by D and thus may be neglected from the Hamiltonian (Kehayias *et al.*, 2019). This low-field Hamiltonian H_{LF} is given by

$$H_{LF}/h = (D + \mathcal{M}_z + d_{\parallel}E_z)S_z^2 + \frac{g_e\mu_B}{h}B_{0,z}S_z + (d_{\perp}E_x + \mathcal{M}_x)(S_y^2 - S_x^2) + (d_{\perp}E_y + \mathcal{M}_y)(S_xS_y + S_yS_x).$$
(A61)

We focus on the interplay between different terms in $H_{\rm LF}$ that shift the NV⁻ spin resonance frequencies in opposite directions, including $B_{0,z}$, E_x , E_y , \mathcal{M}_x , and \mathcal{M}_y . In contrast, dephasing associated with variations in terms that shift the resonance frequencies in common mode $(D, E_z, \text{ and } \mathcal{M}_z)$ can be mitigated by employing double-quantum coherence magnetometry (see Sec. IV.B) and are ignored herein. In addition to shifting the spin resonance frequencies, transverse electric fields E_x and E_y and transverse spin-strain coupling terms \mathcal{M}_x and \mathcal{M}_y mix the $m_s = \pm 1$ spin states into

$$|+\rangle = \cos\left(\frac{\theta}{2}\right)|+1\rangle + e^{i\phi}\sin\left(\frac{\theta}{2}\right)|-1\rangle, \quad (A62)$$

$$|-\rangle = \sin\left(\frac{\theta}{2}\right)|+1\rangle - e^{i\phi}\cos\left(\frac{\theta}{2}\right)|-1\rangle, \quad (A63)$$

where $\tan(\phi)=(d_{\perp}E_y+\mathcal{M}_y)/(d_{\perp}E_x+\mathcal{M}_x)$ and $\tan(\theta)=\xi_{\perp}/\beta_z$. Here $\beta_z=(g_e\mu_B/h)B_{0,z}$ represents the magnetic field coupling to the NV⁻ spin and $\xi_{\perp}=\sqrt{(d_{\perp}E_x+\mathcal{M}_x)^2+(d_{\perp}E_y+\mathcal{M}_y)^2}$ combines the effects of

TABLE XIII. NV⁻ decay rates measured at room temperature. Averages over measured NV⁻ centers are weighted by reported uncertainties. Ellipses indicate values not reported. Branching ratios can be derived from the given data. Although not tabulated, vibrational decay within the ${}^{3}E$ state is fast, with Huxter *et al.* (2013) observing a \sim 4 ps timescale, and Ulbricht *et al.* (2018) observing a \sim 50 fs timescale. The ${}^{1}A_{1}$ lifetime was measured to be \approx 100 ps at 78 K (Ulbricht and Loh, 2018) and is likely shorter at room temperature.

Reference	Tetienne <i>et al.</i> (2012)	Gupta, Hacquebard, and Childress (2016)	Robledo et al. (2011)	Acosta, Jarmola et al. (2010)	
NV ⁻ centers probed	4	3	2	Ensemble	Units
Values reported	Average (max, min)	Average (max, min)	Average		
${}^{3}E(m_s=0) \rightarrow {}^{3}A_2(m_s=0)$	67.9 (63.2, 69.1)	66.16 (66.08, 66.43)	64.2		μ s ⁻¹
${}^{3}E(m_{s}=\pm 1) \rightarrow {}^{3}A_{2}(m_{s}=\pm 1)$	67.9 (63.2, 69.1)	66.16 (66.08, 66.43)	64.9		μ s ⁻¹
$^{3}E(m_s=0) \rightarrow {}^{1}A_1$	5.7 (5.2, 10.8)	11.1 (10.9, 11.2)	11.2		μ s ⁻¹
${}^{3}E(m_{s}=\pm 1) \rightarrow {}^{1}A_{1}$	49.9 (48.6, 60.7)	91.8 (89.3, 92.9)	80.0		μ s ⁻¹
${}^{1}E \rightarrow {}^{3}A_{2}(m_{s}=0)$	1.0 (0.7, 1.5)	4.87 (4.75, 4.90)	3.0		μ s ⁻¹
${}^{1}E \rightarrow {}^{3}A_{2}(m_{s} = \pm 1)$	0.75 (0.4, 1.4)	2.04 (2.03, 2.13)	2.6		μ s ⁻¹
¹ E lifetime	• • •	144.5 (144.3, 145.3)	178 ± 6	219 ± 3	ns

TABLE XIV. Compiled constants for the electronic ground state of the NV⁻ center in diamond. Data are reproduced in part from Doherty *et al.* (2013).

Constant	Description	Value	Reference
g_{\parallel}	Axial g factor	2.0028 ± 0.0003	Loubser and van Wyk (1978)
- 11	_	2.0029 ± 0.0002	Felton et al. (2009)
g_{\perp}	Transverse g factor	2.0028 ± 0.0003	Loubser and van Wyk (1978)
		2.0031 ± 0.0002	Felton et al. (2009)
A_{\parallel}	¹⁴ N axial magnetic hyperfine constant	$\pm 2.32 \pm 0.01 \; \mathrm{MHz}$	Loubser and van Wyk (1978)
"		$2.30 \pm 0.02~\mathrm{MHz}$	He, Manson, and Fisk (1993)
		$-2.14 \pm 0.07 \text{ MHz}$	Felton et al. (2008)
		$-2.166 \pm 0.01 \; \mathrm{MHz}$	Steiner <i>et al.</i> (2010)
		$-2.162 \pm 0.002 \text{ MHz}$	Smeltzer, McIntyre, and Childress (2009)
	¹⁵ N axial magnetic hyperfine constant	-3.1 MHz	Rabeau et al. (2006)
		$3.01 \pm 0.05 \text{ MHz}$	Fuchs et al. (2008)
		$3.03 \pm 0.03 \; \mathrm{MHz}$	Felton et al. (2009)
A_{\perp}	¹⁴ N transverse magnetic hyperfine constant	$+2.10 \pm 0.10 \text{ MHz}$	He, Manson, and Fisk (1993)
		$-2.70 \pm 0.07 \text{ MHz}$	Felton et al. (2008)
	¹⁵ N transverse magnetic hyperfine constant	-3.1 MHz	Rabeau et al. (2006)
		$3.01 \pm 0.05 \; \mathrm{MHz}$	Fuchs et al. (2008)
		$3.65 \pm 0.03 \; \mathrm{MHz}$	Felton et al. (2009)
P	¹⁴ N nuclear electric quadrupole parameter	-5.04 ± 0.05	He, Manson, and Fisk (1993)
		-5.01 ± 0.06	Felton et al. (2008)
		-4.945 ± 0.01	Steiner et al. (2010)
		-4.945 ± 0.005	Smeltzer, McIntyre, and Childress (2009)
d_{\parallel}	Axial dipole moment	$3.5 \pm 0.02 \times 10^{-3} \text{ Hz/(V/m)}$	van Oort and Glasbeek (1990)
$d_{\perp}^{"}$	Transverse dipole moment	$0.165 \pm 0.007 \; Hz/(V/m)$	Michl et al. (2019)
		$0.175 \pm 0.030 \; Hz/(V/m)$	Dolde et al. (2011)
		$0.17 \pm 0.025 \; Hz/(V/m)$	van Oort and Glasbeek (1990)

transverse strain and electric fields. The transition frequencies $|0\rangle\leftrightarrow|+\rangle$ and $|0\rangle\leftrightarrow|-\rangle$ are

$$u_{\pm} = D + \mathcal{M}_z + d_{\parallel} E_z \pm \sqrt{\xi_{\perp}^2 + \beta_z^2},$$
(A64)

and the coupling strength of transverse strain and electric fields to the NV^- spin resonance frequencies is given by

$$\frac{\partial \nu_{\pm}}{\partial \xi_{\perp}} = \frac{\pm 1}{\sqrt{1 + (\beta_z/\xi_{\perp})^2}}.$$
 (A65)

In the linear Stark regime, characterized by $\beta_z \ll \xi_\perp$, the spin eigenstates become, approximately, equal superpositions of $|+1\rangle$ and $|-1\rangle$, and the transition frequencies exhibit maximal sensitivity to variations in ξ_\perp :

$$\left| \frac{\partial \nu_{\pm}}{\partial \xi_{\perp}} \right|_{\beta_{z} \ll \xi_{1}} = 1 - \frac{1}{2} \left(\frac{\beta_{z}}{\xi_{\perp}} \right)^{2} + \mathcal{O} \left[\left(\frac{\beta_{z}}{\xi_{\perp}} \right)^{4} \right]. \tag{A66}$$

In contrast, in the linear Zeeman regime, characterized by $\beta_z \gg \xi_\perp$, the spin eigenstates become, approximately, $|+1\rangle$

and $|-1\rangle$, and sensitivity to strain and electric fields is suppressed by the ratio ξ_{\perp}/β_z :

$$\left| \frac{\partial \nu_{\pm}}{\partial \xi_{\perp}} \right|_{\beta_{z} \gg \xi_{\perp}} = \frac{\xi_{\perp}}{\beta_{z}} - \frac{1}{2} \left(\frac{\xi_{\perp}}{\beta_{z}} \right)^{3} + \mathcal{O} \left[\left(\frac{\xi_{\perp}}{\beta_{z}} \right)^{5} \right]. \tag{A67}$$

By performing magnetic sensing in the linear Zeeman regime, spatial and temporal variations in transverse electric fields and strain couple less strongly to the NV⁻ spin, and thus their contribution to T_2^* is diminished. The linear Zeeman regime is best suited for high-sensitivity magnetometry not only because of the T_2^* extension from suppressed sensitivity to variations in ξ_{\perp} , but also because magnetic field changes couple most strongly to $\nu\pm$ in this regime:

$$\left| \frac{\partial \nu_{\pm}}{\partial \beta_{z}} \right|_{\beta_{z} \gg \xi_{\perp}} = 1 - \frac{1}{2} \left(\frac{\xi_{\perp}}{\beta_{z}} \right)^{2} + \mathcal{O} \left[\left(\frac{\xi_{\perp}}{\beta_{z}} \right)^{4} \right]. \tag{A68}$$

Experiments that must operate at near-zero \vec{B}_0 for other reasons, such as to protect ferromagnetic samples, should use low-strain diamonds to avoid operating in the unfavorable regime where $\beta_z \ll \xi_\perp$ (Fu *et al.*, 2014; Backlund, Kehayias,

TABLE XV. Absorption cross section at 532 nm for the NV⁻³ $A_2 \rightarrow {}^3E$ transition. The value from Fraczek *et al.* (2017) was calculated from their data under the assumption that the NV⁻ and NV⁰ absorption cross sections are equal to within a factor of 2.

Cross section	Value	Reference
$\sigma_{^{3}A_{2} \rightarrow ^{3}E}(\lambda = 532 \text{ nm})$ $\sigma_{^{3}A_{2} \rightarrow ^{3}E}(\lambda = 532 \text{ nm})$	$(3.1 \pm 0.8) \times 10^{-17} \text{ cm}^2$ $(9.5 \pm 2.5) \times 10^{-17} \text{ cm}^2$ $(2.6 \pm 0.5) \times 10^{-17} \text{ cm}^2$ $2.4 \times 10^{-17} \text{ cm}^2$	Wee et al. (2007) Chapman and Plakhotnik (2011) Fraczek et al. (2017) Subedi et al. (2019)

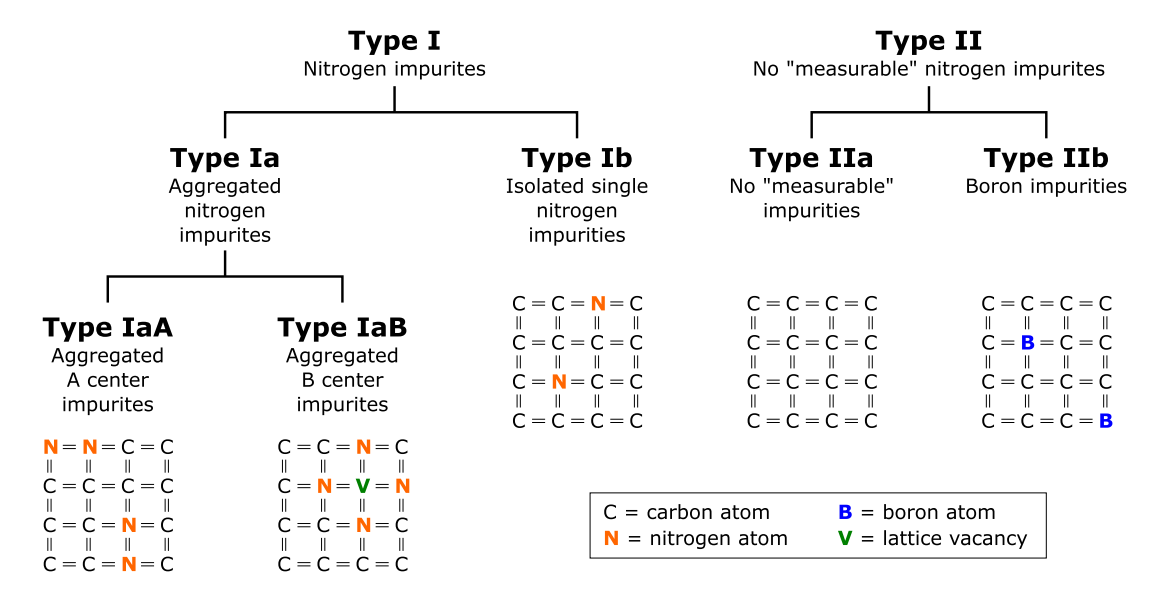


FIG. 36. Diamond type classification system as described in the main text. Adapted from Breeding and Shigley, 2009.

and Walsworth, 2017; Glenn *et al.*, 2017; Zheng *et al.*, 2019). In this linear Stark regime, not only is sensitivity to magnetic signals suppressed by the ratio β_z/ξ_{\perp} ,

$$\left| \frac{\partial \nu_{\pm}}{\partial \beta_{z}} \right|_{\beta_{z} \ll \xi_{\perp}} = \frac{\beta_{z}}{\xi_{\perp}} - \frac{1}{2} \left(\frac{\beta_{z}}{\xi_{\perp}} \right)^{3} + \mathcal{O} \left[\left(\frac{\beta_{z}}{\xi_{\perp}} \right)^{5} \right], \quad (A69)$$

but also T_2^* may be shortened by electric field and strain variations.

10. Example annealing calculations

We present some calculations to estimate parameters necessary for LPHT annealing to form NV- centers. Using $D_0 = 1.6 \times 10^{-3}$ cm²/s (Fletcher and Brown, 1953) for the diffusion constant, $E_a = 2.3$ eV for the activation energy, and T = 800 °C for the annealing temperature, we expect D =2.5 nm²/s. When annealing at T = 800 °C and $t_{anneal} =$ 12×3600 s, a single vacancy in a perfect lattice is expected (based on the model presented here) to have made $\sim 2.7 \times 10^7$ lattice jumps, visited 1.5×10^7 distinct lattice sites (Vineyard, 1963; Fastenau, 1982), and diffused a root-mean-square distance of $\langle r_{\rm rms} \rangle \approx 0.8 \ \mu \text{m}$, assuming $\langle r_{\rm rms} \rangle = \sqrt{6Dt_{\rm anneal}}$. The uncertainties in these estimates are dominated by the ± 0.3 eV uncertainty in E_a (Davies et al., 1992; Mainwood, 1999), which can lead to an order of magnitude variation in D for T = 800 °C. Ignoring small repulsive forces between substitutional nitrogen and monovacancies (Davies et al., 1992), a vacancy is expected to visit $\sim 10^6/4$ lattice sites in a 1 ppm [N_S] diamond to form an NV. The factor of 4 arises from the four closest sites to a substitutional nitrogen while the 10⁶ arises because only 1 out of every 10⁶ lattice sites is occupied by a substitutional nitrogen. Because the number of distinct lattice sites visited is substantially greater than the number of sites needed to form an NV center [i.e., $(1.5 \times 10^7)/(10^6/4) \gg 1$], the chosen values of T and t_{anneal} are expected to ensure adequate NV center formation. The simple analysis stated here is complicated by the uncertainty in D_0 and E_a , as well as the presence of other vacancies, vacancy aggregates, dislocations, surfaces, etc., which can also trap vacancies, but are beyond the scope of this paper. For additional detail and discussion, see Alsid *et al.* (2019).

This analysis is derived only from first-principles calculations and the measured value of E_a . More accurate behavior may be predicted by employing measured values of D at a given temperature, such as $D \approx 1.1 \text{ nm}^2/\text{s}$ at 750 °C (Martin et al., 1999) and $D \approx 1.8 \text{ nm}^2/\text{s}$ at 850 °C (Alsid et al., 2019).

11. The diamond type classification system

We briefly overview the "diamond type" classification system introduced in the 1930s and outlined by Robertson, Fox, and Martin (1933, 1936). In spite of the system's shortcomings, it has been widely adopted by the gemstone community and is partially used by the scientific community today. In the mid-1930s Robertson, Fox, and Martin (1933, 1936) noted that although the vast majority of natural diamonds exhibited absorption lines in the 225-300 nm band and near 8 μ m, these same absorption features were absent in a small minority of diamonds. They further observed that diamonds lacking these same absorption features tended to exhibit lower birefringence and higher photoconductivity relative to their peers (Robertson, Fox, and Martin, 1933, 1936). Kaiser and Bond (1959) attributed the observed infrared absorption features to carbon-nitrogen molecular vibrations, signaling the presence of nitrogen. Nitrogen was found to be the most common impurity occurring in natural diamonds, which made its presence or absence a logical basis for diamond classification.

In this nitrogen-based diamond classification system, all diamonds are categorized into one of two primary types: Type I diamonds contain measurable quantities of nitrogen while type II diamonds do not, as shown in Fig. 36. There is no wide consensus on what constitutes "measurable" in an age of ever-advancing characterization tools, although a common

definition is a quantity detectable with an FTIR spectrometer (Breeding and Shigley, 2009). Most sources suggest a delineation somewhere between 0.5 ppm (Zaitsev, 2001) and 20 ppm (Dischler, 2012; Gaillou *et al.*, 2012). This delineation uncertainty is particularly unfortunate for the NV⁻ community, as many diamonds employed for ensemble NV⁻ experiments fall in this range.

Type I diamonds can be further classified by the specific nitrogen complexes incorporated into the carbon lattice. For example, type Ia diamonds contain aggregated nitrogen impurities and describe the vast majority of natural diamonds (>95%, depending on the delineation nitrogen concentration) (Zaitsev, 2001; Breeding and Shigley, 2009). Typical nitrogen concentrations in natural type Ia diamonds are in the hundreds of ppm (e.g., 500 ppm) (Zaitsev, 2001) but can be as high as 3000 ppm (Neves and Nazaré, 2001). If the aggregated nitrogen predominantly forms A centers consisting of two substitutional nitrogens located adjacent in the diamond lattice, the diamond is classified as type IaA. If the aggregated nitrogen predominantly forms B centers consisting of four substitutional nitrogens surrounding a lattice vacancy, the diamond is classified as type IaB. In contrast, diamonds containing predominantly isolated single nitrogen impurities are classified as type Ib and make up about 0.1% of all natural diamonds (Zaitsey, 2001). As higher nitrogen density promotes aggregation, type Ib diamonds typically exhibit nitrogen concentrations at or below the 100 ppm level (Zaitsev, 2001), less than typical for type Ia diamonds (Zaitsey, 2001).

Type II diamonds containing no measurable nitrogen can be additionally classified as well. Type IIa diamonds contain no other measurable impurities and make up the majority of gemgrade diamonds in spite of comprising only 1% to 2% of natural diamonds. These diamonds are the most optically transparent diamonds: while type IIa diamonds with low levels of impurities may exhibit pale shades of yellow, pink, or purple, extremely pure type IIa diamonds are colorless (Zaitsev, 2001). Nearly all single NV⁻ experiments employ type IIa diamonds. As boron is another common impurity in natural diamond, type II diamonds with measurable boron are categorized as type IIb. These diamonds make up about 0.1% of all natural diamonds and may exhibit a bluish or grey-ish hue.

Although the diamond type classification system was developed for natural diamonds, it appropriately describes synthetic diamonds as well. CVD-grown diamonds without nitrogen doping are type IIa. Man made HPHT diamonds of types IaA, Ib, IIa, and IIb have been created. Further diamond types exist: see Zaitsev (2001).

REFERENCES

Abe, E., and K. Sasaki, 2018, J. Appl. Phys. **123**, 161101. Abe, E., *et al.*, 2010, Phys. Rev. B **82**, 121201.

Abragam, A., 1983a, *The Principles of Nuclear Magnetism* (Clarendon Press, Oxford), Chap. 4.

Abragam, A., 1983b, *The Principles of Nuclear Magnetism* (Clarendon Press, Oxford), Chap. 3.

Abragam, A., 1983c, *The Principles of Nuclear Magnetism* (Clarendon Press, Oxford).

Achard, J., A. Tallaire, V. Mille, M. Naamoun, O. Brinza, A. Boussadi, L. William, and A. Gicquel, 2014, Phys. Status Solidi A 211 2264

Acosta, V. M., 2011, "Optical Magnetometry with Nitrogen-Vacancy Centers in Diamond," Ph.D. thesis (University of California Berkeley).

Acosta, V. M., E. Bauch, A. Jarmola, L. J. Zipp, M. P. Ledbetter, and D. Budker, 2010, Appl. Phys. Lett. 97, 174104.

Acosta, V. M., E. Bauch, M. P. Ledbetter, A. Waxman, L.-S. Bouchard, and D. Budker, 2010, Phys. Rev. Lett. **104**, 070801.

Acosta, V. M., A. Jarmola, E. Bauch, and D. Budker, 2010, Phys. Rev. B 82, 201202.

Acosta, V. M., et al., 2009, Phys. Rev. B 80, 115202.

Ahmadi, S., H. A. R. El-Ella, J. O. B. Hansen, A. Huck, and U. L. Andersen, 2017, Phys. Rev. Applied 8, 034001.

Ahmadi, S., H. A. R. El-Ella, A. M. Wojciechowski, T. Gehring, J. O. B. Hansen, A. Huck, and U. L. Andersen, 2018a, in *Conference on Lasers and Electro-Optics* (Optical Society of America, Washington, DC), p. JF3B.2.

Ahmadi, S., H. A. R. El-Ella, A. M. Wojciechowski, T. Gehring, J. O. B. Hansen, A. Huck, and U. L. Andersen, 2018b, Phys. Rev. B 97, 024105.

Aiello, C. D., M. Hirose, and P. Cappellaro, 2013, Nat. Commun. 4,

Alsid, S. T., J. F. Barry, L. M. Pham, J. M. Schloss, M. F. O'Keeffe, P. Cappellaro, and D. A. Braje, 2019, Phys. Rev. Applied 12, 044003. Ammerlaan, C. A. J., and E. A. Burgemeister, 1981, Phys. Rev. Lett. 47, 954.

Angerer, A., T. Nöbauer, G. Wachter, M. Markham, A. Stacey, J. Majer, J. Schmiedmayer, and M. Trupke, 2015, arXiv:1509.01637. Angus, J. C., H. A. Will, and W. S. Stanko, 1968, J. Appl. Phys. 39, 2015.

Arai, K., C. Belthangady, H. Zhang, N. Bar-Gill, S. J. DeVience, P. Cappellaro, A. Yacoby, and R. L. Walsworth, 2015, Nat. Nanotechnol. 10, 859.

Arai, K., J. Lee, C. Belthangady, D. R. Glenn, H. Zhang, and R. L. Walsworth, 2018, Nat. Commun. 9, 4996.

Ariyaratne, A., D. Bluvstein, B. A. Myers, and A. C. B. Jayich, 2018, Nat. Commun. 9, 2406.

Arroyo-Camejo, S., A. Lazariev, S. W. Hell, and G. Balasubramanian, 2014, Nat. Commun. 5, 4870.

Ashbaugh III, C. E., 1988, Gems Gemol. 24, 196.

Aslam, N., G. Waldherr, P. Neumann, F. Jelezko, and J. Wrachtrup, 2013, New J. Phys. **15**, 013064.

Aslam, N., et al., 2017, Science 357, 67.

Babinec, T. M., H. Fedder, J. T. Choy, I. Bulu, M. W. Doherty, P. R. Hemmer, J. Wrachtrup, and M. Loncar, 2012, in *Conference on Lasers and Electro-Optics 2012* (Optical Society of America, Washington, DC), p. JW1I.6.

Babinec, T. M., B. J. M. Hausmann, M. Khan, Y. Zhang, J. R. Maze, P. R. Hemmer, and M. Loncar, 2010, Nat. Nanotechnol. 5, 195. Backlund, M. P., P. Kehayias, and R. L. Walsworth, 2017, Phys. Rev. Applied 8, 054003.

Baker, J., 2007, Diam. Relat. Mater. 16, 216.

Balasubramanian, G., et al., 2008, Nature (London) 455, 648.

Balasubramanian, G., et al., 2009, Nat. Mater. 8, 383.

Balmer, R. S., et al., 2009, J. Phys. Condens. Matter 21, 364221.

Bangert, U., R. Barnes, M. H. Gass, A. L. Bleloch, and I. S. Godfrey, 2009, J. Phys. Condens. Matter 21, 364208.

Baranov, P. G., H. J. von Bardeleben, F. Jelezko, and J. Wrachtrup, 2017, "Retrospectives: Magnetic resonance studies of intrinsic defects in semiconductors," in *Magnetic Resonance*

- of Semiconductors and Their Nanostructures: Basic and Advanced Applications (Springer, Vienna), pp. 179–211.
- Barfuss, A., M. Kasperczyk, J. Kölbl, and P. Maletinsky, 2019, Phys. Rev. B **99**, 174102.
- Bar-Gill, N., L. M. Pham, C. Belthangady, D. Le Sage, P. Cappellaro, J. R. Maze, M. D. Lukin, A. Yacoby, and R. Walsworth, 2012, Nat. Commun. 3, 858.
- Bar-Gill, N., L. M. Pham, A. Jarmola, D. Budker, and R. L. Walsworth, 2013, Nat. Commun. 4, 1743.
- Barry, J. F., M. J. Turner, J. M. Schloss, D. R. Glenn, Y. Song, M. D. Lukin, H. Park, and R. L. Walsworth, 2016, Proc. Natl. Acad. Sci. U.S.A. 113, 14133.
- Barson, M. S. J., E. Krausz, N. B. Manson, and M. W. Doherty, 2019, Nanophotonics 8, 1985.
- Barson, M. S. J., et al., 2017, Nano Lett. 17, 1496.
- Bauch, E., 2010, "Nitrogen-Vacancy Defects in Diamond for sub-millimeter Magnetometry," master's thesis (Technische Universität Berlin and University of California Berkeley).
- Bauch, E., C. A. Hart, J. M. Schloss, M. J. Turner, J. F. Barry, P. Kehayias, S. Singh, and R. L. Walsworth, 2018, Phys. Rev. X 8, 031025.
- Bauch, E., et al., 2019, arXiv:1904.08763.
- Beha, K., A. Batalov, N.B. Manson, R. Bratschitsch, and A. Leitenstorfer, 2012, Phys. Rev. Lett. **109**, 097404.
- Belthangady, C., N. Bar-Gill, L. M. Pham, K. Arai, D. Le Sage, P. Cappellaro, and R. L. Walsworth, 2013, Phys. Rev. Lett. 110, 157601.
- Bernien, H., et al., 2013, Nature (London) 497, 86.
- Berry, M. V., 1984, Proc. R. Soc. A 392, 45.
- Bluvstein, D., Z. Zhang, and A. C. B. Jayich, 2019, Phys. Rev. Lett. **122**, 076101.
- Boesch, B. P., et al., 2016, "DNV magnetic field detector," WO Patent No. 2016/118791 Al.
- Bogdanov, S., et al., 2017, Phys. Rev. B 96, 035146.
- Bonato, C., M. S. Blok, H. T. Dinani, D. W. Berry, M. L. Markham, D. J. Twitchen, and R. Hanson, 2016, Nat. Nanotechnol. 11, 247.
- Boss, J. M., K. Chang, J. Armijo, K. Cujia, T. Rosskopf, J. R. Maze, and C. L. Degen, 2016, Phys. Rev. Lett. 116, 197601.
- Boss, J. M., K. S. Cujia, J. Zopes, and C. L. Degen, 2017, Science **356**, 837.
- Botsoa, J., T. Sauvage, M.-P. Adam, P. Desgardin, E. Leoni, B. Courtois, F. Treussart, and M.-F. Barthe, 2011, Phys. Rev. B 84, 125209
- Bourgeois, E., A. Jarmola, P. Siyushev, M. Gulka, J. Hruby, F. Jelezko, D. Budker, and M. Nesladek, 2015, Nat. Commun. 6, 8577.
- Bourgeois, E., et al., 2017, Phys. Rev. B 95, 041402.
- Boyd, S. R., I. Kiflawi, and G. S. Woods, 1994, Philos. Mag. B **69**, 1149.
- Braun, D., G. Adesso, F. Benatti, R. Floreanini, U. Marzolino, M. W. Mitchell, and S. Pirandola, 2018, Rev. Mod. Phys. **90**, 035006.
- Breeding, C. M., and J. E. Shigley, 2009, Gems Gemol. 45, 96.
- Breeze, J. D., E. Salvadori, J. Sathian, N. M. Alford, and C. W. M. Kay, 2018, Nature (London) 555, 493.
- Breuer, S. J., and P. R. Briddon, 1995, Phys. Rev. B 51, 6984.
- Bube, R., 1960, Photoconductivity of Solids (Wiley, New York).
- Buchan, J. T., M. Robinson, H. J. Christie, D. L. Roach, D. K. Ross, and N. A. Marks, 2015, J. Appl. Phys. 117, 245901.
- Bucher, D. B., D. R. Glenn, H. Park, M. D. Lukin, and R. L. Walsworth, 2018, arXiv:1810.02408.
- Budker, D., and M. Romalis, 2007, Nat. Phys. 3, 227.

- Bursill, L. A., and R. W. Glaisher, 1985, Am. Mineral. **70**, 608, https://pubs.geoscienceworld.org/msa/ammin/article/70/5-6/608/41757/Aggregation-and-dissolution-of-small-and-extended.
- Bylander, J., S. Gustavsson, F. Yan, F. Yoshihara, K. Harrabi, G. Fitch, D. G. Cory, Y. Nakamura, J.-S. Tsai, and W. D. Oliver, 2011, Nat. Phys. 7, 565.
- Cai, J., F. Jelezko, M. B. Plenio, and A. Retzker, 2013, New J. Phys. 15, 013020.
- Campbell, B., W. Choudhury, A. Mainwood, M. Newton, and G. Davies, 2002, Nucl. Instrum. Methods Phys. Res., Sect. A 476, 680
- Campbell, B., and A. Mainwood, 2000, Phys. Status Solidi A 181, 99.
- Cann, B. L., 2009, "Magnetic resonance studies of point defects in diamond," Ph.D. thesis (University of Warwick).
- Cao, G. Z., F. A. J. M. Driessen, G. J. Bauhuis, L. J. Giling, and P. F. A. Alkemade, 1995, J. Appl. Phys. **78**, 3125.
- Cao, J., 1994, J. Magn. Reson., Ser. B 103, 296.
- Casola, F., T. van der Sar, and A. Yacoby, 2018, Nat. Rev. Mater. 3, 17088.
- Chapman, R., and T. Plakhotnik, 2011, Chem. Phys. Lett. **507**, 190. Charles, S. J., J. E. Butler, B. N. Feygelson, M. E. Newton, D. L. Carroll, J. W. Steeds, H. Darwish, C.-S. Yan, H. K. Mao, and R. J. Hemley, 2004, Phys. Status Solidi A **201**, 2473.
- Chatzidrosos, G., A. Wickenbrock, L. Bougas, N. Leefer, T. Wu, K. Jensen, Y. Dumeige, and D. Budker, 2017, Phys. Rev. Applied 8, 044019.
- Chen, X.-D., S. Li, A. Shen, Y. Dong, C.-H. Dong, G.-C. Guo, and F.-W. Sun, 2017, Phys. Rev. Applied 7, 014008.
- Childress, L., M. V. Gurudev Dutt, J. M. Taylor, A. S. Zibrov, F. Jelezko, J. Wrachtrup, P. R. Hemmer, and M. D. Lukin, 2006, Science 314, 281.
- Choi, J., et al., 2017, Phys. Rev. Lett. 118, 093601.
- Choi, S., N. Y. Yao, and M. D. Lukin, 2017a, Phys. Rev. Lett. 119, 183603
- Choi, S., N. Y. Yao, and M. D. Lukin, 2017b, arXiv:1801.00042.
- Choy, J. T., I. Bulu, B. J. M. Hausmann, E. Janitz, I.-C. Huang, and M. Loncar, 2013, Appl. Phys. Lett. **103**, 161101.
- Choy, J. T., B. J. M. Hausmann, T. M. Babinec, I. Bulu, M. Khan, P. Maletinsky, A. Yacoby, and M. Loncar, 2011, Nat. Photonics 5, 738
- Chrostoski, P., H. R. Sadeghpour, and D. H. Santamore, 2018, Phys. Rev. Applied **10**, 064056.
- Chu, Y., et al., 2014, Nano Lett. 14, 1982.
- Clevenson, H., M. E. Trusheim, C. Teale, T. Schroder, D. Braje, and D. Englund, 2015, Nat. Phys. 11, 393.
- Collins, A. T., 2002, J. Phys. Condens. Matter 14, 3743.
- Collins, A. T., 2007, New Diamond Front. Carbon Technol. 17, http://myukk.xsrv.jp/free_journal/download.php?fn=NDFCT532 _full.pdf.
- Collins, A. T., H. Kanda, and H. Kitawaki, 2000, Diam. Relat. Mater. 9, 113.
- Cook, R. J., and D. H. Whiffen, 1966, Proc. R. Soc. A 295, 99.
- Cramer, J., N. Kalb, M. A. Rol, B. Hensen, M. S. Blok, M. Markham, D. J. Twitchen, R. Hanson, and T. H. Taminiau, 2016, Nat. Commun. 7, 11526.
- Cruddace, R., 2007, "Magnetic resonance and optical studies of point defects in single crystal CVD diamond," Ph.D. thesis (University of Warwick).
- Cui, S., and E. L. Hu, 2013, Appl. Phys. Lett. 103, 051603.
- Cywiński, L., R. M. Lutchyn, C. P. Nave, and S. Das Sarma, 2008, Phys. Rev. B 77, 174509.

- Dale, M. W., 2015, "Colour Centres on Demand in Diamond," Ph.D. thesis (University of Warwick).
- Dannefaer, S., T. Bretagnon, and D. Kerr, 1993, Diam. Relat. Mater. **2**, 1479.
- Dannefaer, S., P. Mascher, and D. Kerr, 1992, Diam. Relat. Mater. 1, 407.
- Davies, G., 1976, J. Phys. C 9, L537.
- Davies, G., 1979, J. Phys. C 12, 2551.
- Davies, G., 1981, Rep. Prog. Phys. 44, 787.
- Davies, G., B. Campbell, A. Mainwood, M. Newton, M. Watkins, H. Kanda, and T. Anthony, 2001, Phys. Status Solidi A 186, 187.
- Davies, G., and T. Evans, 1972, Proc. R. Soc. A 328, 413.
- Davies, G., and M. F. Hamer, 1976, Proc. R. Soc. A 348, 285.
- Davies, G., S. C. Lawson, A. T. Collins, A. Mainwood, and S. J. Sharp, 1992, Phys. Rev. B **46**, 13157.
- Davis, H. C., P. Ramesh, A. Bhatnagar, A. Lee-Gosselin, J. F. Barry, D. R. Glenn, R. L. Walsworth, and M. G. Shapiro, 2018, Nat. Commun. 9, 131.
- Deák, P., B. Aradi, M. Kaviani, T. Frauenheim, and A. Gali, 2014, Phys. Rev. B **89**, 075203.
- Degen, C. L., 2008, Appl. Phys. Lett. 92, 243111.
- Degen, C. L., F. Reinhard, and P. Cappellaro, 2017, Rev. Mod. Phys. **89**, 035002.
- DeGiorgio, V., and M. O. Scully, 1970, Phys. Rev. A 2, 1170.
- de Lange, G., T. van der Sar, M. Blok, Z.-H. Wang, V. Dobrovitski, and R. Hanson, 2012, Sci. Rep. 2, 382.
- de Lange, G., Z. H. Wang, D. Ristè, V. V. Dobrovitski, and R. Hanson, 2010, Science 330, 60.
- de Sousa, R., 2009, "Electron spin as a spectrometer of nuclear-spin noise and other fluctuations," in *Electron Spin Resonance and Related Phenomena in Low-Dimensional Structures* (Springer, Berlin/Heidelberg), pp. 183–220.
- DeVience, S. J., et al., 2015, Nat. Nanotechnol. 10, 129.
- D'Haenens-Johansson, U. F., K. S. Moe, P. Johnson, S. Y. Wong, R. Lu, and W. Wang, 2014, Gems Gemol. **50**, 30.
- D'Haenens-Johansson, U. F., et al., 2015, Gems Gemol. 51, 260.
- Dischler, B., 2012, Handbook of Spectral Lines in Diamond: Volume 1: Tables and Interpretations (Springer, New York), Vol. 1.
- Dobrinets, I. A., V. G. Vins, and A. M. Zaitsev, 2013, *HPHT-Treated Diamonds: Diamonds Forever* (Springer, New York).
- Dobrovitski, V. V., A. E. Feiguin, D. D. Awschalom, and R. Hanson, 2008, Phys. Rev. B 77, 245212.
- Dodson, J., et al., 2011, Proc. SPIE Int. Soc. Opt. Eng. 8016, 80160L.
- Doherty, M. W., F. Dolde, H. Fedder, F. Jelezko, J. Wrachtrup, N. B. Manson, and L. C. L. Hollenberg, 2012, Phys. Rev. B **85**, 205203.
- Doherty, M. W., N. B. Manson, P. Delaney, F. Jelezko, J. Wrachtrup, and L. C. Hollenberg, 2013, Phys. Rep. **528**, 1.
- Doherty, M. W., C. A. Meriles, A. Alkauskas, H. Fedder, M. J. Sellars, and N. B. Manson, 2016, Phys. Rev. X 6, 041035.
- Doherty, M. W., et al., 2014, Phys. Rev. Lett. 112, 047601.
- Doi, Y., et al., 2014, Phys. Rev. X 4, 011057.
- Doi, Y., et al., 2016, Phys. Rev. B 93, 081203.
- Dolde, F., I. Jakobi, B. Naydenov, N. Zhao, S. Pezzagna, C. Trautmann, J. Meijer, P. Neumann, F. Jelezko, and J. Wrachtrup, 2013, Nat. Phys. **9**, 139.
- Dolde, F., et al., 2011, Nat. Phys. 7, 459.
- Drake, M., E. Scott, and J. A. Reimer, 2016, New J. Phys. 18, 013011.
- Dréau, A., M. Lesik, L. Rondin, P. Spinicelli, O. Arcizet, J.-F. Roch, and V. Jacques, 2011, Phys. Rev. B **84**, 195204.
- Dréau, A., J.-R. Maze, M. Lesik, J.-F. Roch, and V. Jacques, 2012, Phys. Rev. B 85, 134107.

- Dumeige, Y., et al., 2013, Phys. Rev. B 87, 155202.
- Dwyer, K. J., J. M. Pomeroy, and D. S. Simons, 2013, Appl. Phys. Lett. **102**, 254104.
- Edmonds, A. M., 2008, "Magnetic resonance studies of point defects in single crystal diamond," Ph.D. thesis (University of Warwick).
- Edmonds, A. M., U. F. S. D'Haenens-Johansson, R. J. Cruddace, M. E. Newton, K.-M. C. Fu, C. Santori, R. G. Beausoleil, D. J. Twitchen, and M. L. Markham, 2012, Phys. Rev. B **86**, 035201.
- Eichhorn, T. R., C. A. McLellan, and A. C. B. Jayich, 2019, Phys. Rev. Mater. 3, 113802.
- Eisenach, E. R., J. F. Barry, L. M. Pham, R. G. Rojas, D. R. Englund, and D. A. Braje, 2018, Rev. Sci. Instrum. 89, 094705.
- El-Ella, H. A. R., S. Ahmadi, A. M. Wojciechowski, A. Huck, and U. L. Andersen, 2017, Opt. Express 25, 14809.
- Epstein, R. J., F. M. Mendoza, Y. K. Kato, and D. D. Awschalom, 2005, Nat. Phys. 1, 94.
- Fang, K., V. M. Acosta, C. Santori, Z. Huang, K. M. Itoh, H. Watanabe, S. Shikata, and R. G. Beausoleil, 2013, Phys. Rev. Lett. 110, 130802.
- Farchi, E., Y. Ebert, D. Farfurnik, G. Haim, R. Shaar, and N. Bar-Gill, 2017, SPIN **07**, 1740015.
- Farfurnik, D., N. Alfasi, S. Masis, Y. Kauffmann, E. Farchi, Y. Romach, Y. Hovav, E. Buks, and N. Bar-Gill, 2017, Appl. Phys. Lett. 111, 123101.
- Farfurnik, D., A. Jarmola, L. M. Pham, Z. H. Wang, V. V. Dobrovitski, R. L. Walsworth, D. Budker, and N. Bar-Gill, 2015, Phys. Rev. B 92, 060301.
- Farrer, R., 1969, Solid State Commun. 7, 685.
- Fastenau, R., 1982, "Diffusion limited reactions in crystalline solids," Ph.D. thesis (Technische Hogeschool Delft).
- Fávaro de Oliveira, F., D. Antonov, Y. Wang, P. Neumann, S. A. Momenzadeh, T. Häußermann, A. Pasquarelli, A. Denisenko, and J. Wrachtrup, 2017, Nat. Commun. 8, 15409.
- Fávaro de Oliveira, F., S. A. Momenzadeh, D. Antonov, J. Scharpf, C. Osterkamp, B. Naydenov, F. Jelezko, A. Denisenko, and J. Wrachtrup, 2016, Nano Lett. 16, 2228.
- Fedder, H., F. Dolde, F. Rempp, T. Wolf, P. Hemmer, F. Jelezko, and J. Wrachtrup, 2011, Appl. Phys. B **102**, 497.
- Felton, S., B. L. Cann, A. M. Edmonds, S. Liggins, R. J. Cruddace, M. E. Newton, D. Fisher, and J. M. Baker, 2009, J. Phys. Condens. Matter 21, 364212.
- Felton, S., A. M. Edmonds, M. E. Newton, P. M. Martineau, D. Fisher, and D. J. Twitchen, 2008, Phys. Rev. B 77, 081201.
- Fescenko, I., A. Laraoui, J. Smits, N. Mosavian, P. Kehayias, J. Seto, L. Bougas, A. Jarmola, and V. M. Acosta, 2019, Phys. Rev. Applied 11, 034029.
- Fisher, D., D. J. F. Evans, C. Glover, C. J. Kelly, M. J. Sheehy, and G. C. Summerton, 2006, Diam. Relat. Mater. 15, 1636.
- Fletcher, R. C., and W. L. Brown, 1953, Phys. Rev. 92, 585.
- Forneris, J., S. Ditalia Tchernij, A. Tengattini, E. Enrico, V. Grilj, N. Skukan, G. Amato, L. Boarino, M. Jakšić, and P. Olivero, 2017, Carbon 113, 76.
- Fraczek, E., V. G. Savitski, M. Dale, B. G. Breeze, P. Diggle, M. Markham, A. Bennett, H. Dhillon, M. E. Newton, and A. J. Kemp, 2017, Opt. Mater. Express 7, 2571.
- Fu, K.-M. C., C. Santori, P. E. Barclay, and R. G. Beausoleil, 2010, Appl. Phys. Lett. 96, 121907.
- Fu, R. R., et al., 2014, Science 346, 1089.
- Fuchs, G. D., V. V. Dobrovitski, R. Hanson, A. Batra, C. D. Weis, T. Schenkel, and D. D. Awschalom, 2008, Phys. Rev. Lett. **101**, 117601.
- Fujita, N., R. Jones, S. Öberg, and P. Briddon, 2009, Diam. Relat. Mater. 18, 843.

- Fukui, T., et al., 2014, Appl. Phys. Express 7, 055201.
- Gaillou, E., J. E. Post, D. Rost, and J. E. Butler, 2012, Am. Mineral.
- Gammelmark, S., and K. Mølmer, 2011, New J. Phys. 13, 053035.Gaukroger, M., P. Martineau, M. Crowder, I. Friel, S. Williams, and D. Twitchen, 2008, Diam. Relat. Mater. 17, 262.
- Glenn, D. R., D. B. Bucher, J. Lee, M. D. Lukin, H. Park, and R. L. Walsworth, 2018, Nature (London) 555, 351.
- Glenn, D. R., R. R. Fu, P. Kehayias, D. Le Sage, E. A. Lima, B. P. Weiss, and R. L. Walsworth, 2017, Geochem. Geophys. Geosyst. 18, 3254.
- Glenn, D. R., K. Lee, H. Park, R. Weissleder, A. Yacoby, M. D. Lukin, H. Lee, R. L. Walsworth, and C. B. Connolly, 2015, Nat. Methods 12, 736.
- Glover, C., 2003, "A Study of Defects in Single Crystal CVD Diamond," Ph.D. thesis (University of Warwick).
- Glover, C., M. E. Newton, P. Martineau, D. J. Twitchen, and J. M. Baker, 2003, Phys. Rev. Lett. **90**, 185507.
- Glover, C., M. E. Newton, P. M. Martineau, S. Quinn, and D. J. Twitchen, 2004, Phys. Rev. Lett. **92**, 135502.
- Goldman, M. L., M. W. Doherty, A. Sipahigil, N. Y. Yao, S. D. Bennett, N. B. Manson, A. Kubanek, and M. D. Lukin, 2015, Phys. Rev. B **91**, 165201.
- Goldman, M. L., A. Sipahigil, M. W. Doherty, N. Y. Yao, S. D. Bennett, M. Markham, D. J. Twitchen, N. B. Manson, A. Kubanek, and M. D. Lukin, 2015, Phys. Rev. Lett. 114, 145502.
- Goss, J. P., P. R. Briddon, V. Hill, R. Jones, and M. J. Rayson, 2014, J. Phys. Condens. Matter 26, 145801.
- Goss, J. P., P. R. Briddon, S. Papagiannidis, and R. Jones, 2004, Phys. Rev. B **70**, 235208.
- Goss, J. P., P. R. Briddon, M. J. Rayson, S. J. Sque, and R. Jones, 2005, Phys. Rev. B **72**, 035214.
- Green, B. L., B. G. Breeze, and M. E. Newton, 2017, J. Phys. Condens. Matter 29, 225701.
- Green, B. L., M. W. Dale, M. E. Newton, and D. Fisher, 2015, Phys. Rev. B **92**, 165204.
- Grezes, C., et al., 2015, Phys. Rev. A 92, 020301.
- Grinolds, M. S., M. Warner, K. De Greve, Y. Dovzhenko, L. Thiel, R. L. Walsworth, S. Hong, P. Maletinsky, and A. Yacoby, 2014, Nat. Nanotechnol. 9, 279.
- Groot-Berning, K., et al., 2014, Phys. Status Solidi A 211, 2268.
- Grosz, A., M. J. Haji-Sheikh, and S. C. Mukhopadhyay, 2017, *High Sensitivity Magnetometers* (Springer, New York).
- Grotz, B., et al., 2012, Nat. Commun. 3, 729.
- Gulka, M., et al., 2017, Phys. Rev. Applied 7, 044032.
- Gullion, T., D. B. Baker, and M. S. Conradi, 1990, J. Magn. Reson. **89**, 479.
- Gupta, A., L. Hacquebard, and L. Childress, 2016, J. Opt. Soc. Am. B 33, B28.
- Häberle, T., T. Oeckinghaus, D. Schmid-Lorch, M. Pfender, F. F. de Oliveira, S. A. Momenzadeh, A. Finkler, and J. Wrachtrup, 2017, Rev. Sci. Instrum. **88**, 013702.
- Hacquebard, L., and L. Childress, 2018, Phys. Rev. A 97, 063408.
 Hadden, J. P., J. P. Harrison, A. C. Stanley-Clarke, L. Marseglia, Y. L. D. Ho, B. R. Patton, J. L. O'Brien, and J. G. Rarity, 2010, Appl. Phys. Lett. 97, 241901.
- Hahn, E. L., 1950, Phys. Rev. 80, 580.
- Hall, L. T., J. H. Cole, and L. C. L. Hollenberg, 2014, Phys. Rev. B **90**, 075201.
- Hall, L. T., P. Kehayias, D. A. Simpson, A. Jarmola, A. Stacey, D. Budker, and L. C. L. Hollenberg, 2016, Nat. Commun. 7, 10211.
- Hämäläinen, M., R. Hari, R.J. Ilmoniemi, J. Knuutila, and O.V. Lounasmaa, 1993, Rev. Mod. Phys. **65**, 413.

- Hanson, R., V. V. Dobrovitski, A. E. Feiguin, O. Gywat, and D. D. Awschalom, 2008, Science 320, 352.
- Hanson, R., F.M. Mendoza, R.J. Epstein, and D.D. Awschalom, 2006, Phys. Rev. Lett. **97**, 087601.
- Hartland, C. B., 2014, "A Study of Point Defects in CVD Diamond Using Electron Paramagnetic Resonance and Optical Spectroscopy," Ph.D. thesis (University of Warwick).
- Hauf, M. V., et al., 2011, Phys. Rev. B 83, 081304.
- Hauf, M. V., et al., 2014, Nano Lett. 14, 2359.
- He, X.-F., N. B. Manson, and P. T. H. Fisk, 1993, Phys. Rev. B 47, 8816.
- Hensen, B., et al., 2015, Nature (London) 526, 682.
- Heremans, F. J., G. D. Fuchs, C. F. Wang, R. Hanson, and D. D. Awschalom, 2009, Appl. Phys. Lett. **94**, 152102.
- Hernández-Gómez, S., F. Poggiali, P. Cappellaro, and N. Fabbri, 2018, Phys. Rev. B **98**, 214307.
- Himics, L., S. Tóth, M. Veres, Z. Balogh, and M. Koós, 2014, Appl. Phys. Lett. 104, 093101.
- Hoa, L. T. M., T. Ouisse, D. Chaussende, M. Naamoun, A. Tallaire, and J. Achard, 2014, Cryst. Growth Des. 14, 5761.
- Hobbs, P. C., 2011, Building Electro-optical Systems: Making it all Work (Wiley, New York).
- Hopper, D. A., R. R. Grote, A. L. Exarhos, and L. C. Bassett, 2016, Phys. Rev. B 94, 241201.
- Hopper, D. A., R. R. Grote, S. M. Parks, and L. C. Bassett, 2018, ACS Nano 12, 4678.
- Hopper, D. A., H. J. Shulevitz, and L. C. Bassett, 2018, Micromachines 9, 437.
- Horsley, A., P. Appel, J. Wolters, J. Achard, A. Tallaire, P. Maletinsky, and P. Treutlein, 2018, Phys. Rev. Applied 10, 044039.
- Hounsome, L. S., R. Jones, P. M. Martineau, D. Fisher, M. J. Shaw, P. R. Briddon, and S. Öberg, 2006, Phys. Rev. B 73, 125203.
- Hrubesch, F. M., G. Braunbeck, M. Stutzmann, F. Reinhard, and M. S. Brandt, 2017, Phys. Rev. Lett. 118, 037601.
- Hsieh, S., et al., 2019, Science 366, 1349.
- Hu, X., Y. Dai, R. Li, H. Shen, and X. He, 2002, Solid State Commun. 122, 45.
- Huxter, V. M., T. A. A. Oliver, D. Budker, and G. R. Fleming, 2013, Nat. Phys. 9, 744.
- Iakoubovskii, K., G. J. Adriaenssens, and M. Nesladek, 2000, J. Phys. Condens. Matter 12, 189.
- Iakoubovskii, K., and A. Stesmans, 2002, Phys. Rev. B 66, 045406.
 Ishikawa, T., K.-M. C. Fu, C. Santori, V. M. Acosta, R. G. Beausoleil, H. Watanabe, S. Shikata, and K. M. Itoh, 2012, Nano Lett. 12, 2083.
- Itano, W. M., J. C. Bergquist, J. J. Bollinger, J. M. Gilligan, D. J. Heinzen, F. L. Moore, M. G. Raizen, and D. J. Wineland, 1993, Phys. Rev. A 47, 3554.
- Itoh, K. M., and H. Watanabe, 2014, MRS Commun. 4, 143.
- Ivády, V., T. Simon, J. R. Maze, I. A. Abrikosov, and A. Gali, 2014, Phys. Rev. B 90, 235205.
- Jacques, V., P. Neumann, J. Beck, M. Markham, D. Twitchen, J. Meijer, F. Kaiser, G. Balasubramanian, F. Jelezko, and J. Wrachtrup, 2009, Phys. Rev. Lett. 102, 057403.
- Jakobi, I., S. A. Momenzadeh, F. F. de Oliveira, J. Michl, F. Ziem, M. Schreck, P. Neumann, A. Denisenko, and J. Wrachtrup, 2016, J. Phys. Conf. Ser. 752, 012001.
- Jamonneau, P., et al., 2016, Phys. Rev. B 93, 024305.
- Jarmola, A., V. M. Acosta, K. Jensen, S. Chemerisov, and D. Budker, 2012, Phys. Rev. Lett. 108, 197601.
- Jaskula, J.-C., E. Bauch, S. Arroyo-Camejo, M. D. Lukin, S. W. Hell, A. S. Trifonov, and R. L. Walsworth, 2017, Opt. Express 25, 11048.

- Jaskula, J.-C., B. J. Shields, E. Bauch, M. D. Lukin, A. S. Trifonov, and R. L. Walsworth, 2019, Phys. Rev. Applied 11, 064003.
- Jayakumar, H., S. Dhomkar, J. Henshaw, and C. A. Meriles, 2018, Appl. Phys. Lett. 113, 122404.
- Jensen, K., V. M. Acosta, A. Jarmola, and D. Budker, 2013, Phys. Rev. B 87, 014115.
- Jensen, K., P. Kehayias, and D. Budker, 2017, in Smart Sensors, Measurement and Instrumentation: High Sensitivity Magnetometers (Springer, Cham, Switzerland), Vol. 19, pp. 553–576, .
- Jensen, K., N. Leefer, A. Jarmola, Y. Dumeige, V. M. Acosta, P. Kehayias, B. Patton, and D. Budker, 2014, Phys. Rev. Lett. 112, 160802.
- Jeske, J., J. H. Cole, and A. D. Greentree, 2016, New J. Phys. 18, 013015.
- Jeske, J., et al., 2017, Nat. Commun. 8, 14000.
- Ji, P., and M. V. G. Dutt, 2016, Phys. Rev. B 94, 024101.
- Jiang, L., et al., 2009, Science 326, 267.
- Jones, R., J. Goss, H. Pinto, and D. Palmer, 2015, Diam. Relat. Mater. 53, 35.
- Jones, R., L. S. Hounsome, N. Fujita, S. Öberg, and P. R. Briddon, 2007, Phys. Status Solidi A 204, 3059.
- Jones, R., J. E. Lowther, and J. Goss, 1996, Appl. Phys. Lett. 69, 2489
- Kageura, T., et al., 2017, Appl. Phys. Express 10, 055503.
- Kaiser, W., and W. Bond, 1959, Phys. Rev. 115, 857.
- Kalish, R., 1999, Carbon 37, 781.
- Kanda, H., 2000, Braz. J. Phys. 30, 482.
- Karaveli, S., O. Gaathon, A. Wolcott, R. Sakakibara, O. A. Shemesh, D. S. Peterka, E. S. Boyden, J. S. Owen, R. Yuste, and D. Englund, 2016, Proc. Natl. Acad. Sci. U.S.A. 113, 3938.
- Katagiri, M., J. Isoya, S. Koizumi, and H. Kanda, 2004, Appl. Phys. Lett. **85**, 6365.
- Kato, H., M. Wolfer, C. Schreyvogel, M. Kunzer, W. Müller-Sebert, H. Obloh, S. Yamasaki, and C. Nebel, 2013, Appl. Phys. Lett. 102, 151101.
- Kaupp, H., T. Hümmer, M. Mader, B. Schlederer, J. Benedikter, P. Haeusser, H.-C. Chang, H. Fedder, T. W. Hänsch, and D. Hunger, 2016, Phys. Rev. Applied 6, 054010.
- Kehayias, P., M. W. Doherty, D. English, R. Fischer, A. Jarmola, K. Jensen, N. Leefer, P. Hemmer, N. B. Manson, and D. Budker, 2013, Phys. Rev. B **88**, 165202.
- Kehayias, P., M. J. Turner, R. Trubko, J. M. Schloss, C. A. Hart, M. Wesson, D. R. Glenn, and R. L. Walsworth, 2019, Phys. Rev. B 100, 174103.
- Kehayias, P., et al., 2017, Nat. Commun. 8, 188.
- Kessler, E. M., I. Lovchinsky, A. O. Sushkov, and M. D. Lukin, 2014, Phys. Rev. Lett. 112, 150802.
- Khan, R. U. A., B. L. Cann, P. M. Martineau, J. Samartseva, J. J. P. Freeth, S. J. Sibley, C. B. Hartland, M. E. Newton, H. K. Dhillon, and D. J. Twitchen, 2013, J. Phys. Condens. Matter 25, 275801.
- Khan, R. U. A., P. M. Martineau, B. L. Cann, M. E. Newton, and D. J. Twitchen, 2009, J. Phys. Condens. Matter 21, 364214.
- Kiflawi, I., A. T. Collins, K. Iakoubovskii, and D. Fisher, 2007, J. Phys. Condens. Matter 19, 046216.
- Kim, E., V. M. Acosta, E. Bauch, D. Budker, and P. R. Hemmer, 2012, Appl. Phys. Lett. 101, 082410.
- Kim, M., H. J. Mamin, M. H. Sherwood, K. Ohno, D. D. Awschalom, and D. Rugar, 2015, Phys. Rev. Lett. 115, 087602.
- Kirschner, F. K. K., F. Flicker, A. Yacoby, N. Y. Yao, and S. J. Blundell, 2018, Phys. Rev. B **97**, 140402.
- Kirui, J., J. van Wyk, and M. Hoch, 2013, Diam. Relat. Mater. **39**, 78. Kitching, J., 2018, Appl. Phys. Rev. **5**, 031302.
- Kittel, C., and E. Abrahams, 1953, Phys. Rev. 90, 238.

- Kleinsasser, E. E., M. M. Stanfield, J. K. Q. Banks, Z. Zhu, W.-D. Li, V. M. Acosta, H. Watanabe, K. M. Itoh, and K.-M. C. Fu, 2016, Appl. Phys. Lett. 108, 202401.
- Knowles, H. S., D. M. Kara, and M. Atatüre, 2014, Nat. Mater. 13, 21.
- Koike, J., D. M. Parkin, and T. E. Mitchell, 1992, Appl. Phys. Lett. **60**, 1450.
- Kolkowitz, S., et al., 2015, Science 347, 1129.
- Kucsko, G., P. C. Maurer, N. Y. Yao, M. Kubo, H. J. Noh, P. K. Lo, H. Park, and M. D. Lukin, 2013, Nature (London) 500, 54.
- Kucsko, G., et al., 2018, Phys. Rev. Lett. 121, 023601.
- Kwan, C. L., and T. F. Yen, 1979, Anal. Chem. 51, 1225.
- Lawson, S. C., D. Fisher, D. C. Hunt, and M. E. Newton, 1998, J. Phys. Condens. Matter 10, 6171.
- Layden, D., and P. Cappellaro, 2018, npj Quantum Inf. 4, 30.
- Layden, D., S. Zhou, P. Cappellaro, and L. Jiang, 2019, Phys. Rev. Lett. 122, 040502.
- Lazariev, A., S. Arroyo-Camejo, G. Rahane, V. K. Kavatamane, and G. Balasubramanian, 2017, Sci. Rep. 7, 6586.
- Lea-wilsonf, M. A., J. N. Lomer, and J. A. V. Wyk, 1995, Philos. Mag. B **72**, 81.
- Le Sage, D., and K. Arai, 2011 (personal communication).
- Le Sage, D., K. Arai, D. R. Glenn, S. J. DeVience, L. M. Pham, L. Rahn-Lee, M. D. Lukin, A. Yacoby, A. Komeili, and R. L. Walsworth, 2013, Nature (London) 496, 486.
- Le Sage, D., L. M. Pham, N. Bar-Gill, C. Belthangady, M. D. Lukin, A. Yacoby, and R. L. Walsworth, 2012, Phys. Rev. B 85, 121202.
- Lesik, M., J.-P. Tetienne, A. Tallaire, J. Achard, V. Mille, A. Gicquel, J.-F. Roch, and V. Jacques, 2014, Appl. Phys. Lett. **104**, 113107.
- Levitt, M. H., 2008, Spin Dynamics: Basics of Nuclear Magnetic Resonance (John Wiley & Sons, New York), Chap. 11, 2nd ed.
- Li, L., E. H. Chen, J. Zheng, S. L. Mouradian, F. Dolde, T. Schröder, S. Karaveli, M. L. Markham, D. J. Twitchen, and D. Englund, 2015, Nano Lett. 15, 1493.
- Liggins, S., 2010, "Identification of point defects in treated single crystal diamond," Ph.D. thesis (University of Warwick).
- Lim, T.-S., J.-L. Chern, and K. Otsuka, 2002, Opt. Lett. **27**, 1037. Liu, Y.-X., A. Ajoy, and P. Cappellaro, 2019, Phys. Rev. Lett. **122**, 100501.
- Lobaev, M., A. Gorbachev, S. Bogdanov, A. Vikharev, D. Radishev, V. Isaev, V. Chernov, and M. Drozdov, 2017, Diam. Relat. Mater. 72, 1.
- Lomer, J. N., and A. M. A. Wild, 1973, Radiat. Eff. 17, 37.
- Londero, E., E. Bourgeois, M. Nesladek, and A. Gali, 2018, Phys. Rev. B 97, 241202.
- Loretz, M., S. Pezzagna, J. Meijer, and C. L. Degen, 2014, Appl. Phys. Lett. 104, 033102.
- Loretz, M., T. Rosskopf, and C. L. Degen, 2013, Phys. Rev. Lett. **110**, 017602.
- Loubser, J. H. N., and J. A. van Wyk, 1978, Rep. Prog. Phys. 41, 1201.
- Lovchinsky, I., et al., 2016, Science 351, 836.
- Lovchinsky, I., et al., 2017, Science 355, 503.
- Low, G. H., T. J. Yoder, and I. L. Chuang, 2014, Phys. Rev. A 89, 022341.
- Lyons, J. L., and C. G. V. de Walle, 2016, J. Phys. Condens. Matter **28**, 06LT01.
- Ma, Z., S. Zhang, Y. Fu, H. Yuan, Y. Shi, J. Gao, L. Qin, J. Tang, J. Liu, and Y. Li, 2018, Opt. Express 26, 382.
- Maclaurin, D., M. W. Doherty, L. C. L. Hollenberg, and A. M. Martin, 2012, Phys. Rev. Lett. 108, 240403.
- MacQuarrie, E. R., T. A. Gosavi, A. M. Moehle, N. R. Jungwirth, S. A. Bhave, and G. D. Fuchs, 2015, Optica 2, 233.

- Maertz, B. J., A. P. Wijnheijmer, G. D. Fuchs, M. E. Nowakowski, and D. D. Awschalom, 2010, Appl. Phys. Lett. **96**, 092504.
- Mainwood, A., 1999, Phys. Status Solidi A 172, 25.
- Malinauskas, T., K. Jarasiunas, E. Ivakin, V. Ralchenko, A. Gontar, and S. Ivakhnenko, 2008, Diam. Relat. Mater. 17, 1212.
- Mamin, H. J., M. H. Sherwood, M. Kim, C. T. Rettner, K. Ohno, D. D. Awschalom, and D. Rugar, 2014, Phys. Rev. Lett. 113, 030803.
- Manson, N. B., and J. P. Harrison, 2005, Diam. Relat. Mater. 14, 1705.
- Manson, N. B., M. Hedges, M. S. J. Barson, R. Ahlefeldt, M. W. Doherty, H. Abe, T. Ohshima, and M. J. Sellars, 2018, New J. Phys. **20**, 113037.
- Markham, M. J. Dodson, G. Scarsbrook, D. Twitchen, G. Scarsbrook, D. Scar
- Markham, M., J. Dodson, G. Scarsbrook, D. Twitchen, G. Balasubramanian, F. Jelezko, and J. Wrachtrup, 2011, Diam. Relat. Mater. 20, 134.
- Marseglia, L., et al., 2011, Appl. Phys. Lett. 98, 133107.
- Martin, J., R. Wannemacher, J. Teichert, L. Bischoff, and B. Köhler, 1999, Appl. Phys. Lett. **75**, 3096.
- Martineau, P. M., M. P. Gaukroger, K. B. Guy, S. C. Lawson, D. J. Twitchen, I. Friel, J. O. Hansen, G. C. Summerton, T. P. G. Addison, and R. Burns, 2009, J. Phys. Condens. Matter 21, 364205.
- Maurer, P. C., et al., 2010, Nat. Phys. 6, 912.
- Maurer, P. C., et al., 2012, Science 336, 1283.
- Maze, J. R., A. Dréau, V. Waselowski, H. Duarte, J.-F. Roch, and V. Jacques, 2012, New J. Phys. 14, 103041.
- Maze, J. R., et al., 2008, Nature (London) 455, 644.
- McCloskey, D., D. Fox, N. O'Hara, V. Usov, D. Scanlan, N. McEvoy, G. S. Duesberg, G. L. W. Cross, H. Z. Zhang, and J. F. Donegan, 2014, Appl. Phys. Lett. **104**, 031109.
- McLellan, C. A., B. A. Myers, S. Kraemer, K. Ohno, D. D. Awschalom, and A. C. Bleszynski Jayich, 2016, Nano Lett. 16, 2450.
- Meiboom, S., and D. Gill, 1958, Rev. Sci. Instrum. 29, 688.
- Meirzada, I., Y. Hovav, S. A. Wolf, and N. Bar-Gill, 2018, Phys. Rev. B 98, 245411.
- Meirzada, I., S. A. Wolf, A. Naiman, U. Levy, and N. Bar-Gill, 2019, Phys. Rev. B **100**, 125436.
- Michl, J., et al., 2014, Appl. Phys. Lett. 104, 102407.
- Michl, J., et al., 2019, Nano. Lett. 19, 4904.
- Mita, Y., 1996, Phys. Rev. B 53, 11360.
- Mitchell, E. W. J., 1965, "Radiation damage in diamond," in *Physical Properties of Diamond*, edited by R. Berman (Clarendon Press, Oxford).
- Miyazaki, T., Y. Miyamoto, T. Makino, H. Kato, S. Yamasaki, T. Fukui, Y. Doi, N. Tokuda, M. Hatano, and N. Mizuochi, 2014, Appl. Phys. Lett. **105**, 261601.
- Mizuochi, N., et al., 2009, Phys. Rev. B 80, 041201.
- Mkhitaryan, V. V., and V. V. Dobrovitski, 2014, Phys. Rev. B **89**, 224402.
- Mkhitaryan, V. V., F. Jelezko, and V. V. Dobrovitski, 2015, Sci. Rep. 5, 15402.
- Momenzadeh, S. A., R. J. Stöhr, F. F. de Oliveira, A. Brunner, A. Denisenko, S. Yang, F. Reinhard, and J. Wrachtrup, 2015, Nano Lett. 15, 165.
- Morishita, H., S. Kobayashi, M. Fujiwara, Hiromitsu Kato, Toshiharu Makino, Satoshi Yamasaki, and N. Mizuochi, 2020, Sci. Rep. 10, 792.
- Morishita, H., et al., 2011, Appl. Phys. Express 4, 021302.
- Mrózek, M., D. Rudnicki, P. Kehayias, A. Jarmola, D. Budker, and W. Gawlik, 2015, EPJ Quantum Techno. **2**, 22.

- Murai, T., et al., 2018, Appl. Phys. Lett. 112, 111903.
- Myers, B. A., A. Ariyaratne, and A. C. B. Jayich, 2017, Phys. Rev. Lett. **118**, 197201.
- Myers, B. A., A. Das, M. C. Dartiailh, K. Ohno, D. D. Awschalom, and A. C. Bleszynski Jayich, 2014, Phys. Rev. Lett. 113, 027602.
- Naydenov, B., F. Reinhard, A. Lämmle, V. Richter, R. Kalish, U. F. S. D'Haenens-Johansson, M. Newton, F. Jelezko, and J. Wrachtrup, 2010, Appl. Phys. Lett. 97, 242511.
- Neu, E., P. Appel, M. Ganzhorn, J. Miguel-Sánchez, M. Lesik, V. Mille, V. Jacques, A. Tallaire, J. Achard, and P. Maletinsky, 2014, Appl. Phys. Lett. 104, 153108.
- Neumann, P., J. Beck, M. Steiner, F. Rempp, H. Fedder, P.R. Hemmer, J. Wrachtrup, and F. Jelezko, 2010, Science 329, 542.
- Neumann, P., et al., 2009, New J. Phys. 11, 013017.
- Neumann, P., et al., 2010, Nat. Phys. 6, 249.
- Neumann, P., et al., 2013, Nano Lett. 13, 2738.
- Neves, A., and M. H. Nazaré, 2001, Properties, Growth and Applications of Diamond, Vol. 26 (Institution of Engineering and Technology, London).
- Newell, A. N., D. A. Dowdell, and D. H. Santamore, 2016, J. Appl. Phys. **120**, 185104.
- Newton, M., B. Campbell, D. Twitchen, J. Baker, and T. Anthony, 2002, Diam. Relat. Mater. 11, 618.
- Newton, M. E., 2007, EPR, ENDOR and EPR Imaging of Defects in Diamond (Royal Society of Chemistry, London), Chap. 6.
- Nöbauer, T., A. Angerer, B. Bartels, M. Trupke, S. Rotter, J. Schmiedmayer, F. Mintert, and J. Majer, 2015, Phys. Rev. Lett. 115, 190801.
- Nöbauer, T., K. Buczak, A. Angerer, S. Putz, G. Steinhauser, J. Akbarzadeh, H. Peterlik, J. Majer, J. Schmiedmayer, and M. Trupke, 2013, arXiv:1309.0453.
- Ohno, K., F. Joseph Heremans, L. C. Bassett, B. A. Myers, D. M. Toyli, A. C. Bleszynski Jayich, C. J. Palmstrøm, and D. D. Awschalom, 2012, Appl. Phys. Lett. **101**, 082413.
- O'Keeffe, M. F., L. Horesh, J. F. Barry, D. A. Braje, and I. L. Chuang, 2019, New J. Phys. **21**, 023015.
- Onoda, S., K. Tatsumi, M. Haruyama, T. Teraji, J. Isoya, W. Kada, T. Ohshima, and O. Hanaizumi, 2017, Phys. Status Solidi A 214, 1700160.
- Orwa, J., et al., 2012, Diam. Relat. Mater. 24, 6.
- Osterkamp, C., J. Lang, J. Scharpf, C. Müller, L. P. McGuinness, T. Diemant, R. J. Behm, B. Naydenov, and F. Jelezko, 2015, Appl. Phys. Lett. **106**, 113109.
- Palyanov, Y. N., I. N. Kupriyanov, A. F. Khokhryakov, and V. G. Ralchenko, 2015, "Crystal growth of diamond," in *Handbook of Crystal Growth: Bulk Crystal Growth*, 2nd ed., edited by P. Rudolph (Elsevier, New York), pp. 671–713.
- Pelliccione, M., B. A. Myers, L. M. A. Pascal, A. Das, and A. C. Bleszynski Jayich, 2014, Phys. Rev. Applied **2**, 054014.
- Pfender, M., et al., 2017, Nano Lett. 17, 5931.
- Pham, L. M., 2013, "Magnetic Field Sensing with Nitrogen-Vacancy Color Centers in Diamond," Ph.D. thesis (Harvard University).
- Pham, L. M., N. Bar-Gill, C. Belthangady, D. Le Sage, P. Cappellaro, M. D. Lukin, A. Yacoby, and R. L. Walsworth, 2012, Phys. Rev. B 86, 045214.
- Pham, L. M., N. Bar-Gill, D. Le Sage, C. Belthangady, A. Stacey, M. Markham, D. J. Twitchen, M. D. Lukin, and R. L. Walsworth, 2012, Phys. Rev. B 86, 121202.
- Pham, L. M., et al., 2011, New J. Phys. 13, 045021.
- Pham, L. M., et al., 2016, Phys. Rev. B 93, 045425.
- Pinto, H., R. Jones, D. W. Palmer, J. P. Goss, P. R. Briddon, and S. Öberg, 2012, Phys. Status Solidi A **209**, 1765.

- Plakhotnik, T., M. W. Doherty, J. H. Cole, R. Chapman, and N. B. Manson, 2014, Nano Lett. 14, 4989.
- Poggiali, F., P. Cappellaro, and N. Fabbri, 2018, Phys. Rev. X 8, 021059.
- Poole, C. P., 1996, Electron Spin Resonance: A Comprehensive Treatise on Experimental Techniques, 2nd ed. (Dover Publications, Mineola, NY).
- Popa, I., T. Gaebel, M. Domhan, C. Wittmann, F. Jelezko, and J. Wrachtrup, 2004, Phys. Rev. B 70, 201203.
- Pu, A., V. Avalos, and S. Dannefaer, 2001, Diam. Relat. Mater. 10, 585.
- Pu, A., T. Bretagnon, D. Kerr, and S. Dannefaer, 2000, Diam. Relat. Mater. 9, 1450.
- Rabeau, J. R., P. Reichart, G. Tamanyan, D. N. Jamieson, S. Prawer, F. Jelezko, T. Gaebel, I. Popa, M. Domhan, and J. Wrachtrup, 2006, Appl. Phys. Lett. 88, 023113.
- Rabi, I. I., 1937, Phys. Rev. 51, 652.
- Raghunandan, M., J. Wrachtrup, and H. Weimer, 2018, Phys. Rev. Lett. 120, 150501.
- Rajendran, S., N. Zobrist, A. O. Sushkov, R. Walsworth, and M. Lukin, 2017, Phys. Rev. D **96**, 035009.
- Ramsey, N. F., 1950, Phys. Rev. 78, 695.
- Riedel, D., D. Rohner, M. Ganzhorn, T. Kaldewey, P. Appel, E. Neu, R. J. Warburton, and P. Maletinsky, 2014, Phys. Rev. Applied 2, 064011.
- Riedel, D., I. Söllner, B. J. Shields, S. Starosielec, P. Appel, E. Neu, P. Maletinsky, and R. J. Warburton, 2017, Phys. Rev. X 7, 031040.
- Robertson, R., J. J. Fox, and A. E. Martin, 1933, Phil. Trans. R. Soc. A 232, 463.
- Robertson, R., J. J. Fox, and A. E. Martin, 1936, Proc. R. Soc. A **157**, 579.
- Robledo, L., H. Bernien, T. v. d. Sar, and R. Hanson, 2011, New J. Phys. **13**, 025013.
- Rogers, L. J., S. Armstrong, M. J. Sellars, and N. B. Manson, 2008, New J. Phys. **10**, 103024.
- Romach, Y., A. Lazariev, I. Avrahami, F. Kleißler, S. Arroyo-Camejo, and N. Bar-Gill, 2019, Phys. Rev. Applied 11, 014064. Romach, Y., *et al.*, 2015, Phys. Rev. Lett. 114, 017601.
- Rondin, L., J.-P. Tetienne, T. Hingant, J.-F. Roch, P. Maletinsky, and V. Jacques, 2014, Rep. Prog. Phys. 77, 056503.
- Rondin, L., et al., 2010, Phys. Rev. B 82, 115449.
- Rong, X., J. Geng, F. Shi, Y. Liu, K. Xu, W. Ma, F. Kong, Z. Jiang, Y. Wu, and J. Du, 2015, Nat. Commun. 6, 8748.
- Rose, A., 1963, Concepts in Photoconductivity and Allied Problems (Interscience Publishers, New York).
- Rosskopf, T., A. Dussaux, K. Ohashi, M. Loretz, R. Schirhagl, H. Watanabe, S. Shikata, K. M. Itoh, and C. L. Degen, 2014, Phys. Rev. Lett. **112**, 147602.
- Rugar, D., H. J. Mamin, M. H. Sherwood, M. Kim, C. T. Rettner, K. Ohno, and D. D. Awschalom, 2015, Nat. Nanotechnol. 10, 120.
- Rutledge, K. M., and K. K. Gleason, 1998, "Characterization methods," in *Handbook of Industrial Diamonds and Diamond Films* (CRC Press, Boca Raton), Chap. 9.
- Sakaguchi, I., M. Nishitani-Gamo, K. P. Loh, H. Haneda, and T. Ando, 1999, J. Appl. Phys. **86**, 1306.
- Santori, C., P. E. Barclay, K.-M. C. Fu, and R. G. Beausoleil, 2009, Phys. Rev. B 79, 125313.
- Savitski, V. G., 2017, J. Phys. D 50, 475602.
- Schirhagl, R., K. Chang, M. Loretz, and C. L. Degen, 2014, Annu. Rev. Phys. Chem. 65, 83.
- Schloss, J. M., 2019, "Optimizing Nitrogen-Vacancy Diamond Magnetic Sensors and Imagers for Broadband Sensitivity," Ph.D. thesis (Massachusetts Institute of Technology).

- Schloss, J. M., J. F. Barry, M. J. Turner, and R. L. Walsworth, 2018, Phys. Rev. Applied 10, 034044.
- Schmitt, S., et al., 2017, Science 356, 832.
- Schoenfeld, R. S., and W. Harneit, 2011, Phys. Rev. Lett. **106**, 030802.
- Schreyvogel, C., V. Polyakov, R. Wunderlich, J. Meijer, and C. E. Nebel, 2015, Sci. Rep. 5, 12160.
- Schreyvogel, C., M. Wolfer, H. Kato, M. Schreck, and C. E. Nebel, 2014, Sci. Rep. 4, 3634.
- Schröder, T., F. Gädeke, M. J. Banholzer, and O. Benson, 2011, New J. Phys. 13, 055017.
- Schwander, M., and K. Partes, 2011, Diam. Relat. Mater. 20, 1287. Schwartz, J., S. Aloni, D. F. Ogletree, and T. Schenkel, 2012, New J. Phys. 14, 043024.
- Schwartz, J., P. Michaelides, C. D. Weis, and T. Schenkel, 2011, New J. Phys. 13, 035022.
- Shao, L., M. Zhang, M. Markham, A. M. Edmonds, and M. Loncar, 2016, Phys. Rev. Applied 6, 064008.
- Shaw, M. J., P. R. Briddon, J. P. Goss, M. J. Rayson, A. Kerridge, A. H. Harker, and A. M. Stoneham, 2005, Phys. Rev. Lett. 95, 105502.
- Shi, F., et al., 2015, Science 347, 1135.
- Shields, B. J., Q. P. Unterreithmeier, N. P. de Leon, H. Park, and M. D. Lukin, 2015, Phys. Rev. Lett. **114**, 136402.
- Shin, C. S., et al., 2012, J. Appl. Phys. 112, 124519.
- Simpson, D. A., J.-P. Tetienne, J. M. McCoey, K. Ganesan, L. T. Hall, S. Petrou, R. E. Scholten, and L. C. L. Hollenberg, 2016, Sci. Rep. 6, 22797.
- Siyushev, P., M. Nesladek, E. Bourgeois, M. Gulka, J. Hruby, T. Yamamoto, M. Trupke, T. Teraji, J. Isoya, and F. Jelezko, 2019, Science **363**, 728.
- Slepetz, B., and M. Kertesz, 2014, Phys. Chem. Chem. Phys. 16, 1515.
- Slichter, C.P., 1990, *Principles of Magnetic Resonance* (Springer, Berlin/Heidelberg).
- Smeltzer, B., J. McIntyre, and L. Childress, 2009, Phys. Rev. A 80, 050302
- Smith, W. V., P. P. Sorokin, I. L. Gelles, and G. J. Lasher, 1959, Phys. Rev. 115, 1546.
- Smits, J., J. T. Damron, P. Kehayias, A. F. McDowell, N. Mosavian, I. Fescenko, N. Ristoff, A. Laraoui, A. Jarmola, and V. M. Acosta, 2019, Sci. Adv. 5, aaw7895.
- Stanwix, P. L., L. M. Pham, J. R. Maze, D. Le Sage, T. K. Yeung, P. Cappellaro, P. R. Hemmer, A. Yacoby, M. D. Lukin, and R. L. Walsworth, 2010, Phys. Rev. B **82**, 201201.
- Staudacher, T., F. Shi, S. Pezzagna, J. Meijer, J. Du, C. A. Meriles, F. Reinhard, and J. Wrachtrup, 2013, Science **339**, 561.
- Steiner, M., P. Neumann, J. Beck, F. Jelezko, and J. Wrachtrup, 2010, Phys. Rev. B **81**, 035205.
- Steinert, S., F. Dolde, P. Neumann, A. Aird, B. Naydenov, G. Balasubramanian, F. Jelezko, and J. Wrachtrup, 2010, Rev. Sci. Instrum. **81**, 043705.
- Steinert, S., F. Ziem, L. T. Hall, A. Zappe, M. Schweikert, N. Götz, A. Aird, G. Balasubramanian, L. Hollenberg, and J. Wrachtrup, 2013, Nat. Commun. 4, 1607.
- Stepanov, V., and S. Takahashi, 2016, Phys. Rev. B **94**, 024421. Stürner, F. M., *et al.*, 2019, Diam. Relat. Mater. **93**, 59.
- Subedi, S. D., V. V. Fedorov, J. Peppers, D. V. Martyshkin, S. B. Mirov, L. Shao, and M. Loncar, 2019, Opt. Mater. Express 9, 2076. Sushkov, A. O., *et al.*, 2014, Nano Lett. 14, 6443.
- Tahara, K., H. Ozawa, T. Iwasaki, N. Mizuochi, and M. Hatano, 2015, Appl. Phys. Lett. 107, 193110.

- Tallaire, A., L. Mayer, O. Brinza, M. A. Pinault-Thaury, T. Debuisschert, and J. Achard, 2017, Appl. Phys. Lett. 111, 143101.
- Tallaire, A., V. Mille, O. Brinza, T. N. T. Thi, J. Brom, Y. Loguinov, A. Katrusha, A. Koliadin, and J. Achard, 2017, Diam. Relat. Mater. 77, 146.
- Tang, C., A. Neves, and A. Fernandes, 2004, Diam. Relat. Mater. 13, 203.
- Taylor, J. M., P. Cappellaro, L. Childress, L. Jiang, D. Budker, P. R. Hemmer, A. Yacoby, R. Walsworth, and M. D. Lukin, 2008, Nat. Phys. 4, 810.
- Teraji, T., T. Taniguchi, S. Koizumi, Y. Koide, and J. Isoya, 2013, Appl. Phys. Express 6, 055601.
- Teraji, T., et al., 2015, Phys. Status Solidi A 212, 2365.
- Tetienne, J.-P., N. Dontschuk, D. A. Broadway, A. Stacey, D. A. Simpson, and L. C. L. Hollenberg, 2017, Sci. Adv. 3, e1602429.
- Tetienne, J.-P., T. Hingant, L. Rondin, A. Cavaillès, L. Mayer, G. Dantelle, T. Gacoin, J. Wrachtrup, J.-F. Roch, and V. Jacques, 2013, Phys. Rev. B **87**, 235436.
- Tetienne, J.-P., L. Rondin, P. Spinicelli, M. Chipaux, T. Debuisschert, J.-F. Roch, and V. Jacques, 2012, New J. Phys. 14, 103033.
- Tetienne, J.-P., et al., 2018, Phys. Rev. B 97, 085402.
- Thiering, G., and A. Gali, 2018, Phys. Rev. B 98, 085207.
- Tokuda, N., 2015, "Homoepitaxial diamond growth by plasmaenhanced chemical vapor deposition," in *Novel Aspects of Diamond: From Growth to Applications*, edited by N. Yang (Springer International Publishing, Cham), pp. 1–29.
- Toyli, D. M., D. J. Christle, A. Alkauskas, B. B. Buckley, C. G. Van de Walle, and D. D. Awschalom, 2012, Phys. Rev. X 2, 031001.
- Toyli, D. M., C. F. de las Casas, D. J. Christle, V. V. Dobrovitski, and D. D. Awschalom, 2013, Proc. Natl. Acad. Sci. U.S.A. 110, 8417.
- Trusheim, M. E., and D. Englund, 2016, New J. Phys. **18**, 123023. Tucker, O. D., M. E. Newton, and J. M. Baker, 1994, Phys. Rev. B **50**, 15586.
- Twitchen, D., D. Hunt, M. Newton, J. Baker, T. Anthony, and W. Banholzer, 1999, Physica B (Amsterdam) 273–274, 628.
- Twitchen, D. J., S. L. Geoghegan, and N. Perkins, 2010, "Method for treating single crystal CVD diamond and product obtained," WO Patent No. 2010/149775 Al.
- Twitchen, D. J., M. E. Newton, J. M. Baker, T. R. Anthony, and W. F. Banholzer, 1999, Phys. Rev. B 59, 12900.
- Udvarhelyi, P., V. O. Shkolnikov, A. Gali, G. Burkard, and A. Pályi, 2018, Phys. Rev. B **98**, 075201.
- Uedono, A., K. Mori, N. Morishita, H. Itoh, S. Tanigawa, S. Fujii, and S. Shikata, 1999, J. Phys. Condens. Matter 11, 4925.
- Ulbricht, R., S. Dong, A. Gali, S. Meng, and Z.-H. Loh, 2018, Phys. Rev. B **97**, 220302.
- Ulbricht, R., and Z.-H. Loh, 2018, Phys. Rev. B 98, 094309.
- Unden, T., et al., 2016, Phys. Rev. Lett. 116, 230502.
- van der Sar, T., F. Casola, R. Walsworth, and A. Yacoby, 2015, Nat. Commun. 6, 7886.
- Vandersypen, L. M. K., and I. L. Chuang, 2005, Rev. Mod. Phys. **76**, 1037.
- Vanier, J., and C. Audoin, 1989, *The Quantum Physics of Atomic Frequency Standards* (A. Hilger, London).
- van Oort, E., and M. Glasbeek, 1990, Chem. Phys. Lett. **168**, 529. van Wyk, J. A., E. C. Reynhardt, G. L. High, and I. Kiflawi, 1997, J. Phys. D **30**, 1790.

- Vineyard, G. H., 1963, J. Math. Phys. (N.Y.) 4, 1191.
- Vins, V., 2007, "Technique of production of fancy red diamonds," U.S. Patent No. 2007/0053823 A1.
- Waldermann, F., et al., 2007, Diam. Relat. Mater. 16, 1887.
- Waldherr, G., J. Beck, M. Steiner, P. Neumann, A. Gali, T. Frauenheim, F. Jelezko, and J. Wrachtrup, 2011, Phys. Rev. Lett. **106**, 157601.
- Waldherr, G., et al., 2014, Nature (London) 506, 204.
- Walsworth, R., 2017, "Absorption-based detection of spin impurities in solid-state spin systems," U.S. Patent No. 9,658,301 B2.
- Wang, Q., C. P. Smith, M. S. Hall, C. M. Breeding, and T. M. Moses, 2005, Gems Gemol. 41, 6.
- Wang, Z.-H., G. de Lange, D. Ristè, R. Hanson, and V. V. Dobrovitski, 2012, Phys. Rev. B 85, 155204.
- Wang, Z.-H., and S. Takahashi, 2013, Phys. Rev. B 87, 115122.
- Wee, T.-L., Y.-K. Tzeng, C.-C. Han, H.-C. Chang, W. Fann, J.-H. Hsu, K.-M. Chen, and Y.-C. Yu, 2007, J. Phys. Chem. A 111, 9379.
- Weerdt, F.D., and A. Collins, 2008, Diam. Relat. Mater. 17, 171.
- Wickenbrock, A., H. Zheng, L. Bougas, N. Leefer, S. Afach, A. Jarmola, V. M. Acosta, and D. Budker, 2016, Appl. Phys. Lett. 109, 053505.
- Wieser, M. E., et al., 2013, Pure Appl. Chem. 85, 1047.
- Witzel, W. M., M. S. Carroll, A. Morello, Ł. Cywiński, and S. Das Sarma, 2010, Phys. Rev. Lett. **105**, 187602.
- Wolf, S. A., I. Rosenberg, R. Rapaport, and N. Bar-Gill, 2015, Phys. Rev. B **92**, 235410.
- Wolf, T., P. Neumann, K. Nakamura, H. Sumiya, T. Ohshima, J. Isoya, and J. Wrachtrup, 2015, Phys. Rev. X 5, 041001.
- Wood, J. D. A., D. A. Broadway, L. T. Hall, A. Stacey, D. A. Simpson, J.-P. Tetienne, and L. C. L. Hollenberg, 2016, Phys. Rev. B **94**, 155402.
- Wort, C. J., and R. S. Balmer, 2008, Mater. Today 11, 22.
- Wu, Y., F. Jelezko, M. B. Plenio, and T. Weil, 2016, Angew. Chem., Int. Ed. Engl. 55, 6586.
- Yafet, Y., 1963, in *Solid State Physics* (Elsevier, New York), Vol. 14, pp. 1–98.
- Yale, C. G., F. J. Heremans, B. B. Zhou, A. Auer, G. Burkard, and D. D. Awschalom, 2016, Nat. Photonics 10, 184.
- Yamamoto, T., C. Müller, L. P. McGuinness, T. Teraji, B. Naydenov, S. Onoda, T. Ohshima, J. Wrachtrup, F. Jelezko, and J. Isoya, 2013, Phys. Rev. B 88, 201201.
- Yamamoto, T., et al., 2013, Phys. Rev. B 88, 075206.
- Yamano, H., et al., 2017, Jpn. J. Appl. Phys. 56, 04CK08.
- Yeung, T. K., D. L. Sage, L. M. Pham, P. L. Stanwix, and R. L. Walsworth, 2012, Appl. Phys. Lett. **100**, 251111.
- Zaitsev, A., K. Moe, and W. Wang, 2017, Diam. Relat. Mater. 71, 38.Zaitsev, A. M., 2001, *Optical Properties of Diamond* (Springer, Berlin).
- Zhang, X., and E. L. Hu, 2016, Appl. Phys. Lett. 109, 081101.
- Zhao, N., S.-W. Ho, and R.-B. Liu, 2012, Phys. Rev. B 85, 115303.Zhao, N., J. Wrachtrup, and R.-B. Liu, 2014, Phys. Rev. A 90, 032319.
- Zheng, H., et al., 2019, Phys. Rev. Applied 11, 064068.
- Zhou, B.B., P.C. Jerger, V.O. Shkolnikov, F.J. Heremans, G. Burkard, and D.D. Awschalom, 2017, Phys. Rev. Lett. 119, 140503.
- Zu, C., W. B. Wang, L. He, W. G. Zhang, C. Y. Dai, F. Wang, and L. M. Duan, 2014, Nature (London) 514, 72.